Late-type Giants in the Inner Galaxy

PROEFSCHRIFT

ter verkrijging van
de graad van Doctor aan de Universiteit Leiden,
op gezag van de Rector Magnificus Dr. D.D. Breimer,
hoogleraar in de faculteit der Wiskunde en
Natuurwetenschappen en die der Geneeskunde,
volgens besluit van het College voor Promoties
te verdedigen op woensdag 30 juni 2004
klokke 16.15 uur

door

Maria Messineo
geboren te Petralia Soprana (Italië)
in 1970

Promotiecomissie

Promotor :   Prof. dr. H. J. Habing
Referent :   Dr. J. Lub

Overige leden : Prof. dr. W. B. Burton
                Dr. M.R. Cioni (European Southern Observatory, Garching bei München)
                Prof. dr. K. Kuijken
                Prof. dr. K. M. Menten (Max-Planck-Institut fuer Radioastronomie, Bonn)
                Prof. dr. A. Omont (Institut d'Astrophysique de Paris)
                Prof. dr. P. T. de Zeeuw

A Lucia e Leonardo

Front cover: "I Girasoli" by Renato Guttuso. Permission to reproduce this painting was kindly granted by Dr. Fabio Carapezza Guttuso and authorised by SIAE 2004 (Italian Society of Authors and Publishers).

Back cover: ISOGAL image taken at 7 μm (LW5 filter) of a field of $20' \times 20'$ centred on $(l, b) = -0.27°, -0.6°$, field FC–00027–00006.

Contents

Contents

Contents

Chapter 1

Introduction

The Milky Way is the cornerstone of our understanding of galaxies. The structure and kinematics of its gas and stars can be studied in unique detail due to their relative proximity. However, being located well within the Galactic disk and thereby observing the Milky Way in non–linear projection makes it difficult to properly map its large-scale morphology.

One of the interesting findings has been that observations of molecular line emission (CO, HI) and stellar motions show signatures of a Galactic Bar in the inner Galaxy. However, its characteristics such as elongation, thickness and viewing angle are still poorly constrained. One of the main obstacles has been the strong obscuration by interstellar dust toward the inner Galaxy, which makes optical studies of the stellar population in that region almost impossible. The extinction is less severe at near- and mid-infrared wavelengths. To characterise the structure and formation history of the Milky Way, several infrared surveys were conducted during the past decade: ISOGAL, MSX, DENIS, 2MASS. These data contain a wealth of information on the structure of the stellar populations that has yet to be fully analysed. Having entered a golden age for Galactic astronomy, soon even more detailed imaging and spectroscopy will be provided by the Spitzer Space Telescope, while the GAIA satellite will provide unprecedented astrometry.

My thesis research has focused on the structure and stellar population of the inner 4 kpc of the Milky Way. I have analysed data from recent infrared surveys and obtained SiO radio maser line observations of late-type giants to study the star formation history and the gravitational potential of the inner Galaxy. With ages ranging from less than 1 to 15 Gyr, the infrared-luminous late-type giant stars are representative of the bulk of the Galactic stellar population, and hence trace its star formation history. Their spatial abundance variation maps the stellar mass distribution, and thereby probes the Galactic gravitational potential. The reddening of their spectral energy distribution can be used to map the interstellar extinction. Their envelopes often emit strong molecular masers (OH, SiO) that can be detected throughout the Galaxy, and through the precise measurement of the maser line velocity they reveal the stars' line-of-sight velocities. Therefore they are ideal tracers of the Galactic kinematics and gravitational potential.
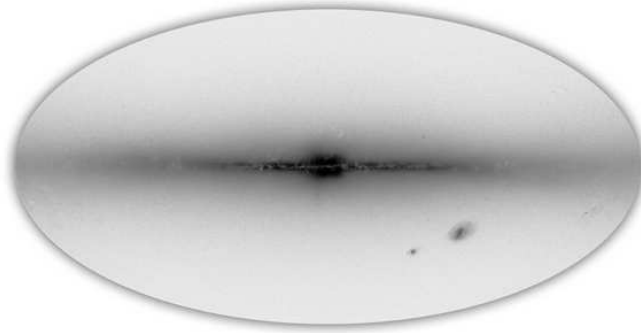
Figure 1.1: *This infrared image taken by the 2MASS satellite shows the plane of our Milky Way Galaxy as a thin disk. Dust obscuration makes the optical appearance of the Milky Way much more patchy.*

1.1 Late-type giants

In this section I shall briefly discuss the life cycle of stars, with emphasis on the red giant and asymptotic giant branch phases.

A low- to intermediate-mass star ($M_* < 8\,M_\odot$) spends 80 to 90 percent of its life on the so called main-sequence phase. This phase ends when a large fraction of the star's hydrogen has been converted to helium. Then the stellar core contracts and heats until hydrogen fusion starts in a shell surrounding the core. This causes the stellar envelope to expand to about 50 to 100 solar diameters, while the surface temperature decreases. Stars in this phase are called red giant branch (RGB) stars.

When the core temperature is high enough, helium nuclei fuse into carbon and oxygen. For stellar masses less than 2.3 solar masses (low mass stars), the core is degenerate and core helium burning begins abruptly in a so called core helium flash. In the Hertzsprung-Russell (HR) diagram this event marks the tip of the red giant branch. For higher mass stars helium burning begins more gradually. The core helium-burning phase lasts between 10 and 25 percent of a star's main-sequence lifetime.

When the core helium is exhausted, the core contracts, the envelope expands and the stellar surface temperature decreases. The star is now powered by hydrogen and helium burning in shells surrounding the core, which consists of carbon and oxygen nuclei with a degenerate distribution of electrons. A star in this phase is called an asymptotic giant branch (AGB) star. This name originates from the fact that in the HR diagram for low mass stars the AGB branch approaches the RGB sequence asymptotically. They can be as large as several hundred solar radii
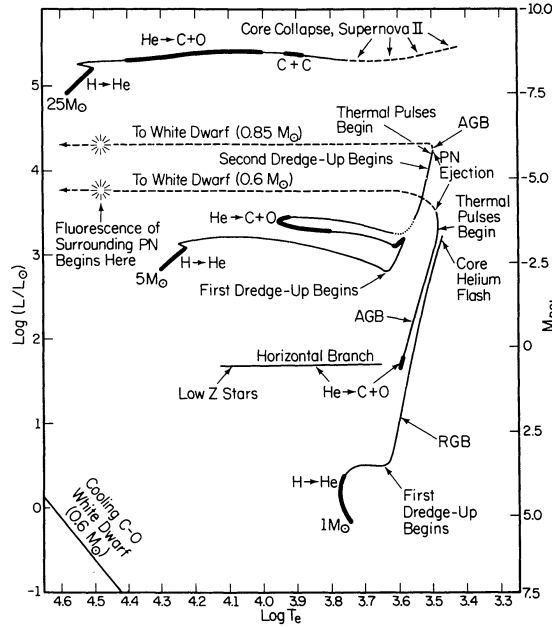
Figure 1.2: *Stellar evolution tracks of 1, 5, and 25 M$_\odot$ stars in the H-R diagram (Iben 1985).*

and have a relatively cool surface temperature of about 3000 K.

At the beginning of the AGB phase, helium shell burning prevails over shell hydrogen burning, so the C-O core grows steadily in mass, approaching the hydrogen shell (E-AGB). When the mass of helium between the core and the hydrogen shell drops below a critical value, the helium shell exhibits oscillations that eventually develop into the first helium shell flash and the thermally pulsating (TP-AGB) phase begins. A dredge-up (the third dredge-up) may take place during this phase, bringing carbon to the surface.

Mass-loss reduces the envelope mass until the residual envelope is ejected in a short superwind phase. The strength of the wind controls the decrease of the stellar mass (as the star climbs the AGB in the HR diagram), which also affects the evolution of its surface composition. Mass-loss may occur also in RGB stars close to the RGB tip, but with much lower intensity than in AGB stars.

The third dredge-up is fundamental to explain the conversion of a fraction of oxygen-rich AGB stars into carbon-rich AGB stars (for which [C/O]> 1) and predicts that the latter form only above a specific minimum luminosity. Carbon stars are virtually absent in the Galactic bulge, whereas they are numerous in the Magellanic Clouds, suggesting that the lower metallicity there provides for a more

3

efficient dredge-up.

AGB stars produce roughly one third of the carbon in the Galaxy, almost the same amount as supernovae and Wolf-Rayet stars. By returning dust and gas to the interstellar medium, RGB and AGB stars pave the way for the formation of future generations of stars and planets.

Due to their low surface temperatures, late-type giants (RGB and AGB) are bright at infrared wavelengths. Facing a high interstellar extinction toward the central regions of the Milky Way that obscures stars at visible wavelengths, red giants are the best targets for studies of the stellar populations, dynamics, and star formation history in the inner Galaxy.

1.1.1 AGB star and variability

An important property of AGB stars with direct applications to Galactic structure studies is their luminosity variability. The radial pulsations of AGB stars are confined to the large convective envelopes and should not be confused with the thermal pulse that originates in the helium burning shell. The latter leads to a longer-term variability.

Variable AGB stars are named in several different ways based on the light curve properties and periods: large amplitude variables (LAV), long period variables (LPV), Mira variables, semiregular (SR) and irregular variables.

By definition, Mira stars show pulsations with large amplitudes at visual wavelengths (more than 2.5 mag) and vary relatively regularly with typical periods of 200 to 600 days. Semiregular variables show smaller amplitudes (less than 2.5 mag) and they have a definite periodicity. Since they are obscured in the visual, this classification cannot be applied to inner Galactic variable AGB stars. Therefore, for inner Galactic variable stars 'LAVs' and 'LPVs' refer to variations in the K-band. Mira stars are usually LAVs with K-band variation amplitudes larger than 0.3 mag.

Another important class of AGB variable stars are OH/IR stars, which are dust-enshrouded infrared variable stars. They are discovered in the infrared and show 1612 MHz OH maser emission. Their periods are typically longer than 600 days and can exceed 1500 days.

Recent observations from the MACHO, EROS and OGLE surveys initiated a discussion on the pulsation modes of long period variables and on the period-luminosity relations. Such period-luminosity relations are important for Galactic structure studies as they yield estimates for a star's distance. The new data reveals four parallel period-luminosity sequences (A-D). However, the classical period-luminosity relation discovered by Feast et al. (1989), which is based on visual observations of Mira stars, still holds and coincides with the C sequence. Large amplitude variables with a single periodicity, like probably most of our SiO targets, populate this sequence.

4

1.1.2 Circumstellar maser emission

MASER stands for Microwave Amplification by Stimulated Emission of Radiation. In 1964 Charles Townes, Nicolay Gennadiyevich Basov and Aleksandr Mikhailovich Prochorov received the Nobel Prize for their discovery of the maser phenomenon. Now, forty years later, we know of thousands of astronomical masers, "radio radiation detected in some lines of certain astronomical molecules, attributed to the natural occurrence of the maser phenomenon" (Elitzur).

Maser radiation is caused by a population inversion in the energy levels of atoms or molecules. The non-equilibrium inversion is caused by different pumping mechanisms, in astronomical objects usually infrared radiation and collisions.

An observed line can be identified as a maser line on the basis of its unusually narrow line-width, or when line ratios indicate deviations from thermal equilibrium.

Various molecules can show maser emission. Astronomical masers are found around late-type stars (circumstellar masers), and in the cores of dense molecular clouds (interstellar masers). A comprehensive review of astronomical masers was given by Elitzur (1992) and Reid & Moran (1988). In this thesis we study circumstellar maser emission.

The circumstellar envelopes of oxygen-rich late-type stars can exhibit maser emission from SiO, H_2O, and OH molecules (Habing 1996). Masers occur in distinct regions at various distances from the central star. SiO masers at 43 and 86 GHz originate from near the stellar photosphere, within the dust formation zone (Reid & Menten 1997). Water masers originate further out, at distances of up to 10^{15} cm from the central star, while OH masers are found in the cooler outer regions of the stellar envelope, about ten times further out.

The presence or absence of particular maser lines in a circumstellar envelope appears to depend on the opacity at 9.7μm: a higher mass-loss rate leads to a more opaque dust shell, which shields molecules better against photodissociation by interstellar UV radiation.

SiO masers arise from rotational transitions in excited vibrational states. These levels can be highly populated only near the star where the excitation rates are high. SiO maser emission has been detected in different transitions towards oxygen-rich AGB stars (i.e. Mira variables, semi-regular variables, OH/IR stars) and supergiants. The relative intensity of different SiO maser lines varies among different sources, indicating that the SiO maser pumping mechanism depends on the mass-loss rate. Maser pumping is dominantly radiative, as suggested by the observed correlation between the maser intensity and the stellar infrared luminosity. However, collisional pumping cannot be ruled out. A maser line can show the stellar line of sight velocity with an accuracy of a few $km\,s^{-1}$.

H_2O (22 GHz) and OH (1612 MHz, 1667 MHz and 1665 MHz) masers originate from transitions in the ground vibrational state. H_2O maser spectra are irregular and variable. Therefore they are not useful for an accurate determination of stellar line of sight velocities. The 1612 MHz OH maser line is pumped by radiation from the circumstellar dust, which excites the 35 μm OH line and has a typical

double-peaked profile. The stellar velocity lies between the two peaks and the distance between the two peaks yields a measure of the expansion velocity of the circumstellar envelope.

Lewis (1989) analysed colours of and masers from IRAS stars, suggesting a chronological sequence of increasing mass-loss rate: from SiO, via H_2O to OH masers. This sequence links AGB stars via the Mira and OH/IR stages with Planetary Nebulae. However, parameters other than mass-loss, such as stellar abundance, probably also play an important role (Habing 1996).

1.2 The Milky Way galaxy
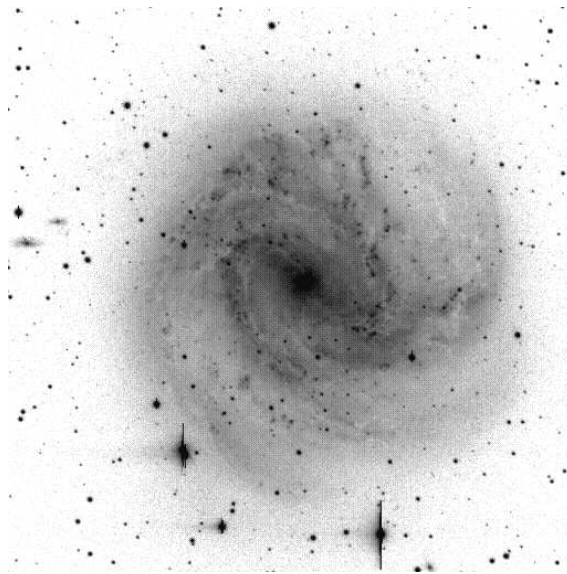
Figure 1.3: *The Southern Pinwheel galaxy, M83, was classified as intermediate between normal and barred spiral galaxies by G. de Vaucouleurs. It has both a pronounced disk component exhibiting a spiral structure, and a prominent nuclear region, which is part of a notable bulge/halo component. The Milky Way might look similar to M83.*

Our home Galaxy, the Milky Way, is a large disk galaxy. It is likely to be of Hubble type SBbc, with its main components being the bulge, the disk, and the halo.

The Milky Way today is the result of star formation, gas flow, and mergers integrated over time. The different Galactic components were not formed by independent events, and their formation history is largely unknown. The pos-

sible connection between the star formation history and the formation of Galactic structures is equally unknown.

Halo
The halo is composed of a dark matter and a stellar halo. The dark halo is of yet unknown nature and dominates the total Galactic mass, as suggested by dynamical studies of satellite galaxies. The stellar halo, a roughly spherical distribution of stars whose chemical composition, kinematics, and evolutionary history are quite different from stars in the disk, contains the most metal-poor and possibly some of the oldest stars in the Galaxy. It retains important information on the Galactic accretion history. The recent discovery of stellar streams in the halo (e.g. Helmi et al. 1999; Ibata et al. 1994) supports the hierarchical clustering and merging scenario of galaxy formation.

Disk
The disk is usually divided into two components, the thin and thick disks. The thick disk (Gilmore & Reid 1983) is older that 10 Gyr. Its metallicity ranges from -1.7 to -0.5 [Fe/H], it has a scale height of 0.7-1.5 kpc, a scale length of 2-3.5 kpc and a vertical velocity dispersion of 40 km s^{-1}. The thin disk has a scale-height of about 250 pc and contains stars of all ages. The thick disk was probably formed from the thin disk during a merger event that heated the disk (Gilmore et al. 2002).

Bulge
There is some confusion in the use of the term "bulge". In the literature it is often used to indicate everything in the inner few kiloparsec of the Galaxy, i.e., the bar and the nuclear disk. Wyse et al. (1997) prefer to define a "bulge" as a "centrally concentrated stellar distribution with an amorphous, smooth appearance. This excludes gas, dust and recent star formation by definition, ascribing all such phenomena in the central parts of the Galaxy to the central disk, not to the bulge with which it cohabits."

The "bulge" is dominated by an old stellar component (10 Gyr). Its abundance distribution is broad, with a mean of [Fe/H]~ -0.25 dex (McWilliam & Rich 1994). It has a scale height of about 0.4 kpc, and a radial velocity dispersion of about 100 km s^{-1}.

There is growing evidence of a non-axisymmetric mass distribution in the inner Galaxy. This is found from the near-infrared light distribution, source counts, gas and stellar kinematics, and microlensing studies. However, it is not clear yet whether a distinction should be made between the triaxial Galactic bulge and the bar in the disk – a bar is defined as a thin, elongated structure in the plane.

In face-on galaxies, it is not unusual to observe both a central bulge and a bar (i.e. NGC1433). In general, bars may be populated by both old and young stars. In addition, barred galaxies often show a ring around the bar. From studies of edge-on galaxies there is indication that peanut-shaped or box-shaped (rather than spheroidal) bulges may be associated with bars. The Milky Way provides the closest example of a box-shaped bulge, and therefore it is a unique laboratory

to investigate the structure and kinematics of a boxy bulge and its relation with the disk. A bar and a triaxial bulge could both be present, distinct, and coexisting.

The existence of a distinct disk-like dense molecular cloud complex in the central few hundred pc of our Galaxy, the Central Molecular Zone (CMZ), was established in the early 1970s. Observations of ongoing star formation and the presence of ionizing stars suggest that this is a component different from the bulge. In the longitude-velocity diagram (Fig. 1.4) it generates a remarkable feature called the 180 pc-Nuclear Ring. It can be understood as a gaseous shock region at the transition between the innermost non intersecting X1 orbits and the retrograde X2 orbits (Binney et al. 1991). The total mass of the CMZ (including the central stellar cluster) amounts to $(1.4 \pm 0.6)10^9 M_\odot$, of which 99% is stellar mass, and 1% gaseous mass. Its stellar luminosity amounts to $(2.5 \pm 1)10^9 L_\odot$, 5% of the total luminosity of the Galactic disk and bulge taken together (Launhardt et al. 2002).
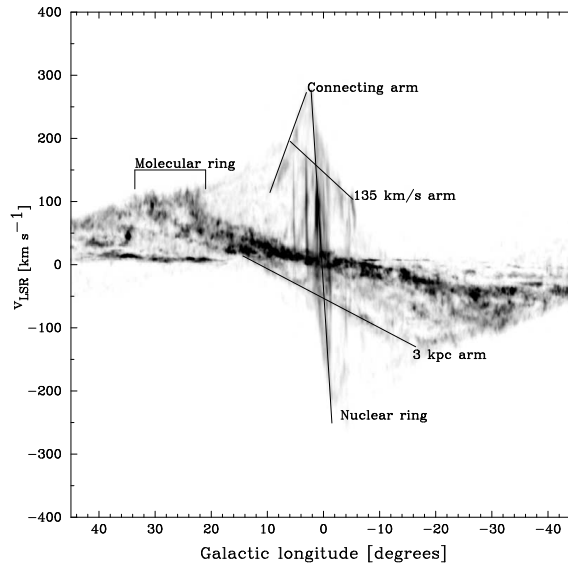
Figure 1.4: *CO (l, v) diagram from Dame et al. (2001). Gas features are labelled as in Fig. 1 of Fux (1999).*

The centre of our Galaxy contains a massive black hole. The advent of adaptive optics has permitted high spatial resolution imaging studies of the Galactic centre. A dense cluster of stars surrounds Sgr A, and proper motions of these stars were recently obtained, showing them to have high velocities of up to 5000 $km\,s^{-1}$. Thereby the mass of the central black hole has been estimated to be $(3.3 \pm 0.7) \times 10^6$ $M_\odot$ (e.g. Ghez et al. 2000; Schödel et al. 2003). Massive star formation is still going on in the central parsec of the Galaxy.

1.2.1 Stellar line of sight velocity surveys and the importance of maser surveys

Though the AGB phase is very short ($\sim 10^6$ yr) and therefore AGB stars are rare among stars, they are representative of all low and intermediate mass stars, i.e. of the bulk of the Galactic population. They are evolved stars and therefore dynamically relaxed and their kinematics traces the global Galactic gravitational potential. Thermally pulsing AGB stars are surrounded by a dense envelope of dust and molecular gas. They are bright at infrared wavelengths and can be detected even throughout highly obscured regions. Furthermore, the OH and SiO maser emission from their envelopes can be detected throughout the Galaxy, providing stellar line-of-sight velocities to within a few km s^{-1}. AGB stars thus permit a study of the Galactic kinematics, structure and mass-distribution.

This is especially useful in the inner regions of the Galaxy where the identification of other tracers like Planetary Nebulae is extremely difficult. Observations of Hα and [OIII] emission lines which easily reveal velocities of Planetary Nebulae are hampered by high interstellar extinction. A dynamical study of planetary nebulae ($-5° < b < -10°$) was performed by Beaulieu et al. (2000), who found that the spatial distribution of planetary nebulae agrees very well with the COBE light distribution. However, no conclusive results were found comparing the stellar kinematics properties with models of a barred Galaxy. The poor statistics was the main problem.

Performing radio maser surveys is the most efficient way to obtain line of sight velocities in the inner Galaxy. Two extensive blind surveys have been made at 1612 MHz searching for OH/IR stars in the Galactic plane ($|l| < 45°$, $|b| < 4°$), one in the South using the ATCA, and another in the North using the VLA (Sevenster et al. 1997a,b, 2001), yielding a sample of 766 compact OH-masing sources.

Searches at 43 or 86 GHz for SiO maser emission are also successful. SiO maser lines have the advantage to be found more frequently than 1612 MHz OH maser and the disadvantage that they can only be searched in targeted surveys, since the cost of an unbiased search is too high. Several 43 GHz SiO maser surveys of IRAS point sources have been conducted by Japanese groups using the Nobeyama telescope (e.g. Deguchi et al. 2000a,b; Izumiura et al. 1999). However, those surveys are not complete at low latitudes, since there IRAS suffers from confusion.

Up to day more than 1000 maser stars are known in the inner Galaxy. A kinematical analysis of Sevenster's sample of OH/IR stars (Debattista et al. 2002; Sevenster 1999b) shows clear signs of a barred potential. However, the number of line of sight velocities is still too small to allow us an unambiguous determination of the parameters of the bar. Furthermore, although most of the Galactic mass is in stars, a stellar longitude-velocity, $(l-v)$, diagram alone is not sufficient to constrain a model of Galactic dynamics, mainly due to the dispersion velocity of stars, which smooths the various features.

Improved statistics together with additional information on the distance distribution of masing stars will notably improve the understanding of the Galactic $(l-v)$ diagram. Low latitude stars are of particular importance since their motion

may contain a signature of in-plane Galactic components, e.g. the nuclear ring, and they may show better the effect of a thin bar. New targeted maser surveys in the Galactic plane are now possible using ISOGAL and MSX sources, it is this simple idea from which the work presented in this thesis originates.

1.3 Outline of this thesis

To increase the number of measured line of sight velocities in the inner Galaxy ($30° < l < -30°$, mostly at $|b| < 1°$), we began a survey of 86 GHz ($v = 1, J = 2 \rightarrow 1$) SiO maser emission. In **Chapter 2** we present the survey that was conducted with the IRAM 30-m telescope. Stars were selected from the ISOGAL and MSX catalogues to have colours of Mira-like stars. SiO maser emission was detected in 271 sources (a detection rate of 61%), doubling the number of maser derived line-of-sight velocities toward the inner Galaxy. I observed and detected the first line on August 26th, 2000: it was an unforgettable moment of joy!

The collection of near- and mid-infrared measurements of SiO targets allow us to study their energy distribution and determine their luminosity and mass-loss. **Chapter 3** describes a compilation of DENIS, 2MASS, ISOGAL, MSX and IRAS 1–25μm photometry of the 441 late-type stars which we searched for 86 GHz SiO maser emission. The comparison between DENIS and 2MASS J and K_{S} magnitudes shows that most of the sources are variable stars. MSX colours and the IRAS $[12] - [25]$ colour are consistent with those of Mira type stars with a dust silicate feature at 9.7 μm in emission, indicating only a moderate mass-loss rate.

Towards the inner Galaxy the visual extinction can exceed 30 magnitudes, and even at infrared wavelengths the extinction is significant. In **Chapter 4** we carry out the analysis of 2MASS colour magnitude diagrams of several fields in the plane at longitudes l between 0 and 30° in order to obtain extinction estimates for all SiO targets. With this analysis we are also able to put new constraints on the near-infrared extinction power-law.

The luminosity of our SiO targets is derived in **Chapter 5** and compared to that of a sample of OH/IR stars. We computed stellar bolometric magnitudes by direct integration under the observed energy distribution. Assuming a distance of 8 kpc for all stars within 5° from the Galactic centre we find the luminosity distribution to peak at $\mathrm{M_{bol}} = -5$ mag, which coincides with the peak shown by OH/IR stars in the Galactic centre. We found that the main difference between SiO targets and OH/IR stars is mass loss, which is higher in OH/IR stars. This fact offers several advantages. In contrast to OH/IR stars, SiO target stars are readily detectable in the near-infrared and therefore ideal for follow-up studies to better characterise the central star.

Considerations on the kinematics of SiO targets and future work plans are reported in **Chapter6**.

Finally in the last Chapter (**Chapter 7**) I briefly describe the ISOGAL survey, which is a 7 and 15 μm survey of $\sim$16 deg^2 towards selected fields along the

Galactic plane, mostly toward the Galactic centre. In collaboration with A. Omont (P.I.) and the ISOGAL team, I worked on the finalisation of the ISOGAL point source catalogue (Omont et al. 2003; Schuller et al. 2003). In this Chapter, I emphasise the importance of having several recent infrared surveys, such as DENIS, 2MASS, ISOGAL and MSX, in a common effort to unveil the overall structure of the Milky Way and in particular of its central and most obscured regions. These surveys require a huge amount of technical work which is of primary importance to obtain a reliable point source catalogue that can be used to perform such studies.

It is thanks to these new catalogues that the SiO maser project, i.e. the present thesis, could be performed.

References

Beaulieu, S. F., Freeman, K. C., Kalnajs, A. J., Saha, P., & Zhao, H. 2000, AJ, 120, 855

Binney, J., Gerhard, O. E., Stark, A. A., Bally, J., & Uchida, K. I. 1991, MNRAS, 252, 210

Dame, T. M., Hartmann, D., & Thaddeus, P. 2001, ApJ, 547, 792

Debattista, V. P., Gerhard, O., & Sevenster, M. N. 2002, MNRAS, 334, 355

Deguchi, S., Fujii, T., Izumiura, H., et al. 2000a, ApJS, 130, 351

Deguchi, S., Fujii, T., Izumiura, H., et al. 2000b, ApJS, 128, 571

Elitzur, M. 1992, ARA&A, 30, 75

Feast, M. W., Glass, I. S., Whitelock, P. A., & Catchpole, R. M. 1989, MNRAS, 241, 375

Fux, R. 1999, A&A, 345, 787

Ghez, A. M., Morris, M., Becklin, E. E., Tanner, A., & Kremenek, T. 2000, Nature, 407, 349

Gilmore, G. & Reid, N. 1983, MNRAS, 202, 1025

Gilmore, G., Wyse, R. F. G., & Norris, J. E. 2002, ApJ, 574, L39

Habing, H. J. 1996, A&A Rev., 7, 97

Helmi, A., White, S. D. M., de Zeeuw, P. T., & Zhao, H. 1999, Nature, 402, 53

Ibata, R. A., Gilmore, G., & Irwin, M. J. 1994, Nature, 370, 194

Iben, I. 1985, QJRAS, 26, 1

Izumiura, H., Deguchi, S., Fujii, T., et al. 1999, ApJS, 125, 257

Launhardt, R., Zylka, R., & Mezger, P. G. 2002, A&A, 384, 112

Lewis, B. M. 1989, ApJ, 338, 234

McWilliam, A. & Rich, R. M. 1994, ApJS, 91, 749

Omont, A., Gilmore, G. F., Alard, C., et al. 2003, A&A, 403, 975

Reid, M. J. & Menten, K. M. 1997, ApJ, 476, 327

Chapter 1: Introduction

Reid, M. J. & Moran, J. M. 1988, in Galactic and Extragalactic Radio Astronomy, 255–294

Schödel, R., Ott, T., Genzel, R., et al. 2003, ApJ, 596, 1015

Schuller, F., Ganesh, S., Messineo, M., et al. 2003, A&A, 403, 955

Sevenster, M. N. 1999, MNRAS, 310, 629

Sevenster, M. N., Chapman, J. M., Habing, H. J., Killeen, N. E. B., & Lindqvist, M. 1997a, A&AS, 122, 79

Sevenster, M. N., Chapman, J. M., Habing, H. J., Killeen, N. E. B., & Lindqvist, M. 1997b, A&AS, 124, 509

Sevenster, M. N., van Langevelde, H. J., Moody, R. A., et al. 2001, A&A, 366, 481

Wyse, R. F. G., Gilmore, G., & Franx, M. 1997, ARA&A, 35, 637

Chapter 2

86 GHz SiO maser survey of late-type stars in the Inner Galaxy I. Observational data

M. Messineo, H. J. Habing, L. O. Sjouwerman, A. Omont, and K. M. Menten

Abstract

We present 86 GHz ($v = 1, J = 2 \rightarrow 1$) SiO maser line observations with the IRAM 30-m telescope of a sample of 441 late-type stars in the Inner Galaxy ($-4° < l < +30°$). These stars were selected on basis of their infrared magnitudes and colours from the ISOGAL and MSX catalogues. SiO maser emission was detected in 271 sources, and their line-of-sight velocities indicate that the stars are located in the Inner Galaxy. These new detections double the number of line-of-sight velocities available from previous SiO and OH maser observations in the area covered by our survey and are, together with other samples of e.g. OH/IR stars, useful for kinematic studies of the central parts of the Galaxy.

2.1 Introduction

There has been a growing interest in studies characterizing the kinematics and the spatial distribution of stars in the Inner Galaxy ($30° < l < -30°$). Many recent studies attempt to determine the parameters that describe the dynamics and structure of the Inner Galaxy, i.e. its central bar and/or its bulge tri-axial mass distribution.

One approach is to map the spatial density of a stellar population. This has been done, e.g., for stars detected by IRAS toward the Galactic bulge (Nakada et al. 1991; Weinberg 1992), bulge Mira variables (Whitelock & Catchpole 1992), bulge red clump stars (Stanek et al. 1994) and giant stars seen in fields at symmetric longitudes with respect to the Galactic centre (Unavane & Gilmore 1998).

Optical studies of the Inner Galaxy are much hindered by the high interstellar extinction, which can exceed $A_V \approx 30$ (e.g. Schultheis et al. 1999), and thus are limited to small optical windows (Holtzman et al. 1998; Zhao et al. 1994). At infrared and radio wavelengths however, interstellar extinction is much less severe,

or even absent. Extensive infrared point source catalogues have recently become available from the ground based DENIS (Epchtein et al. 1994) and 2MASS (Beichman et al. 1998) near-infrared (nIR) surveys, the mid-infrared (mIR) ISO satellite survey (ISOGAL: Omont et al. 1999; Omont & the ISOGAL collaboration 2002), and the Midcourse Space Experiment (MSX: Egan et al. 1999; Price et al. 1997). These data have given new insights into the *spatial* stellar density distribution in the Inner Galaxy. To interpret the information given by the recent observations, detailed models all include some kind of tri-axiality: a tri-axial Galactic bulge or bar (e.g. Alard 2001; Debattista et al. 2002; López-Corredoira et al. 2001a,b; Ortwin 2002). However, the bar characteristics such as length, pattern speed, and position angle, are still poorly constrained.

Spatial density studies often neglect an important measurable dimension of phase space: the stellar line-of-sight velocity. In contrast to the large number of data points in the spatial domain of phase-space, the available data on the line-of-sight velocities of the stars is sparse because it is still difficult to measure velocities from optical or infrared studies. Asymptotic Giant Branch (AGB) stars with large mass-loss are a valuable exception, since their envelopes often harbour masers which are strong enough to be detected throughout the Galaxy and thereby reveal the line-of-sight velocity of the star to within a few $km\,s^{-1}$; frequently detected maser lines are from OH at 1.6 GHz, H_2O at 22 GHz, and SiO at 43 GHz and 86 GHz (for a review see Habing 1996). Previous SiO and OH maser surveys in the Galaxy have demonstrated that locating the circumstellar masers is an effective way to measure line-of-sight velocities of the AGB stars (e.g. Baud et al. 1979; Blommaert et al. 1994; Lindqvist et al. 1992; Deguchi et al. 2000a,b; Sevenster et al. 1997a,b, 2001; Izumiura et al. 1999; Sjouwerman et al. 1998).

Until recently, only a few hundred stellar line-of-sight velocities were known toward the inner regions of the Milky Way ($30° < l < -30°$ and $|b| < 1$), mainly from OH/IR stars, AGB stars with OH maser emission in the 1612 MHz line, mostly undetected at visual wavelengths. This number is too small to allow for a good quantitative multicomponent analysis of the Galactic structure and dynamics (Vauterin & Dejonghe 1998). Obtaining more line-of-sight velocities therefore remains an issue of prime importance. However, masers are rare among stars, because sustaining a maser requires a special physical environment. Most of the mid-infrared brightest OH/IR stars close to the Galactic plane were probably already detected in the blind OH surveys or in the targeted OH or 43 GHz SiO maser observations of colour-selected sources from the IRAS survey (e.g. van der Veen & Habing 1988). H_2O surveys (e.g. Levine 1995) are probably incomplete because the H_2O masers are strongly variable.

SiO maser emission is detected from several transitions towards oxygen-rich AGB stars and red supergiants. On the basis of the shape and the amplitude of their visual light curve AGB stars have been classified as semi-regular (SR) stars and Mira stars. Variable AGB stars may also be classified as long period variable (LPV) stars, when their periods are longer than 100 days (Habing 1996). Almost all OH/IR stars are variable and have periods longer than 500 days. In the IRAS color-color diagram the oxygen-rich AGB stars are distributed on a well-

defined sequence of increasing shell opacity and stellar mass-loss rate (e.g. Olnon et al. 1984; van der Veen & Habing 1988), which goes from Miras with the bluest colors and the 9.7 μm silicate feature in emission, to OH/IR stars with the reddest colors and the 9.7 μm silicate feature in absorption. The relative strengths of different SiO maser lines are observed to vary with AGB type (Bujarrabal et al. 1996; Nyman et al. 1993, 1986), indicating that the SiO maser properties depend on the stellar mass loss rate and on the stellar variability. The ratio of the SiO maser intensities of 43 over 86 GHz is found to be much lower in Mira stars and in supergiants than in OH/IR stars. This implies that the 86 GHz ($v = 1$) SiO maser transition is a good tool to measure stellar line-of-sight velocities of Mira-like stars. Another advantage is that Mira stars are far more numerous than OH/IR stars. However, these conclusions are based on small number statistics, and have neglected effects of variability.

To significantly enlarge the number of known stellar line-of-sight velocities we have conducted a targeted survey for the 86 GHz SiO ($v = 1, J = 2 \rightarrow 1$) maser line toward an infrared selected sample of late-type stars. Here we describe the selection of sources and the observational results. A detailed discussion of the kinematic and physical properties of the detected stars will be addressed in a forthcoming paper (Messineo et al. 2002a, in preparation). All velocities in this paper refer to line-of-sight velocities, measured with respect to the Local Standard of Rest (LSR).

2.2 Source selection

The stars to be searched for maser emission were selected from a preliminary version of the combined ISOGAL-DENIS catalogue and from the MSX catalogue. The search was limited to the Galactic plane between $l = -4°$ and $l = +30°$ and $|b| \lesssim 1°$; the lower limit in longitude is imposed by the northern latitude of the IRAM 30-m telescope.

ISOGAL is a 7 and 15 μm survey made with ISOCAM on board of ISO of $\sim$16 deg^2, in selected fields along the Galactic plane, mostly toward the Galactic centre. The 7 and 15 μm observations were generally taken at different epochs. With a sensitivity of 10 mJy (two orders of magnitude deeper than IRAS) and a resolution of 3-6″ ISOGAL detected over 100,000 objects. The combination of the mIR data with the *I, J,* and K_S-band DENIS photometric catalogue (Epchtein et al. 1994) allows for a good determination of the nature of these sources. ISOGAL has sampled the AGB population in the Galactic bulge ranging from the highly obscured, mIR luminous OH/IR stars, to the lower mass-loss Mira and SR stars near the tip of Red Giant Branch, at $K_o \sim 8.2$ at the adopted distance of 8.0 kpc to the Galactic centre (Alard et al. 2001; Glass 1999; Ortiz et al. 2002; Omont et al. 1999). The Midcourse Space Experiment (MSX) is a survey at five mIR wavelengths (from 4.3 μm [B1 band], to 21.4 μm [E band]) which covers the entire Galactic plane to $\pm 5°$ Galactic latitude (Egan et al. 1999). With a sensitivity of 0.1 Jy in band A (8.28 μm) and a spatial resolution of 18.3″, the MSX Galactic plane

survey detected more than 300,000 objects.

Since the ISOGAL survey only covered a limited number of small fields, the MSX survey was used to obtain a more even distribution of candidate maser sources in the area of interest. Figure 2.1 shows the location of the observed sources.
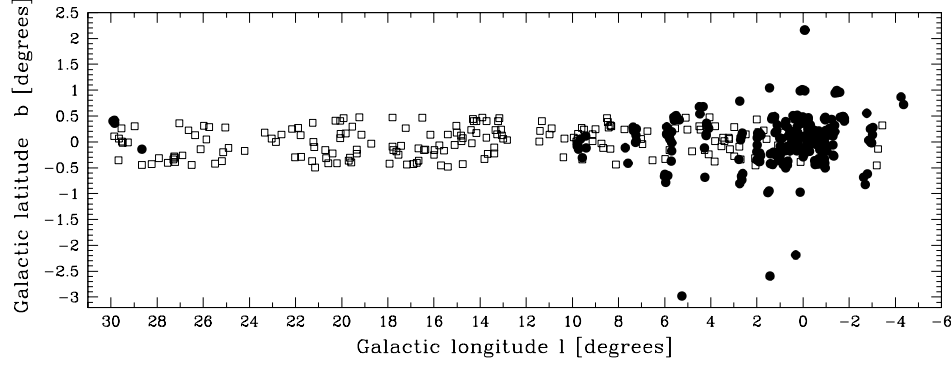
Figure 2.1: *Location of the observed sources, irrespective of detection and non-detections, in Galactic coordinates. The MSX sources are shown as open squares and the ISOGAL sources as filled circles.*

In the selection of targets, three important earlier observations were taken into account as a guideline:

- *SiO maser emission occurs more frequently towards M-type Mira stars than towards other AGB stars* (Bujarrabal 1994; Haikala et al. 1994; Habing 1996; Lewis 1990; Matsuura et al. 2000).

- *86 GHz SiO maser emission is fainter towards OH/IR stars than towards Mira stars* (Lewis 1990; Nyman et al. 1993, 1986). Nyman et al. (1993, 1986) found that the ratio of the 43 over 86 GHz ($v = 1$) SiO maser line flux is much higher for OH/IR stars, varying from 2 to 10 with increasing mass-loss rate, than for Mira stars (0.4) as found by Lane (1982). For typical 43 GHz maser line intensities measured for Galactic bulge OH/IR stars (Lindqvist et al. 1991; Sjouwerman et al. 2002a), and for the low 86 to 43 GHz line flux ratios generally seen towards OH/IR stars, such stars should be weak at 86 GHz and at the distance of the Galactic centre, while Mira stars should be stronger.

- *The SiO maser line flux correlates with the mIR continuum flux density* (Alcolea et al. 1989; Bujarrabal 1994; Bujarrabal et al. 1987; Jiang 2002). Previous studies have shown that the 43 GHz ($v = 1$ and $v = 2$) line peak intensity correlates with the ($\sim$ 7-12 μm) mIR continuum flux density (Bujarrabal 1994). The mIR and maser intensities vary together during the stellar cycle. Measuring the respective flux densities at the maximum, Bujarrabal et al.

(1987) found that the $IR_{8\ \mu m}/SiO_{43\ GHz,v=1}$ ratio is ~ 5 in O-rich Mira stars. The $IR_{12\ \mu m}/SiO_{86\ GHz,v=1}$ ratio was found to be ~ 10, albeit with a large scatter, by Bujarrabal et al. (1996) in a sample of O-rich late-type stars.

These observations provided us with criteria for our target selection, such as a lower IR flux density limit in order to detect the maser and IR colours to exclude the high mass-loss AGB stars. To avoid OH/IR stars, for which kinematic data is already known, we compiled a list of known OH/IR stars by combining the catalogues of Sevenster et al. (1997a,b, 2001), Sjouwerman et al. (1998) and Lindqvist et al. (1992).

2.2.1 ISOGAL selection criteria

The ISOGAL catalogue lists the measurements at 7 and 15 μm in magnitudes, here indicated as [7] and [15], respectively. The magnitudes of the sources in the ISOGAL-DENIS catalogue were corrected for extinction using an extinction map derived from the DENIS data by Schultheis et al. (1999) and using the extinction ratios $(A_V : A_I : A_J : A_K : A_7 : A_{15}) = (1 : 0.469 : 0.256 : 0.089 : 0.020 : 0.025)$ (Glass 1999; Hennebelle et al. 2001; Teyssier et al. 2002).

We cross-referenced the Galactic centre LPV positions (Glass et al. 2001, 0.5″ accuracy) with the ISOGAL-DENIS catalogues and found 180 possible counterparts out of 194 variables located in fields observed by ISOGAL. The missing sources can be explained by blending with other sources or by high background emission (the complete description of this cross-correlation will be the subject of a forthcoming paper). Analyzing the locations of the LPV stars in the different ISOGAL-DENIS colour-magnitude diagrams (e.g. Fig. 2.2 and Fig. 2.3), where extinction corrected values are indicated by the suffix ″o″, we found that in the $(K_o - [15]_o)$ versus $[15]_o$ colour-magnitude diagram the LPVs without OH masers separate well from the OH/IR stars (at $(K_o - [15]_o) \approx 4$; Fig. 2.2).

The OH/IR stars, having 10^2 to 10^3 times higher mass-loss rates than Mira stars, are the brightest objects at 15 μm and have $(K_o - [15]_o)$ colour redder than 4 mag (Ortiz et al. 2002). This colour is an excellent indicator of infrared emission by the stellar envelope (Omont et al. 1999).

We selected sources from the ISOGAL catalogue by their $[15]_o$ magnitude, and their $(K_o - [15]_o)$ and $([7]_o - [15]_o)$ colours. See the search boxes in Fig. 2.2 and 2.3. We excluded the brightest 15 μm sources, $[15]_o < 1.0$, and those with $([7]_o - [15]_o) < 0.7$ and with $(K_o - [15]_o) < 1.95$, since they are likely to be foreground stars. We further excluded sources with $[15]_o > 3.4$ since they are –given the general correlation of SiO maser emission and IR luminosity– likely to show SiO maser emission fainter than our detection limit of 0.2 Jy. Sources with $([7]_o - [15]_o) > 2.3$ were excluded since they are likely to be compact HII regions or young stellar objects (Felli et al. 2000; Schuller 2002), and those with $(K_o - [15]_o) > 4.85$ because they are likely to be OH/IR stars with a high mass-loss rate (Fig. 2.2) or young stellar objects. To conservatively avoid duplicating the OH maser line-of-sight data points, sources near (50″) a known OH maser were excluded.

As the final photometry of ISO has changed slightly from the preliminary input catalogue, 16 of the selected sources no longer obey the selection criteria strictly. 253 objects were observed from the selected ISOGAL-DENIS sources.
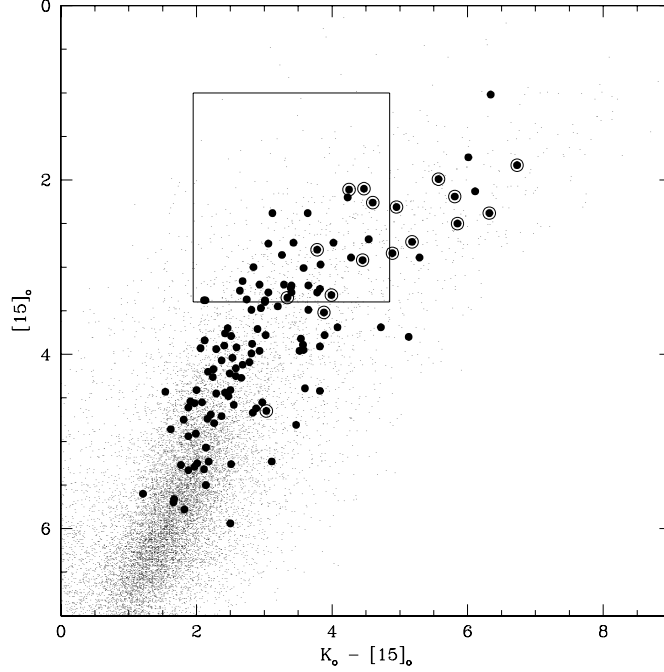
Figure 2.2: $[15]_o$ *versus ($K_o - [15]_o$) ISOGAL-DENIS colour-magnitude diagram; extinction correction has been applied. LPV stars from Glass et al. (2001) are shown as big dots of which the encircled ones mark the variables with known OH maser emission. For comparison, the numerous small dots indicate all the ISOGAL sources within 5 degrees from the Galactic centre. The rectangular box defines the region of our sample. Note that the very red variables without OH emission to the right of the box in this figure correspond to outliers without OH emission in Fig. 2.3.*

2.2.2 MSX selection criteria

Since the MSX catalogue gives the source flux density, F, in Jy, here we use this unit. Magnitudes are obtained adopting as zero points: 58.55 Jy in A (8.26 μm) band, 26.51 Jy in C (12.12 μm) band, 18.29 Jy in D (14.65 μm) band and 8.75 Jy in E (21.41 μm) band.

NIR data from DENIS or 2MASS was not available for the MSX sources at the time of our observations. For the source selection we used flux densities in the A
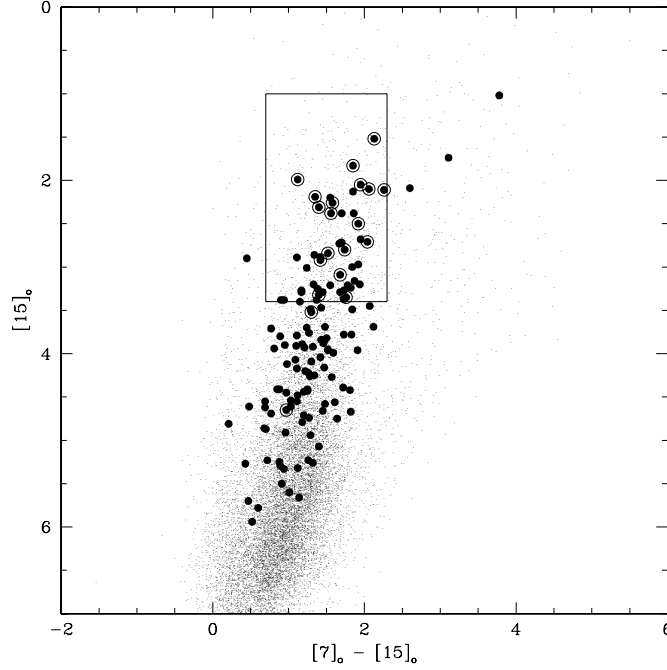
Figure 2.3: $[15]_o$ *versus* $([7]_o - [15]_o)$ *ISOGAL-DENIS colour-magnitude diagram; symbols as in Fig. 2.2. Note that a K_o is not known for all plotted sources, and they thus are missing in Fig. 2.2.*

and D bands which have wavelength ranges similar to the ISOGAL 7 and 15 μm bands. We selected those not-confused, good quality sources in band A and D (flag > 3), which show variability in band A. We avoided the reddest, $F_D/F_A > 2.29$, sources, which are likely to be OH/IR stars or young stellar objects, and the bluest and most luminous (likely foreground) stars with $F_D/F_A < 0.63$ and $F_D > 6$ Jy. Furthermore, following the work of Kwok et al. (1997) on IRAS sources with low-resolution spectra, we used the C to E band ratio to discard very red ($F_E/F_C > 1.4$) sources, which are likely to be young stellar objects or OH/IR stars with thick envelopes. Moreover, sources within 50 arcsec of a known OH maser were discarded, as the kinematic data are already known. We observed 188 sources from this MSX-selected sample.

2.3 Observations and data reduction

The observations were carried out with the IRAM 30-m telescope (Pico Veleta, Spain) between August 2000 and September 2001 (Table 2.1). Two receivers were

Table 2.1: *IRAM 30-m observing dates*

Period No.	Dates	JD-2450000
1	26-27 August 2000	1782-1783
2	04-17 December 2000	1882-1895
3	22-24 January 2001	1931-1933
4	09-24 February 2001	1949-1964
5	23-28 May 2001	2052-2057
6	15 August - 04 September 2001	2136-2156

used to observe the two orthogonal linear polarizations of the SiO ($v = 1, J = 2 \rightarrow 1$) transition at 86.24335 GHz. For each receiver we used one quarter of the low resolution, 1 MHz 1024 channel analog filter bank (3.5 km s^{-1} spectral resolution, and 890 km s^{-1} total velocity coverage), and in parallel the AOS auto-correlator at a resolution of 312.5 kHz (1.1 km s^{-1}) with a bandwidth of 280 MHz (973 km s^{-1} total velocity coverage). The telescope pointing errors were typically 2-4″, which is small compared to the beam FWHM of 29″. The observations were made in wobbler switching mode, with the wobbler throw varying between 100 and 200 arcsec. The on-source integration time was between 5 and 20 minutes per source, depending on the system temperature which varied between 100 and 300 K because of the weather, source elevation (typically 10 to 30°), and amount of continuum emission in the beam.

Flux calibration was done in a standard way from regular observations of a hot (ambient) and cold (liquid nitrogen) load. A sky-opacity-correction was computed from measuring the blank sky emissivity and using a model of the atmosphere structure. The conversion factor from antenna temperature to flux density changed from 6.0 to 6.2 Jy K^{-1} on December 12th 2000.

2.3.1 Flux stability

Two of the strongest SiO maser sources that were found in December 2000, were subsequently monitored in order to test them as possibly secondary flux calibrators. Figure 2.4 shows the measured source fluxes, in terms of antenna temperature, as a function of time over nine months. Within each observing period (up to a few weeks) the line flux measurements of the two sources are consistent within the measurement errors, with a typical day-to-day flux variation of 20 %. Over the whole period, however, the flux of the two sources varied up to a factor two. We did not notice variations of the average system temperature that might have caused systematic errors of this magnitude in the long-term flux calibration. The flux variation of both sources is therefore due to intrinsic source variability, and this makes these sources of limited use as long-term secondary flux calibrators. We shall adopt the observed short-term apparent flux variations as an indication of the absolute flux uncertainty for all our observations (i.e. $\lesssim$ 20 %).
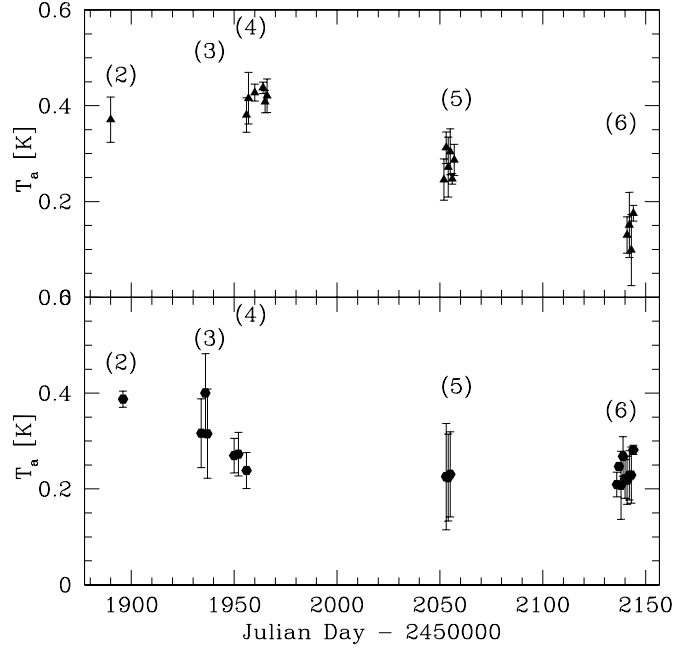
Figure 2.4: *Antenna temperatures versus time for the 2 'reference' lines: sources #265 plotted with filled hexagons (bottom) and #163 with triangles (top). The observing date on the horizontal axis is expressed in Julian day minus 2450000. The labels refer to the observing periods in Table 2.1. The measurements of a single period agree within 20 %. A long term intrinsic variation (up to a factor of 2 in T_a) is apparent in both sources.*

2.3.2 Detection criteria

The data were reduced using the CLASS software package. The spectra taken with the two receivers were combined, yielding a typical rms of 15 mK (~ 100 mJy) in the AOS channels. The line width (FWHM) and the integrated antenna temperature were determined by fitting the data from the autocorrelator with a gaussian after subtracting a linear baseline. Bad channels were eliminated by comparing the analog filter bank and autocorrelator spectra.

We considered as a detection only lines with peak antenna temperature greater than three times the rms noise level in the autocorrelator spectrum at the original resolution. Because of possible confusion with $H^{13}CN$ lines, a problem discussed in the following subsection, single component emission lines detected at line-of-sight velocity less than -30 km s^{-1} were interpreted as SiO maser lines only if their line width is smaller than 7.5 km s^{-1}.

2.3.3 Confusion with interstellar H^{13}CN emission

The total autocorrelator spectral bandwidth is 280 MHz, centered at the 86243.350 MHz rest frequency of the ($v = 1, J = 2 \rightarrow 1$) SiO maser transition. This observing band also includes the three ($J = 1 \rightarrow 0$) hyperfine transitions of H^{13}CN at 86338.767, 86340.184, and 86342.274 MHz. The H^{13}CN lines show up at velocity offsets of about -335 km s^{-1} (-329, -336, -343 km s^{-1}) relative to the SiO line.

The H^{13}CN line was observed in many interstellar clouds and also in the direction of Sgr A (e.g. Fukui et al. 1977; Hirota et al. 1998). In our spectra this H^{13}CN line was also detected in the direction of the Galactic centre, at $3.5° < l < -1.5°$, $|b| < 0.5°$, in 55 % of our pointings. H^{13}CN spectra generally have multiple broad components and appear in absorption as well as in emission, depending on the line intensity in the on- and off-target position (Fig. 2.5). The (l, b) distribution of the spectra that contain the H^{13}CN ($J = 1 \rightarrow 0$) line is similar to that of the Galactic centre molecular clouds, confirming that the origin is interstellar (see for example the ^{13}CO distribution in Fig. 2 of Bally et al. 1988). The H^{13}CN line has been detected also from circumstellar envelopes of carbon stars (e.g. Dayal & Bieging 1995), but will not be detectable in AGB stars at the distance of the Galactic centre (e.g. Olofsson et al. 1998).

Considering that the maximum gas velocity observed in the Galactic centre is less than 300 km s^{-1}, for example in the CO distribution (e.g. Dame et al. 2001), and considering the frequency differences between the three H^{13}CN ($J = 1 \rightarrow 0$) hyperfine transitions and the SiO ($v = 1, J = 2 \rightarrow 1$) transition, the H^{13}CN ($J = 1 \rightarrow 0$) line may be confused with SiO ($v = 1, J = 2 \rightarrow 1$) lines at velocities below -30 km s^{-1}. All lines detected at those velocities are therefore suspect and their line widths were examined in order to distinguish between SiO maser and H^{13}CN lines. The typical line width of the H^{13}CN and SiO emission is very different (Fig. 2.5). From the SiO lines detected at velocities larger than -30 km s^{-1}, i.e. where no confusion is expected, the SiO line width distribution ranges between 1.7 and 16.3 km s^{-1} with a peak at ≈ 4 km s^{-1} (Fig. 2.6); the H^{13}CN line is much wider and can be up to 100 km s^{-1} wide. With the spectral resolution of the AOS, 1 km s^{-1}, in case the H^{13}CN emission is not spatially extended, one should be able to resolve two or three of the hyperfine components, which are separated by 7 km s^{-1}. We therefore identify a spectral line at velocity below -30 km s^{-1} as an SiO maser only if it is a single emission component and if its line width (FWHM) is narrower than 7.5 km s^{-1}. For an unambiguous SiO identification further observations would be required, e.g. by searching for the 43 GHz SiO maser lines, or by using interferometric 86 GHz observations to locate the position and to determine the extent of the emission.

We have probably rejected a few SiO lines because of suspected confusion with H^{13}CN. Of the 202 SiO lines detected at velocities larger than -30 km s^{-1} 25 (12 %) have widths larger than 7.5 km s^{-1}. Within $3°$ from the Galactic centre, we found 75 SiO lines at velocities larger than -30 km s^{-1}; while at velocities smaller than -30 km s^{-1} we found 51 emission line sources with widths < 7.5 km s^{-1} (SiO lines) and 29 emission lines with widths > 7.5 km s^{-1} and with single com-
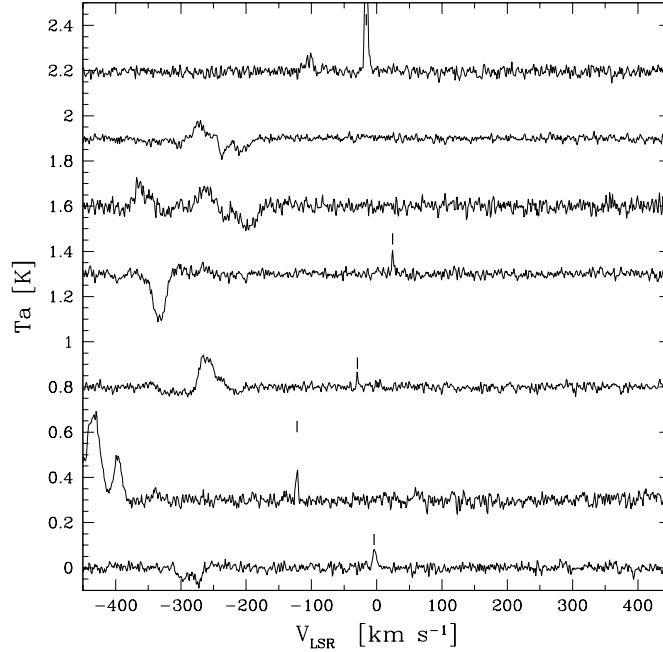
Figure 2.5: *Some spectra with interstellar H^{13}CN emission, shown for clarity with arbitrary antenna temperature offsets. The small thick vertical bars indicate the detected SiO maser line. The H^{13}CN and SiO lines are usually clearly distinct.*

ponent which we conservatively classified as H^{13}CN. Considering the above 12 %, we estimate that we could have eliminated about 7 real SiO lines.

Only one spectrum taken at a position away from the central molecular complex shows a line which is classified as H^{13}CN emission (at $l = 23°$ for source #423); this is further discussed in Sect. 4.6.

2.3.4 Confusion with interstellar SiO emission

In the interstellar medium almost all Si atoms are supposedly locked up in silicate dust particles. There is, however, some SiO emission seen towards interstellar molecular clouds (Lis et al. 2001; Martin-Pintado et al. 1992, 1997), in which case shocks have probably destroyed the refractory grain cores, releasing the silicon back into the gas phase.

However, our stellar SiO maser survey is little affected by confusion with this interstellar SiO emission for several reasons. First, we have targeted mIR sources. The bulk of the interstellar SiO emission in the Galactic centre is not associated with mIR radiation (Martin-Pintado et al. 1997). Furthermore, our SiO maser
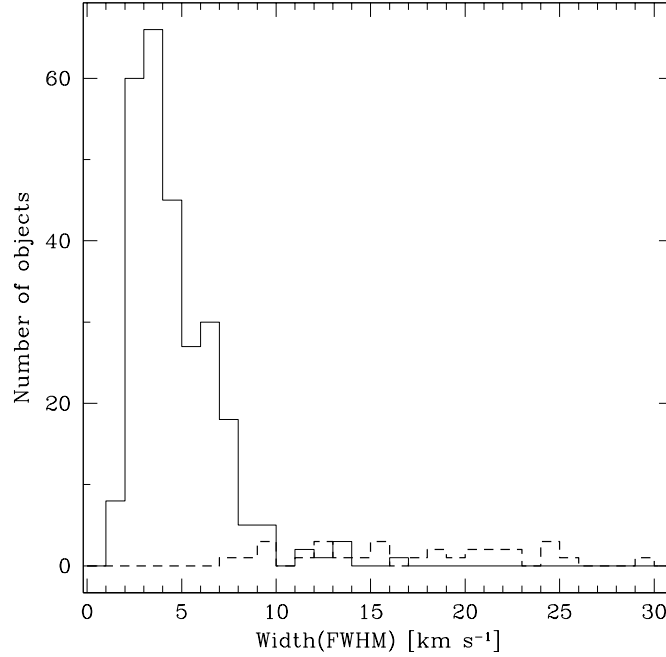
Figure 2.6: *Histogram of the line widths. The solid line shows the distribution of the SiO line widths; the dashed line shows the distribution of the lines with a single component in emission which we classified as H^{13}CN emission.*

lines are generally narrower than the 10-50 km s^{-1} found for shocked and energetic outflows associated with young stars. Young stellar objects would also be located in a different region of the colour-magnitude diagrams of Figs. 2.2 and 2.3 (Felli et al. 2000). Finally, follow-up observations with the Very Large Array (VLA) at 43 GHz have shown that 38 of 39 sources for which we detected 86 GHz SiO emission do also show unresolved 43 GHz SiO emission (Sjouwerman et al. 2002b, in preparation). It is therefore unlikely that any of this emission arises from interstellar molecular clouds.

We have also analyzed the 7 SiO lines (from Table 2.2) which have widths larger than 10 km s^{-1} (#113, #117, #129, #135, #173, #203, #223). They represent 2.5 % of our total number of detections and are located at longitudes between 2 and 18 degrees. The corresponding seven targeted mIR objects were all detected in the DENIS K band and some in the J band, and their IR colours are typical of late-type stars. Towards two of the sources, #113 and #117, we also detected H^{13}CN emission with a difference in radial velocity between the H^{13}CN and the 86 GHz SiO line of -42 and -22 km s^{-1}, respectively. The fit of the width of #113 is however noisy and can very well be less than 10 km s^{-1} or a blend of two lines.

For #117 it could be a molecular cloud line, since a difference in radial velocity between the $H^{13}CN$ and the SiO lines up to $25\,km\,s^{-1}$ has been already observed towards molecular outflows (Martin-Pintado et al. 1992). However, #117 is clearly a $\lesssim 7\,km\,s^{-1}$ wide, 43 GHz ($v = 1$ and $v = 2, J = 1 \rightarrow 0$) SiO maser point source in our VLA follow-up observations (Sjouwerman et al. 2002b, in preparation). We conclude that the mIR emission, and 43 and 86 GHz SiO lines are all related to an AGB star, although we cannot completely rule out interstellar $H^{13}CN$ emission for source #117.

Two SiO emission features are probably of interstellar origin; see comments in Sec. 4.6 for remarks on the individual sources #94 and #288.

2.4 Results

Tables 2.2 and 2.3 summarize, in order of RA, our 271 SiO maser detections and 173 non-detections, respectively. The columns of Table 2.2 are as follows: an identification number (ID), followed by the Right Ascension (RA), and Declination (DEC), (in J2000) of the telescope pointing, the velocity of the peak intensity (V_{LSR}), as well as the peak antenna temperature (T_a) and the rms noise (rms), the integrated flux density (A) plus its formal error and the line width ($FWHM$) with its formal error, and finally the observing date ($Obs.Date$). If appropriate, comments are added in an extra column. The line width was calculated using a gaussian fit. Table 2.3, with the non-detections, lists only an identification number (ID), the RA and DEC of the telescope pointing, the achieved noise (rms) and the observing date ($Obs.Date$). An additional column is used for comments on individual pointings.

Figure 2.7 shows the spectra of the detected SiO ($J = 2 \rightarrow 1, v = 1$) lines. In each panel the spectrum obtained with the autocorrelator (lower spectrum) and the one obtained with the filter bank (upper spectrum) is given. The latter is shifted arbitrarily upwards for clarity.

The Table with all the additional IR measurements (from DENIS-ISOGAL and from MSX data) will follow in the next paper where the physical properties of the sources will be discussed (Messineo et al. 2002a, in preparation).

2.4.1 Detection rate

We have observed 441 positions, and detected SiO ($v = 1, J = 2 \rightarrow 1$) maser lines in 268 of them. Since 3 spectra show two SiO lines at different velocities (#21 and #22; #64 and #65; #77 and #78) the total number of detected lines is 271 (see Table 2.2 for the detections and 2.3 for non-detections). The total detection rate is 61%.

The spectra with two detections in one single beam are most probably detections of another AGB masing star by chance in the beam ($29''$) of our targeted sources (see Sec. 4.6). The number of these detections is a function of the stellar density: the three chance detections are located within $1°$ from the Galactic centre. Considering that chance detections are distributed randomly among the overall

Table 2.2: *Sources with SiO maser detected*,**. The conversion factor from antenna temperature to flux density is 6.2 Jy K^{-1}.*

ID	RA [J2000]	DEC [J2000]	V_{LRS} [km s^{-1}]	T_a [K]	rms [K]	A [K km s^{-1}]	FWHM [km s^{-1}]	Obs.Date [yymmdd]	Comments
1	17 31 40.9	−32 03 56	−8.3	0.120	0.018	0.34 ± 0.05	2.7 ± 0.5	010216	
2	17 36 42.2	−30 59 12	−146.2	0.089	0.023	0.26 ± 0.08	3.0 ± 1.4	010219	
3	17 37 07.3	−31 21 31	−209.2	0.079	0.017	0.26 ± 0.05	3.5 ± 0.9	010216	
4	17 37 29.4	−31 17 17	−232.0	0.110	0.023	0.52 ± 0.10	6.4 ± 1.5	010219	
5	17 38 11.5	−31 46 30	10.2	0.059	0.010	0.20 ± 0.03	3.5 ± 0.6	010524/010528	
6	17 38 12.5	−29 39 38	113.4	0.074	0.017	0.48 ± 0.07	7.9 ± 1.3	010526	
7	17 38 17.0	−29 42 32	18.9	0.060	0.015	0.36 ± 0.10	8.3 ± 4.1	010822	
8	17 38 29.0	−31 26 16	−38.7	0.039	0.011	0.22 ± 0.04	6.3 ± 1.1	010219/010903	
9	17 38 32.5	−31 20 43	−73.4	0.082	0.013	0.45 ± 0.05	6.4 ± 0.8	000827	29716[b]
10	17 38 35.7	−29 36 38	1.5	0.074	0.018	0.21 ± 0.04	2.2 ± 0.4	010523	

* The full table contains 271 objects and is available in electronic form at the CDS via anonymous ftp to cdsarc.u-strasbg.fr (130.79.128.5) or via http://cdsweb.u-strasbg.fr/cgi-bin/qcat?J/A+A/(vol)/(page).

** Question marks denote marginal detections (T_a/rms < 3.5).

a Identification number from Table 2 of Glass et al. (2001).

b Identification number from Table 2 of Schultheis et al. (2000).
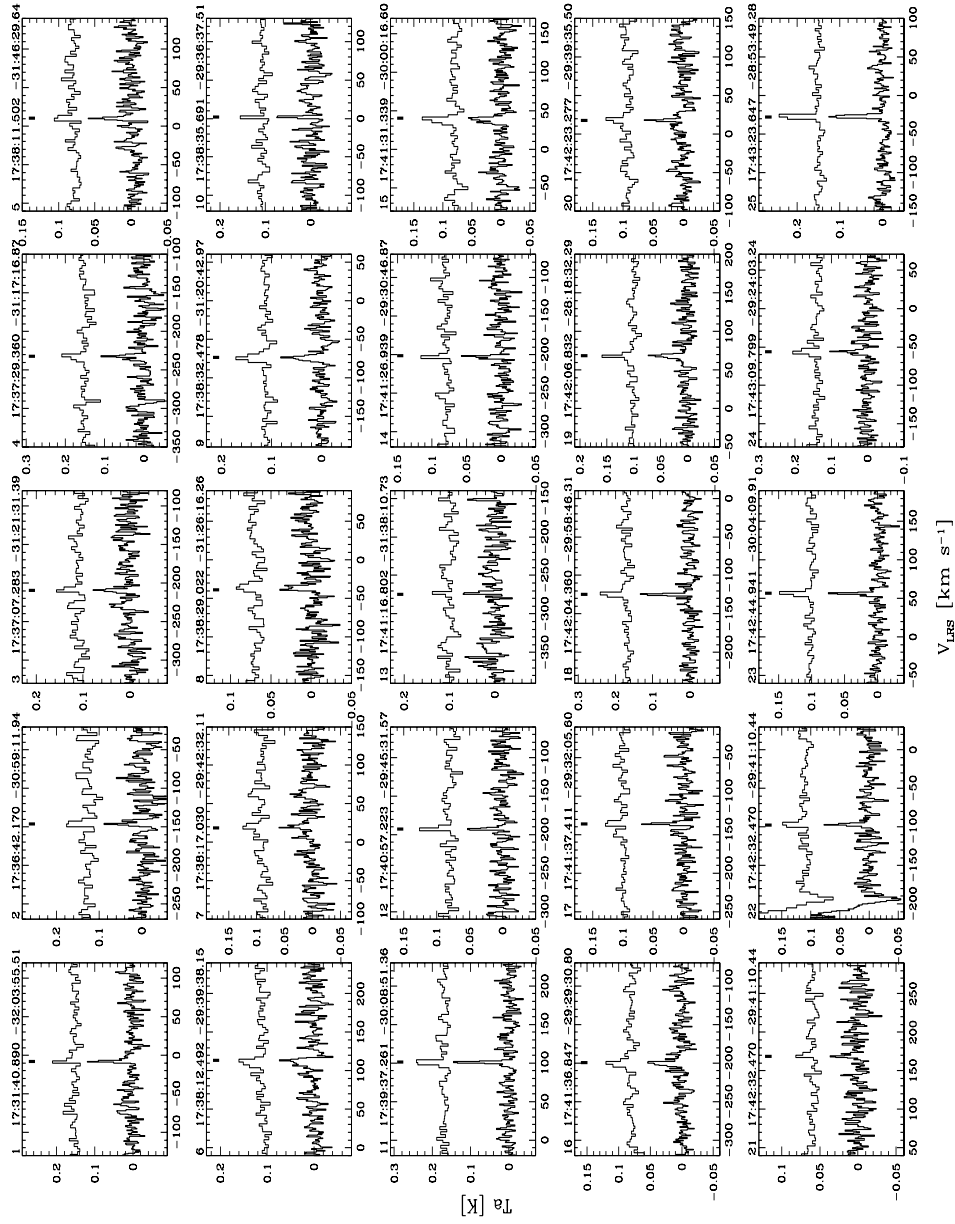
Figure 2.7: *Spectra of SiO ($J = 2 \rightarrow 1, v = 1$). Each panel shows the spectrum obtained with the autocorrelator (lower spectrum) and the one obtained with the filter bank (upper spectrum). The latter is shifted arbitrarily upwards for clarity. The full figure shows 271 spectra and is available only in the electronic version of the paper at http://www.edpsciences.org.*

27

Table 2.3: *Sources with no SiO maser detected*.The conversion factor from antenna temperature to flux density is 6.2 Jy K^{-1}.*

ID	RA [J2000]	DEC [J2000]	rms [K]	Obs.Date [yymmdd]	Comments
272	17 31 57.6	−32 14 11	0.018	010216	
273	17 35 56.2	−31 40 42	0.016	010528	
274	17 37 04.2	−27 52 04	0.017	010523	
275	17 37 07.7	−27 51 06	0.016	010523	
276	17 37 42.9	−31 24 56	0.021	010216	
277	17 38 01.6	−29 46 60	0.010	000827	
278	17 38 26.5	−31 28 22	0.011	010815	
279	17 39 29.8	−30 10 20	0.011	010219/010903	
280	17 39 30.4	−30 13 33	0.012	000826	41172[b]
281	17 39 30.7	−30 08 50	0.016	010219	37877[b]
282	17 39 35.7	−31 53 42	0.019	010523	

[*]   The full table contains 173 objects and is available in electronic form at the CDS via anonymous ftp to ftp://cdsarc.u-strasbg.fr or via http://cdsweb.u-strasbg.fr/cgi-bin/qcat?J/A+A/(vol)/(page).

[a]   Identification number from Table 2 of Glass et al. (2001).

[b]   Identification number from Table 2 of Schultheis et al. (2000).

detections and non-detections of targeted sources, we deduce 6 as the number of chance detections within one degree from the Galactic centre. This corresponds to 5 % of the 123 observations performed in that region, which in total cover 86 square arcmin. The obtained spatial density of chance detections is consistent with the 43 GHz SiO maser density, 360 sources per square degree (8.5 sources in 86 square arcmin), obtained in the Galactic centre by Miyazaki et al. (2001). This indicates that any blind survey will be less efficient than a targeted survey even in the central few degrees of our Galaxy.

The SiO maser detection rate tends to slightly increase with the mIR flux density at 7 and 15 μm. In Fig. 2.8 we show the detection rate as function of the (ISOGAL) magnitude at 15 μm, [15], or the MSX D band magnitude if no 15 μm ISOGAL magnitude is available. The detection rate is 71 % for the bright mIR sources at magnitude [15] $\sim$ 1.8 ($\sim$ 3.8 Jy), and decreases to 53 % for the less bright mIR sources at magnitude [15] $\sim$ 3.2 ($\sim$ 1 Jy).

We detected SiO maser emission in 143 out of 253 targets observed from the ISOGAL catalogue (57 %). The MSX targets give a higher detection rate: 125 de-
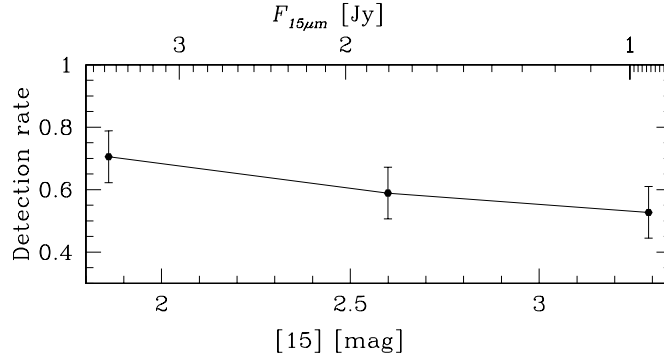
Figure 2.8: *Detection rate as a function of the magnitude at 15 μm (ISOGAL [15] or MSX D band). Each bin contains ∼ 145 sources.*

tections out of 188 sources (66 %). This is due to the correlation between the mIR flux density and the detection rate and to the different sensitivity of the ISOGAL and MSX surveys. In fact, the ISOGAL sources were selected to have magnitude at 15 μm lower than 3.4, i.e., flux density larger than ∼800 mJy, while most of the MSX targets have a flux density in the D band higher than 1.5 Jy. If we restrict our analysis to the brightest ISOGAL sources ($F_{15} > 1.5$ Jy, [15] < 2.75), we find similar results for both samples.

2.4.2 Variability

We observed 15 LPVs found by Glass et al. (2001) and detected SiO maser emission from 11 of them (73 %). Since the observations were taken at a random pulsation phase and since the SiO maser intensity is known to vary during the stellar phase by up to a factor ten (Bujarrabal 1994), this detection rate is a lower limit to the actual percentage of LPV sources characterized by 86 GHz SiO maser emission. Only 16 % of those LPV stars have associated OH emission (Glass et al. 2001), and among those within our defined colour-magnitude regions only 23 %. Among large amplitude variable AGB stars the 86 GHz SiO masers are much more frequent than OH masers.

Our sample of ISOGAL-DENIS sources also includes 19 sources from a list of Schultheis et al. (2000) of candidate variable stars, which were selected on the basis of repeated observations within the DENIS survey. We detected SiO maser emission in 8 of those stars. The low detection rate in these candidate variable stars may be due to their low mIR brightness, [15] ~ 3.2 (see Fig. 2.9 and 2.8), and the uncertain indication of variability.

For the rest of our sources the only available information on variability is given by the photometric flag in the MSX catalogue (Egan et al. 1999). The sources we
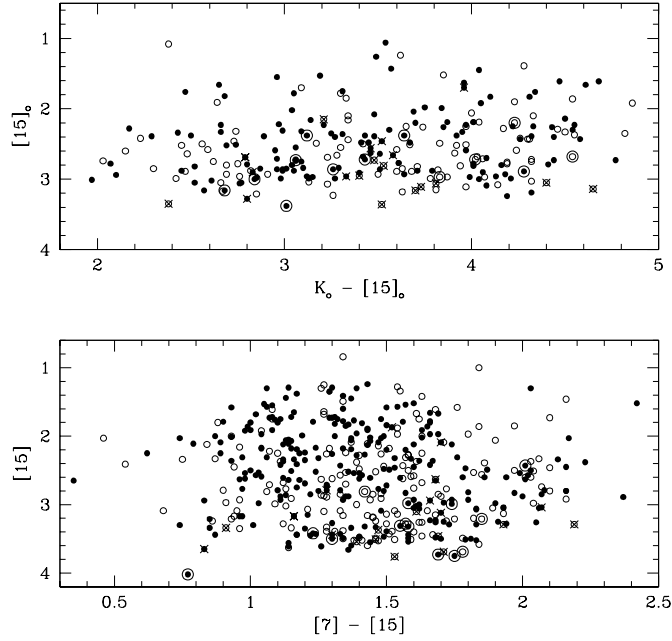
Figure 2.9: *Lower panel:* $[15]$ *versus* $([7] - [15])$ *colour-magnitude diagram; where ISOGAL magnitudes, or the A and D MSX magnitudes if no ISOGAL magnitude is available, are used. Upper panel:* $[15]_o$ *versus* $(K_o - [15]_o)$ *ISOGAL-DENIS extinction corrected colour-magnitude diagram. Detections are shown as filled circles; non detections as open circles. The LPVs from Glass et al. (2001) are marked with a larger open circle, whereas the sources from Schultheis et al. (2000) are marked with crosses. Note that two points fall outside the figure.*

selected from the MSX catalogue all have an indication of variability in band A. Of the ISOGAL-selected sources with a MSX counterpart (Messineo et al. 2002a, in preparation), about half show variability in at least one MSX band. The ISOGAL catalogue does not contain any variability information. Alard et al. (2001) have combined ISOGAL and MACHO data in Baade's Windows and found that 90 % of the objects detected in the MACHO and ISOGAL show well-defined variability (SR and Mira stars); however, for most SRs the amplitude of the variation is small. The Mira stars among these are generally the most luminous dust emitters (Fig. 1 in Alard et al. 2001). With $[15] < 3.4$, our sources are brighter than the Mira stars in Baade's Windows, the latter having shorter periods than the Galactic centre LPVs and lower luminosity (Blum et al. 1996; Glass et al. 2001). Thus, most of our sources are probably strongly variable long period AGB stars. Follow-up variability studies are recommended.

2.4.3 Line intensity

In spite of the many observational studies of SiO maser emission, its pumping mechanism is still unclear. Previous 43 GHz SiO maser and mIR observations show a linear correlation between the respective flux densities (Bujarrabal et al. 1996, 1987; Jiang 2002; Nyman et al. 1993). This correlation argues in favor of radiative pump of the SiO masers, and against collisional pumping models. The average ratio between the 86 GHz SiO ($v = 1$) maser peak intensity and the 12 μm IRAS flux density is 0.1, though with a large scatter (Bujarrabal et al. 1996).

The dotted line in Fig. 2.10 is the best fit found by Jiang (2002) between the 43 GHz SiO maser intensity and the MSX band A flux density. Our results do not constrain the linear relation between the SiO maser and the mIR flux densities. Unfortunately, our data are not suitable to study this relation because the SiO intensity distribution is limited by sensitivity and the data span less than one order of magnitude of the mIR flux density, which is narrower than the data of previous work. The scatter is caused partly by the intrinsic source variability and the non-simultaneity of the mIR and SiO maser observations, and partly by a wide range of source distances. We looked at the distance effects considering the magnitudes $\log(F_{SIO}/F_D)$ and $\log(F_A/F_D)$, which are independent of the distance, and we obtained a similar scattered diagram.
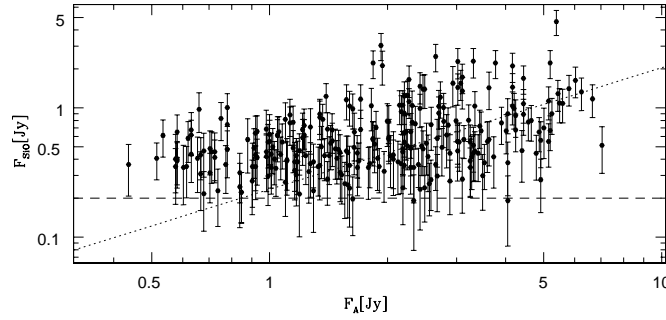
Figure 2.10: *86 GHz SiO peak intensity as a function of MSX A band or ISOGAL 7 μm flux density. The dashed horizontal line shows the average 3σ detection limit. The dotted line shows the relation obtained by Jiang (2002) from 43 GHz data.*

2.4.4 Longitude-velocity diagram

In Figure 2.11 we compare the longitude-velocity ($l - v$) distribution of our SiO maser stars with that of the ^{12}CO line emission (Dame et al. 2001). The gas kinematics is a good tracer of the dynamical mass in the Galaxy. Main features of the distribution of the CO in the Inner Galaxy are labelled in Fig. 2.11, following Fig. 1 of Fux (1999). The line-of-sight velocities of our SiO maser sources range from
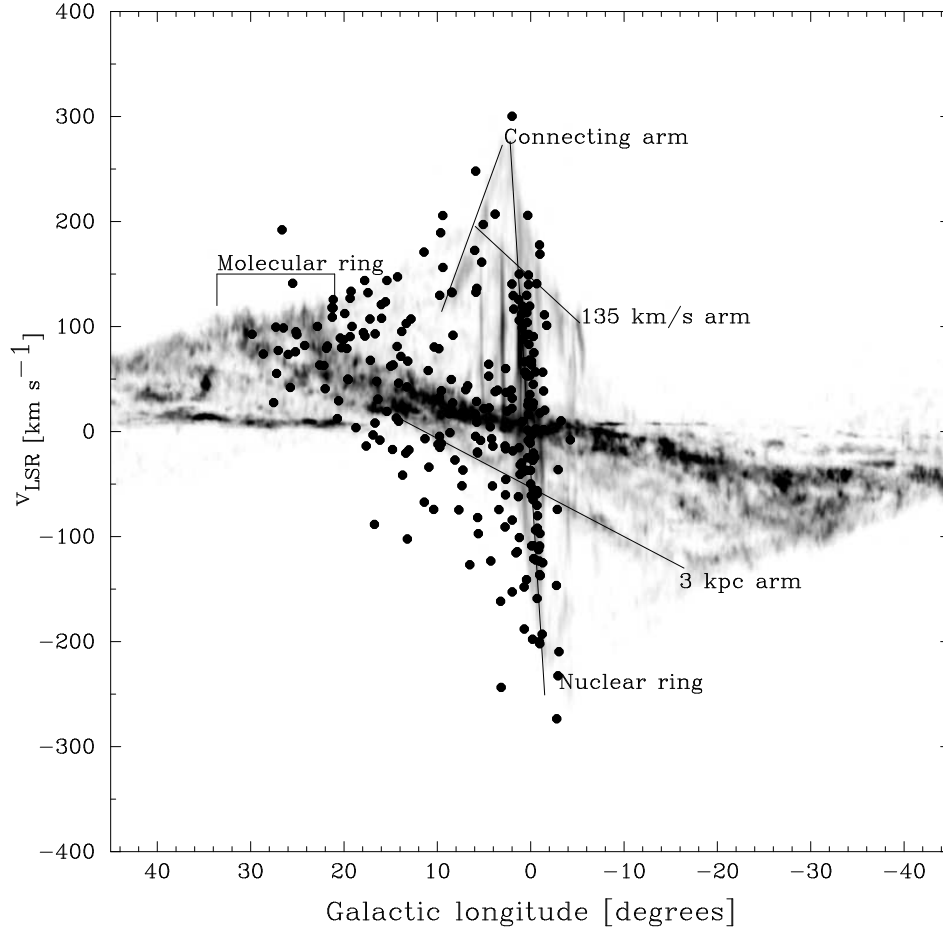
Figure 2.11: *Stellar longitude-velocity diagram overlayed on the grayscale CO (l − v) diagram from Dame et al. (2001). The SiO 86 GHz masers are shown as dots.*

−274 to 300 km s^{-1}, consistent with previous stellar maser measurements and with the CO velocities. An appreciable number of SiO sources are away from the CO emission contours, in a region forbidden for pure circular rotation, at negative velocities between $20° > l > 0°$. Around longitude $0°$ the stellar distribution follows the high velocity gas component of the nuclear disk. Similar results were found by Sevenster et al. (2001). We defer a more detailed analysis of the kinematic properties of the new SiO maser sample to a future paper.

In Figure 2.12 we have marked, as open circles, the location of the H^{13}CN lines we detected at velocities smaller than −30 km s^{-1} with widths wider than 7.5
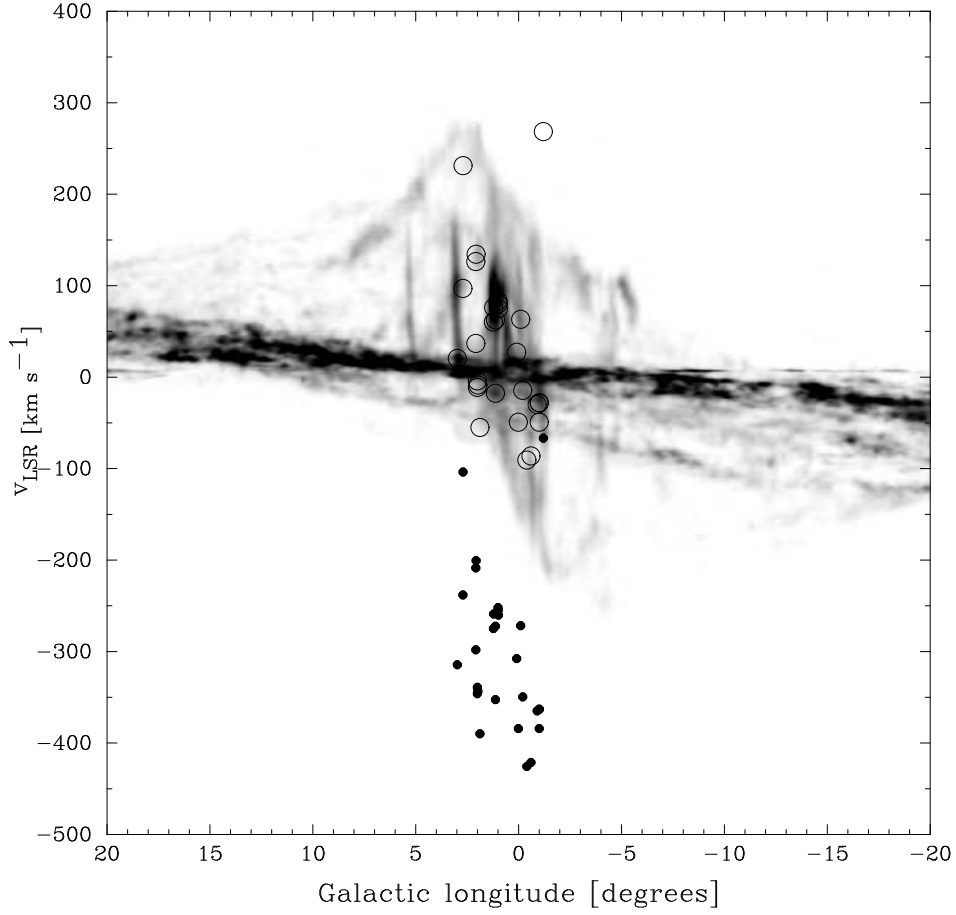
Figure 2.12: *The grayscale is the CO (l − v) diagram from Dame et al. (2001). The open circles indicate H^{13}CN lines, their location is in agreement with the CO distribution. The dots represent the position of the same lines if considered as SiO lines. The (l − v) diagram confirms the interstellar origin of those lines. The open circle located above the CO distribution at l = −1.2 (source #288) is discussed in Sec. 4.6.*

km s^{-1}. Their distribution mostly follows the central gas distribution, confirming their interstellar origin and the validity of the adopted classification criteria based on the line width.

2.4.5 Comparison with previous detections

All OH/IR stars from the catalogues by Sevenster et al. (1997a,b, 2001); Sjouwerman et al. (1998) and Lindqvist et al. (1992) were excluded from our target list since their velocities are already known from the OH maser lines. Besides, previous studies (Nyman et al. 1993, 1986) anticipate a low detectability of 86 GHz SiO masers in OH/IR stars toward the Galactic centre, which also seems to be consistent with the results of our recent 30-m IRAM survey for 86 GHz SiO masers in Galactic center OH/IR stars Messineo et al. (2002b), in preparation.

Nobeyama 43 GHz surveys

There is a small overlap between the regions observed for the Japanese 43 GHz SiO maser surveys of IRAS point sources (Deguchi et al. 2000a,b; Izumiura et al. 1999) and the region observed for our survey. Using a search radius of 25″ around each of our sources, which is about half the 43 GHz main beam at the Nobeyama telescope and almost the full 86 GHz beam of the IRAM 30-m, we found 19 matches between our positions and the IRAS sources positions (Table 2.4). The velocities at 86 and 43 GHz of 7 sources detected in both lines agree within a few $km\,s^{-1}$. Source #256 (IRAS 18301-0900) shows a difference of 8 $km\,s^{-1}$ between the SiO maser line at 43 GHz and at 86 GHz, but this source clearly has a double peak in the 43 GHz spectrum and the 86 GHz peak corresponds to one of the 43 GHz peaks. The low number of sources which are detected in both surveys needs further study, but can partially be due to source variability. Considering those 19 sources in common between the two surveys, the SiO maser detection rate appears higher at 43 GHz (68 %) than at 86 GHz (52 %). However, this small sample of sources is not representative of our full sample and of our 86 GHz SiO maser detection rate (66 % for MSX); it is biased toward redder A-D colour (higher mass-loss rate).

To avoid saturation of the detector, the very centre of the Galaxy was not observed by ISOGAL (see Ortiz et al. 2002). Therefore, none of our sources is located in the regions centered on SgrA, which were mapped at 43 GHz by Miyazaki et al. (2001) and Deguchi et al. (2002).

Imai et al. (2002) report 43 GHz SiO maser detections towards LPV stars found by Glass et al. (2001). Seven LPV stars detected at 43 GHz coincide with sources in our 86 GHz SiO maser survey (#48 = g23−5, #49 = g23−8, #52 = g21−39, #56 = g22−11, #73=g6−25, #80=g14−2, #332=g12−21). In 4 cases there is a corresponding SiO maser detection in the 86 GHz spectrum at a velocity consistent with the 43 GHz line. Sources #80 and #49 were both detected at 86 GHz, but there is a significant difference between the 86 and 43 GHz velocities of 7 and 17 $km\,s^{-1}$, respectively. The reason for this is unclear because the 43 GHz spectra were not published in Imai et al (2002). Finally, #332 was detected at 43 but not at 86 GHz, which is probably due to source variability.

Table 2.4: *Overlap between our 86 GHz SiO maser survey and the 43 GHz SiO maser survey in IRAS sources by Deguchi et al. (2000a,b); Izumiura et al. (1999). Column (1) lists the source ID number, column (2) the IRAS name, column (3) the 86 GHz line-of-sight velocity, column (4) the 43 GHz line-of-sight velocity and column (5) the separation between the IRAS position and our position.*

ID	IRAS	V_{LSR} [km s^{-1}]		separation [arcsec]
		86 GHz	43 GHz	
72	17429−2935	2.6	−0.8	22.2
125	17497−2607	−162.5	−163.1	7.6
141	17524−2419	196.0	no det	10.8
154	17563−2402	136.2	no det	15.9
162	17586−2329	−125.6	no det	7.6
166	18000−2127	134.1	134.1	6.1
187	18056−1923	−34.3	−32.2	8.7
197	18106−1734	−16.9	−16.7	21.6
236	18229−1122	112.3	111.4	4.5
256	18301−0900	101.5	109.6	5.5
361	17483−2613	no det	163.2	7.0
363	17492−2636	no det	88.8	14.9
365	17497−2608	no det	no det	4.7
371	17509−2516	no det	−93.8	5.3
400	18037−2026	no det	68.2	6.4
411	18167−1517	no det	no det	12.3
417	18238−1135	no det	180.0	6.9
418	18246−1125	no det	80.0	2.8
423	18302−0848	no det	no det	9.2

43 GHz SiO masers in the Sagittarius B2 Region

Shiki et al. (1997) mapped a subregion of Sgr B2 at 43 GHz and found seven SiO maser lines, only two of which could be identified with an IRAS source (Shiki's #3 and #6). We found an ISOGAL counterpart within 17″ in all cases, and from their mIR colours, we confirm that those seven detections are stellar maser sources in the line-of-sight of the giant molecular cloud Sgr B2. Two of those ISOGAL sources were observed in our 86 GHz survey, and for both sources the 43 and 86 GHz line velocities are consistent (see Table 2.5).

Table 2.5: *Cross identification with sources detected by Shiki et al. (1997). Reference numbers from Shiki et al. (1997) and our names are listed in column 1, and 2 respectively. The separation from the closest ISOGAL source and its name in column 3 and 4. Finally the velocities at 43 and 86 GHz in columns 8 and 9. Shiki's source number 2 is not in the ISOGAL catalogue prepared for the first release, but it is clearly a strong source in the ISOCAL image, and probably is associated with a foreground supergiant (Shiki et al 1997).*

REF	ID	separation [arcsec]	ISOGAL name	V_{LRS} [km s^{-1}]	
				43 GHz	86 GHz
1	88	6.51	$PJ174656.2-283105$	56.5	55.8
2				-25.7	
3		2.03	$PJ174720.3-282305$	82.3	
4		7.19	$PJ174812.0-281817$	80.9	
5		16.46	$PJ174823.7-282018$	81.0	
6		10.56	$PJ174814.6-280852$	101.2	
7	99	6.95	$PJ174813.2-281941$	-38.7	-36.5

2.4.6 Comments on individual objects

#21 and #22

Sources #21 and #22 were detected in the same beam. The peak intensity of #21 is only 3 times the noise rms and we list the line as a marginal detection. However, a second ISOGAL source, ISOGAL$-$PJ174232.9$-$294124, happened to fall inside the beam, at 15.6″ from the position we targeted. This source is less bright at 15 μm ([15] = 4.73) than the targeted ISOGAL$-$PJ174232.5$-$294110 ([15] = 3.17) and this suggests that the original targeted ISOGAL$-$PJ174232.5$-$294110 is the mIR counterpart of the stronger SiO line, #22, while ISOGAL$-$PJ174232.9 $-$ 294124 is probably the counterpart of #21. Observations at 86 GHz and/or both of the 43 GHz SiO lines, at both stellar positions, may confirm our conclusion.

#64 and #65

Two very narrow SiO line sources #64 and #65 were detected in the same spectrum. Both lines have the same peak intensity, but different velocities, 53.7 and -7.2 km s^{-1}, respectively. This suggests that the two lines are generated in the envelopes of two different AGB stars. The ISOGAL catalogue does not give another source within 30″ of the position of targeted ISOGAL-PJ174528.8-284734, neither does inspection of the ISOGAL images at 7 and 15 μm. However, at that position there is strong background emission which may have limited detection of fainter stellar mIR sources.

#77 and #78

Sources #77 and #78 were detected in the same spectrum at velocities of 141.6 and 27.6 km s^{-1}, respectively. The targeted ISOGAL source, ISOGAL-PJ174618.9-284439, is separated by 12.5″ from ISOGAL-PJ174619.5-284448. However, the latter is a weak mIR source only detected at 7 μm ([7] = 8.73) by ISOGAL. Again, observing at 86 or 43 GHz at both stellar positions may resolve the mIR counterpart associated with the SiO maser line.

#94

This double peaked source is located in the Sgr B2 region. The two lines have similar intensities and are at velocities −36.6 and −28.8 km s^{-1} with respect to SiO (or 299.4 and 307.2 with respect to H^{13}CN), with widths of 5 and 3 km s^{-1}, respectively. The small velocity separation between the peaks suggests that the two emissions are related. The velocity separation is also consistent with two different H^{13}CN hyperfine transitions, but one of the two peaks has a velocity larger than −30 km s^{-1} and does not fall in our H^{13}CN classification criteria. The location of this source on the $(l - v)$ diagram agrees with the CO distribution when considered as an SiO line. Thus the source is listed here among the SiO line detections. In Sgr B2, other double peaked profiles have been seen in SiO emission with line widths of $\sim$ 100 km s^{-1} and at velocities from $\sim$ −25 to $\sim$ 100 km s^{-1} (Martin-Pintado et al. 1997). The SiO emission in #94 may not be associated with the circumstellar envelope close to the star as in all other cases, as its profile may be more typical to that of bipolar molecular outflows.

#117

See the discussion in Sect. 3.4.

#288

We detected a 14.7 km s^{-1} wide line at a velocity of −66.6 km s^{-1} with respect to SiO (or 269.4 with respect to H^{13}CN), which we classified as likely being an H^{13}CN line. However, Fig. 2.12 shows that the point if regarded as H^{13}CN is far from any CO emission. The source, $(l, b) = (358.779°, 0.227°)$, is located in the region of the X-ray transient (EXS17379−2952), a region of interest to many other observers. In that region, Durouchoux et al. (1998) detect a few dense CO molecular clouds, of which one at a velocity of −60 km s^{-1}. We suggest that the SiO line at the position of #288 has an interstellar origin and is associated with the CO cloud of Durouchoux et al. (1998).

#423

At the position of #423 we detected a line which according to our criteria is an H^{13}CN line. This is the only detection outside the Galactic centre region, at a longitude of 23 degrees, that is found at high negative velocity, −204.7 km s^{-1} (with respect to SiO) and with a fairly wide line width (22 km s^{-1}). Its position as SiO line does not fit the velocity-longitude diagram (it does fit when regarded as H^{13}CN emission, then at velocity 131.3 km s^{-1}), and Izumiura et al. (1999)

searched for 43 GHz SiO maser without any success. The MSX maps do not show any extended mIR emission or dark region at that position that could suggest the presence of a cloud, however CO maps show a strong concentration of molecular matter (Dame et al. 2001). Also IRAS detected a mIR source, IRAS18302−0848, within 10″ from the MSX position, and with IRAS flux densities consistent with the MSX flux densities. For this highly reddened source, Stephenson (1992) found a strong excess (4-5 magnitudes) in the $R − I$ colour and absence of molecular bands in the I-spectrum, and concluded that any intrinsic contribution to the redness should be small.

Following his conclusion, that IRAS 18302-0848 is a distant luminous star (which has also been supported by Creese et al. 1995), we conclude that #423 is not an 86 GHz SiO maser emitter and that the origin of reddening of this star is also the origin of the H^{13}CN emission we detected.

2.5 Conclusions

We have observed 441 colour-selected ISOGAL and MSX sources in the Inner Galaxy ($30° < l < −4°$ and $|b|$ mostly < 1), in the SiO ($v = 1, J = 2 → 1$) maser transition and detected 271 lines. We thereby obtained 255 new line-of-sight velocities which doubles the number of maser line-of-sight velocities known in the region we surveyed. To search for 86 GHz ($v = 1$) SiO maser lines in colour-selected mIR sources has proven to be an efficient way to obtain stellar radial velocities in the Inner Galaxy. In the central 2 degrees we notice some confusion with interstellar H^{13}CN emission, but usually the interstellar H^{13}CN and the stellar SiO line can be separated well by using their radial velocities and line widths. The SiO maser emission was detected towards 61 % of our sources, objects which lie in a transition region of the IR-colour space between Mira and OH/IR stars. The SiO maser detectability decreases with decreasing mIR flux density. We observed 15 sources from the sample of LPV stars by Glass et al. (2001) and found 86 GHz SiO maser emission in 11 of them (73 %), while only 23 % of the LPV stars which follow our selection criteria show OH maser emission. Therefore 86 GHz SiO maser emission is more frequent than OH maser emission. In a later study we will use our new catalogue of stellar line-of-sight velocities for a quantitative analysis of stellar kinematics and SiO maser properties in the Inner Galaxy.

References

Alard, C. 2001, A&A, 379, L44

Alard, C., Blommaert, J. A. D. L., Cesarsky, C., et al. 2001, ApJ, 552, 289

Alcolea, J., Bujarrabal, V., & Gallego, J. D. 1989, A&A, 211, 187

Bally, J., Stark, A. A., Wilson, R. W., & Henkel, C. 1988, ApJ, 324, 223

Baud, B., Habing, H. J., Matthews, H. E., & Winnberg, A. 1979, A&AS, 35, 179

Beichman, C. A., Chester, T. J., Skrutskie, M., Low, F. J., & Gillett, F. 1998, PASP, 110, 480

Blommaert, J. A. D. L., van Langevelde, H. J., & Michiels, W. F. P. 1994, A&A, 287, 479

Blum, R. D., Sellgren, K., & Depoy, D. L. 1996, AJ, 112, 1988

Bujarrabal, V. 1994, A&A, 285, 953

Bujarrabal, V., Alcolea, J., Sanchez Contreras, C., & Colomer, F. 1996, A&A, 314, 883

Bujarrabal, V., Planesas, P., & del Romero, A. 1987, A&A, 175, 164

Creese, M., Jones, T. J., & Kobulnicky, H. A. 1995, AJ, 110, 268

Dame, T. M., Hartmann, D., & Thaddeus, P. 2001, ApJ, 547, 792

Dayal, A. & Bieging, J. H. 1995, ApJ, 439, 996

Debattista, V. P., Gerhard, O., & Sevenster, M. N. 2002, MNRAS accepted (astro-ph/0203375)

Deguchi, S., Fujii, T., Izumiura, H., et al. 2000a, ApJS, 130, 351

—. 2000b, ApJS, 128, 571

Deguchi, S., Fujii, T., Miyoshi, M., & Nakashima, J. 2002, PASJ, 54, 61

Durouchoux, P., Vilhu, O., Corbel, S., et al. 1998, ApJ, 507, 781

Egan, M. P., Price, S. D., Moshir, M. M., et al. 1999, AFRL-VS-TR-1999, 1522

Epchtein, N., de Batz, B., Copet, E., et al. 1994, Ap&SS, 217, 3

Felli, M., Comoretto, G., Testi, L., Omont, A., & Schuller, F. 2000, A&A, 362, 199

Fukui, Y., Iguchi, T., Kaifu, N., et al. 1977, PASJ, 29, 643

Fux, R. 1999, A&A, 345, 787

Glass, I. S. 2000, The Observatory, 120, 153

Glass, I. S., Matsumoto, S., Carter, B. S., & Sekiguchi, K. 2001, MNRAS, 321, 77

Habing, H. J. 1996, A&A Rev., 7, 97

Haikala, L. K., Nyman, L.-A., & Forsstroem, V. 1994, A&AS, 103, 107

Hennebelle, P., Pérault, M., Teyssier, D., & Ganesh, S. 2001, A&A, 365, 598

Hirota, T., Yamamoto, S., Mikami, H., & Ohishi, M. 1998, ApJ, 503, 717

Holtzman, J. A., Watson, A. M., Baum, W. A., et al. 1998, AJ, 115, 1946

Imai, H., Deguchi, S., Fujii, T., et al. 2002, PASJ, 54, L19

Izumiura, H., Deguchi, S., Fujii, T., et al. 1999, ApJS, 125, 257

Jiang, B. W. 2002, ApJ, 566, L37

Kwok, S., Volk, K., & Bidelman, W. P. 1997, ApJS, 112, 557

López-Corredoira, M., Cohen, M., & Hammersley, P. L. 2001a, A&A, 367, 106

López-Corredoira, M., Hammersley, P. L., Garzón, F., et al. 2001b, A&A, 373, 139

Lane, A. P. 1982, Ph.D. Thesis

Levine, D. A. 1995, Ph.D. Thesis

Lewis, B. M. 1990, AJ, 99, 710

Lindqvist, M., Winnberg, A., Habing, H. J., & Matthews, H. E. 1992, A&AS, 92, 43

Lindqvist, M., Winnberg, A., Johansson, L. E. B., & Ukita, N. 1991, A&A, 250, 431

Lis, D. C., Serabyn, E., Zylka, R., & Li, Y. 2001, ApJ, 550, 761

Martin-Pintado, J., Bachiller, R., & Fuente, A. 1992, A&A, 254, 315

Martin-Pintado, J., de Vicente, P., Fuente, A., & Planesas, P. 1997, ApJ, 482, L45

Matsuura, M., Yamamura, I., Murakami, H., et al. 2000, PASJ, 52, 895

Messineo, M., Habing, H., Sjouwerman, L., Omont, A., & Menten, K. 2002a, in preparation

—. 2002b, in preparation

Miyazaki, A., Deguchi, S., Tsuboi, M., Kasuga, T., & Takano, S. 2001, PASJ, 53, 501

Nakada, Y., Onaka, T., Yamamura, I., et al. 1991, Nature, 353, 140

Nyman, L.-A., Hall, P. J., & Le Bertre, T. 1993, A&A, 280, 551

Nyman, L.-A., Johansson, L. E. B., & Booth, R. S. 1986, A&A, 160, 352

Olnon, F. M., Habing, H. J., Baud, B., et al. 1984, ApJ, 278, 41

Olofsson, H., Lindqvist, M., Nyman, L.-A., & Winnberg, A. 1998, A&A, 329, 1059

Omont, A., Ganesh, S., Alard, C., et al. 1999, A&A, 348, 755

Omont, A. & the ISOGAL collaboration. 2002, in preparation

Ortiz, R., Blommaert, J. A. D. L., Copet, E., et al. 2002, A&A, 388, 279

Ortwin. 2002, To appear in: Matter in the Universe, eds. Jetzer P., Pretzl K., von Steiger R., Space Science Reviews, Kluwer.

Price, S. D., Egan, M. P., Shipman, R. F., et al. 1997, American Astronomical Society Meeting, 191

Schuller, F. & the ISOGAL collaboration. 2002, in preparation

Schultheis, M., Ganesh, S., Glass, I. S., et al. 2000, A&A, 362, 215

Schultheis, M., Ganesh, S., Simon, G., et al. 1999, A&A, 349, L69

Sevenster, M. N., Chapman, J. M., Habing, H. J., Killeen, N. E. B., & Lindqvist, M. 1997a, A&AS, 122, 79

—. 1997b, A&AS, 124, 509

Sevenster, M. N., van Langevelde, H. J., Moody, R. A., et al. 2001, A&A, 366, 481

Shiki, S., Ohishi, M., & Deguchi, S. 1997, ApJ, 478, 206

Sjouwerman, L. O., Lindqvist, M., van Langevelde, H. J., & Diamond, P. J. 2002a, submitted to A&A

Sjouwerman, L. O., Messineo, M., & Habing, H. 2002b, in preparation

Sjouwerman, L. O., van Langevelde, H. J., Winnberg, A., & Habing, H. J. 1998, A&AS, 128, 35

Stanek, K. Z., Mateo, M., Udalski, A., et al. 1994, ApJ, 429, L73

Stephenson, C. B. 1992, AJ, 103, 263

Teyssier, D., Hennebelle, P., & Pérault, M. 2002, A&A, 382, 624

Unavane, M. & Gilmore, G. 1998, MNRAS, 295, 145

van der Veen, W. E. C. J. & Habing, H. J. 1988, A&A, 194, 125

Vauterin, P. & Dejonghe, H. 1998, ApJ, 500, 233

Weinberg, M. D. 1992, ApJ, 384, 81

Whitelock, P. 1992, in ASP Conf. Ser. 30: Variable Stars and Galaxies, 11

Zhao, H., Spergel, D. N., & Rich, R. M. 1994, AJ, 108, 2154

Chapter 3

86 GHz SiO maser survey of late-type stars in the Inner Galaxy II. Infrared photometry

M. Messineo, H. J. Habing, K. M. Menten, L. O. Sjouwerman and A. Omont

Abstract

We present a compilation and study of DENIS, 2MASS, ISOGAL, MSX and IRAS 1–25μm photometry for a sample of 441 late-type stars in the inner Galaxy, which we previously searched for 86 GHz SiO maser emission (Chapter II). The comparison of the DENIS and 2MASS J and K_S magnitudes shows that most of the SiO targets are indeed variable stars. The MSX colours and the IRAS $[12] - [25]$ colour of our SiO targets are consistent with those of Mira type stars with dust silicate feature at 9.7 μm feature in emission, indicating only a moderate mass-loss rate.

3.1 Introduction

Stars of intermediate mass, $1 < M_* < 6\,M_\odot$, enter a phase of intense mass loss when they reach the Asymptotic Giant Branch (AGB). As a consequence, they are surrounded by a dense envelope of dust and molecular gas. Due to the low effective temperature and the dust thermal emission, AGB stars are bright at infrared wavelengths and can be detected even towards highly obscured regions. Furthermore, the maser emission from their envelopes is strong enough to be detected throughout the Galaxy, and radio spectroscopic observations can provide the stellar line-of-sight velocities to within a few $\mathrm{km\,s^{-1}}$ (e.g. Habing 1996). AGB stars thus permit a study of Galactic kinematics, structure, and mass-distribution.

To understand the Galactic structure and kinematics it is important to combine the kinematic information and the stellar properties, e.g. luminosities, which can provide a distance estimate. Good photometry on infrared point sources toward the inner Galaxy is now available from large surveys such as DENIS (Epchtein et al. 1994), 2MASS (Cutri et al. 2003), ISOGAL (Omont et al. 2003; Schuller et al.

2003) and MSX (Egan et al. 1999; Price et al. 2001). Since the high extinction toward the inner Galaxy precludes studies at optical wavelengths, these infrared data permit a unique view of its stellar population. The combination of near- and mid-infrared photometry enable us to examine the nature of the stars, i.e. to derive their luminosities, mass-loss rates, and to discriminate agaۯnts foreground stars.

To improve the line-of-sight velocity statistics, we conducted 86 GHz $v = 1, J = 2 \rightarrow 1$ SiO maser line observations of 441 late-type stars in the inner Galaxy ($30° < l < -4°, |b| < 1$) with the IRAM 30-m telescope (Chapter II). This paper is part of a series devoted to characterise the properties, i.e. mass-loss rates and luminosities, of the 441 sources previously targeted to search for 86 GHz SiO maser emission (Chapter II).

Here (Chapter III) we present the available near- and mid-infrared photometry of the targeted sources ("SiO targets" hereafter). In another chapter (Messineo et al. 2004a,hereafter Chapter IV) we deal with extinction correction and finally in chapter (Messineo et al. 2004a,hereafter Chapter V) we compute and analyse the luminosities of the SiO targets.

The spatial distribution of the 441 targets is shown in Fig. 3.1. These SiO targets are divided into two subsamples: 253 sources were selected from the ISOGAL catalogue, ("the ISOGAL sample"), and 188 sources from the MSX catalogue, ("the MSX sample"). The ISOGAL and MSX samples are examined to test whether both are drawn from the same "parent population". Brightness variability is studied by a comparison of the DENIS and 2MASS photometry.

The structure of the paper is as follows: in Sect. 3.2 we identify our SiO targets in various infrared catalogues and collect their magnitudes finding for many stars up to fourteen different measurements. In Sect. 3.3 we compare the statistical differences between our ISOGAL and MSX samples. In Sect. 3.4 we summarise additional information found with SIMBAD, e.g. variability and other types of masers, and we derive the probability of association between the radio maser and the infrared counterpart. The brightness variability of the stars is discussed in Sect. 3.5. In Sects. 3.6 and 3.7 we analyse the mid-infrared colours of the stars and compare them with those of OH/IR stars. The main conclusions are summarised in Sect. 5.8.

The individual source numbers (e.g #99) are taken from Table 2 (86 GHz SiO maser detections) and Table 3 (non-detections) in Chapter II unless otherwise indicated. The SiO maser emission in this paper generally refers to the 86 GHz ($v = 1, J = 2 \rightarrow 1$) SiO maser only and not to the 43 GHz ($J = 1 - 0$) SiO masers. Velocities in this paper refer to line-of-sight velocities with respect to the Local Standard of Rest.

Figure 3.1: *Location of the 441 SiO targets in Galactic coordinates. The 379 MSX counterparts are shown as open circles, the 267 ISOGAL counterparts as crosses. Overlap of MSX and ISOGAL sources resemble filled symbols. Four points fall outside the figure.*

3.2 Identification of the SiO targets in various infrared catalogues

We cross identified all SiO targets, whether taken from the ISOGAL or from the MSX database, with all infrared catalogues available to us, the DENIS, 2MASS, ISOGAL, MSX and IRAS survey catalogues. The results are summarised in Table 3.1. In the following, we briefly recall the criteria used for the selection of the ISO-GAL and the MSX samples and describe the modality of the cross-correlations. More details on the selection criteria can be found in Chapter II.

Table 3.1: *Number of counterparts of our SiO targets*

		2MASS all sky data release[a]			DENIS bulge PSC[b]			ISOGAL PSC 1.0[c]	MSX PSC 1.2[d]	IRAS PSC 2.0[e]
		J	H	K_S	I	J	K_S			
ISO	253	252	252	252	53	217	253	253	191	43
MSX	188	187	187	187	42	149	188	14	188	122
Total	441	+439	++439	439	95	*366	**441	267	379	165

[a]Cutri et al. (2003), [b]Simon (2003), [c]Schuller et al. (2003), [d]Egan et al. (1999), [e]Beichman et al. (1988).

+ 72 are upper limits   *   16 have magnitudes above saturation limits

++ 13 are upper limits   ** 104 have magnitudes above saturation limits

3.2.1 ISOGAL data

ISOGAL (Omont et al. 2003) is a 7 and 15 μm survey taken with ISOCAM (Cesarsky et al. 1996) aboard the Infrared Space Observatory (ISO) satellite (Kessler et al. 1996). The 16 deg^2 survey consists of selected sub-fields along the Galactic plane, mostly concentrating on the Galactic Centre. With a sensitivity approaching 10 mJy (two orders of magnitude deeper than IRAS and one order of magnitude deeper than MSX) and a resolution of 3-6$''$ ISOGAL has detected over 100,000 objects. The ISOCAM data have been correlated with the DENIS near-infrared I, J and K_S band data to produce the five band ISOGAL-DENIS point source catalogue (ID-PSC) (Schuller et al. 2003). The ID-PSC reports the photometric data in magnitudes. The astrometric accuracy of the ID-PSC is determined by the present DENIS astrometric accuracy better than 0.5$''$.

Sources were selected from a preliminary version of the ISOGAL catalogue by their extinction-corrected 15 μm magnitude, $[15]_0$, and their ($K_{S0} - [15]_0$) and ($[7]_0 - [15]_0$) colours approximately corrected for extinction (Sect. 7.3.2 Chapter II). The brightest 15 μm sources, $[15]_0 < 1.0$, and those with ($[7]_0 - [15]_0$) < 0.7 and with ($K_{S0} - [15]_0$) < 1.95 were excluded since they are likely to be foreground stars or non-AGB stars or AGB stars with very small mass-loss. Further, sources with $[15]_0 > 3.4$ were excluded since they are likely to show SiO maser emission fainter than our detection limit of 0.2 Jy. Sources with ($[7]_0 - [15]_0$) > 2.3 were excluded since they are likely to be compact HII regions or other young stellar objects or planetary nebulae. Those with ($K_{S0} - [15]_0$) > 4.85 were excluded because they are likely to be OH/IR stars with a high mass-loss rate or young stellar objects. Moreover, known OH/IR stars were discarded as the kinematic data are already known.

3.2.2 MSX data

The Midcourse Space Experiment (MSX) is a survey at five mid-IR bands ranging from 4.3 μm [$B1$ band] to 21.4 μm [E band], with a sensitivity of 0.1 Jy in A band (8.28 μm) and a spatial resolution of 18.3$''$ (Price et al. 2001). The survey covers the Galactic plane to $\pm5°$ latitude. Version 1.2 of the MSX-PSC (Egan et al. 1999) lists more than 300,000 point sources with an rms astrometric accuracy of $\sim 2''$. The MSX catalogue gives the source flux density, F, in Jy. Magnitudes are obtained adopting the following zero-points: 58.49 Jy in A (8.26 μm) band, 26.51 Jy in C (12.12 μm) band, 18.29 Jy in D (14.65 μm) band and 8.80 Jy in E (21.41 μm) band (Egan et al. 1999).

For the MSX source selection we used flux densities in the A and D bands which have wavelength ranges roughly similar to the ISOGAL 7 and 15 μm bands. We selected those non-confused, good-quality sources in A and D band (flag > 3), which show variability in the A band. We avoided the reddest stars, $F_D/F_A > 2.3$ ($A - D > 2.2$ mag). We also avoided the bluest and most luminous stars with $F_D/F_A < 0.6$ ($A - D < 0.75$ mag) and $F_D > 6$ Jy ($D < 1.2$ mag) since they are likely to be foreground stars or supergiants (Schuller 2002; Schultheis
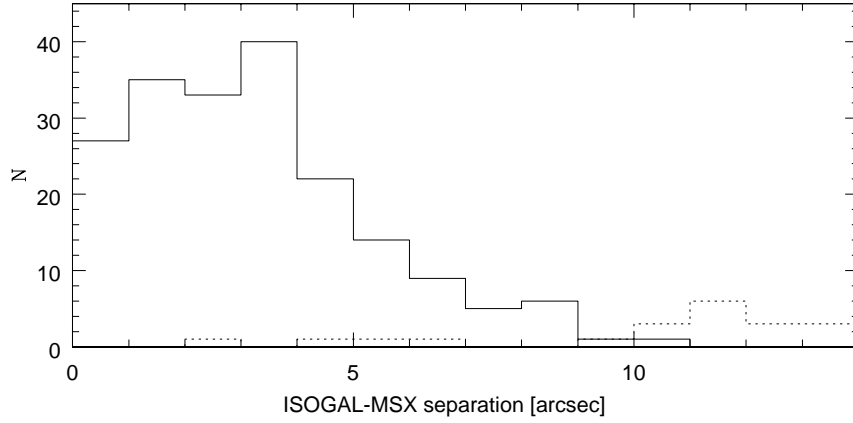
Figure 3.2: *Associations between our SiO ISOGAL targets and the MSX catalogues. The distribution of the angular separations (″) between the ISOGAL and the MSX positions (continuum line). For comparison, the dashed line is the total distribution of the chance associations, found by performing five shifting experiments.*

et al. 2003). Furthermore, following the classification of Kwok et al. (1997) of IRAS sources with low-resolution spectra, we used the C to E band ratio to discard very red ($F_E/F_C > 1.4$, $C - E > 1.55$ mag) sources, which are likely to be young stellar objects or OH/IR stars with thick envelopes. Known OH/IR stars were excluded.

3.2.3 ISOGAL-MSX cross-identifications

More than half (253) of our sample of SiO targets were selected from the ISOGAL survey, indeed from a preliminary version of the ID-PSC (Chapter II). They are all in an area covered by the MSX survey. For each of our 253 ID-PSC selected SiO targets we searched for the closest associated source in the MSX-PSC within $15''$ from the SiO target position. We found counterparts for 191 of them, 190 of which were unique. The distribution of the angular separations is shown in Fig. 3.2; the mean and median angular separation are $3.3''$ and $3.0''$ with a standard deviation of $2.1''$, the maximum separation is $10.4''$. To estimate the likely number of chance associations, we repeated the cross-correlation after shifting all ID-PSC positions between $30''$ and $100''$ finding that the probability of spurious associations within $11''$ is less than 1%. The 62 ISOGAL sources without a counterpart in the MSX-PSC are mostly (55) concentrated in the central 3 degrees from the Galactic Centre. Their 7 μm ISOGAL fluxes range from 0.4 Jy to 1.5 Jy, whereas for the 191 associated sources, the flux is on average 1.6 Jy with a standard deviation of 1.3 Jy. Thus, the ISOGAL/non-MSX sources are likely to have been excluded from the MSX-PSC because of confusion due to the high stel-
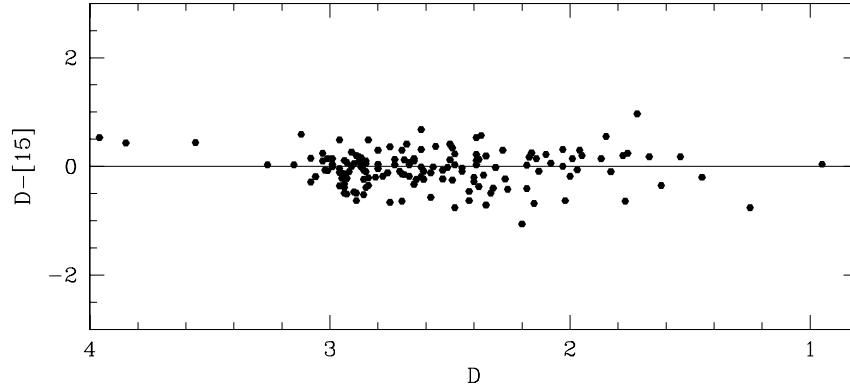
Figure 3.3: *Difference between the MSX band D magnitude, D, and the ISOCAM 15 μm magnitudes, [15], versus the D. Magnitude zero point in D band was taken from Egan et al. (1999). The continuous line is $D - [15] = 0.0$ mag*

lar density in the inner Galaxy. The fraction of our ISOGAL stars without MSX identifications is ∼11% for those with 7 μm magnitude $[7] < 4.5$ ($F_7 > 1.3$ Jy).

Out of the 188 SiO targets selected from the MSX catalogue, only 14 are located in an ISOGAL field, and we found ID-PSC identifications for all of those within $5''$ from the MSX positions. For the remaining 174 sources we searched the DENIS PSC.

As the ISOCAM 15 μm and MSX D filters are similar, we compared the ISO-CAM 15 μm magnitudes, [15], and the MSX D band magnitudes, D, of the 154 sources detected at 15 μm in both surveys and found good agreement (Fig. 3.3); the average difference $D - [15]$ is -0.04 magnitude and the standard deviation is 0.3 mag, resulting from the combination (~ 0.15 mag) of the photometric errors of both catalogues and from the possible intrinsic source variability.

3.2.4 DENIS data

DENIS is a simultaneous I (0.8 μm), J (1.25 μm), and K_S (2.15 μm) band survey of the southern hemisphere using the ESO 1-meter telescope at La Silla (Epchtein et al. 1994). The 3σ detection limit in the respective bands is 0.05 mJy (19 mag), 0.5 mJy (16 mag) and 2.5 mJy (13.5 mag), and the saturation limit is at magnitudes 10, 7.5 and 6, respectively. The absolute DENIS astrometry is fixed using the USNO-A2.0 catalogue. The current absolute astrometric accuracy of DENIS is better than $0.5''$ (rms) (see Sect. 4.2 in Schuller et al. 2003).

ISOGAL sample and DENIS identifications

For the SiO targets selected from the ISOGAL survey, a proper DENIS identification and photometry had already been provided (Schuller et al. 2003; Simon 2003). For each ISOGAL field, a sample of DENIS point sources from the same area was extracted. DENIS coordinates were retained as the astrometric reference system and a polynomial distortion correction was applied to the ISOGAL coordinates in order to match as best as possible the ISOGAL and DENIS reference coordinates. To reduce the number of spurious associations, only DENIS sources with a K_S detection were selected and a K_S upper limit was imposed according to field density (Schuller et al. 2003). Among our 253 ISOGAL targets all have a DENIS K_S identification, while only 86% and 21% have J and I detections, respectively.

MSX sample and DENIS identifications

We searched for possible DENIS counterparts to the 188 SiO targets which we had selected from the MSX catalogue. For all sources from the MSX sample we searched the provisional bulge DENIS PSC (Schuller et al. 2003; Simon 2003) for the nearest K_S band object. As late-type stars are intrinsically red, only K_S band counterparts were examined. As saturated sources are usually given in the catalogue with null magnitude, DENIS photometry from other observations (Epchtein et al. 1994) and the K_S images were used as additional checks for saturated counterparts to the MSX SiO targets. Fortunately, such DENIS data was available for all MSX sources that we observed; however, a large number of bright sources saturated the detector in the K_S band. While all sources were detected in the K_S band, the fraction of detections in the J and I band was 79% and 22%, respectively.

The distribution of angular separations of the K_S band counterparts identified is shown in Fig. 3.4. The mean and median separations are 3.0″ and 2.7″ with a standard deviation of 1.8″, respectively, which is consistent with the expected scatter due to positional uncertainties for the MSX and DENIS catalogues.

To find the distribution of chance associations we again searched the nearest neighbours after shifting the coordinates of the SiO targets by 30″. The resulting distribution of separations and magnitudes is also shown in Fig. 3.4. The real associations are on average much brighter and closer than the chance associations. To compute the expected number of incorrect identifications we divided the "chance" distribution in magnitude bins, $(m, m + \Delta m)$, and in each bin computed the normalised cumulative chance distribution of the separations, $f(m, r)$, i.e., the fraction of all chance associations with those magnitudes and within a radius r. We then computed the sum $\Sigma f(m, r)$ over all "real" associations, each being characterised by m and r. Thus, $f(m, r)$ gives the probability for an association to be spurious, and the sum over all sources yields the total expected number of spurious identifications. When we consider only the brightest identifications for the 154 sources with a $K_S < 9$ mag counterpart, only two spurious
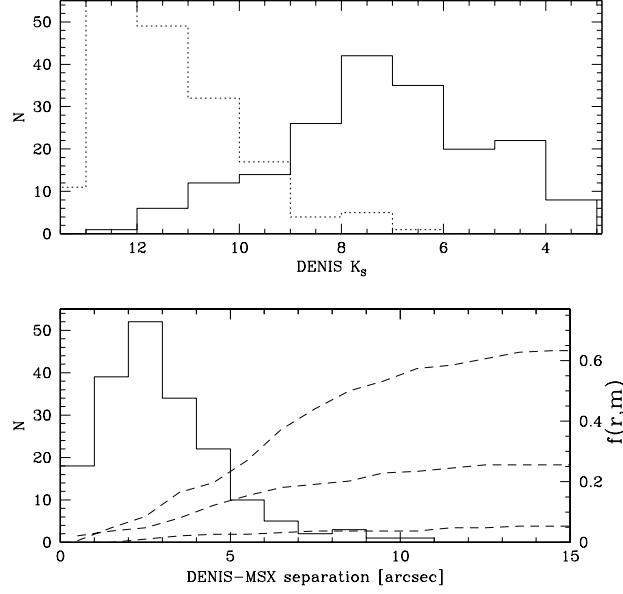
Figure 3.4: *Associations of our SiO MSX targets in the DENIS catalogue.* **Top panel***: distribution of K_S magnitudes for the associations (continuum line) and for the chance associations (dashed line).* **Lower panel***: The continuous line shows the distribution of angular separations. The dashed lines show the normalised cumulative distributions, $f(r, m)$, of chance associations found by misaligning the catalogue and MSX SiO targets, where we plot separately, starting from the bottom, the distributions of sources with $K_S < 9$, $9 < K_S < 11$, and $K_S > 11$ mag, respectively.*

identifications are expected. For the 34 possible identifications with $K_S > 9$ mag, we would expect three to be spurious. In total, we expect that about five of our identifications may be incorrect.

Since for the fainter possible counterparts the chance of a false identification is higher, we looked for brighter possible identifications somewhat further away, which due to the lower surface density of brighter sources might have a higher probability to be the actual counterpart. In a few cases (#231, #243, #367, #405, #406, and #424) we found brighter sources somewhat further away but with a lower value of $f(m, r)$ than the closest identification. This suggested that these brighter sources were more likely to be the correct counterparts, which we therefore retained. For these MSX targets with dubious near-infrared association, we additionally examined other MSX sources in their surrounding and checked for possible astrometric shifts between the DENIS and MSX coordinates which could uniquely identify the correct near-infrared counterpart. However, because of the low MSX source density (~ 1 source per $4' \times 4'$), only few associations could be confirmed in this way. Seven sources could only be associated with a $K_S > 11$

mag counterpart (#162,#273,#363,#403,#417,#423,#443) within 15″ (beam size of the IRAM telescope).

3.2.5 2MASS data

The Two Micron All Sky Survey (2MASS) has surveyed the entire sky at near-infrared wavelengths from the Whipple Observatory on Mt. Hopkins, AZ, and the Cerro Tololo InterAmerican Observatory (CTIO). The cameras observed simultaneously in the J (1.25 μm), H (1.65 μm) and K_S (2.17 μm) bands with a 10 σ sensitivity limit in uncrowded fields of 15.8, 15.1 and 14.3 mag, respectively (Beichman et al. 1998; Cutri et al. 2003). The absolute astrometry has typical uncertainty of 0.1″ (rms) and is based on the Tycho-2 and UCACr10 catalogue (a new version of the USNO's ACT catalogue). The on-line 2MASS PSC (all sky data release) is accessible at the Infrared Processing and Analysis Center (IPAC). 2MASS data was available for all our positions. We retrieved 2MASS sources for our 441 SiO target positions and we searched for the closest positional match. Since the astrometric accuracy is better than 0.5″ for the ISOGAL targets but only $\sim$2″ for the MSX targets, a different distribution of angular separations is expected for the MSX-2MASS and ISOGAL-2MASS associations.

To avoid misidentification, because of the high source density of the 2MASS survey and because the DENIS counterparts are mostly brighter than 11 mag in K_S, we limited the 2MASS K_S magnitude to $K_S < 11$. However, seven sources in our sample, #162, #273, #363, #403, #413, #421 and #423, could be associated only with 2MASS sources fainter than $K_S = 11$ (those sources are also faint in DENIS) within 15″, which is the beam size of the IRAM telescope. Positional associations were confirmed via overplotting the 2MASS counterpart image with both the SiO targets and the DENIS sources. Finding charts were obtained for all the stars with 2MASS images, an example of which is given in Fig. 3.5. We found 439 2MASS counterparts and missed only two. In fact, after image inspections, the potential 2MASS counterparts for two sources, #224 and #298, were eliminated as their positions on the 2MASS images were marked by artifacts.

ISOGAL sample and 2MASS identifications

The mean, median separations between the ISOGAL SiO targets (positions as in Chapter II,without rounding RA to one tenth of second) and the 2MASS associations are 0.7″ and 0.3″ with a standard deviation of 1.0″, (see Fig. 3.6).

There is a non-Gaussian tail at large separations. We have individually checked all the sources with separation larger than 3″ and note that they all have $K_S < 6$. We attribute the large separation to saturation of the DENIS detector. Saturated pixels are an obstacle to the correct determination of the source centroid and this affects the astrometry of saturated stars. Furthermore, most of these bright sources do not have any I associations and therefore the J/K_S astrometry is kept. The mean, median and standard deviation of the separations between the ISOGAL SiO targets and the 2MASS associations with $K_S > 6.5$ mag are 0.4″, 0.3″ and
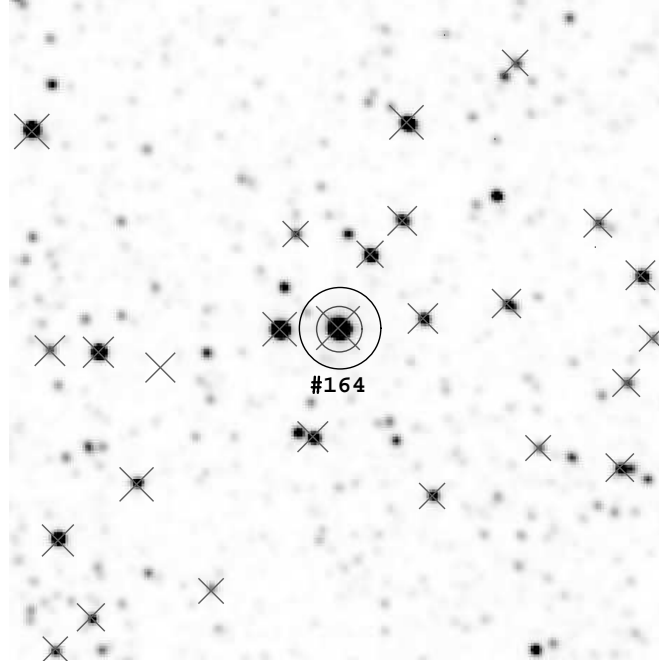
Figure 3.5: *2MASS K_S image $230'' \times 230''$ centred at the position of #164. The black circle delimits the main beam (FWHM) of the IRAM telescope used for the SiO maser search. A small gray circle marks the 2MASS association and finally crosses mark sources detected by ISOGAL. In agreement with the discussion in the text, all the ISOGAL and 2MASS positions are in excellent agreement. Note that the targeted source is the only mid-infrared source falling inside the IRAM telescope beam.*

$0.4''$; while for 2MASS associations with $K_S < 6.5$ mag they are $1.9''$, $2.1''$ and $1.5''$.

MSX sample and 2MASS identifications

We found 187 2MASS counterparts of MSX SiO targets. The mean, median and standard deviations of the separations between the MSX SiO targets (using the MSX coordinates) and the 2MASS associations are $2.9''$, $2.6''$ and $1.8''$, the same as the separations between the MSX SiO targets and the DENIS associations (see Sect. 3.2.4). This is again consistent with the expected scatter due to positional uncertainties of sources in the MSX and 2MASS catalogues. The mean, median and standard deviation of the separations between the MSX SiO targets (using the DENIS coordinates) and the 2MASS associations are $0.6''$, $0.4''$ and $0.7''$, respectively. The mean, median and standard deviation of the separations in right ascension RA are $0.0''$, $0.0''$ and $0.5''$; while the mean, median and standard deviation of the separations in declination DEC are $-0.2''$, $-0.1''$ and $0.6''$.
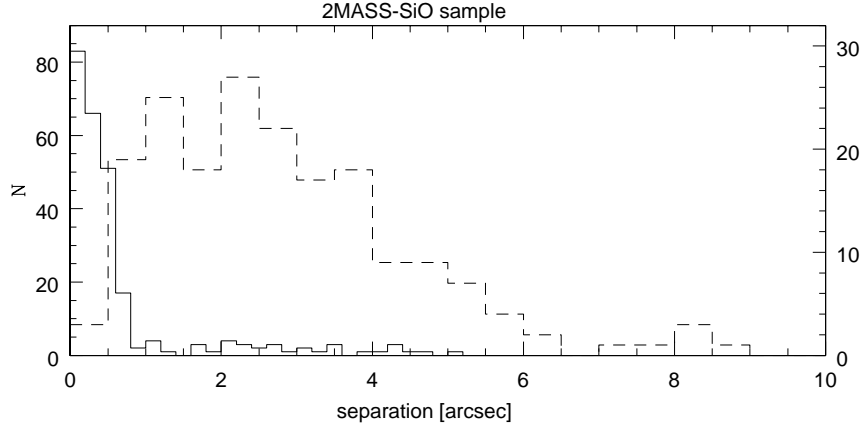
Figure 3.6: *Distribution of the angular separations between the SiO targets (positions as in Chapter II) and the 2MASS associations. The continuum line shows the distribution of the ISOGAL SiO targets and the corresponding y-axis is on the left side. The dashed line shows the distribution of the MSX SiO targets and the relative y-axis is on the right side.*

3.2.6 SiO targets and IRAS identifications

We checked for counterparts to our SiO targets in the Infrared Astronomical Satellite Point Source Catalogue (IRAS PSC). Toward the galactic plane the IRAS survey is strongly limited by confusion at the low resolution of the IRAS instruments ($0.5'$ at 12μm), especially in the longer wavelength bands. Since much of the past work on maser surveys of late-type stars is based on the IRAS data, it may be useful to have an according comparison.

We selected only the 165 IRAS associations within 3.5σ error ellipse of the IRAS PSC, to reduce the chances of spurious associations to $\sim 2\%$ (3 sources). A comparison of 12μm fluxes of the prospective counterparts with the ISOGAL and MSX fluxes (Fig. 3.8) shows a good agreement, confirming that the IRAS identifications are proper. About 35% of our SiO targets have counterparts in the IRAS PSC: 65% of the MSX sample and 17% of the ISOGAL sample. Of those, 96% are detected at 12μm, 87% at 25μm, 6% at 60μm and 4% at 100μm, and 56% are reported in the IRAS catalogue as variables (flag> 80).

3.2.7 SiO targets and visual identifications

Within a radius of $5''$ to our SiO targets we searched for possible visual counterparts in the Tycho 2 and USNO-A2.0 catalogues. We found possible associations for 85 SiO targets, of which 27 are validated by corresponding *I* band counterparts. Their R magnitudes range from 10.9 to 17.9 and B magnitudes from 13.4 to 20.6. Considering that the pulsation amplitude of Mira stars increases at shorter
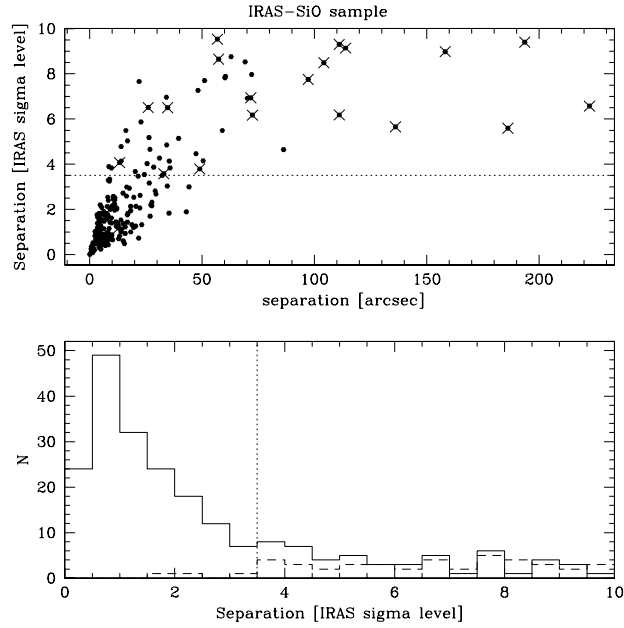
Figure 3.7: Upper panel: *Separation of the possible IRAS counterparts, expressed in IRAS sigma units, against angular separation. Crosses indicate IRAS sources with possible MSX counterparts closer than those associated with the SiO targets; these are likely to be unrelated to the SiO targets. The dotted horizontal line is the upper limit that is selected.* **Lower panel:** *The continuum line shows the distribution of the separations (in sigma units) of the possible IRAS counterparts. The dashed line shows the distribution of the chance associations obtained shifting the source coordinates by 250''. The dotted vertical line is our chosen upper limit of 3.5 σ.*

wavelenghts and can be up to 8 mag in the visual (Smak 1964), all those visual stars are possible counterparts of our SiO targets. Most of them are located at latitude $|b| < 0.8°$, but the extinction value inferred by their colours are much smaller than the median of their surrounding stars (Chapter IV). Therefore they are likely to be foreground stars. Two SiO targets, #7 with $(l, b, vel) = (-1.50°, 0.95°, 18.9$ km s^{-1}) and #139 with $(l, b, vel) = (0.31°, -2.18°, 205.7$ km s^{-1}), have extinction value inferred by their colours $A_V = 5.5$ and 3 mag, respectively, consistent with the median extinction of their surrounding stars (Chapter IV). Furthermore, the velocity of #139 is inconsistent with being a foreground star. Therefore we conclude that they are likely located in the Galactic bulge, in regions of low interstellar extinction. In fact, #139 is located in the optical window $W0.2 - 2.1$ at $(l, b) = (0.2°, -2.15°)$ (Dutra et al. 2002; Stanek 1998), and #7 has an extinction value typical of bulge ISOGAL fields with $b \sim +1°$ (Ojha et al. 2003).
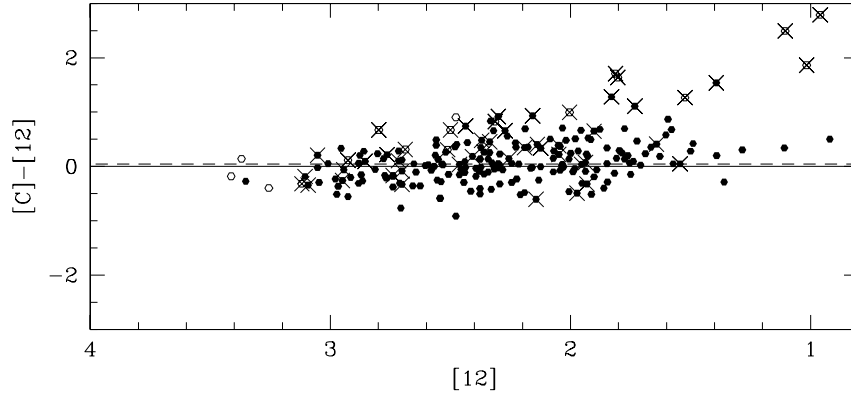
Figure 3.8: *Difference between the MSX magnitude in the C band, and the IRAS 12μm magnitudes, [12], (filled circles) versus the [12] . The 18 open circles indicate sources without C measurement, for which the 15μm ISOGAL measurement is plotted. Crosses are likely spurious MSX-IRAS associations (angular separation larger than 3.5σ). The plotted IRAS magnitudes are $-2.5\log(F[\text{Jy}]/28.3)$. The continuous line is $C - [12] = 0.00$ mag and the dashed line is $C - [12] = 0.05$ mag, which is the mean $C - [12]$ colour.*

3.2.8 The table

Table 3.2 lists the infrared photometry of the SiO targets. The columns of Table 3.2 are as follows: an identification number (ID), the same as in Table 2 and 3 of Chapter II, followed by the Right Ascension (RA), and Declination (DEC), in J2000 of the 2MASS counterpart; the DENIS (I, J, K_S) magnitudes, the ISOGAL ([7], [15]) magnitudes, the 2MASS (J, H, K_S) magnitudes; the angular separation (dis), between the adopted near-infrared position and the MSX position, the MSX (A, C, D, E) magnitudes, the IRAS 12 and 25 μm magnitudes and finally a variability flag (var), defined as described in Sect. 3.5. An additional column is used for comments on individual stars.

3.3 A comparison between the ISOGAL and MSX samples

A large variety of names exists to indicate oxygen-rich AGB stars characterized by different pulsation properties and/or mass-loss rate: semi-regular (SR) stars and Mira stars (Hα in emission, visual pulsation amplitude larger than 2.5 mag), large amplitude variables (LAV), long period variable (LPV) stars (when their periods are longer than 100 days), and OH/IR stars (with 1612MHz OH maser emission). In the IRAS colour-colour diagram the oxygen-rich AGB stars are distributed on a well-defined sequence of increasing shell opacity and stellar mass-loss rate (e.g.

Table 3.2: *Infrared counterparts of the SiO targets.* * *The identification numbers are the same as in Table 2 and Table 3 of Chapter II.*

ID	RA(J2000)	DEC(J2000)	DENIS−ISOGAL					2MASS				MSX				IRAS			Comments
	[hhmmss]	[degmmss]	I [mag]	J [mag]	K [mag]	[7] [mag]	[15] [mag]	J [mag]	H [mag]	K [mag]	dis	A [mag]	C [mag]	D [mag]	E [mag]	[12] [mag]	[25] [mag]	var	
1	173140.98	−320355.9	12.77	8.28	5.16	3.48	2.89	12.53	9.66	8.10	3.6	5.40	2.60	2.35	1.17	2.97	1.58	1	
2	173642.18	−305911.7	14.92	8.16	4.89	3.06	3.02	14.67	10.42	8.09	1.0	3.82	3.18	2.92				0	
3	173707.29	−312131.3	12.22	7.53	4.99	3.55	2.93	12.42	9.30	7.60	2.5	4.74	3.04	2.86				2	
4	173729.35	−311716.6	18.29	7.97	4.31	3.44	2.93	15.41	10.59	8.08	3.6	4.94	2.76	2.57				2	
5	173811.78	−314627.0	15.01	7.02			3.09	11.62	8.70	7.02	4.5	3.36	3.14	3.02	1.25	2.51	1.56	1	
6	173812.49	−293938.5	11.78	8.06	5.26		2.70	11.73	9.69	8.29								2	
7	173817.07	−294232.4	17.36	6.42	4.63		3.05	7.75	6.22	5.38	1.8	3.92	2.58	2.58				2	M6
8	173829.01	−312617.5	12.65	6.85	4.04		3.56	11.01	7.94	6.29	3.5	4.35	2.75	2.42		2.80	0.95	2	
9	173832.50	−312042.7	10.68	7.67	4.74		2.03	14.14	9.99	7.75						2.81	1.30	2	
10	173835.69	−293637.2	19.15	7.33	4.59		2.00	12.58	9.80	8.12	1.5	3.76	1.99	1.97	1.34	2.86	0.69	2	
11	173937.28	−300851.6	16.94	6.63	4.57		2.85	10.02	7.90	6.67	3.3	4.27	2.43	2.14				2	
12	174057.23	−294531.4	11.60	7.16	4.07		3.40	11.87	8.87	7.48	2.4	4.32	1.99	2.61				1	
13	174116.81	−313810.6	13.54	8.30	4.98		3.12	14.04	10.49	8.43	2.2	3.98	3.57	3.56		2.98	1.33	2	
14	174126.93	−293047.0	11.80	7.39	4.48		2.95	12.00	9.17	7.39								2	
15	174131.31	−300018.9	16.43	6.36	3.24		4.64	7.73	5.73	4.64	1.2	3.09	3.12	2.99				1	
16	174136.86	−292931.0	12.23	7.06	3.79		3.08	12.69	9.53	7.58	4.3	3.43	2.93	2.95	1.04			2	
17	174137.41	−293205.7	12.26	7.37	4.60		2.71	12.18	9.08	7.30	2.8	4.52	2.20	1.83	1.02			2	
18	174204.36	−295846.4		7.33	4.83		1.93	13.12	9.88	8.06								2	noIband
19	174206.86	−281832.4	15.86	6.87	4.82		2.16	9.64	7.89	6.88	0.9	4.66	2.42	2.18	3.20			2	
20	174223.28	−293935.6	12.52	7.60	5.11		2.76	12.13	9.13	7.46	0.8	4.49	2.75	2.53				2	
21	174232.91	−294125.1	17.23	7.79			2.45	11.62	9.15	7.76								1	
22	174232.48	−294110.7	11.78	7.19			2.88	12.55	9.46	7.67	2.3	4.57	2.72	2.48				2	
23	174244.87	−300408.1	16.27	6.40	4.29		2.96	9.10	6.87	5.67								2	
24	174309.81	−292403.3	14.50	7.53	3.65		2.95	15.54	10.79	8.19	2.2	3.43			0.90			2	
25	174323.46	−285350.3	15.73	5.99	2.87			8.44	6.21	4.97	3.2	3.14						1	
26	174325.26	−294528.6	15.23	8.99	4.92			15.88	11.69	9.09	2.5	4.29						2	
27	174332.72	−291539.4	12.06	6.91	3.94			13.34	9.63	7.47	2.5	3.67			1.31			2	
28	174333.13	−295133.1	15.00	8.41	4.68			15.02	10.83	8.42								1	
29	174334.79	−294030.4		9.15	4.65			16.90	13.15	9.76								1	
30	174335.12	−292447.2		8.82	4.97			18.47	12.22	9.09	4.0	4.79	2.87	2.85				1	

* The full table is available in electronic form at the CDS via anonymous ftp to cdsarc.u-strasbg.fr (130.79.128.5) or via http://cdsweb.u-strasbg.fr/cgi-bin/qcat?J/A+A/(vol)/(page).
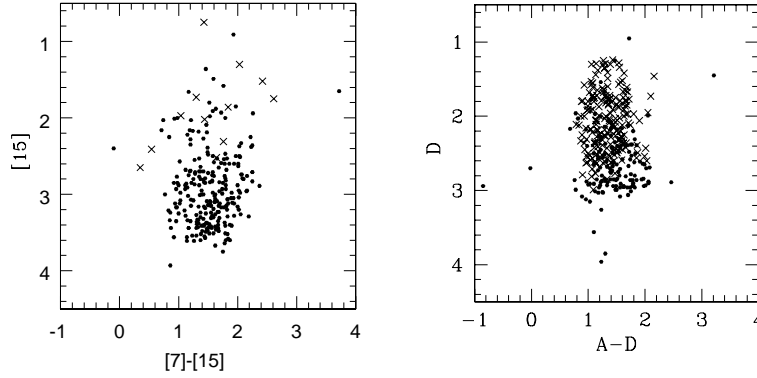
Figure 3.9: *Mid-infrared colour-magnitude diagrams.* **Left-hand panel:** *all data from ISOGAL.* **Right-hand panel:** *all data from MSX. Filled circles indicate targets from the ISOGAL sample and crosses indicate targets from the MSX sample. The two samples have similar mid-infrared colours, due to selection criteria. The numbers of MSX and ISOGAL targets between the two panels vary as explained in Sect. 3.2.3*

Habing 1996), which goes from SRs and Miras with the bluest late-type colours and the 9.7 μm silicate feature in emission, to the coldest OH/IR stars with the reddest colours and the 9.7 μm silicate feature in absorption. The sequence of increasing shell opacity corresponds also to an increasing $K_S - [15]$ or $K_S - [12]$ colour (e.g. Ojha et al. 2003; Olivier et al. 2001; Whitelock et al. 1994,ChapterII).

SiO maser emission is generated in the envelopes of mass-losing AGB stars, close to their stellar photospheres and it occurs more frequently towards oxygen-rich Mira stars than towards other AGB stars (including SR and OH/IR stars) (Bujarrabal 1994; Nyman et al. 1993). Therefore, for our 86 GHz SiO maser survey we selected the brightest sources at 15 μm with colours of Mira-like stars (Chapter II). The ISOGAL and MSX samples were selected to have similar 7 and 15 μm colours, as shown in Fig. 3.9. For the ISOGAL sample a range of intrinsic $(K_S - [15])-$colour was selected (see Sect. 3.2.1), but for the MSX sample no near-infrared counterparts were available at the time of the observations, and thus no K_S magnitudes. As an alternative to the $(K_S - [15])$ criterion, for the MSX sample we imposed an upper limit to the ratio of the fluxes in the E (21μm) and C (12μm) bands ($C - E < 1.55$ mag). Both criteria were defined in order to avoid non-variable objects and thick envelope objects, but these criteria are not equivalent. The emission in the K_S band is dominated by the stellar emission attenuated by the circumstellar absorption, while circumstellar dust emission contributes strongly to the mid-infrared radiation.

AGB stars with thin envelopes have $C - E <\sim 1.5$ mag, while sources with $C - E >\sim 1.5$ mag are AGB stars with thick envelopes, post-AGB stars and young stars (Lumsden et al. 2002; Sevenster 2002). Our sample of SiO targets includes

very few sources with $C - E > 1.5$.
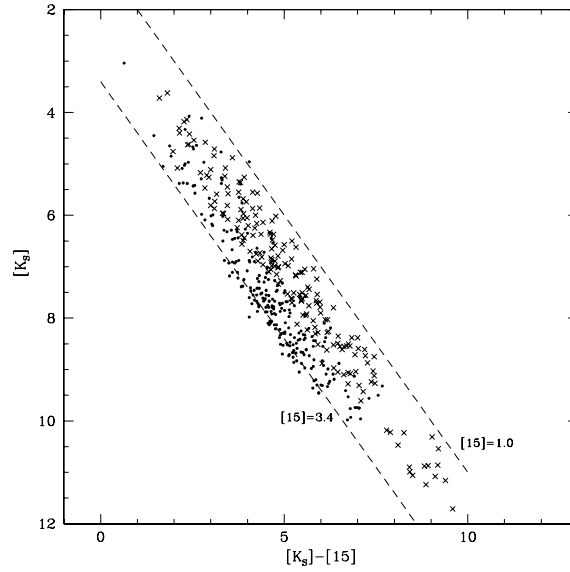
Figure 3.10: *2MASS K_S versus ($K_S-[15]$) or (K_S-D). Filled circles indicate objects from the ISOGAL sample, for which we plot ($K_S-[15]$); and crosses indicate objects from the MSX sample, for which we plot (K_S-D). The two dashed lines correspond to $[15] = 3.4$ and 1.0 mag.*

The $K_S-[15]$ and $K_S-[12]$ are good indicators of mass-loss rate for AGB star with shells at few hundred Kelvin. All Miras have redder $K_S-[12]$ than non-Mira stars from 1.8 mag up to 6 or even 14 mag (e.g. Olivier et al. 2001; Whitelock et al. 1994). Thick-envelope OH/IR stars have typically $K_S-[15] > 4$ (Ortiz et al. 2002). The ISOGAL SiO target sample is characterised by a smaller range of ($K_S-[15]$) or (K_S-D) values than the MSX sample, as shown in Fig. 3.10, suggesting that the MSX sample includes a tail of sources with optically thick envelopes. However, this will be verified after correction for extinction (Chapter V; Chapter IV).

Figure 3.10 shows a strong correlation, between K_S and ($K_S-[15]$) or (K_S-D), which is due to the way we selected our original sample. In fact, due to the general correlation of SiO maser emission and infrared luminosity (Bujarrabal et al. 1987), we selected only sources with $[15] < 3.4$ in order to be able to detect the expected SiO line. The $[15]$ and D magnitudes range from ~ 3.4 to ~ 1.0. This narrow range generates the correlation seen in Fig. 3.10.

Figure 10 also shows that the two samples, ISOGAL and MSX, overlap largely, although there are some minor systematic differences. There is a vertical shift between the ISOGAL and MSX sequence, with the MSX sources brighter for a given colour. This effect is due to the different sensitivity between the MSX D band

and ISOGAL surveys. MSX targets have on average a brighter D (or [15]) magnitude than the ISOGAL targets (see Fig. 3.9). This fact translates in differences in distance between the two samples and suggest that the MSX stars are closer on average; the two samples are also distributed differently in longitude (see Fig. 3.1).

On the basis of this comparison in the following we combine the results obtained with the ISOGAL sample with those obtained with the MSX sample, taking into account that there are some minor differences between the two samples.

3.4 Some other remarks on the SiO targets

3.4.1 SIMBAD search

A SIMBAD search revealed some extra information about our SiO targets.

Sources #7, #286 and #303 are included in the catalogue of late-type stars in the inner Galactic region by Raharto et al. (1984) as spectral types M6, M7 and M6.5, respectively.

#153 is a well known Mira star, TLE 53, with a period of 480 d, located in Baade's window (e.g. Glass et al. 1995). Our sample also includes 15 LPVs found by Glass et al. (2001) within 0.3° from the Galactic center and 19 candidate variable stars from the list of Schultheis et al. (2000) (listed in Table 2 and 3 of Chapter II).

A few sources are given in the literature as possible red supergiants or extremely luminous AGB stars: #25, #32, #92 and #295 correspond to sources #6, #8, #31 and #5 of Nagata et al. (1993), respectively; #356 is classified as bulge M supergiant by Raharto (1991) and Stephenson (1992) also lists it among distant luminous early type stars.

#127 (IRAS 17500−2512), #178 (IRAS 18040−2028), #188 (IRAS 18060−1857), #252 (IRAS 18285−1033), #265 (IRAS 18367−0507) and #434 (IRAS 18415−0355) are listed by (Kwok et al. 1997) among sources detected with the IRAS Low Resolution Spectrometer, in the range 8-23 μm and with a resolution, $\lambda/\Delta\lambda, \sim 20 − 40$. Four spectra are noisy or incomplete, while the spectra of #178 (IRAS 18040−2028), #434 (IRAS 18415−0355) are classified as featureless; they are probably evolved stars with negligible amounts of circumstellar dust. For those two objects, at longitudes 9.7 and 28.6° respectively, we also compute a moderate mass-loss rate of $5 − 7 \times 10^{-7}$ M$_\odot$ yr^{-1} (Chapter IV).

#164, IRAS 17590−2412, is classified as a Li K giant star by de La Reza et al. (1997). There is a significant difference between the SiO heliocentric velocity $V_{hel} = +4.4 \pm 1.0$ km s^{-1} and the optical heliocentric velocity $V_{hel} = −14.5 \pm 1.0$ km s^{-1} (Torres 1999,de La Reza *priv. communication*). Since the SiO maser velocity is usually coincident with the stellar velocity within few km s^{-1} (e.g. Habing 1996), we suggest that the SiO emitter is not associated with the G8II star, IRAS 17590−2412/PDS 482, which however is the only mid-infrared source within the IRAM beam and the association between the ISOGAL and DENIS source is of

excellent quality (flag=5).

#189, IRAS 18059−2554, is given by Lynch & Rossano (1990) as a possible member of the globular cluster NGC6553. The stellar line-of-sight velocity, obtained through the SiO maser line, is 161.2 km s^{-1}. Because the cluster mean line-of-sight velocity is 7 km s^{-1} with $\sigma = 14$ km s^{-1} (Coelho et al. 2001), we conclude that IRAS 18059−2554 is not a member of the cluster.

Twenty-eight of our 86 GHz SiO targets were previously observed for 43 GHz SiO maser emission. These are discussed in Sect. 4.5 of Chapter II. For the strongest 86 GHz maser sources within 2.2° of the Galactic Centre from Chapter II we recently used the Very Large Array (VLA) to observe the two 43 GHz SiO maser lines (v=0 and v=1) simultaneously (Sjouwerman et al. 2004).

We excluded from our SiO maser survey the OH/IR stars detected by Sevenster et al. (1997a,b, 2001), Sjouwerman et al. (1998) and Lindqvist et al. (1992). However, due to intrinsic source variability and the limited sensitivity of the Sevenster et al. surveys, we still included 4 OH/IR stars, as found with a SIMBAD search: #181, #226 and #257, all with detected SiO maser emission, coincide in position and velocity with OH9.84+0.01, OH17.43−0.08 and OH25.05+0.28, respectively (Blommaert et al. 1994); #409 (IRAS 18142−1600), not detected in our SiO survey, corresponds to OH #280 (OH14.805+0.150) listed by Te Lintel Hekkert et al. (1989).

3.4.2 Is the targeted star the actual SiO emitter?

Using the IRAM-30m telescope, we detected 86 GHz SiO maser emission toward 268 of our targeted positions, where three positions showed a double detection (#21-#22, #64-#65 and #77-#78) [1]. To confirm that our targets are the actual SiO emitters, we need to examine all other possible objects falling inside the 29″ (FWHM) IRAM beam. Due to the correlation between intensity of the maser line and mid-infrared brightness (Bujarrabal et al. 1987), we can restrict the analysis to only mid-infrared objects. Considering the 379 SiO targets with an MSX identification, we found in all but one case only one target inside the 86 GHz beam. Considering the 267 SiO targets with an ISOGAL identification, 89% are unique ISOGAL objects inside the main beam. SiO maser emission was detected towards 19 of our 29 positions with more than one ISOGAL source in the beam and in all cases the targeted star is the brightest 15 μm source.

3.5 Variability

The 86 GHz SiO maser line intensity is observed to be stronger in O-rich Mira stars than in other types of AGB stars (Bujarrabal 1994; Nyman et al. 1993). To in-

---

[1] Throughout the paper for statistic computations only one infrared source, the targeted, is considered for these three positions. A second mid-infrared source is found within the IRAM beam at the position of the SiO sources #77 and #78 (separation ∼ 12″), and at the position of the SiO sources #21 and #22 (separation of ∼ 15″) (see Chapter II) and is given in Table 3.2.
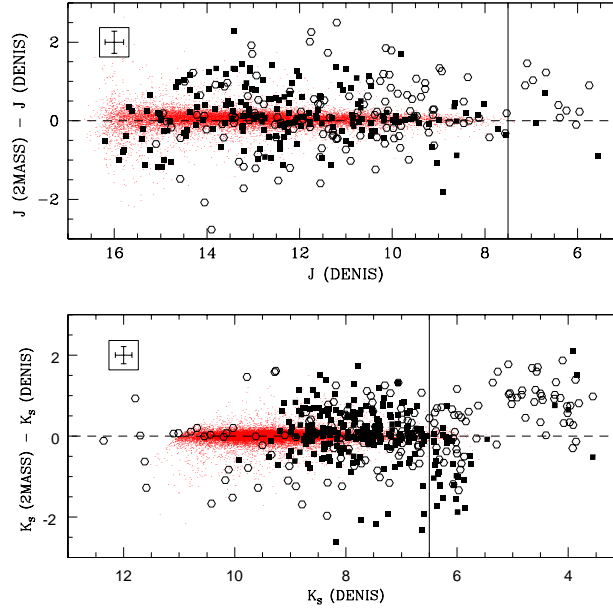
Figure 3.11: Upper Panel: *Difference between 2MASS and DENIS J magnitudes versus the DENIS J magnitude. Filled squares represent the ISOGAL SiO targets. For comparison small dots show ID-PSC and 2MASS associations obtained in several ISO-GAL fields, which have a distribution of their J variations consistent with a gaussian distribution centred at zero. No correction for offset in the photometric zeropoint was applied. Open circles represent the MSX targets, which have indications of variability at mid-infrared wavelengths. The error bars shown within the box are $\pm 1\sigma$ mag. The vertical line indicates the DENIS saturation limit.* **Lower Panel:** *Comparison of the 2MASS and DENIS K_S magnitudes versus the DENIS K_S magnitude. Symbols are as in the top panel.*

crease our chance of detecting the SiO maser emission, we tried to select strongly variable sources (Chapter II, and references therein). Therefore, our selected MSX targets all have an indication of variability in the A band. Unfortunately, the ISO-GAL database does not provide direct information on variability. However, from their position in the ISOGAL/DENIS ($K_{S0} - [15]_0$ vs. $[15]_0$) diagram we were expecting that our ISOGAL SiO targets were mainly large amplitude variables (Sect. 4.2 of Chapter II). For 62 ISOGAL targets out of the 191 which have an MSX counterpart, there is an indication of variability in the A band (or for 94 in at least one of the A, C, D, and E bands).

3.5.1 Variability information from DENIS and 2MASS data

The comparison between the near-infrared photometry obtained during the course of the DENIS survey and that of 2MASS again confirms our hypothesis for variability in the ISOGAL sample.

The J and K_S filters used by DENIS and 2MASS are similar and therefore the measurements obtained during the course of the DENIS and 2MASS surveys are directly comparable. For non variable sources, the differences between the J magnitude of DENIS and 2MASS and the K_S magnitude of DENIS and 2MASS are smaller than 0.15 mag (Delmotte et al. 2002; Schultheis & Glass 2001, and present work).

The DENIS observations were performed between 1996 and 2000, while the relevant 2MASS observations were performed between 1998 and 2000; AGB variables have periods from 50 to 1000 days, therefore the interval of time between the observations makes it possible to derive variability information.

For each of the 61 ISOGAL fields containing our SiO targets we retrieved the corresponding 2MASS sub-catalogue, and cross-correlated the ID-PSC and the 2MASS point source positions. For our ISOGAL sample the difference between the 2MASS and DENIS J and K_S magnitudes is shown as a function of the corresponding DENIS magnitude in Fig. 3.11. Figure 3.12 shows the difference between the 2MASS and DENIS J magnitudes plotted against the time between the 2MASS and DENIS observations. The distribution of the magnitude variations of the ISOGAL targets is different compared to that of random field objects. The Kolmogorov-Smirnov test gives a zero probability for the ISOGAL targets and field stars to be extracted from the same population. For 55% of our ISOGAL stars, the difference between both the 2MASS and the DENIS J and the 2MASS and the DENIS K_S magnitudes is larger than 3 times the dispersion measured in the corresponding field. Therefore, our sample contains mostly variable stars.

Due to the simultaneity of the J and K_S measurements in both the DENIS and 2MASS surveys, a correlation is expected between the variation in the J magnitude (ΔJ) and in the K_S magnitude (ΔK_S). As shown in Fig. 3.13 such a correlation exists. A linear least squares fit yields

$$\Delta J = 1.57(\pm 0.03) \times \Delta K_S + 0.05 \pm (0.01).$$

The relative pulsation amplitude in the K_S band is $\sim 60\%$ of the relative amplitude in J band.

For comparison, in Fig. 3.14, we also show the relation between the pulsation amplitudes in the J and K SAAO bands for two different samples of oxygen-rich stars in the solar neighbourhood (Olivier et al. 2001) and the South Galactic Cap (SGC) (Whitelock et al. 1994). The two samples have a different period distribution; most of the stars from the solar neighbourhood sample have periods between 500 and 700 d, while most of the SGC stars have periods between 150 and 450 d. Overplotting our best-fit, we see that it aligns well with the distribution of the two samples of LPVs.

Figure 3.12: *The difference of the 2MASS and DENIS J magnitude versus the time between the 2MASS and DENIS observations.*

A monitoring program of the near-infrared magnitudes of our SiO maser sample will provide pulsation periods and estimates of the source distances through the period-luminosity relation.

3.5.2 Variabity flag

All the available information on variability, from MSX data (variability in at least one of the MSX band), IRAS data (variability flag > 50), DENIS-2MASS data ($\Delta J > 3\sigma(J)$ and $\Delta K > 3\sigma(K)$), or from Glass et al. (2001), from Schultheis & Glass (2001) and from Glass et al. (1995), is summarised defining a flag (var) which is 2 when variability is detected in at least one of the datasets, 1 when variability is not detected but not all the datasets were available and 0 when variability is not detected in any of the datasets. All the 188 MSX targets have the variability flag equal to 2 (due to selection). Among the 253 ISOGAL targets 150 have the flag equal to 2, 81 equal to 1 and 22 equal to 0.

There is no correlation between the variability indication and the detection of SiO maser emission.

3.6 The distribution of the SiO targets in the IRAS two-colour diagram

We cannot determine the distribution of our target sources in the two-colour IRAS diagram of van der Veen & Habing (1988) since for most of our sources we have only upper flux limits at 60 μm. Figure 3.15 shows the distribution of the IRAS
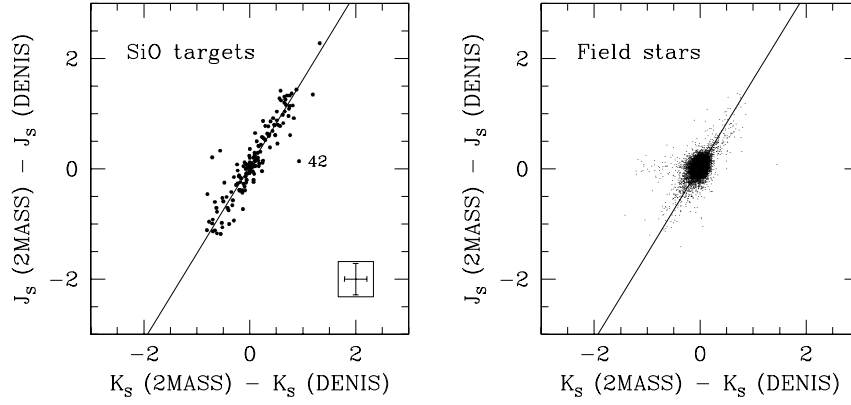
Figure 3.13: *Difference between the 2MASS and DENIS J magnitudes versus the difference of the 2MASS and DENIS K_S magnitudes.* **Left panel**: *SiO maser targets. Upper limit measurements and measurements affected by saturation are excluded. The photometry of #42 is affected by blending with another source. The continuous line shows our best fit. Within the box the typical error for sources in our range of magnitude is drawn.* **Right panel**: *for comparison, field stars with $J < 14$ mag.*
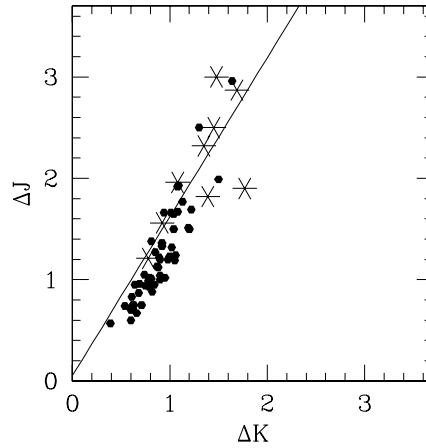
Figure 3.14: *Pulsation amplitude in J band versus amplitude in K band for two samples of oxygen-rich variable stars: one in the solar neighbourhood from Olivier et al. (2001) (starred points) and another in the South Galactic Cap from Whitelock et al. (1994) (filled circles). Superimposed is our best fit from Fig. 3.13.*

$[12] - [25]$ colours and recalls the regions of the IRAS two-colour diagram that separate different classes of evolved stars with circumstellar envelopes, from the

Figure 3.15: *Distribution of the IRAS* $[12] - [25]$ *colours,* $-2.5 \log(F_{12}/F_{25})$. *The continuous thin line indicate the distribution of our SiO targets; the thick line indicates the distribution of SiO targets with* $K_{\rm S} < 6.5$ *mag. For comparison, the dashed thin line indicates the distribution of the colours of OH/IR stars of Sevenster (2002). Upper limit flux densities are excluded. In the upper right corner, we recall the IRAS two-colour diagram.*

bluer Mira to the thick envelope OH/IR stars. The $[12] - [25]$ colours of our selected sources range from -1.0 to 0.4, peaking at -0.2, corresponding mostly to regions IIIa and VIb. Region IIIa represents sources with moderate dust emission, being populated mostly by oxygen-rich stars with silicate emission (Kwok et al. 1997; van der Veen & Habing 1988). Region VIb, whith 60μm excess, contains a mixed population of early type stars with line emission and planetary nebula; however this region is scarcely polulated. Considering the distribution of the IRAS good quality sources, only 5% of them are located in region VIb. We conclude that our targets are mostly Mira stars with moderate mass-loss rate, in agreement with the selection criteria. For comparison, the distribution of the $[12]-[25]$ colours of the OH/IR stars of Sevenster (2002) is also shown in Fig. 3.15. OH/IR stars are distributed over a larger and redder colour range, although par-

tially overlapping with the colours of the SiO sample; they can have significantly (~ 1 mag) redder colours than the SiO targets. This can not be accounted for by interstellar reddening, which is only 0.1-0.2 mag for $A_V \sim 20 - 30$ mag. The stars in our sample brighter than $K_S < 6.5$ mag are bluer than those with $K_S > 6.5$ mag. They are likely to be mostly foreground stars with thinner shell, but still IRAS detectable due to their proximity.

#177 (IRAS 18039$-$2052) is the only source with $[12] - [25] > 1.0$, which resembles those colours of an embedded young stellar object. However, methanol and water maser emission was unsuccessfully searched for toward this source (MacLeod et al. 1998; Molinari et al. 1996; Palla et al. 1991). Furthermore, the detection of SiO maser emission confirms that the source is a late-type star, since SiO maser emission is extremely rare in star-forming regions, with only three (extremely luminous) sources detected to date (e.g. Engels & Heske 1989; Snyder & Buhl 1974; Ukita et al. 1987). Though both the 12μm and 25μm IRAS flux densities have good quality, their association is unreliable. In fact, the corresponding MSX source has measurements in the A, C and D bands consistent with the 12 μm IRAS detection, but is not detected at 21 μm.

3.7 MSX colour-colour diagrams

Sevenster (2002) analysed the mid-infrared properties of her OH/IR sample using IRAS and MSX data. Studying a possible correspondence between regions in the two-colour IRAS diagram and the MSX $A - C$ versus $D - E$ plane she suggested that the MSX diagram can distinguish between the AGB and the post-AGB phases. The transition from a blue (< 1.8) to red (> 1.8) $A - C$ colour may correspond to a transition off the AGB to proto-planetary nebulae: the star had its last thermal pulse, and ceased to be variable. The transition from a blue (< 1.5) to a red (> 1.5) $D - E$ colour indicates a later evolutionary transition, when mass-loss starts to drop down of several order of magnitudes and there is the onset of the fast wind. Most of our SiO targets with a clear MSX counterpart show $A - C < 1.8$ and $D - E < 1.5$, as expected for AGB stars, and comparable to the bulk of Sevenster's OH/IR sample.

According to Sevenster' criteria, only two objects, #76 and #99, which are both SiO maser emitters, are likely to be post-AGB stars. The odd colour of #99 is due to an extremely high flux density of 39 Jy measured in the C band, while the flux density in both the A and D bands is only ~ 1.7 Jy. However, the inspection of the MSX C band image does not confirm the presence of a such bright object and we conclude that the C photometry (despite its good flag) of #99 is unreliable. Source #76, LPV 12-352 (Glass et al. 2001), is located on a region of extended emission which is associated with a star forming region (Schuller 2002); this could have affected the mid-infrared colours of #76. In conclusion: the anomalous position of the sources #99 and #76 is probably due to the assignment of incorrect magnitudes.

The $A - C$ versus $D - E$ colour diagram is useful to locate post-AGB stars,
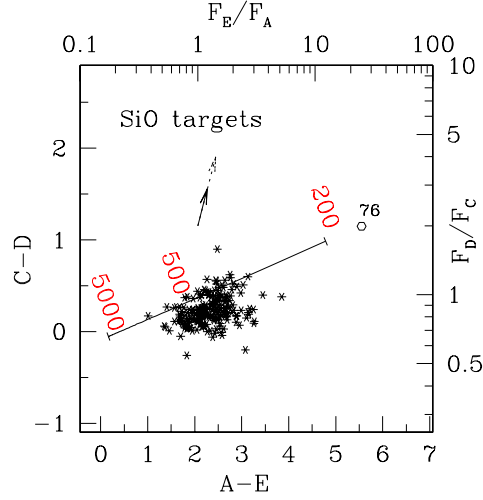
Figure 3.16: *MSX colour-colour plot for our SiO maser targets, similar to Fig. 5 of Lumsden et al. (2002). Stars represent AGB stars, open circles early post-AGB stars, following the classification of Sevenster (2002). Black body spectra follow the continuous line. A reddening vector for $A_V = 40$ and extinction law from Mathis (1990) is given by the solid arrow, while another one obtained using the extinction law of Lutz (1999) is represented by the dashed arrow. Note that the two vectors point in the same direction. Our SiO targets have colours similar to the objects with 9.7 μm silicate emission in Kwok et al. (1997) and Lumsden et al. (2002). Object #99 is outside of the plotted region $(A - E = 3.01$ mag, $F_E/F_A = 2.4$; $C - D = -2.99$ mag, $F_D/F_C = 0.04)$ (see also text).*

which have redder colours due to their colder envelopes. However, this diagram can hardly distinguish between different thickness of the envelopes of AGB stars. Using a sample of IRAS sources with IRAS low resolution spectra (Kwok et al. 1997), Lumsden et al. (2002) showed that a different combination of MSX filters can distinguish between circumstellar envelopes with silicate feature at 9.7 μm in emission and in absorption. Miras and OH/IR stars with the silicate feature in emission are located below the black body line in the $C - D$ versus $A - E$ diagram, while OH/IR stars with silicate feature in absorption lie above this line. In optically thick envelopes, self-absorption causes a decrease of the flux in the C and A bands, leading to an increase in $C - D$. Figure 3.16 shows that our SiO targets are distributed like objects with the silicate feature in emission. We note that the MSX two colour plot is not corrected for reddening. However, the reddening correction makes the sources bluer in the $C - D$ colour independently of the adopted extinction law. Furthermore, in the $C - D$ versus $A - E$ diagram the distribution of the ISOGAL and MSX samples are similar. For comparison, in Fig. 3.17 the MSX colour-colour plots of the Sevenster's OH/IR stars is shown,
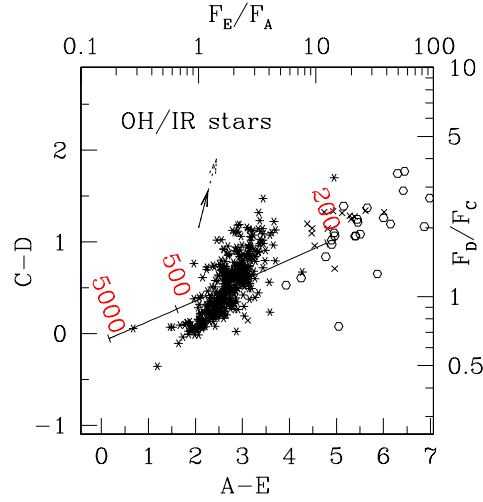
Figure 3.17: *MSX colour-colour plot as in Fig. 5 of Lumsden et al. (2002) for the OH/IR sample of Sevenster (2002). Symbols are as in Fig. 3.16, plus crosses which represent late post-AGB stars, following the classification of Sevenster (2002)*

which are distributed over a wider and redder range of colours.

3.8 Conclusion

To increase the number of line-of-sight velocities measured toward the inner Galaxy we searched for 86 GHz SiO maser emission in a sample of 441 late-type stars. While the radio survey was described elsewhere (Messineo et al. 2002), this paper presents the infrared photometry of all our SiO targets as derived from the various accessible infrared catalogues: DENIS, 2MASS, MSX, ISOGAL and IRAS catalogues.

As described in Chapter II, we initially selected the SiO targets from the ISO-GAL and MSX catalogues on the basis of their near- and mid-infrared colours, and their 15 μm magnitudes. We tried to select objects with colours typical of pulsating AGB stars with thin envelopes (Mira-like stars), while avoiding OH/IR stars and other sources with thick circumstellar envelopes.

Our analysis of the targeted stars' multi-band photometry showed that these selection criteria were quite reliable. A comparison between the DENIS and 2MASS data shows that most of them are variable stars, and moreover the correlation between the J and K_S band brightness variations is similar to that found in local dust-enshrouded Mira variable stars (Olivier et al. 2001).

The IRAS $[12] - [25]$ colours of the SiO targets confirms that they populate mostly the region IIIa of the van der Veen and Habing classical two-colour IRAS

diagram, which is a region of stars with moderate mass-loss rates and with silicate feature at 9.7 μm in emission. The distribution of the $[12] - [25]$ colours of the SiO targets overlaps with the distribution of the colours of OH/IR stars, which however are distributed over a larger and redder range of colours (mostly in region IIIa and IIIb). Following the work of Sevenster (2002) and Lumsden et al. (2002), those properties can be translated and seen in the MSX $C - D$ vs. $A - E$ diagram. The SiO targets have a narrower $C - D$ colour range and are located below the black-body line, differently from the thick-envelope OH/IR stars.

The two subsamples, the MSX-selected objects and the ISOGAL selected objects have very similar infrared properties but differ slightly in the average apparent magnitude, the MSX sample being on average a little brighter. This difference is, however, smaller than the spread in magnitudes of each subsample. In forthcoming papers we usually will combine the two subsamples into one.

References

Beichman, C. A., Chester, T. J., Skrutskie, M., Low, F. J., & Gillett, F. 1998, PASP, 110, 480

Beichman, C. A., Neugebauer, G., Habing, H. J., Clegg, P. E., & Chester, T. J. 1988, in NASA RP-1190, Vol. 1 (1988)

Blommaert, J. A. D. L., van Langevelde, H. J., & Michiels, W. F. P. 1994, A&A, 287, 479

Bujarrabal, V. 1994, A&A, 285, 953

Bujarrabal, V., Planesas, P., & del Romero, A. 1987, A&A, 175, 164

Cesarsky, C. J., Abergel, A., Agnese, P., et al. 1996, A&A, 315, L32

Coelho, P., Barbuy, B., Perrin, M.-N., et al. 2001, A&A, 376, 136

Cutri, C. M., Skrutskie, M. F., & Van Dyk, S. 2003, avalaible on line at http://www.ipac.caltech.edu/2mass/

de La Reza, R., Drake, N. A., da Silva, L., Torres, C. A. O., & Martin, E. L. 1997, ApJ, 482, L77

Delmotte, N., Loup, C., Egret, D., Cioni, M.-R., & Pierfederici, F. 2002, A&A, 396, 143

Dutra, C. M., Santiago, B. X., & Bica, E. 2002, A&A, 381, 219

Egan, M. P., Price, S. D., Moshir, M. M., et al. 1999, AFRL-VS-TR-1999, 1522

Engels, D. & Heske, A. 1989, A&AS, 81, 323

Epchtein, N., de Batz, B., Copet, E., et al. 1994, Ap&SS, 217, 3

Glass, I. S., Matsumoto, S., Carter, B. S., & Sekiguchi, K. 2001, MNRAS, 321, 77

Glass, I. S., Whitelock, P. A., Catchpole, R. M., & Feast, M. W. 1995, MNRAS, 273, 383

Habing, H. J. 1996, A&A Rev., 7, 97

Kessler, M. F., Steinz, J. A., Anderegg, M. E., et al. 1996, A&A, 315, L27

Kwok, S., Volk, K., & Bidelman, W. P. 1997, ApJS, 112, 557

Lindqvist, M., Winnberg, A., Habing, H. J., & Matthews, H. E. 1992, A&AS, 92, 43

Lumsden, S. L., Hoare, M. G., Oudmaijer, R. D., & Richards, D. 2002, MNRAS, 336, 621

Lutz, D. 1999, in ESA SP-427: The Universe as Seen by ISO, Vol. 427, 623

Lynch, D. K. & Rossano, G. S. 1990, AJ, 100, 719

MacLeod, G. C., van der Walt, D. J., North, A., et al. 1998, AJ, 116, 2936

Mathis, J. S. 1990, ARA&A, 28, 37

Messineo, M., Habing, H. J., Sjouwerman, L. O., Omont, A., & Menten, K. M. 2002, A&A, 393, 115 (Chapter II)

—. 2004b, A&A in preparation (Chapter V)

Messineo, M., Habing, H. J., Menten, K. M., Omont, A., Sjouwerman, L. O., & Bertoldi, F. 2004a, A&A submitted (Chapter IV)

Molinari, S., Brand, J., Cesaroni, R., & Palla, F. 1996, A&A, 308, 573

Nagata, T., Hyland, A. R., Straw, S. M., Sato, S., & Kawara, K. 1993, ApJ, 406, 501

Nyman, L.-A., Hall, P. J., & Le Bertre, T. 1993, A&A, 280, 551

Ojha, D. K., Omont, A., Schuller, F., et al. 2003, A&A, 403, 141

Olivier, E. A., Whitelock, P., & Marang, F. 2001, MNRAS, 326, 490

Omont, A., Gilmore, G. F., Alard, C., et al. 2003, A&A, 403, 975

Ortiz, R., Blommaert, J. A. D. L., Copet, E., et al. 2002, A&A, 388, 279

Palla, F., Brand, J., Comoretto, G., Felli, M., & Cesaroni, R. 1991, A&A, 246, 249

Price, S. D., Egan, M. P., Carey, S. J., Mizuno, D. R., & Kuchar, T. A. 2001, AJ, 121, 2819

Raharto, M. 1991, Proceedings of the Astronomical Society of Australia, 9, 306

Raharto, M., Hamajima, K., Ichikawa, T., Ishida, K., & Hidayat, B. 1984, Annals

of the Tokyo Astronomical Observatory, 19, 469

Schuller, F. 2002, PhD Thesis: Université Pierre et Marie Curie, Paris 6.

Schuller, F., Ganesh, S., Messineo, M., et al. 2003, A&A, 403, 955

Schultheis, M., Ganesh, S., Glass, I. S., et al. 2000, A&A, 362, 215

Schultheis, M. & Glass, I. S. 2001, MNRAS, 327, 1193

Schultheis, M., Lançon, A., Omont, A., Schuller, F., & Ojha, D. K. 2003, A&A, 405, 531

Sevenster, M. N. 2002, AJ, 123, 2772

Sevenster, M. N., Chapman, J. M., Habing, H. J., Killeen, N. E. B., & Lindqvist, M. 1997a, A&AS, 122, 79

—. 1997b, A&AS, 124, 509

Sevenster, M. N., van Langevelde, H. J., Moody, R. A., et al. 2001, A&A, 366, 481

Simon, G. 2003, in preparation

Sjouwerman, L. O., Messineo, M., & Habing, H. J. 2004, PASJ, 56, 45

Sjouwerman, L. O., van Langevelde, H. J., Winnberg, A., & Habing, H. J. 1998, A&AS, 128, 35

Smak, J. 1964, ApJS, 9, 141

Snyder, L. E. & Buhl, D. 1974, ApJ, 189, L31

Stanek, K. Z. 1998, Using the DIRBE/IRAS All-Sky Reddening Map to Select Low-Reddening Windows Near the Galactic Plane, preprint [astro-ph/9802307]

Stephenson, C. B. 1992, AJ, 103, 263

Te Lintel Hekkert, P., Versteege-Hensel, H. A., Habing, H. J., & Wiertz, M. 1989, A&AS, 78, 399

Torres, C. A. O. 1999, Publicação Especial do Observatorio Nacional 10

Ukita, N., Hasegawa, T., Kaifu, N., et al. 1987, in IAU Symp. 115: Star Forming Regions, 178

van der Veen, W. E. C. J. & Habing, H. J. 1988, A&A, 194, 125

Whitelock, P., Menzies, J., Feast, M., et al. 1994, MNRAS, 267, 711

Chapter 4

86 GHz SiO maser survey of late-type stars in the Inner Galaxy III. Interstellar extinction and colours

M. Messineo, H. J. Habing, K. M. Menten, A. Omont,
L. O. Sjouwerman and F. Bertoldi

Abstract

We have computed extinction corrections for a sample of 441 late-type stars in the inner Galaxy using the 2MASS near-infrared photometry of the surrounding stars and assuming the intrinsic source colours. From this, the near-infrared power law is found to be $A_\lambda \propto \lambda^{-1.9\pm0.1}$. Near- and mid-infrared colour-colour properties of known Mira stars are also reviewed. From the distribution of the dereddened infrared colours of the SiO target stars we infer mass-loss rates between 10^{-7} and 10^{-5} $M_\odot$ yr^{-1}.

In this article we study the interstellar extinction toward a sample of evolved late-type stars in the inner Galaxy (-4° $< l <$ +30°, $|b| <$ 1°) which were searched for SiO maser emission ("SiO targets" hereafter; Messineo et al. 2002, Chapter II). The maser emission reveals the stellar line of sight velocities with an accuracy of a few km s^{-1}, making the maser stars ideal for Galactic kinematics studies.

The combination of the kinematic information with the physical properties of the SiO targets, e.g. their intrinsic colours and bolometric magnitudes, will enable a revised kinematic study of the inner Galaxy, revealing which Galactic component and which epoch of Galactic star formation the SiO targets are tracing.

A proper correction for interstellar extinction is of primary importance for our photometric study of the stellar population of the inner Galaxy, where extinction can be significant even at infrared wavelengths. The extinction hampers an accurate determination of the stellar intrinsic colours and bolometric magnitudes.

This is especially critical in the central Bulge region where interstellar extinction is larger than 30 visual magnitudes and the uncertainty in the stellar bolo-

metric luminosities of evolved late-type stars is at least 1 magnitude due to the current uncertainty in the near-infrared extinction law (30%).

The available near- and mid-infrared photometry of the SiO targets from the DENIS[1] (Epchtein et al. 1994), 2MASS[2] (Cutri et al. 2003), ISOGAL[3] (Omont et al. 2003; Schuller et al. 2003) and MSX[4] (Egan et al. 1999; Price et al. 2001) surveys were already presented by Messineo et al. (2004b, Chapter III).

The corrections for interstellar extinction of the photometric measurements of each SiO target will enable us to derive the spectral energy distributions and bolometric magnitudes of the SiO targets. The bolometric magnitudes will be presented in a subsequent paper (Messineo et al. 2004a, Chapter V).

Our sample consists mainly of large-amplitude variable AGB stars (Chapter II; Chapter III). The estimates of interstellar extinction toward this class of objects are complicated by the presence of a circumstellar envelope which may have various thickness. Therefore, in order to disentangle circumstellar and interstellar extinction one needs to study the dust distribution along the line of sight toward each AGB star of interest. For each SiO target we adopt the median extinction derived from near-infrared field stars (mainly giants) close to the line of sight of the target. Then the dereddened colour-colour distribution of our targets is compared to those of local Mira stars in order to iteratively improve the extinction correction and to statistically estimate the mass-loss rates of our targets.

In Sect. 4.1 we discuss the uncertainty of the extinction law at near- and mid-infrared wavelengths, and the consequent uncertainty of the stellar luminosities. In Sect. 4.2 we describe the near-infrared colour-magnitude diagrams of field stars toward the inner Galaxy and we use the latter to derive the median extinction toward each target. In Sect. 4.3 we review the location of Mira stars on the colour-magnitude (CMD) and colour-colour diagrams. In Sects. 4.4 and 4.5 we use the median extinction from surrounding field stars to deredden our SiO targets and we discuss their colours and mass-loss rates. The main conclusions are given in Sect. 5.8.

4.1 Interstellar extinction law

The composition and abundance of interstellar dust and its detailed extinction properties remain unclear, limiting the accuracy of stellar population studies in the inner Galaxy. In the following we discuss the near- and mid-infrared extinction law, in order to assess the uncertainty in the extinction correction.

---

[1]DEep Near-Infrared Survey of the southern sky; see
http://www−denis.iap.fr/.

[2]Two Micron All Sky Survey; see
http://www.ipac.caltech.edu/2mass/.

[3]A deep survey of the obscured inner Milky Way with ISO at 7μm and at 15μm; see
http://www−isogal.iap.fr/.

[4]The Midcourse Space Experiment; see
http://www.ipac.caltech.edu/ipac/msx/msx.html.

4.1.1 Near-infrared interstellar extinction

Interstellar extinction at near-infrared wavelengths (1-5 μm) is dominated by graphite grains. Although for historical reasons the near-infrared extinction law is normalised in the visual, practically it is possible to derive near-infrared extinction by measuring the near-infrared reddening of stars of known colour.

Near-infrared photometric studies have shown that the wavelength-dependence of the extinction may be expressed by a power law, $A_\lambda \propto \lambda^{-\alpha}$, where α was found to range between 1.6 (Rieke & Lebofsky 1985) and 1.9 (Glass 1999; Landini et al. 1984; van de Hulst 1946).

When deriving the extinction from broad-band photometric measurements, one needs to properly account for the bandpass, stellar spectral shape, and the wavelength-dependence of the extinction. We have therefore computed an "effective extinction" for the DENIS I and 2MASS J, H and K_s passbands, as a function of the K_S band extinction. This effective extinction was computed by reddening an M0 III stellar spectrum (Fluks et al. 1994) with a power law extinction curve and integrating it over the respective filter transmission curves. When we convolve the filter response with a stellar sub-type spectrum different from the M0 III, the effective I-band extinction slightly differs, e.g. decreasing by 3% for a M7 III spectrum (see also van Loon et al. 2003).

The K_S-band extinction A_{K_S} can then be found from

$$A_{K_s} = C_{JK} \times E(J - K_s),$$

$$A_{K_s} = C_{HK} \times E(H - K_s),$$

where $E(J-K_s)$ and $E(H-K_s)$ are the reddening in the $J-K_s$ and $H-K_s$ colour, respectively, and the C are constants. These relations are independent of visual extinction and of the coefficient of selective extinction, $R_V = A_V/E(B - V)$, but they depend on the slope of the near-infrared power law (see Table 4.1). However, to provide the reader with the traditionally used ratios between near-infrared effective extinction and visual extinction, we also used the commonly adopted extinction law of Cardelli et al. (1989). Such ratios may be useful in low-extinction Bulge windows, where visual data are also available. Cardelli et al. (1989) proposed an analytic expression, which depends only on the parameter R_V, based on multi-wavelength stellar colour excess measurements from the violet to 0.9μm, and extrapolating to the near-infrared using the power law of Rieke & Lebofsky (1985). We extrapolated Cardelli's extinction law to near-infrared wavelengths using a set of different power laws. The results are listed in Table 4.1.

The uncertainty in the slope of the extinction law produces an uncertainty in the estimates of the near-infrared extinction of typically 30% in magnitude (see Table 4.1). For a K_S band extinction of $A_{K_S} = 3$ mag the uncertainty may be up to 0.9 mag, which translates into an uncertainty in the stellar bolometric magnitudes of the same magnitude.

In Sect. 4.2 we show that a power law index $\alpha = 1.6$ is inconsistent with the observed colours of field giant stars toward the inner Galaxy, and that the most

likely value of α is 1.9 ± 0.1.

4.1.2 Mid-infrared interstellar extinction

Mid-infrared extinction (5-25 μm) is characterised by the 9.7 and 18 μm silicate features. The strength and profile of these features are uncertain and appear to vary from one line of sight to another. In the inner Galaxy silicate grains may be more abundant due to the outflows from oxygen-rich AGB stars. Another uncertainty is the minimum of $A_\lambda/A_{2.12}$ at 7μm, which is predicted for standard graphite-silicate mixes, though not observed to be very pronounced toward the Galactic Centre (Lutz 1999; Lutz et al. 1996).

The commonly adopted mid-infrared extinction curve is that of Mathis (1990), which is a combination of a power law and the astronomical silicate profile from Draine & Lee (1984), with $A_{9.7}/A_{2.2} \simeq 0.54$ – a value found in the diffuse interstellar medium toward Wolf-Rayet stars (e.g. Mathis 1998, and references therein). However, using hydrogen recombination lines, Lutz (1999) found $A_{9.7}/A_{2.2} \simeq 1.0$ in the direction of the Galactic centre, and analysing the observed H$_2$ level populations toward Orion OMC-1, Rosenthal et al. (2000) derived $A_{9.7}/A_{2.12} = 1.35$. It seems that the mid-infrared extinction law is not universal.

In order to derive the extinction ratios for all ISOGAL and MSX filters (for definitions see Blommaert et al. 2003; Price et al. 2001), and to analyse the effect of an increase of the depth of the 9.7 μm silicate feature on the extinction ratios, we built a set of extinction curves with different silicate peak strengths at 9.7 μm. We use a parametric mid-infrared extinction curve given by Rosenthal et al. (2000), where the widths of the 9.7 and 18 μm silicate features are those calculated by Draine & Lee (1984) and the depth of the 18 μm feature is assumed to be 0.44 times that of the 9.7 μm feature. Using this parametric fit we constructed two different extinction curves with $A_{9.7}/A_{2.2}$ equal to 1.0, one in combination with the minimum predicted by the models at 4-8 μm (Curve 2) and one without it as suggested by Lutz (1999) (Curve 3). The two curves are shown together with the Mathis curve (Curve 1, $A_{9.7}/A_{2.2} = 0.54$) in Fig. 4.1.

Using the various extinction curves detailed in Table 4.2, we reddened the M-type synthetic spectra from Fluks et al. (1994) (beyond 12.5μm a blackbody extrapolation is used), and convolved the resulting spectra with the ISOCAM and MSX filter transmission curves. The effective extinctions $\langle A \rangle / A_{\mathrm{K_S}}$ in the various ISOCAM and MSX filters are listed in Table 4.2. They are not sensitive to the stellar sub-type used. An increase of the ratio $A_{9.7}/A_{2.2}$ from 0.54 to 1.0 results in an increase between 0.15 and $0.20 \times A_{\mathrm{K_S}}$ of the average attenuation in the $LW3$, $LW9$, C, D and E spectral bands. The spectral bands of the $LW2$ and $LW5$ filters are not very sensitive to the intensity of the silicate feature, but to the minimum of the extinction curve in the 4-8 μm region. Although $\langle A \rangle / A_{\mathrm{K_S}}$ varies with $A_{\mathrm{K_S}}$, these variations are small compared to those arising from different choices of the mid-infrared extinction law.

Hennebelle et al. (2001) obtained observational constraints on mid-infrared extinction ratios from observations of infrared dark clouds within the ISOGAL sur-

Table 4.1: Near-infrared effective extinction, $\langle A \rangle/A_V \propto \lambda^{-\alpha}$, for various filters. A different value of R_V does not affect $A_{K_S}/E(H - K_s)$ and $A_{K_s}/E(H - K_s)$, but the slope of the extinction curve does. Our findings favour a model with $\alpha = 1.9$ (see Sect. 4.2).

A_I/A_V	A_J/A_V	A_H/A_V	A_{K_S}/A_V	$A_{K_S}/E(J - K_S)$	$A_{K_S}/E(H - K_S)$	α	R_V	Ref.
0.592	0.256	0.150	0.089	0.533	1.459	1.85		Glass (1999)
0.584	0.270	0.165	0.103	0.617	1.661	1.73	3.08	He et al. (1995)
0.482	0.282	0.175	0.112	0.659	1.778	1.61	3.09	Rieke & Lebofsky (1985)
0.606	0.287	0.182	0.118	0.696	1.842	1.61	3.10	Cardelli et al. (1989)
0.563	0.259	0.164	0.106	0.696	1.842	1.61	2.50*	"
0.606	0.277	0.169	0.106	0.623	1.684	1.73	3.10	Cardelli et al. (1989)[+]
0.563	0.249	0.152	0.096	0.623	1.684	1.73	2.50	"
0.606	0.267	0.158	0.096	0.561	1.548	1.85	3.10	"
0.563	0.240	0.142	0.086	0.561	1.548	1.85	2.50	"
0.606	0.263	0.153	0.092	0.537	1.496	1.90	3.10	"
0.563	0.237	0.138	0.083	0.537	1.496	1.90	2.50	"
0.606	0.255	0.144	0.084	0.493	1.401	2.00	3.10	"
0.563	0.229	0.130	0.076	0.494	1.400	2.00	2.50	"
0.606	0.238	0.127	0.070	0.420	1.236	2.20	3.10	"
0.563	0.213	0.114	0.063	0.420	1.236	2.20	2.50	"

* recent determination toward the Bulge (e.g. Udalski 2003).

[+] parametric expression modified to extrapolate to $\lambda > 0.9\ \mu m$ with $\lambda^{-\alpha}$.

Table 4.2: *Effective extinction, $\langle A \rangle / A_{K_S}$, using M-giant spectra (Fluks et al. 1994), for different bands defined by the ISOCAM and MSX filters (see Fig. 4.1). $A_{K_S}/A_{2.12} = 0.97$.*

Filter	λ_{ref}	$\Delta\lambda$	Curve 1 (Mathis) $(A_{9.7}/A_{2.12} = 0.54)$	Curve 2 $(A_{9.7}/A_{2.12} = 1.00)$	Curve 3 (Lutz) $(A_{9.7}/A_{2.12} = 1.00$ & no minimum$)$
	μm	μm	$\langle A \rangle / A_{K_S}$	$\langle A \rangle / A_{K_S}$	$\langle A \rangle / A_{K_S}$
LW2	6.7	3.5	0.21	0.21	0.41
LW5	6.8	0.5	0.18	0.15	0.41
LW6	7.7	1.5	0.21	0.26	0.43
LW3	14.3	6.0	0.18	0.34	0.34
LW9	14.9	2.0	0.14	0.29	0.29
A	8.28	4.0	0.26	0.38	0.55
C	12.1	2.1	0.25	0.49	0.49
D	14.6	2.4	0.14	0.29	0.29
E	21.3	6.9	0.17	0.41	0.41
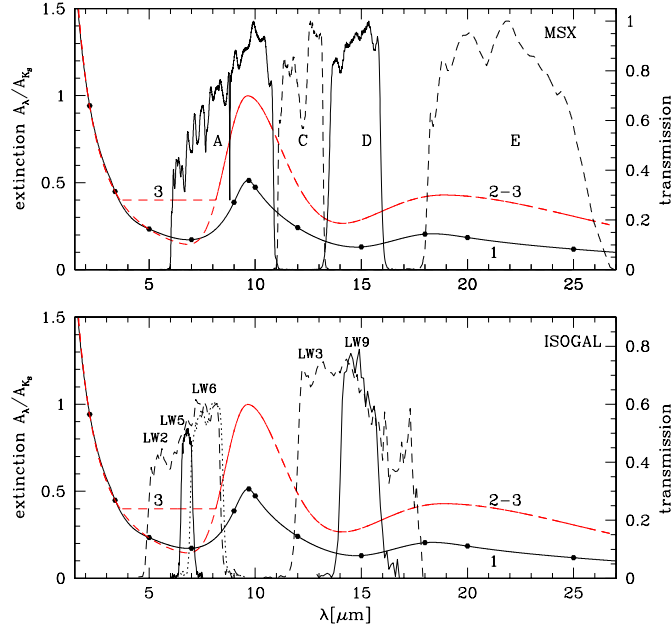
Figure 4.1: *Filter transmission curves and extinction laws as function of wavelength. The continuous line shows the curve (Curve 1) obtained by fitting the values (dots) given by Mathis (1990); the dashed curve shows the parametric expression given by Rosenthal et al. (2000) plotted using a value of the silicate peak $A_{9.7}/A_{2.12} = 1.0$ (Curve 2). The latter is also shown without the minimum around 4-8 μm (Curve 3), following Lutz (1999).* **In the top panel** *the transmission curves of the MSX A, C, D and E filters are also overplotted, while* **in the bottom panel** *the transmission curves of the ISOCAM $LW2, LW3, LW5, LW6$ and $LW9$ filters used in the ISOGAL survey are shown.*

vey. Using observations in the $LW2$ and $LW3$ bands in the inner Galactic disk they obtained $A_{LW2}/A_{LW3} = 0.7$, and using observations in the two bands $LW6$ and $LW9$ in the region ($|l| < 1°$, $0.2° < |b| < 0.4°$) they found $A_{LW6}/A_{LW9} = 0.8$. Both these values are in good agreement with the extinction curve calculated by Draine & Lee (1984) with a silicate peak at 9.7 μm of 1.0 (Curve 2 in Table 4.2). However, for the clouds located at ($|l| < 1°, |b| < 0.2°$) observed in the $LW5$ and $LW9$ bands Hennebelle et al. (2001) found $A_{LW5}/A_{LW9} = 1.07$, which is twice the value predicted by Curve 2 in Table 4.2, but would be consistent with Curve 1 or 3.

For stars in the inner disk Jiang et al. (2003) derived $(A_{K_S} - A_{LW2})/(A_J - A_{K_S}) = 0.35$ and $(A_{K_S} - A_{LW3})/(A_J - A_{K_S}) = 0.39$. These ratios when combined with the near-infrared extinction law imply that A_{LW2}/A_{K_S} must range from 0.35 to 0.47 and A_{LW3}/A_{K_S} from 0.28 to 0.41, which are higher values than those produced by Curve 1 and suggest an attenuation of the minimum at 4-8 μm, consistent with

Curve 3.

Concluding, there is some uncertainty in the mid-infrared extinction law that is in part due to uncertainties in the photometric measurements and possibly due to spatial variations in the strength of the silicate features. In the most obscured regions ($A_{K_S} = 3$) uncertainties for the ISOGAL and MSX filters range from 0.45 mag ($LW3, LW9, D$) to 0.85 mag (A). However, this has a negligible effect (0.1 mag in average) on the calculated M_{bol} of the SiO targets because their energy is emitted mostly at near-infrared wavelengths, and has therefore also a negligible effect on the mass-loss rate estimates (see Sect. 4.5).

In the following we will use the Lutz law (Curve 3) to deredden the colours of our SiO targets, since this law ensures a consistency between mid-infrared and near-infrared stellar colours as found by Jiang et al. (2003).

4.2 Interstellar extinction of field stars from near-infrared colour-magnitude diagrams

Most of the sources detected by DENIS and 2MASS toward the inner Galaxy are red giants and asymptotic giant branch stars. Because the intrinsic $(J - K_S)_0$ colours of giants are well known and steadily increase from 0.6 to 1.5 mag with increasing luminosity, one can study the colour-magnitude diagrams (CMDs) of $(J - K_s)$ versus K_s and of $(H - K_s)$ versus K_s to estimate the average extinction toward a given line of sight for a population of such stars.

Under the assumption that our SiO targets are spatially well mixed with the red giant stars, and that the interstellar extinction is uniform over a $4' \times 4'$ field (corresponding to 9×9 pc^2 at the distance of the Galactic Centre), we estimate the extinction, A_{K_S}, towards our 441 SiO targets by examining the CMDs of 2MASS sources in field of 2-4′ radius around each SiO target. Figure 2 shows a representative sample of these CMDs. We assume that the red giant branch (RGB) has the same intrinsic shape for all red giants in the inner Galaxy: the absolute magnitude of the tip of the RGB, $M_{K_s}(tip)$, and the RGB colour-magnitude relation does not vary. This means that at a given distance, d, along the line of sight the observed RGB extends towards fainter magnitudes from the tip at magnitude $K_s(tip) = M_{K_s}(tip) + DM + A_{K_s}$; here DM is the distance modulus corresponding to d and A_{K_S} the corresponding extinction in the K_S band. With increasing distance along a given line of sight the RGB becomes redder, due to the increase of interstellar extinction. The reddening is proportional to the extinction, A_{K_S}, and the shift to fainter magnitudes equals $DM + A_{K_S}$. In principle we could thus derive both DM and A_{K_S} as a function of distance by locating discrete features of the RGB. Due to small number fluctuations, it is difficult to estimate $K_s(tip)$ and thus $DM + A_{K_S}$. Some of the CMDs contain also the so-called "red clump" stars which all have the same absolute magnitude ($M_{K_s} = -1.65$), so that they can be used to trace the stellar distribution and that of the dust along the line of sight. However, close to the Galactic centre the distance modulus and the extinction shift clump stars below the detection limits of DENIS and 2MASS.
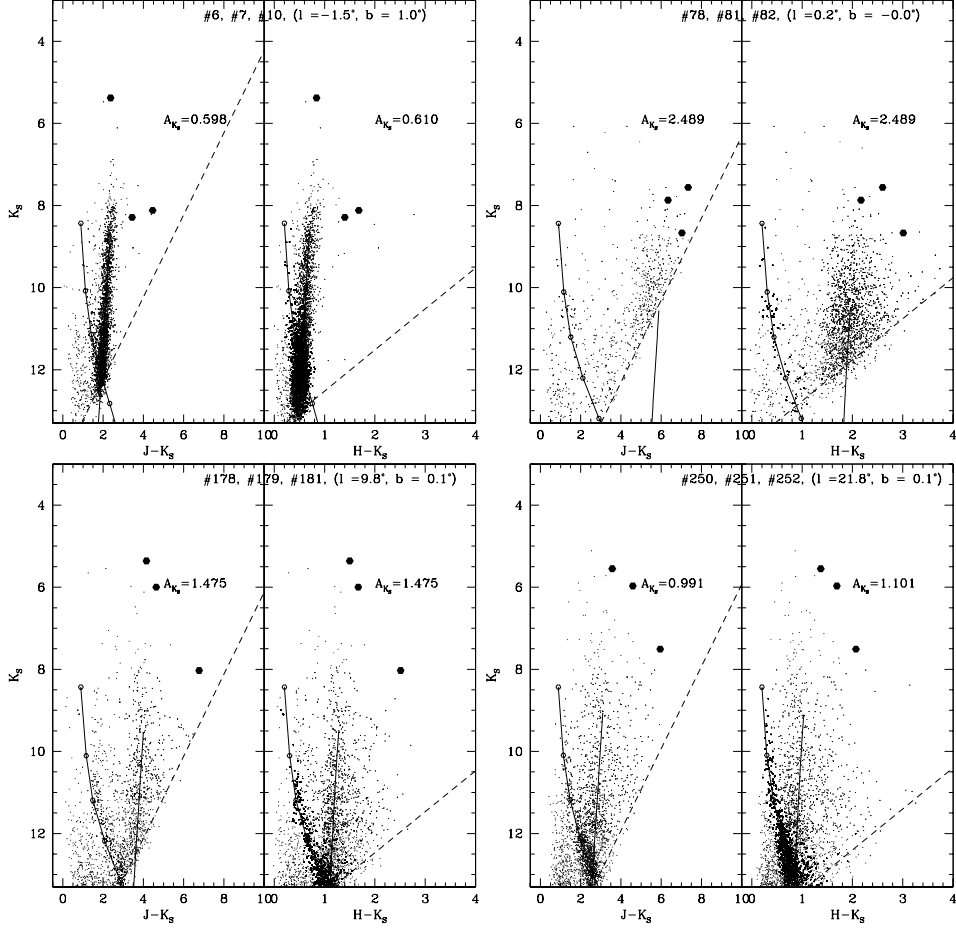
Figure 4.2: *Colour-magnitude diagrams of 2MASS datapoints (small dots) of good quality located within 4′ from the position of the SiO target (big dot). Three fields at equal median extinction are combined in each panel. The right-hand continuous line indicates the locus of the reference RGB curve (see Sect. 4.2.1), adopting a distance of 8 kpc and reddening it with the median extinction of field stars (A_{K_S}). The left-hand continuous curve shows the trace of clump stars for increasing distance and extinction along a given line of sight (see Sect. 4.2.3), obtained using the extinction model by Drimmel et al. (2003) and the absolute magnitudes from Wainscoat et al. (1992). Dashed lines indicate the diagonal cut-offs due to the detection limits in J and H. Circles on the clump trace mark a distance from 1 to 5 kpc with a step of 1 kpc downward.*

The average field extinction can be estimated by assuming a reference isochrone (colour-magnitude relation) for the RGB (Sect. 4.2.1), and by fitting the isochrone to the observed giants. This approach was used by Schultheis et al. (1999) and Du-

tra et al. (2003) to map the extinction in the central region of the Galaxy ($|l| < 10°$). Schultheis et al. (1999) obtained an extinction map within 8° of the Galactic Centre by comparing DENIS (J, K_s) photometry with an isochrone from Bertelli et al. (1994) (metallicity $Z = 0.02$, age 10 Gyr, distance 8 kpc), adopting the extinction law of Glass (1999). A similar map was also produced by Dutra et al. (2003) using 2MASS (J, K_s) data together with an empirical reference RGB isochrone, which is a linear fit to the giants in Baade's windows, and adopting the extinction law of Mathis (1990).

The SiO targets are located at longitudes l between 0° and 30° and mostly at latitude $b < 0.5°$. In this region of high extinction even at near-infrared wavelengths, fits to the apparent ($K_S, J-K_S$) RGB may underestimate the extinction, due to observational bias as explained in Sect. 4.2.2 (see also Cotera et al. 2000; Dutra et al. 2003; Figer et al. 2004). Therefore it is useful to also consider the ($K_S, H-K_S$) plane, which is deep and not sensitive to extinction and therefore less affected by bias.

The extinction toward each of the SiO targets was calculated from individual field stars in both the ($K_S, J-K_S$) and ($K_S, H-K_S$) CMDs by shifting the datapoints on the reference RGB (see Sect. 4.2.1) along the reddening vector. Then, the median extinction of the field was determined in both the ($K_S, J-K_S$) and ($K_S, H-K_S$) planes, applying an iterative 2σ clipping to the extinction distribution in order to exclude foreground stars (Dutra et al. 2003). A comparison of the extinction estimates derived from both diagrams, and possible selection effects are described in Sect. 4.2.2.

SiO targets usually appear redder than neighbouring stars (Fig. 4.2), which implies that they are intrinsically obscured if we assume that the spatial distribution of SiO targets is the same as that of red giant branch stars. About fifty of our 441 SiO target stars are brighter in K_S and bluer than sources in the field, so those must be nearer than the median.

The CMDs contain much information on the distribution of stars and dust in the inner Galaxy. Here we have used them only to estimate a median extinction, A_{K_S}. In a future study we hope to make a more complete analysis of these diagrams with a more self-consistent model. In the following some general remarks from the analysis of the CMDs are summarised:

- We can determine A_{K_S} for individual stars in each CMD and the statistical properties of the extinction values within a given CMD. In most CMDs the interstellar extinction, A_{K_S}, shows a strong concentration, which reflects the Bulge and the Galactic centre. In a minority of CMDs the histogram is broad without clear peaks.

- Broad, diffuse extinction distributions are found at longitudes $20° < l < 30°$. This suggests that stars and dust are spread along these line of sight.

- Lines of sight which pass through complex star forming regions such as M17 are easily identified as regions of anomalously high extinction compared to their surrounding regions.

- Toward some lines of sight, especially at latitudes above $|b| \approx 0.6\,°$, a sharp edge at the high end is found in the extinction distribution. These lines of sight apparently extend to above the dust layer.

Table 4.3: *Extinction values. The identification number (ID) of the SiO target, as in Table 2 and 3 of Chapter II, is followed by the field extinction A_{K_S}, by the corresponding dispersion of individual extinctions of field stars, and by the total extinction in K_S-band toward the target star (tot). Finally, a flag (Fg) is listed, which is equal to unity when the SiO target is classified as a "foreground object". Stars for which not all J, H, K_S measurements were available have no total extinction.*

ID	A_{K_S} mag	$\sigma_{A_{K_S}}$ mag	tot mag	Fg	ID	A_{K_S} mag	$\sigma_{A_{K_S}}$ mag	tot mag	Fg	ID	A_{K_S} mag	$\sigma_{A_{K_S}}$ mag	tot mag	Fg	ID	A_{K_S} mag	$\sigma_{A_{K_S}}$ mag	tot mag	Fg
1	0.96	0.18	1.63		61	1.72	0.29	3.46		121	1.65	0.28	1.91		181	1.38	0.59	2.77	
2	1.23	0.31	2.81		62	1.70	0.28	2.47		122	1.55	0.25	2.10		182	1.29	0.19	1.46	
3	1.90	0.33	1.79		63	2.44	0.42	3.18		123	1.26	0.36	1.51		183	1.32	0.28	1.45	
4	2.16	0.52	3.00		64	2.28	0.42	3.67		124	1.43	0.30	2.18		184	1.44	0.29	1.62	
5	1.51	0.25	1.75		65	2.28	0.42	3.67		125	1.65	0.35	2.26		185	1.37	0.24	0.44	1
6	0.59	0.09	1.16		66	1.71	0.21	1.21	1	126	0.75	0.11	1.59		186	1.57	0.18	1.51	
7	0.57	0.07	0.51		67	1.62	0.26	2.09		127	0.91	0.19	1.78		187	0.97	0.33	1.65	
8	1.98	0.41	1.53	1	68	1.68	0.23	1.09	1	128	1.51	0.24	1.60		188	0.85	0.22	1.06	
9	2.14	0.32	2.59		69	2.17	0.43	2.53		129	0.93	0.24	0.36	1	189	0.21	0.04	1.14	
10	0.61	0.11	1.48		70	1.65	0.36	2.02		130	0.79	0.09	0.52	1	190	1.04	0.59	1.10	
11	0.94	0.17	1.04		71	1.84	0.35	2.12		131	1.69	0.44	1.94		191	2.22	0.75	3.39	
12	1.21	0.17	1.61		72	1.86	0.23	2.24		132	1.61	0.42	2.53		192	0.93	0.33	1.69	
13	1.11	0.23	2.15		73	2.63	0.30	3.94		133	0.99	0.19	0.86		193	0.97	0.34	1.60	
14	1.38	0.14	1.66		74	1.42	0.18	1.92		134	1.52	0.26	2.60		194	1.37	0.20	1.94	
15	1.34	0.27	0.89	1	75	1.36	0.23	1.19		135	1.20	0.27	1.46		195	1.42	0.14	1.71	
16	1.46	0.15	1.99		76	2.71	0.38	3.58		136	1.27	0.13	1.48		196	1.85	0.79	2.84	
17	1.45	0.15	1.86		77	2.49	0.43	2.22		137	1.21	0.24	1.73		197	1.91	0.53	2.02	
18	1.53	0.27	1.89		78	2.49	0.43	3.74		138	1.11	0.19	2.17		198	1.76	0.47	2.46	
19	0.60	0.06	0.71		79	1.88	0.34	1.93		139	0.21	0.04	0.95		199	1.22	0.31	0.57	1
20	1.47	0.21	1.81		80	2.12	0.28	2.81		140	1.03	0.13	0.38	1	200	2.10	1.07	1.97	
21	1.40	0.29	1.35		81	2.53	0.38	2.56		141	1.22	0.17	2.49		201	0.92	0.24	1.49	
22	1.40	0.29	1.82		82	2.45	0.40	3.33		142	1.22	0.16	1.26		202	0.92	0.24	0.14	1
23	1.73	0.63	1.06	1	83	1.58	0.23	1.50		143	1.30	0.19	1.96		203	0.91	0.26	3.15	
24	2.17	0.36	3.07		84	2.34	0.39	2.90		144	1.49	0.32	1.36		204	0.97	0.25	3.04	
25	1.83	0.26	1.10	1	85	2.24	0.44	2.25		145	1.02	0.18	0.98		205	1.19	0.32	1.46	
26	2.26	0.40	2.73		86	2.21	0.68	2.88		146	0.83	0.15	1.06		206	2.36	0.48	0.45	1
27	1.93	0.24	2.19		87	1.69	0.14	1.24	1	147	1.34	0.27	0.89	1	207	1.15	0.29	1.17	
28	2.09	0.36	2.77		88	2.45	0.51	3.07		148	0.80	0.21	0.57	1	208	0.91	0.33	1.41	
29	2.56	0.32	4.31		89	2.60	0.41	2.97		149	1.17	0.25	1.43		209	1.91	0.63	2.70	
30	2.82	0.36	3.92		90	1.90	0.34	2.12		150	1.33	0.31	2.23		210	0.88	0.24	1.64	
31	1.80	0.19	1.72		91	2.82	0.52	3.09		151	1.17	0.32	1.41		211	1.42	0.53	2.50	
32	1.61	0.24	1.78		92	1.66	0.28	1.40		152	1.08	0.39	1.88		212	0.82	0.31	2.02	
33	1.62	0.22	2.69		93	1.87	0.35	1.85		153	0.14	0.15	0.34		213	2.56	1.05	4.03	
34	1.78	0.25	2.67		94	2.07	0.47	3.62		154	1.73	0.64	5.16		214	1.00	0.19	1.13	
35	1.89	0.23	2.50		95	2.11	0.76	4.65		155	1.20	0.30	1.55		215	1.30	0.36	3.56	
36	1.47	0.22	0.80	1	96	1.92	0.32	1.88		156	0.97	0.25	1.75		216	0.89	0.35	1.43	
37	1.87	0.25	3.37		97	2.31	0.61	3.38		157	1.31	0.33	1.42		217	1.02	0.34	1.89	
38	2.98	0.44	3.52		98	2.37	0.61	2.94		158	1.42	0.32	1.60		218	1.30	0.65	1.40	
39	2.91	0.44	3.64		99	2.41	0.56	2.34		159	1.46	0.19	2.15		219	1.48	0.31	2.15	
40	2.29	0.35	2.79		100	2.30	0.56	3.55		160	1.35	0.23	0.81	1	220	2.21	0.57	3.39	
41	2.68	0.40	3.53		101	2.11	0.39	3.89		161	1.84	0.35	2.12		221	1.10	0.35	2.24	
42	2.19	0.41	2.37		102	2.24	0.48	2.24		162	1.66	0.41	3.35		222	1.93	0.37	2.29	
43	1.66	0.26	3.29		103	0.99	0.16			163	1.75	0.47	2.25		223	1.02	0.29	1.87	
44	1.75	0.21	1.86		104	0.92	0.10	1.21		164	1.32	0.30	1.49		224	2.04	0.57		
45	2.67	0.34	3.76		105	1.62	0.31	2.32		165	1.08	0.21	2.67		225	1.53	0.48	2.24	
46	2.89	0.47	4.44		106	1.23	0.54	2.10		166	1.21	0.26	2.44		226	0.84	0.28	1.10	
47	1.34	0.11	1.15	1	107	1.70	0.42	2.56		167	1.26	0.18	1.58		227	1.83	0.26	0.61	1
48	2.25	0.39	2.67		108	2.01	0.56	0.77	1	168	1.35	0.16	1.52		228	0.92	0.32	1.94	
49	2.33	0.41	2.69		109	1.88	0.39	2.98		169	1.11	0.48	1.98		229	1.32	0.43	2.29	
50	1.10	0.16	1.75		110	1.78	0.53	2.64		170	1.19	0.19	1.96		230	0.87	0.26	1.61	
51	2.31	0.39	3.70		111	1.81	0.38	2.10		171	1.57	0.31	1.67		231	0.70	0.22	1.54	
52	2.33	0.38	3.86		112	1.35	0.30	1.32		172	1.09	0.33	2.79		232	1.10	0.35	1.45	
53	2.68	0.34	2.65		113	1.70	0.28	1.14	1	173	1.61	0.63	1.20	1	233	1.64	0.54	1.56	
54	2.31	0.38	2.33		114	1.25	0.28	1.47		174	1.02	0.53	1.49		234	1.18	0.38	2.17	
55	1.71	0.27	2.94		115	1.92	0.43	2.00		175	1.20	0.39	2.09		235	1.00	0.36	1.77	
56	2.34	0.36	2.49		116	1.75	0.46	1.41		176	1.42	0.50	1.46		236	0.81	0.30	1.90	
57	2.55	0.45	3.49		117	1.85	0.41	3.25		177	1.27	0.30	1.51		237	0.75	0.23	2.00	
58	2.20	0.33	3.59		118	2.78	0.59	3.97		178	1.50	0.37	1.48		238	0.95	0.37	1.34	
59	2.25	0.34	2.38		119	1.63	0.60	1.54		179	1.43	0.32	1.79		239	0.83	0.30	1.49	
60	2.11	0.29	2.75		120	1.62	0.29	2.27		180	1.20	0.38	1.05		240	0.76	0.30	2.00	

Table 4.3: *(continued)*

ID	A_{K_S}	$\sigma_{A_{K_S}}$	tot	Fg	ID	A_{K_S}	$\sigma_{A_{K_S}}$	tot	Fg	ID	A_{K_S}	$\sigma_{A_{K_S}}$	tot	Fg	ID	A_{K_S}	$\sigma_{A_{K_S}}$	tot	Fg
	mag	mag	mag			mag	mag	mag			mag	mag	mag			mag	mag	mag	
241	0.92	0.29	2.05		301	2.13	0.33	1.88		361	1.60	0.49	3.67		421	1.06	0.45	3.64	
242	0.88	0.20	0.93		302	2.56	0.33	2.50		362	1.35	0.18			422	1.25	0.44	1.86	
243	0.92	0.32	2.42		303	1.36	0.11	0.63	1	363	1.87	0.41	3.00		423	0.72	0.68	0.32	
244	0.96	0.39	0.99		304	2.07	0.35	3.41		364	0.61	0.09	0.96		424	1.34	0.40	2.28	
245	0.67	0.22	0.89		305	1.79	0.22	2.53		365	1.72	0.26	3.62		425	1.72	0.71	1.37	
246	1.15	0.44	1.65		306	1.88	0.24	2.06		366	0.60	0.15	1.21		426	1.07	0.47	2.53	
247	1.26	0.36	0.79	1	307	1.24	0.13	1.48		367	1.16	0.32	2.95		427	0.90	0.46		
248	1.26	0.39	1.61		308	2.20	0.36	2.92		368	1.57	0.31	0.63	1	428	0.94	0.41	1.53	
249	0.98	0.42	2.31		309	2.26	0.35	2.52		369	1.35	0.22	2.58		429	0.74	0.39	1.70	
250	0.93	0.42	2.36		310	2.79	0.41	2.42		370	1.11	0.23	0.53	1	430	0.88	0.32	1.63	
251	1.39	0.42	1.74		311	2.93	0.51	4.32		371	0.83	0.14	1.49		431	0.83	0.31	1.17	
252	0.92	0.31	1.23		312	1.70	0.28	2.14		372	1.24	0.16	2.13		432	0.97	0.35	1.17	
253	0.96	0.32	2.34		313	1.75	0.28	2.25		373	1.24	0.11	1.12	1	433	0.72	0.29	1.84	
254	1.27	0.55	1.82		314	2.18	0.46	3.18		374	0.95	0.20	1.36		434	1.71	0.60	1.84	
255	1.13	0.30	1.22		315	1.05	0.13	1.47		375	1.03	0.21	1.70		435	1.02	0.45	0.40	1
256	0.84	0.61	2.80		316	1.54	0.22	1.77		376	1.33	0.22	2.97		436	0.97	0.36	0.00	1
257	0.90	0.38	4.34		317	1.32	0.15	1.53		377	1.11	0.22	1.80		437	1.01	0.34	3.31	
258	1.64	0.70	2.88		318	1.63	0.25	2.15		378	0.80	0.24	1.00		438	0.99	0.30	0.38	1
259	0.85	0.48	1.07		319	0.61	0.08	1.16		379	0.84	0.19	0.68		439	0.99	0.34	2.42	
260	1.08	0.43	1.67		320	2.20	0.33	2.60		380	1.03	0.31	2.52		440	1.03	0.32	0.45	1
261	1.62	0.37	2.44		321	2.28	0.43			381	1.79	0.55	2.60		441	1.02	0.44	1.34	
262	1.45	0.34	1.71		322	2.23	0.41	3.79		382	0.86	0.16	0.95		442	1.17	0.53	2.69	
263	0.91	0.49	1.80		323	1.87	0.25	2.92		383	1.13	0.31	1.52		443	0.96	0.57		
264	1.11	0.36	1.78		324	2.41	0.49	3.49		384	1.33	0.35	0.86	1	444	1.16	0.70	0.88	
265	0.84	0.33	1.48		325	2.13	0.43	2.08		385	1.17	0.39	1.67						
266	0.75	0.30	1.52		326	1.74	0.21	2.62		386	1.61	0.20	1.23	1					
267	0.72	0.34	1.04		327	2.17	0.25	3.09		387	2.00	0.55	5.02						
268	0.74	0.30	2.59		328	1.39	0.21	1.95		388	1.77	0.56	3.17						
269	0.82	0.30	1.32		329	1.74	0.24	2.06		389	1.28	0.23	2.15						
270	0.88	0.31	2.22		330	1.90	0.28	2.59		390	1.56	0.32	1.36						
271	1.00	0.54	2.46		331	2.15	0.27	3.22		391	1.58	0.31	2.36						
272	1.48	0.30	1.51		332	2.58	0.37	2.89		392	1.39	0.29	2.19						
273	1.80	0.45			333	2.41	0.44	3.12		393	0.75	0.19	1.39						
274	0.49	0.05	0.96		334	2.59	0.45	2.27		394	1.16	0.46	2.31						
275	0.47	0.05	0.40	1	335	2.33	0.52	2.13		395	0.92	0.22	0.63	1					
276	2.27	0.60	3.76		336	2.14	0.23	2.82		396	1.24	0.26	0.37	1					
277	0.57	0.07	0.49	1	337	1.37	0.15	1.52		397	1.03	0.29	1.04						
278	2.12	0.40	2.92		338	2.23	0.34	2.23		398	1.55	0.29	0.38	1					
279	0.98	0.17	1.23		339	2.28	0.33	2.28		399	1.08	0.29	1.45						
280	1.18	0.21	1.60		340	1.26	0.19	1.50		400	1.39	0.34	4.32						
281	0.93	0.14	1.34		341	2.83	0.58	4.58		401	1.24	0.21	1.34						
282	1.38	0.19	2.09		342	2.62	0.39	3.31		402	1.79	0.27	0.00	1					
283	1.21	0.11	1.51		343	2.60	0.52	2.56		403	1.89	0.51							
284	0.83	0.12	1.54		344	2.69	0.50	2.47		404	3.43	0.48	3.90						
285	1.15	0.14	1.50		345	2.13	0.61	2.61		405	2.49	1.05	0.80	1					
286	0.61	0.06	0.32	1	346	2.51	0.56	2.90		406	1.56	0.21	2.01						
287	0.55	0.06	0.41	1	347	2.89	0.62	0.63	1	407	0.54	0.19	2.59						
288	1.43	0.21	2.15		348	2.04	0.35	3.73		408	1.41	0.16	3.58						
289	1.72	0.31	2.06		349	1.63	0.27	3.79		409	1.00	0.35	2.43						
290	1.51	0.22	1.70		350	1.85	0.41	1.94		410	1.27	0.38	1.85						
291	1.41	0.14	0.96	1	351	1.38	0.28	2.73		411	1.02	0.34	3.10						
292	1.63	0.21	2.07		352	1.25	0.24	1.69		412	1.77	0.46	1.76						
293	1.62	0.30	2.21		353	1.71	0.26	2.28		413	2.13	0.44	3.65						
294	2.23	0.50	2.37		354	1.36	0.25	2.63		414	0.78	0.25	1.57						
295	1.67	0.22	2.18		355	1.55	0.23	2.17		415	0.95	0.25							
296	1.54	0.18	1.54		356	0.82	0.11	1.08		416	0.73	0.27	0.64						
297	2.35	0.28	1.07	1	357	1.84	0.46	3.40		417	0.93	0.27							
298	1.50	0.17			358	1.64	0.31	0.96	1	418	0.94	0.34	3.61						
299	1.54	0.15	1.99		359	1.38	0.27	2.26		419	0.79	0.37	3.41						
300	2.28	0.32	3.73		360	1.46	0.29	1.36		420	1.16	0.39	3.27						
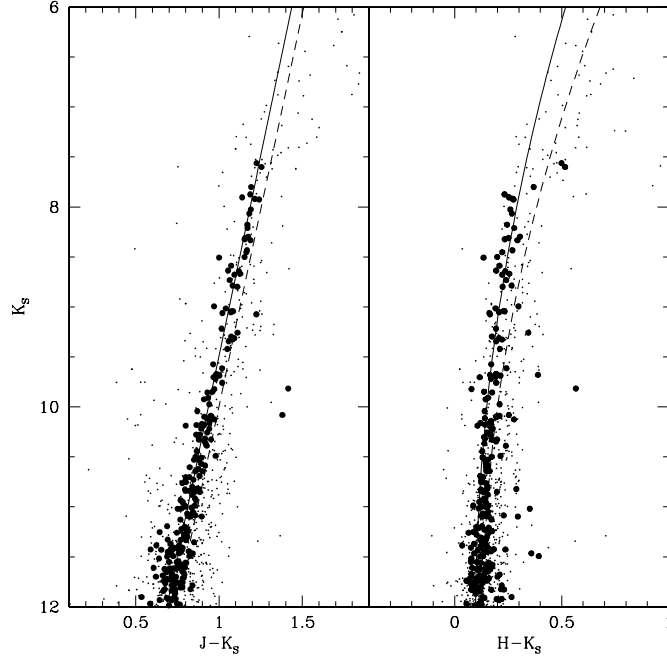
Figure 4.3: *Magnitudes versus colours of 2MASS stars. Large dots are 2MASS sources within 4′ from the centre of the globular cluster 47 Tuc, brought at the distance of 8 kpc adopting a distance modulus of 13.32 (Ferraro et al. 1999). Small dots are dereddened 2MASS Sgr–I field sources, selected within 30″ from Mira stars (Glass et al. 1995) in order to overpopulate the Mira region above the RGB tip. Continuous lines indicate the mean ridge lines for the cluster red giant branch, while dashed lines those of the Sgr–I giants.*

4.2.1 Reference red giant branch

In Figure 4.3 we plot the extinction-corrected 2MASS point sources within 30″ from the positions of Mira stars in the Sgr–I field (Glass et al. 1995). Objects above the RGB tip ($K_S \sim 8.2$ mag) are AGB stars: 63 Mira variables from (Glass et al. 1995) and 24 other stars, most probably semiregular (SR) variables (Alard et al. 2001). In the same diagram we also plot 2MASS sources within 4′ from the centre of the Galactic globular cluster 47 Tuc, moved to a distance of 8 kpc (cluster distance modulus, DM=13.32 mag, from Ferraro et al. 1999).

The upper part ($K_S < 12$ mag) of the 47 Tuc RGB in the $K_{S0}, (J - K_s)_0$ CMD is well represented by a linear fit:

$$(J - K_s)_0 = 2.19(\pm 0.02) - 0.125(\pm 0.002)K_{S0}. \tag{4.1}$$

The 47 Tuc giants appear bluer by 0.05 mag in $(J - K_s)_0$ than the colours of Sgr–I giants, which are more metal rich. However, the cluster $(J - K_s)_0$ vs. K_{S0} RGB has a slope identical to that found in Sgr–I, confirming that the slope does not vary significantly with metallicity (see Dutra et al. 2003; Frogel et al. 1999).

To assess the uncertainty of our extinction estimates, we examined the model RGB colours of Girardi et al. (2000) with two extreme values of metallicity, Z=0.04 and 0.30. These models do not show a significant difference in the CMD slope, and they differ in $(J - K_s)_0$ by only 0.1 mag. A similarly small difference is found for models of 2 Gyr and 16 Gyr old populations. Nominal 2MASS photometric errors are smaller than 0.04 mag for $J < 15$ and $K_S < 13$ mag, but toward the Galactic centre uncertainties are larger because of crowding. However, all the uncertainties have a small impact on the extinction estimates: a change of 0.1 in $(J - K_s)_0$ implies a change of 0.05 in A_{K_s} (0.6 in A_V).

The right-hand panel of Fig. 4.3 shows the $(H - K_s)_0$ vs. K_{S0} diagram of Sgr–I giants and of the 47 Tuc giants. There is again a well defined RGB sequence. A second order polynomial fit well fits 47 Tuc giants with $K_{S0} < 12$ mag:

$$(\mathrm{H} - \mathrm{K_s})_0 = 1.73(\pm 0.22) - 0.268(\pm 0.035) \times \mathrm{K_{S0}} \tag{4.2}$$

$$+ 0.011(\pm 0.002) \times \mathrm{K_{S0}^2}.$$

At $K_{S0} < 8$ mag this fit traces the blue boundary toward Mira stars. A fit of only Sgr–I giants is slightly more shallow:

$$(\mathrm{H} - \mathrm{K_s})_0 = 2.25(\pm 0.13) - 0.347(\pm 0.029) \times \mathrm{K_{S0}} \tag{4.3}$$

$$+ 0.014(\pm 0.002) \times \mathrm{K_{S0}^2}.$$

The $K_s, (H - K_s)$ plane has a lower sensitivity to extinction than the $K_s, (J - K_s)$ plane: here a colour change of 0.1 mag implies a change of ~ 0.15 in A_{K_s}. The models of Girardi et al. (2000) predict variations within $(H - K_s) = 0.04$ mag with metallicity and age variations. The nominal 2MASS photometric errors are smaller than 0.04 for $H < 14$ and $K_S < 13$.

The uncertainty in distance yields only a minor uncertainty in the extinction. A shift in distance modulus of the reference RGB of ± 2 mag results in a change in the extinction of $A_{K_s} \mp 0.15$ mag.

4.2.2 Determination of extinction value and extinction law in the J, H, K_s CMD

Assuming a colour-magnitude relation for red giants, the apparent near-infrared colours of field stars yield information on, both, the magnitude of the extinction and on the shape of the extinction law.

In principle, one can try to fit the observed field star colours to the red giant branch colours in the near-infrared colour-magnitude diagrams, and optimise the fit for both the absolute average extinction in the K_s band along the line of

sight and the spectral index of the extinction power law. To do that, one needs to consider only the region of the colour-magnitude diagram where the upper RGB is well defined, i.e. not affected by large photometric errors or by the diagonal cut-off from the 2MASS detection limits (see Fig. 4.2), which would bias the calculation of the median extinction toward a lower value. In the inner Galaxy, the photometric error is typically below 0.04 for stars with $K_s < 12$ mag. To quantify the incompleteness due to the diagonal cut-off, with zero extinction, our average 2MASS detection limits of $J = 16.0$ and $H = 14.0$ correspond to a RGB K_S magnitude of 15.2 and 13.0 mag, respectively, at a distance of 8 kpc. Accounting for a scatter in the observed colours of ± 0.5 mag, the RGB would be sampled well to $J = 15.5$ and $H = 13.5$ mag, corresponding to $K_S < 14.6$ and 12.6, respectively. With a K_S extinction of 3 mag (~ 5.0 mag in H, ~ 8.6 mag in J), a typical value in the direction of the Galactic centre, these RGB completeness limits would rise to $K_s = 7.1$ and 10.8 mag in the $(K_s, J - K_s)$ and $(K_s, H - K_S)$ planes, respectively. In the J band we would therefore be left with variable AGB stars well above the RGB tip and foreground stars, and only the H band would provide a sufficient number of red giant stars to match the reference RGB. We conclude from this that with the 2MASS data $(K_s, J - K_s)$ colour-magnitude diagrams are useful for extinction determinations only to a K_S extinction of about 1.6 mag, and one must always make sure that only stars above the completeness limit are matched to the RGB. Because of the larger reddening, the $(K_s, J - K_s)$ plane would in principle give more accurate extinction estimates, would it not be affected by the selection effect due to the relatively bright detection limit.

To determine the slope, α, of the near-infrared extinction law we examined the CMDs for field stars which were detected in all three bands, J, H, and K_S, brighter than the K_S completeness limits for the RGB at the extinction of each field. We determined the extinction toward each of our fields separately in the $(K_S, J - K_s)$ and $(K_s, H - K_s)$ CMDs, as the median of the extinctions from individual field stars. The difference of the extinction determinations from the two planes must agree independent from A_{K_S} within the dispersion.

Therefore, we vary α until we get an overall agreement between the extinction estimates from the two planes. Figure 4.4 shows the differences of the median extinction values $A_{K_S}(J,K_S) - A_{K_S}(H,K_S)$ plotted against the A_{K_S} -calculated- for different values of α. The discrepancy between the extinction values increases with A_{K_S} if the assumed value of α is too small. We find that for $\alpha = 1.9$ the two extinction estimates do yield consistent values, within the photometric uncertainties, over the entire range of A_{K_S}.

The main uncertainty in the determination of the extinction power law arises from the uncertainty in the slope of the RGB. Using a fit to the colour-magnitude distribution of the giants in the Sgr–I field ($l = 1.4°$,b$= -2.6$) instead of the 47 Tuc globular cluster giants, that is somewhat steeper in the $(K_S, H - K_S)$ plane, we find that the best value for alpha increases to 2.2.

The slope of the RGB decreases with increasing metallicity, leading to higher values of α. However, since 47 Tuc has a lower metallicity (-0.7 dex) than the average Bulge stars (Frogel et al. 1999; McWilliam & Rich 1994), $\alpha = 1.9$ may be
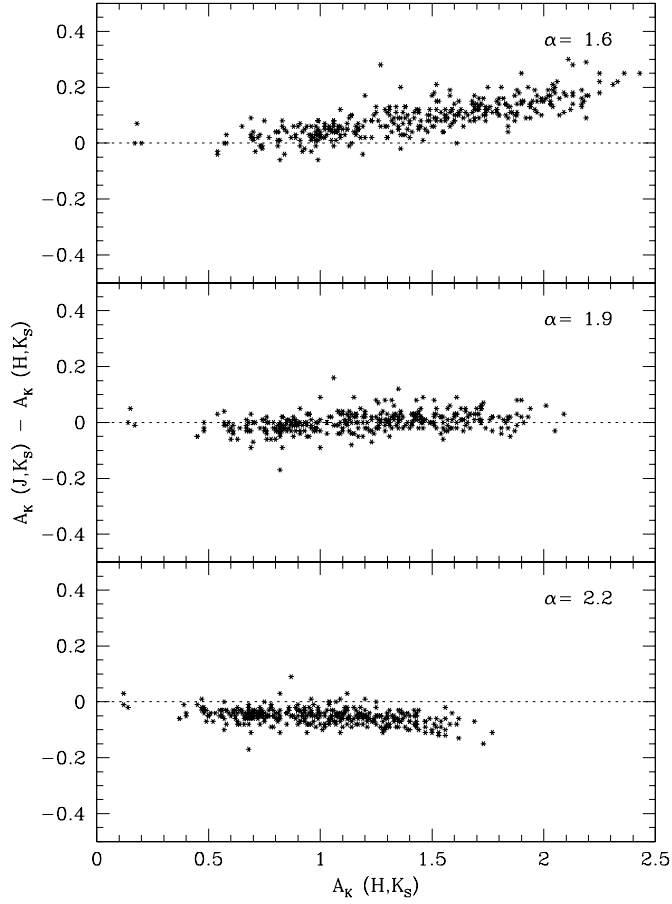
Figure 4.4: *Comparison between the median extinction values toward our fields obtained from the (K_S,$J-K_S$) plane and those from the (K_S,$H-K_S$) plane. Only sources detected in J, H,K_S above the K_S completeness limits are used. In each panel a different value of the spectral index of the extinction power law, α, is adopted.*

taken as a lower limit to the actual value.

We furthermore find that the (K_S,$H-K_S$) distribution of the giants in the low extinction region (A_{K_S}=0.2) at $l = 0.2°$ and b= -2.1 (Dutra et al. 2002; Stanek 1998) match the distribution of the 47 Tuc giants better than that of Sgr–I.

Although complicated by the intrinsic colour-magnitude relation that giant stars follow, the value of the α parameter can be tested using a $J - H$ vs. $H-K_S$ diagram. Using the values from Table 4.1 for power laws with $\alpha = 1.6$, 1.85, 1.9, 2.0, 2.2, the slopes of the reddening vector in the $J - H$ vs. $H-K_S$ diagram are 1.64, 1.75, 1.80, 1.83, 1.94, respectively. Identical slopes are found when red-
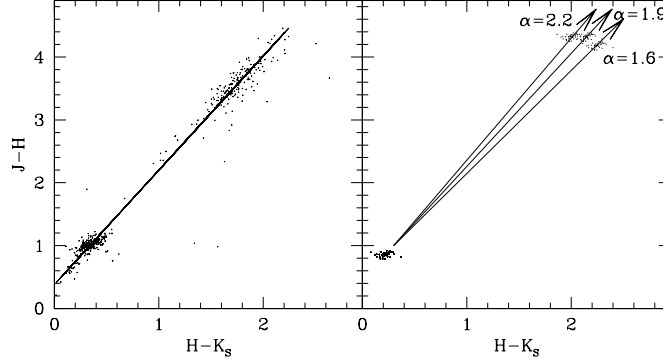
Figure 4.5: $J - H$ *vs.* $H-K_S$ *colours. The arrows are the reddening vectors for a visual extinction of 35 mag and a near-infrared power law slopes α of 1.6, 1.9 and 2.0.* **Left-hand panel:** *Bulge giant stars with $10 < K_s < 8$ mag taken from several Bulge fields at different median extinction.* **Right-hand panel:** *Giant stars from 47 Tuc with $10 < K_s < 8$ mag when brought at the distance of the Galactic centre. The same stars are plotted again reddened using the near-infrared power laws with slope $\alpha = 1.6$, 1.9 and 2.2 and $A_K=2.9$.*

dening artificially the 47 Tuc giants (or the Sgr–I giants) and linearly fitting the non-reddened giants plus the reddened ones. A $J - H$ vs. $H-K_S$ diagram of giant stars from fields with median extinction between $A_{K_S}= 2.0$ and 2.3 mag and from Sgr–I field is shown in Fig. 4.5. The best fit to the datapoints gives a slope of 1.81 ± 0.03, also suggesting that $\alpha = 1.9 \pm 0.1$.

The value $\alpha = 1.9$ is in agreement with the work of Glass (1999) and Landini et al. (1984) and the historical Curve 15 of van de Hulst (1946).

In the rest of the paper we use the extinction calculated assuming $\alpha = 1.9$. For fields with $A_{K_S}< 1.6$ mag we adopt the extinction values determined from the $(K_S, J-K_S)$ plane, otherwise we will use the values from the $(K_S, H-K_S)$ plane.

4.2.3 Outside the Bulge

K2 giant stars are the dominant population of late-type stars seen along the disk (e.g. Drimmel et al. 2003; López-Corredoira et al. 2002). They correspond to red clump stars in metal-rich globular clusters such as 47 Tuc. The location of clump stars on the CMD depends on extinction and distance. This trace was modelled taking the absolute magnitudes of clump stars from Wainscoat et al. (1992) and the distribution of dust and stars in the Galaxy found by Drimmel et al. (2003). The trace of the clump stars is shown by the left curve in Fig. 4.2, and it appears more populated by stars and distinct from the Bulge RGB in the CMD of the field at $l =\sim 10°$.

Toward the Bulge the Bulge RGB population is dominant and therefore the

median interstellar extinction is practically not affected by possible foreground clump stars. This is not the case in the disk, where one must eliminate the foreground clump stars before fitting the RGB in order to properly calculate the median extinction of field giants.

We therefore identified as likely clump stars those located within 0.3 mag from the $J - K_S$ colour of the clump trace, and we identify as giants those stars redder than the clump stars (e.g. López-Corredoira et al. 2002).

4.2.4 Dispersion of the extinctions along a line of sight

Toward a given target star together with the median extinction of field stars A_{K_S} we determined the standard deviation of the distribution of the individual extinctions, $\sigma_{A_{K_S}}$.

The patchy nature of the extinction is visible even within the $2 - 4'$ radius sampling area. This patchiness integrated over a longer path generates larger $\sigma_{A_{K_S}}$ with increasing extinction for Bulge line of sights. The $1\sigma_{A_{K_S}}$ uncertainty in the field extinction varies from ~ 0.2 mag when $A_{K_S} = 0.6$ mag up to ~ 0.7 mag in the regions with the largest extinction ($A_{K_S} > 2.0$). In fields at longitudes longer that $10°$ a larger $\sigma_{A_{K_S}}$ is found than in Bulge fields of similar median extinction. This is probably due to the presence of several Galactic components, e.g. the disk, arms, bar and molecular ring, along these line of sights.

4.3 Near-infrared properties of known Mira stars

As indicated by their variability, their strong 15 μm emission (Chapter III), and their SiO maser emission (Chapter II), our SiO targets are AGB stars in the thermal pulsing phase. At the present time their pulsation periods and amplitudes are not known. However, most of our SiO targets must be large amplitude variables (Chapter III).

Though they are 20 times less numerous than semiregular AGB stars (SRs) (Alard et al. 2001), Mira stars are among the best studied pulsating variable stars. They are regular long period variables (LPV) with visual light amplitude over 2.5 mag, or K band amplitude over ~ 0.3 mag. Since large amplitudes tend to be associated with the most regular light curves (Cioni et al. 2003), the amplitude remains the main parameter for the classification of a Mira star.

To analyse the colours of our SiO targets, in particular to check the quality of the extinction corrections, it is useful to have a comparison sample of large amplitude LPV AGB stars, well studied and covering a wide range of colours.

Therefore, we examined various comparison samples of known Mira stars free of extinction: two samples in the solar vicinity, taken from Olivier et al. (2001) and Whitelock et al. (2000), plus one sample toward the Galactic Cap taken from Whitelock et al. (1994). To account for possible changes in the colour properties of the Mira stars with Galactic position, we also looked at two samples of Bulge Mira stars from regions of low extinction: 18 Mira stars detected by IRAS (Glass

et al. 1995) in the Sgr–I field, and 104 IRAS Mira stars at latitude $6° < b < 7°$ and $|l| < 15°$ (Whitelock et al. 1991); for comparison a sample of LPV in the Large Magellanic Cloud is also considered (Whitelock et al. 2003). All these stars have IRAS 12 μm magnitude, [12], and mean J, H, K magnitudes in the SAAO system (Carter 1990).

The stellar fluxes are given already corrected for reddening only in the work of Olivier et al. (2001). For the LPV stars analysed by Whitelock et al. (2000, 1994, 2003) the effects of interstellar extinction are negligible because these stars are nearby or outside of the Galactic plane and we therefore did not correct these for extinction. We dereddened the Baade Sgr–I window data (Glass et al. 1995) adopting our favourite extinction curve ($\alpha = 1.9$) and $A_{K_S} = 0.15$ mag (consistently with the extinction value adopted in Glass et al. 1995). We corrected for reddening the magnitudes of the outer Bulge Miras (Whitelock et al. 1991) adopting values of A_{K_S} derived from their surrounding stars (see next section).

Next we analyse the location of these well-known Mira stars in the near-infrared CMDs and colour-colour diagrams.

4.3.1 Colour-magnitude diagram of outer Bulge Mira stars and surrounding field stars

Long period variable stars in the outer Bulge as studied by Whitelock et al. (1991) are interesting in several aspects: they were selected on the basis of their IRAS fluxes and colours according to criteria similar to those with which we selected our MSX targets (Chapter II; Chapter III); since their main period ranges from 170 to 722 days and their K amplitudes from 0.4 to 2.7 mag, they are classical Mira stars; their distances were estimated from the period-luminosity relation (Whitelock et al. 1991), resulting in a distribution of the distance moduli peaking at 14.7 mag with a $\sigma = \sim 0.5$ mag; since they are at latitudes between 6 and 7°, they are in regions of low interstellar extinction. All this makes them ideal objects for a comparison with our SiO targets, the study of which is complicated by the large interstellar extinction at their low latitudes.

Fig. 4.6 shows the 2MASS point sources within 1′ of each Mira star. A giant branch is clearly apparent. From an isochrone fitting (see Sect. 4.2) we derived the median extinction toward each field, resulting in values of A_{K_S} ranging from 0.01 to 0.30 mag, with a typical dispersion of 0.01-0.08 mag. On the colour-magnitude diagrams the Mira stars appear mostly brighter than the RGB tip of the field stars ($K = 8.2$ mag at a distance of 8 kpc, see Frogel & Whitford 1987). Due to the presence of a circumstellar envelope, Mira stars have red colours (up to $(H - K_s)_0 = 3$ mag) and lie on the red-side of the giant sequence.

It is therefore not possible to derive the interstellar extinction toward these Mira stars from their colours relative to the RGB. On the other hand, we do not have reasons to assume that the Mira stars are spatially distributed differently than the other giants stars. Therefore, the extinction of its surrounding field stars may serve as an approximation for that of the respective Mira star.
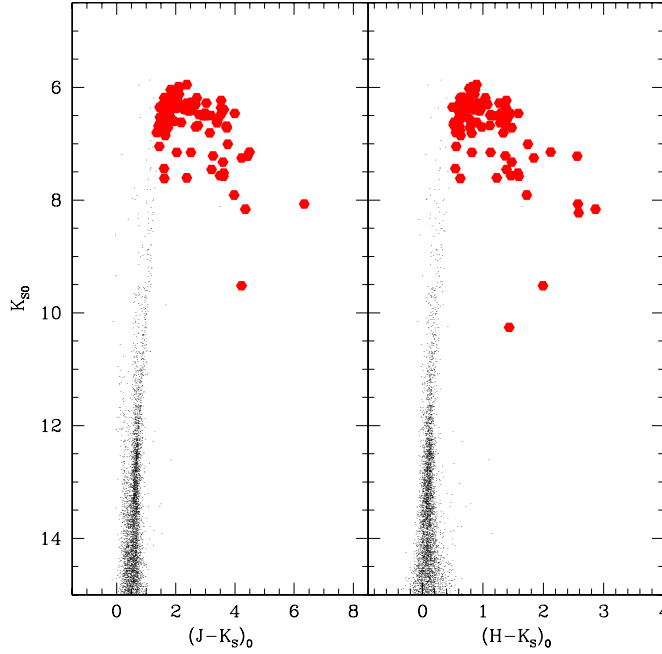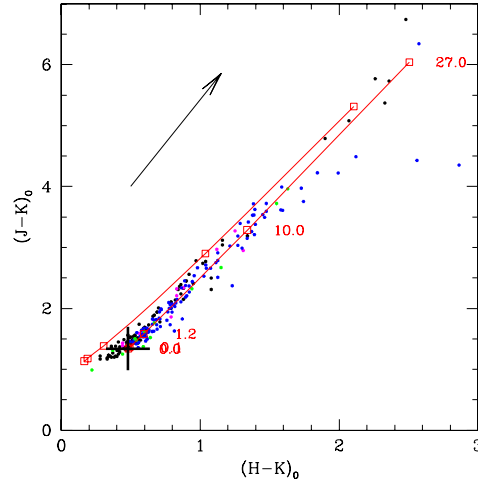
Figure 4.6: *Dereddened colour-magnitude diagrams. Big dots represent the outer Bulge Mira stars found by Whitelock et al. (1991); the magnitudes plotted are mean magnitudes at the equal distance of 8 kpc, adopting the distances of Whitelock et al. (1991). Small dots represent the point sources detected by 2MASS within 1' from each Mira star.*

When going to lower latitude fields, however, the extinction increases and the RGB becomes broader. A worry in the assumption that a Mira star is at the median extinction of the field is the lack of knowledge of the actual distribution of extinction along the line of sight which does not warrant that the extinction of a given Mira star is the median extinction of field stars.

4.3.2 Colour-colour diagram of Mira stars

The $(J - K)_0$ vs. $(H - K)_0$ colours of Mira stars are shown in Fig. 4.7. For stars with low mass-loss rate ($< 10^{-7}$ M$_\odot$ yr^{-1}) $(J - K)_0$ ranges between 1.2 and 1.6 (Whitelock et al. 2000). Dust-enshrouded IRAS AGB stars with mass-loss rates of $10^{-6} - 10^{-4}$ M$_\odot$ yr^{-1} (Olivier et al. 2001) are much redder, $(J - K)_0$ ranging from 2 to 6.5 mag. The overall distribution appears to form a sequence of ever redder colours with increasing mass-loss rate, a trend that is well reproduced, e.g., by a model for an M10 type AGB star with increasing shell opacity (Groenewegen & de Jong 1993). Thus, a higher mass loss has the same effect on $(J - K)_0$ and $(H - K)_0$ colours as more interstellar absorption/reddening, making a distinction

Figure 4.7: *Dereddened colours of known dusty Mira stars (Glass et al. 1995; Olivier et al. 2001; Whitelock et al. 1991, 2000, 1994). Near-infrared mean magnitudes are used. The two curves represent M3 (upper) and an M10 (lower) type stars with increasing mass-loss rates (indicated by squares and labels $\times 10^{-6}$ $M_\odot$/year), as modelled by Groenewegen & de Jong (1993). The cross indicates the position of an M10 star without mass-loss ($(H - K)_0 = 0.48$ and $(J - K)_0 = 1.34$). The arrow shows the reddening vector for $A_K = 1$ mag.*

between intrinsic and interstellar reddening in these colours impossible.

In, both, the $(J - K)_0$ vs. $(K - [12])_0$ and the $(H - K)_0$ vs. $(K - [12])_0$ planes Mira stars are distributed along a broad sequence compared to that seen in the $(J - K)_0$ vs. $(H - K)_0$ plane, as shown in Figs. 4.8 and 4.9.

A comparison with the best fit to the colour-colour sequence of IRAS-selected oxygen-rich AGB stars (van Loon et al. 1998, 1997) shows that in the $(H - K)_0$ vs. $(K - [12])_0$ plane Mira stars lie below that curve, while in the $(J - K)_0$ vs. $(K - [12])_0$ plane there appears no such offset. The offset could be due to water absorption bands in the H band (Frogel & Whitford 1987; Glass et al. 1995), that are found strong in large amplitude variable AGB stars, although we could not find any correlation between colour and variability index for the IRAS stars used by van Loon et al. (Fouque et al. 1992; Guglielmo et al. 1993). The offset might then indicate that for such cold stars the Carter (1990) transformations between the ESO photometry (Fouque et al. 1992; Guglielmo et al. 1993) and the SAAO system (van Loon et al. 1998, 1997) are not adequate.

Mira stars with $0.2 < (H - K)_0 < 3$ mag fit

$$(K - [12])_0 = 4.26(\pm 0.04) + 5.95(\pm 0.17) \log(H - K)_0,$$
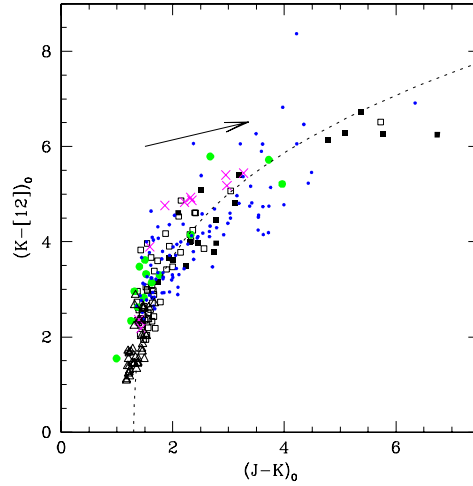
Figure 4.8: *Dereddened colours of infrared-monitored Mira stars (based on the IRAS 12 µm and near-infrared mean magnitudes): in the solar vicinity (filled squares) (Olivier et al. 2001); detected by Hipparcos (open triangles) (Whitelock et al. 2000); toward the South Galactic Cap (open squares) (Whitelock et al. 1994); in the Baade Sgr–I window (big dots) (Glass et al. 1995); in the outer Bulge (small dots) (Whitelock et al. 1991); in the Large Magellanic Cloud (crosses) (Whitelock et al. 1994). The dotted line is the best fit to an IRAS sample of oxygen-rich AGB stars van Loon et al. (1997). The arrow shows the reddening vector for $A_K = 1$ mag.*

with an rms deviation of 0.5 mag. Although we use the SAAO system (Carter 1990), in Appendix A we show that this relation is also valid in the 2MASS photometric system.
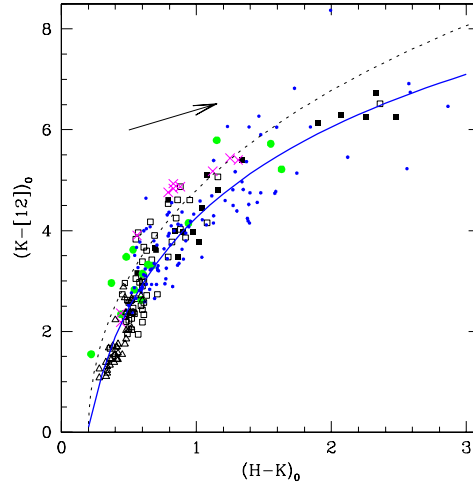
4.4 Interstellar extinction and intrinsic colours of the SiO targets

The observed colours of the SiO target stars are shown in Fig. 4.10. For a given $K_S - [15]$, the $H - K_S$ colours of the SiO target stars are redder than those expected from the colour-colour relation of known Mira stars, and some stars show excess larger than $E(H - K_S) = 1$ mag. This is due to interstellar extinction along the line of sight.

Since observations of Mira stars may suffer from several magnitudes of circumstellar reddening, it not possible to estimate the interstellar extinction toward the SiO target stars by simply assuming an intrinsic colour for a given star.

As seen from Figs. 4.7, 4.8 and 4.9, Mira stars follow near- and mid-infrared colour-colour relations. In the first figure, Fig. 4.7, the reddening vector is paral-

Figure 4.9: *Dereddened colours of infrared-monitored Mira stars, based on the IRAS 12 μm and near-infrared mean magnitudes. Symbols are the same as in Fig. 4.8. The dotted line is the best fit to an IRAS sample of oxygen-rich AGB stars (van Loon et al. 1998). The continuous curve is our best fit for Galactic Mira stars. The arrow shows the reddening vector for $A_K = 1$ mag.*

lel to the distribution of observed stellar colours and to those of models of AGB stars of increasing shell opacity. In contrast, the reddening vectors in Figs. 4.8 and 4.9 have a slope smaller than that of the distribution of observed stellar points and in principle can permit a separation between interstellar and circumstellar extinction. However, the dispersion of the Mira stars around the colour-colour fiducial sequence is large (0.5 mag), due to the non-contemporaneity of the near- and mid-infrared data and because of the dependence of such relations on metallicity and stellar spectral type. The uncertainty of the interstellar extinction estimates by shifting a star along the reddening vector onto the $H - K_s, K_s - [15]$ curve is larger than $A_{K_s} = 1$ mag for $K - [15] > 3.5$ mag.

Therefore, to deredden our targets we prefer to use the "field" extinction values (reported in Table 4.3), i.e. we assume that a given SiO target star is located at the distance of the median extinction along the line of sight. Though the dispersion of individual field star extinctions along a given line of sight is considerable (from 0.1 to 0.8 $\sigma_{A_{K_s}}$), the distribution is strongly peaked, especially in the Bulge region. This means also to assume that the SiO targets are located in the region with the highest stellar density along the line of sight. This assumption is justified by the fact that the lifetime of a star on the AGB evolutionary phase is very short ($\sim 5\%$ of the time spent on the helium core burning phase and from 0.1 to 2% of the time spent on the main sequence phase of such a star; Vassiliadis & Wood 1993) and we therefore expect most of the AGB stars to be located in those regions with
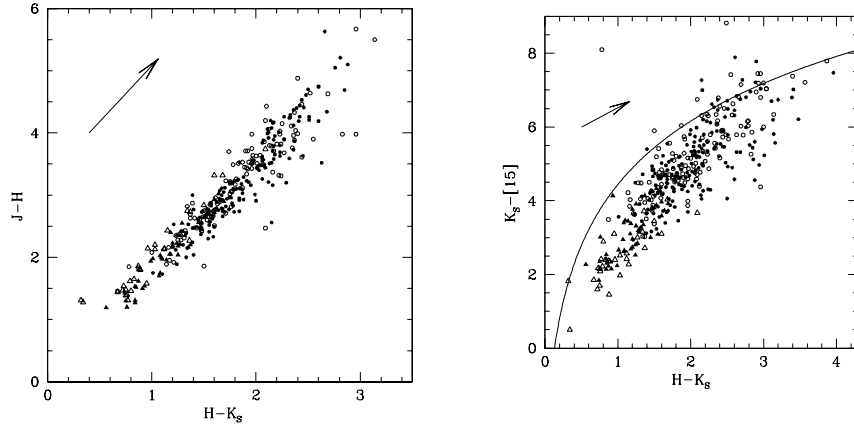
Figure 4.10: Left panel: *2MASS $J - H$ versus $H-K_S$ colours. Stars with upper magnitude limits are not shown. Dots and triangles represent objects with K_S smaller and larger than 6.0 mag, respectively. Filled and open symbols represent SiO detections and non-detections, respectively. The arrow shows the reddening vector for $A_{K_S} = 1$ mag.* **Right panel:** *2MASS $K_S-[15]$ versus $H-K_S$ colours. Symbols are as in the left panel. The curve represents the best fit to the colours of known Mira stars (see Sect. 4.3).*
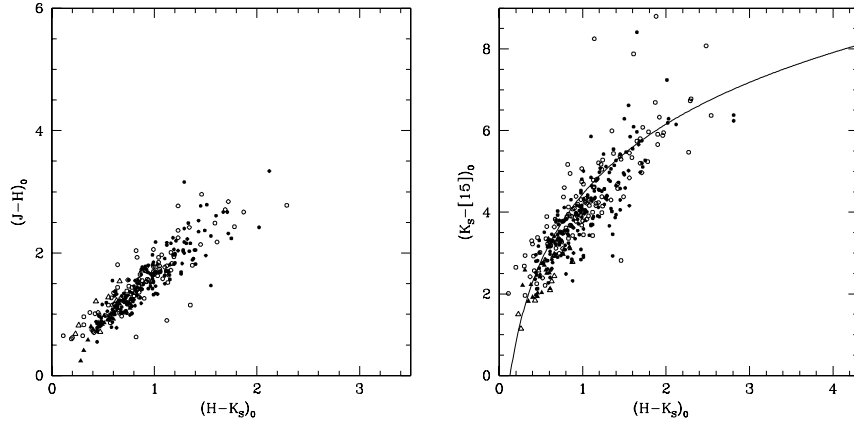
Figure 4.11: Left panel: *Dereddened 2MASS $(J - H)_0$ versus $(H-K_S)_0$ colours.* **Right panel:** *Dereddened 2MASS $(K_S-[15])_0$ versus $(H-K_S)_0$ colours. Symbols are as in Fig. 4.10. "Foreground objects" have been removed.*

higher stellar density.

The distribution of the SiO targets in the dereddened $(H - K_S)_0, (K - [15])_0$ diagram (Fig. 4.11) approaches that of known Mira stars. This confirms that the

"field" median extinction is a good approximation of the interstellar extinction for most of the SiO targets and that the SiO targets do mostly belong to the highest stellar density region, i.e. the inner Galaxy. There is still an asymmetry in the distribution of the SiO targets around the fiducial colour line of known Miras, which suggests that we could have underestimated the interstellar extinction for part of the sample. In regions of high extinction, due to their high near-infrared luminosity, Mira-like stars are detectable to larger distances than ordinary field stars. Deeper infrared observations are needed to obtain more accurate extinction estimates (Figer et al. 2004).

4.4.1 "Foreground objects"

Dereddening all observed points in the $(H - K_s)$ vs. $(J - H)$ diagram (cf. Fig. 4.7) to the $A_{K_S} = 0.0$ position, we can measure the total (circumstellar plus interstellar) extinction of each SiO target (Table 4.3). We assumed a stellar photospheric $(J - K_s)_0$ colour of 1.4 mag and a $H_0 - K_{S0}$ colour of 0.5 mag.

The difference of such total extinction estimates from 2MASS and DENIS J, K_s data gives an rms of $\Delta A_{K_S} = 0.2$ mag, while the estimates from 2MASS $H - K_s$ and $J - K_s$ colours gives an rms difference of $\Delta A_K = 0.13$ mag. For only 12 SiO targets we do not have any observed $H - K_s$ or $J - K_s$ values, and therefore total extinction values are not determined (Table 4.3).

The median interstellar extinction of the field stars surrounding a target star was compared with the individual total extinction of the target star. As expected, on average the target stars show larger total extinctions than their field stars. This is not the case, however, for a group of ~ 50 mostly very bright target stars ($K_S < 6.0$), at various longitudes, marked with flag 1 in Table 4.3, which have total extinctions lower (a least $1\sigma_{A_{K_S}}$) than the "field" extinction and are therefore likely to be significantly less distant. Thereby the extinction was used to identify foreground objects. We dereddened the "foreground objects" by directly shifting them on the $H, K_s, [15]$ colour-colour sequence.

4.5 Intrinsic colours and mass-loss rates

The stellar mass-loss rate is best estimated from measurements of CO rotational lines. The CO emission arises in the circumstellar shell. However, because of confusion with interstellar CO emission it is difficult to obtain such measurements toward stars in the inner Galaxy (Winnberg et al. 1991). Although infrared emission also arises from the stellar photosphere, stellar outflows may be studied from the infrared emission of dust grains which form in the cool circumstellar envelopes. Relations between the infrared colours (e.g. $J - K$, $K - L$, $K - [12]$ or $K - [15]$) of O-rich AGB stars and their mass-loss rate have been established empirically (e.g. Alard et al. 2001; Olivier et al. 2001; Whitelock et al. 1994) and supported by theoretical models (e.g. Ivezíc et al. 1999; Jeong et al. 2003; Groenewegen & de Jong 1993; Ojha et al. 2003).
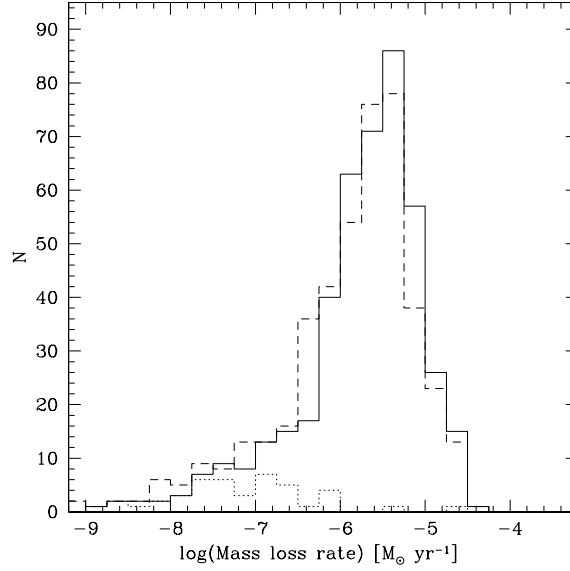
Figure 4.12: *Distribution of mass-loss rates derived from the $K - [15]$ vs. $\dot{M}$ relation Jeong et al. (2003). The continuous line shows the distribution for all SiO targets dereddened using Lutz's extinction law (Curve 3), and the dotted line that of foreground stars. The dashed line is the distribution of all SiO targets using the mid-infrared extinction law of Mathis (Curve 1).*

The empirical relation between the $(K - [15])_0$ colour and the mass loss rate, $\dot{M}$, is very useful to study stars detected in the 2MASS, DENIS, ISOGAL or MSX surveys toward the most obscured regions of the Galaxy.

The uncertainties arising from the variability of the stars and the temporal difference between the K_S and $15\mu m$ measurements, is somewhat alleviated by using an average of the 2MASS and DENIS K_S fluxes and of the ISOGAL and MSX $15\mu m$ measurements (Ojha et al. 2003). The remaining r.m.s. uncertainty of the mass-loss rate is thus a factor ~ 2 for $\dot{M} > 10^{-6}$ $M_\odot$ yr^{-1}.

Following the prescription of Jeong et al. (2003) and Ojha et al. (2003) we obtained mass-loss rates for the SiO targets, the distribution of which is shown in Fig. 4.12. 90% of the sources have implied mass loss rates between 10^{-7} and 2×10^{-5} $M_\odot$ yr^{-1}, with a peak in the range $10^{-6} - 10^{-5}$ $M_\odot$ yr^{-1}, although the apparent distribution is widened by the uncertainty of the mass-loss–colour relation, by the photometric uncertainty and by the effects of variability. Note that the selection criterion on $(K_S - [15])_0$ for the ISOGAL sample completely eliminated sources with $\dot{M} > 10^{-5}$, and that the elimination of OH/IR sources and the criteria on $A - D$ and $C - E$ colours for the MSX sample also considerably reduced the proportion of sources with large mass-loss rates (see Chapter II; Chapter III).

The same results are obtained considering the subsample of targets with the best extinction corrections, i.e. with $\sigma_{A_{K_s}} < 0.2$ mag. The distribution of the mass-loss rates of the SiO targets with detected SiO maser emission appears similar to that of the SiO targets non-detected (Chapter II).

Adopting Mathis' mid-infrared extinction law rather than Luts's one, the distribution of the mass-loss rates only slightly shift toward lower values (see Fig. 4.12).

4.6 Conclusion

We estimated the interstellar extinction toward each of our 441 SiO target stars. For all 2MASS stars within 2-4′ radius field of each target we shifted the $(J - K_s)$ and $(H - K_s)$ colour versus K_s magnitude along the reddening vector onto the reference red giant branch. The use of both colour-magnitude planes enabled us to obtain a mean extinction for each field and new constraints on the index of the near-infrared extinction power law, α. We found that a value of $\alpha = 1.6$ is inconsistent with the colours of inner Galactic stars, and, taking 47 Tuc as a reference for the RGB, we determine $\alpha = 1.9 \pm 0.1$.

For K_S-band extinctions larger than 1.6 mag the 2MASS $(K_S, J - K_s)$ CMD yields too low extinction estimates, due to a selection effect from the J-band dropout of more distant sources. The 2MASS $(K_s, H - K_s)$ CMD suffers less from this bias.

We reviewed near- and mid-infrared dereddened colour-colour relations of Mira stars and use them to test the quality of the extinction corrections for each SiO target.

Under the assumption that SiO targets are spatially distributed similarly to surrounding field stars, we corrected the photometric measurements of the SiO targets adopting the median extinction of their surrounding field stars. Derredened colours of the SiO targets are not perfectly symmetrically distributed around the fiducial colour-colour line derived from known Mira stars, suggesting that for part of the SiO targets we may still be underestimating the interstellar extinction of up to about 15%. About 50 SiO targets lie significantly in the "foreground" of the mean stellar distribution.

Using the relation between mass-loss rate and $(K_S - 15)_0$ colour given by Jeong et al. (2003), we estimated that most of the SiO targets have mass-loss rates in the range 10^{-7} to 10^{-5} M$_\odot$ yr^{-1}.

Appendix A: SAAO and 2MASS colours and magnitudes

Transformation equations between the colours and magnitudes measured in the SAAO Carter (1990) and 2MASS photometric systems have been derived by Carpenter (2001) using a list of mostly blue 94 photometric standards. Figure 12 in Carpenter (2001) shows that the differences between magnitudes and colours obtained with the two systems are smaller than 0.15 mag.

Considering that Mira stars have typically a pulsation amplitude in the near-infrared of 1-2 mag and that 2MASS data are from a single-epoch observation randomly taken with respect to the stellar phase, the system transformations have only a secondary effect in the total colour and magnitude uncertainty, when comparing data from 2MASS with data taken with the SAAO telescope.

Since Mira stars are cold objects, molecular absorption bands characterise their infrared spectra and we must exclude that a combination of molecular bands and filter transmissions could generate a different colour transformation for these special class of objects. To address that we looked for 2MASS counterparts of the 104 outer Bulge Mira stars monitored by Whitelock et al. (1994). As demonstrated in Chapter III, Mira stars are among the brightest objects detected in the K_s band and therefore the identification of their 2MASS counterparts is straightforward. A number of 101 2MASS counterparts were found within $60''$ (mostly within $10''$) from the IRAS position. We excluded three sources because they had not unique counterparts (IRAS 17287$-$1955, IRAS 17030$-$2801, IRAS 18264$-$2720).

The differences between the mean magnitudes obtained with SAAO observations (Whitelock et al. 1991) and the single-epoch 2MASS data have a dispersion of up to 0.8 mag.

We obtain the following mean differences:

$$K_{s(2\mathrm{MASS})} - K_{(\mathrm{SAAO})} = -0.15 \pm 0.06 \text{ mag};$$

$$(J - K_s)_{(2\mathrm{MASS})} - (J - K)_{(\mathrm{SAAO})} = -0.14 \pm 0.05 \text{ mag};$$

$$(H - K_s)_{(2\mathrm{MASS})} - (H - K)_{(\mathrm{SAAO})} = -0.06 \pm 0.03 \text{ mag}.$$

To verify whether the colour-colour relations found in Sect. 4.3, using data in the SAAO photometric system, hold also when using 2MASS photometry, in Fig. A.1 we plot both SAAO data and 2MASS data for the same sample of Mira stars (Whitelock et al. 1991). No systematic trend is present.
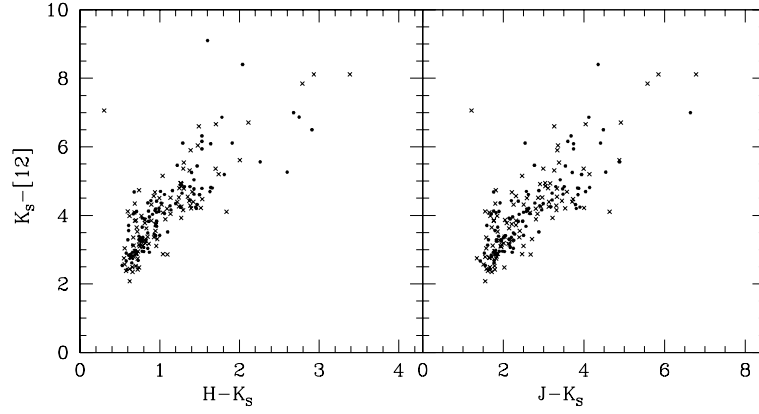
Figure A.1: *Colour-colour plots of Mira stars. The dots indicate average colours of Mira stars obtained from SAAO observations (Whitelock et al. 1991). Crosses indicate colours from single-epoch 2MASS data for the same sample of Mira stars (Whitelock et al. 1991).*
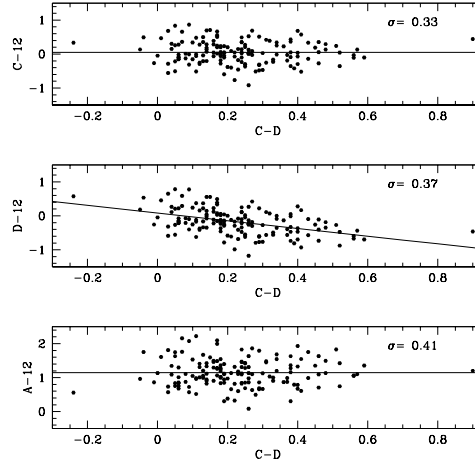
Figure B.2: *Colour-Colour diagrams of our SiO targets. The IRAS 12μm magnitude is defined as* $[12] = -2.5 \log F_{12}[\mathrm{Jy}]/28.3$. *The continuous lines are our best fits.*

Appendix B: IRAS and MSX filters

Most of the past work has been carried out using the IRAS photometry, and therefore the currently available colour-colour relations of Mira stars use mid-infrared data from the IRAS catalogue. A comparison of mid-infrared filters is therefore mandatory to translate old findings into new MSX and ISOGAL colours.

Figure B.2 shows the difference between MSX magnitudes and IRAS 12 μm magnitude for the SiO targets. Note that the D filter excludes the silicate feature

around 9.7 μm, while A and C filters include part of it (see Fig. 4.1). Therefore the $(D-[12])$ colour shows a dependence on the $(C-D)$ colour, which increases when the silicate feature at 9.7 μm starts to be self-absorbed. The $(A-[12])$ and $(C-[12])$ colours do not show any trend with the $(C-D)$ colour. Due to both uncertainties of photometric measurements and source variability the scatter is large, however we derived relations between the A, C, and D and the [12] magnitudes, as follow:

$A - [12] = 1.15 \pm 0.03$ mag

$C - [12] = 0.05 \pm 0.03$ mag

$D - [12] = 0.08(\pm 0.18) - 1.13(\pm 0.05)(C - D)$ mag.

References

Alard, C., Blommaert, J. A. D. L., Cesarsky, C., et al. 2001, ApJ, 552, 289

Bertelli, G., Bressan, A., Chiosi, C., Fagotto, F., & Nasi, E. 1994, A&AS, 106, 275

Blommaert, J. A. D. L., Siebenmorgen, R., Coulais, A., et al., eds. 2003, The ISO Handbook, Volume II - CAM - The ISO Camera

Cardelli, J. A., Clayton, G. C., & Mathis, J. S. 1989, ApJ, 345, 245

Carpenter, J. M. 2001, AJ, 121, 2851

Carter, B. S. 1990, MNRAS, 242, 1

Cioni, M.-R. L., Blommaert, J. A. D. L., Groenewegen, M. A. T., et al. 2003, A&A, 406, 51

Cotera, A. S., Simpson, J. P., Erickson, E. F., et al. 2000, ApJS, 129, 123

Cutri, C. M., Skrutskie, M. F., & Van Dyk, S. 2003, avalaible on line at `http://www.ipac.caltech.edu/2mass/`

Draine, B. T. & Lee, H. M. 1984, ApJ, 285, 89

Drimmel, R., Cabrera-Lavers, A., & López-Corredoira, M. 2003, A&A, 409, 205

Dutra, C. M., Santiago, B. X., & Bica, E. 2002, A&A, 381, 219

Dutra, C. M., Santiago, B. X., Bica, E. L. D., & Barbuy, B. 2003, MNRAS, 338, 253

Egan, M. P., Price, S. D., Moshir, M. M., et al. 1999, AFRL-VS-TR-1999, 1522

Epchtein, N., de Batz, B., Copet, E., et al. 1994, Ap&SS, 217, 3

Ferraro, F. R., Messineo, M., Fusi Pecci, F., et al. 1999, AJ, 118, 1738

Figer, D. F., Rich, R. M., Kim, S. S., Morris, M., & Serabyn, E. 2004, ApJ, 601, 319

Fluks, M. A., Plez, B., The, P. S., et al. 1994, A&AS, 105, 311

Fouque, P., Le Bertre, T., Epchtein, N., Guglielmo, F., & Kerschbaum, F. 1992, A&AS, 93, 151

Frogel, J. A., Tiede, G. P., & Kuchinski, L. E. 1999, AJ, 117, 2296

Frogel, J. A. & Whitford, A. E. 1987, ApJ, 320, 199

Girardi, L., Bressan, A., Bertelli, G., & Chiosi, C. 2000, A&AS, 141, 371

Glass, I. S. 1999, Book Review: Handbook of infrared astronomy (Cambridge U. Press)

Glass, I. S., Whitelock, P. A., Catchpole, R. M., & Feast, M. W. 1995, MNRAS, 273, 383

Groenewegen, M. A. T. & de Jong, T. 1993, A&A, 267, 410

Guglielmo, F., Epchtein, N., Le Bertre, T., et al. 1993, A&AS, 99, 31

He, L., Whittet, D. C. B., Kilkenny, D., & Spencer Jones, J. H. 1995, ApJS, 101, 335

Hennebelle, P., Pérault, M., Teyssier, D., & Ganesh, S. 2001, A&A, 365, 598

Ivezíc, Z., Nenkova, M., & Elitzur, M. 1999, User Manual for DUSTY (Lexington: Univ. Kentucky)

Jeong, K. S., Winters, J. M., Le Bertre, T., & Sedmayr, E. 2003, Proceeding of WS on Mass-Losing Pulsating Stars and their Circumstellar Matter, Sendai, Japan, Y.Nakada & M.Honma (eds), Kluwer ASSL series

Jiang, B. W., Omont, A., Ganesh, S., Simon, G., & Schuller, F. 2003, A&A, 400, 903

López-Corredoira, M., Cabrera-Lavers, A., Garzón, F., & Hammersley, P. L. 2002, A&A, 394, 883

Landini, M., Natta, A., Salinari, P., Oliva, E., & Moorwood, A. F. M. 1984, A&A, 134, 284

Lutz, D. 1999, in ESA SP-427: The Universe as Seen by ISO, Vol. 427, 623

Lutz, D., Feuchtgruber, H., Genzel, R., et al. 1996, A&A, 315, L269

Mathis, J. S. 1990, ARA&A, 28, 37

—. 1998, ApJ, 497, 824

McWilliam, A. & Rich, R. M. 1994, ApJS, 91, 749

Messineo, M., Habing, H. J., Menten, K. M., Omont, A., & Sjouwerman, L. O. 2004a, A&A in preparation (Chapter V)

—. 2004b, A&A, 418, 103 (Chapter III)

Messineo, M., Habing, H. J., Sjouwerman, L. O., Omont, A., & Menten, K. M. 2002, A&A, 393, 115 (Chapter II)

Ojha, D. K., Omont, A., Schuller, F., et al. 2003, A&A, 403, 141

Olivier, E. A., Whitelock, P., & Marang, F. 2001, MNRAS, 326, 490

Omont, A., Gilmore, G. F., Alard, C., et al. 2003, A&A, 403, 975

Price, S. D., Egan, M. P., Carey, S. J., Mizuno, D. R., & Kuchar, T. A. 2001, AJ, 121, 2819

Rieke, G. H. & Lebofsky, M. J. 1985, ApJ, 288, 618

Rosenthal, D., Bertoldi, F., & Drapatz, S. 2000, A&A, 356, 705

Schuller, F., Ganesh, S., Messineo, M., et al. 2003, A&A, 403, 955

Schultheis, M., Ganesh, S., Simon, G., et al. 1999, A&A, 349, L69

Stanek, K. Z. 1998, Using the DIRBE/IRAS All-Sky Reddening Map to Select Low-Reddening Windows Near the Galactic Plane, preprint [astro-ph/9802307]

Udalski, A. 2003, ApJ, 590, 284

van de Hulst, H. C. 1946, Optics of spherical particles. (Amsterdam, Drukkerij J. F. Duwaer, 1946.), 1

van Loon, J. T., Gilmore, G. F., Omont, A., et al. 2003, MNRAS, 338, 857

van Loon, J. T., Zijlstra, A. A., Whitelock, P. A., et al. 1998, A&A, 329, 169

—. 1997, A&A, 325, 585

Vassiliadis, E. & Wood, P. R. 1993, ApJ, 413, 641

Wainscoat, R. J., Cohen, M., Volk, K., Walker, H. J., & Schwartz, D. E. 1992, ApJS, 83, 111

Whitelock, P., Feast, M., & Catchpole, R. 1991, MNRAS, 248, 276

Whitelock, P., Marang, F., & Feast, M. 2000, MNRAS, 319, 728

Whitelock, P., Menzies, J., Feast, M., et al. 1994, MNRAS, 267, 711

Whitelock, P. A., Feast, M. W., van Loon, J. T., & Zijlstra, A. A. 2003, MNRAS, 342, 86

Winnberg, A., Lindqvist, M., Olofsson, H., & Henkel, C. 1991, A&A, 245, 195

Chapter 5

86 GHz SiO maser survey of late-type stars in the Inner Galaxy IV. Bolometric magnitudes

M. Messineo, H. J. Habing, K. M. Menten, A. Omont, L. O. Sjouwerman

Abstract

We present a study of DENIS, 2MASS, ISOGAL and MSX photometry for a sample of evolved late–type stars in the inner Galaxy, which we previously searched for 86 GHz SiO maser emission (Messineo et al. 2002). Bolometric magnitudes are computed for each SiO star by direct integration of the observed energy distribution, and bolometric corrections as a function of colours are derived. Adopting a distance of 8 kpc the SiO stars within 5° from the Galactic Centre show a distribution of bolometric magnitudes that peaks at $M_{\mathrm{bol}} = -5.1$ mag, i.e., very similar to the OH/IR stars close to the Galactic centre. From their bolometric luminosities and interstellar extinction we find that 11% of the SiO stars are likely to be foreground to the bulge. Furthermore the small velocity dispersions of those foreground stars suggest a disk component. The 15 known large amplitude variables included in our sample fall above the Mira period–luminosity relation of Glass et al. (1995), which suggests a steepening of the period–luminosity relation for periods larger than 450 days, as also seen in the Magellanic Clouds. From this period–luminosity relation and from their colours, the envelopes of SiO stars appear less evolved than those of OH/IR stars, which have thicker shells due to higher mass–loss rates.

5.1 Introduction

The early 1960's observations of non-circular gas motions in the inner Galaxy produced evidence for the existence of a Galactic bar (de Vaucouleurs 1964). Its existence is also supported by an apparent asymmetry of the integrated light as seen in COBE maps (Blitz & Spergel 1991) and of the stellar counts (Nakada et al.

1991). Thus, stellar kinematic studies provided less stringent constraints, due to the small number of measured stellar radial velocities. OH and SiO maser emission lines from the envelopes of evolved late-type stars can measure stellar line-of-sight velocities with an accuracy of a few $km\,s^{-1}$ throughout the Galaxy. Maser emission thereby provides a ready means to measure line-of-sight velocities in the Galactic plane even where the optical interstellar extinction is high.

Lewis (1989) analysed the colours and maser emission of IRAS sources, suggesting a chronological sequence of increasing mass-loss from SiO, to H_2O and OH maser emission. This sequence links AGB stars through the Mira and OH/IR stages with Planetary Nebulae. The presence of particular maser lines apparently depends on the envelope's mid-infrared opacity: a higher mass-loss rate makes a more opaque dust shell, which better shields molecules against photodissociation. However, parameters other than mass-loss, such as initial stellar masses and chemical abundances, probably also play an important role (Habing 1996).

A number of maser surveys have been carried out to measure stellar line-of-sight velocities toward the inner Galaxy, between $30°$ and $-30°$ in longitude, (e.g. Baud et al. 1979; Blommaert et al. 1994; Lindqvist et al. 1992; Deguchi et al. 2000a,b; Sevenster et al. 1997a,b, 2001; Sjouwerman et al. 1998; Izumiura et al. 1999). These surveys mostly detected visually obscured OH/IR stars, i.e., AGB stars with 1612 MHz OH maser emission and high mass-loss rates.

Our survey of 86 GHz SiO maser emission towards infrared-selected Mira-like stars in the inner Galaxy, mostly at $b < 0.5°$, (Messineo et al. 2002, hereafter Chapter II) led to the determination of 255 new line-of-sight velocities. The sample of targets (hereafter "SiO targets") was selected to be complementary to previous OH/IR surveys, so the sources with the reddest mid- and near-infrared colours were excluded.

In studying Galactic structure and kinematics it is important to combine the kinematic information and the stellar properties, such as luminosities, to explore any differences in the velocity fields of different tracers. In particular, it must be clarified whether OH/IR and SiO masing stars trace the same dynamic population, so that they can simply be combined to study the kinematics of the inner Galaxy.

The infrared photometry of our 441 SiO targets, derived from the large surveys DENIS (Epchtein et al. 1994), 2MASS (Cutri et al. 2003), ISOGAL (Omont et al. 2003; Schuller et al. 2003) and MSX (Egan et al. 1999; Price et al. 2001), was given by Messineo et al. (2004b, hereafter Chapter III). Corrections for interstellar extinction were discussed by Messineo et al. (2004a, hereafter Chapter IV). The present paper derives the bolometric magnitude of each target star, which we then compare with those of a sample of OH/IR stars.

Since most of the SiO targets are variable stars (Chapter III), their characterisation would require long-term, multi-frequency flux monitoring programs, which are not available yet. A first, although necessarily approximate discussion of their luminosities is possible even with single epoch observations, making use of the most recent infrared surveys.

The individual source numbers (e.g #99) are taken from Table 2 (86 GHz SiO

maser detections) and Table 3 (non-detections) of Chapter II.

5.2 Apparent bolometric magnitudes

The photometric measurements of each SiO target (Chapter IV) were corrected for interstellar extinction using the mean K_S–band extinction found from the surrounding field stars. For the wavelength-dependence of the extinction, we assume a power law $A_\lambda/A_K = (\lambda/2.12\mu m)^{-1.9}$, so that for the individual bands we find effective band extinctions $(A_I, A_J, A_H) = (6.78, 2.86, 1.66) A_{K_S}$. For the mid-infrared range we use the extinction law of Lutz (the extinction ratios are given in Table 2 of Chapter IV).

The bolometric stellar magnitudes, m_{bol}, were computed by integrating over frequency ν using linear interpolations between the dereddened flux densities, $F_\nu(\nu)$. At the low frequency end we extrapolated to $F_{\nu=0} = 0$, and at the upper end we extrapolated the two highest frequency data–points, provided the flux decreases, to zero intensity. Loup et al. (2004) presented a comparison of different methods commonly used to compute bolometric magnitudes. Using model spectra of O-rich AGB stars (from Groenewegen & de Jong 1993), they showed that the integration method we adopt yields bolometric magnitudes which should on average be accurate within 0.3 mag. Since the DENIS I, J,K_S as well as the 2MASS J, H,K_S observations were each taken simultaneously, but both sets at different times, we computed the bolometric magnitudes separately using either the DENIS or 2MASS data. The SiO targets are mostly variable stars (Chapter III), so a comparison of both datasets yields some information on their average variability.

For all but two of the SiO target stars the low-frequency extrapolation is insignificant since it contains a negligible fraction of the total flux. Only for sources #76 and #347 the low-frequency extrapolation contributes more than 20% to the total integrated flux.

Given that usually $(K_S-[15])_0 < 5$ mag, the main uncertainty in computing the bolometric magnitudes of the SiO target stars arises from the extrapolation at high frequencies. For 20 SiO targets a linear extrapolation was not possible because the flux density rises at high frequencies. For another 100 targets the blue extrapolation using 2MASS data or DENIS data contributes more than 20% to the bolometric flux.

For about half of our SiO stars (233 stars) we could compute bolometric magnitudes through a direct integration using either the DENIS or 2MASS data, with the flux in the extrapolated regions contributing less than 20% to the total. Unless otherwise stated, we adopt the average of these two integrations to attenuate the effect of variability.

For the other half of our sample, a bolometric magnitude could be integrated from only one dataset, since either the other data set is incomplete or the blue extrapolation is too uncertain in that the extrapolated spectral region contributes more than 20% to the total flux. For this half of the sample, when both the DENIS and 2MASS K_S measurements were available, we estimate bolometric magni-
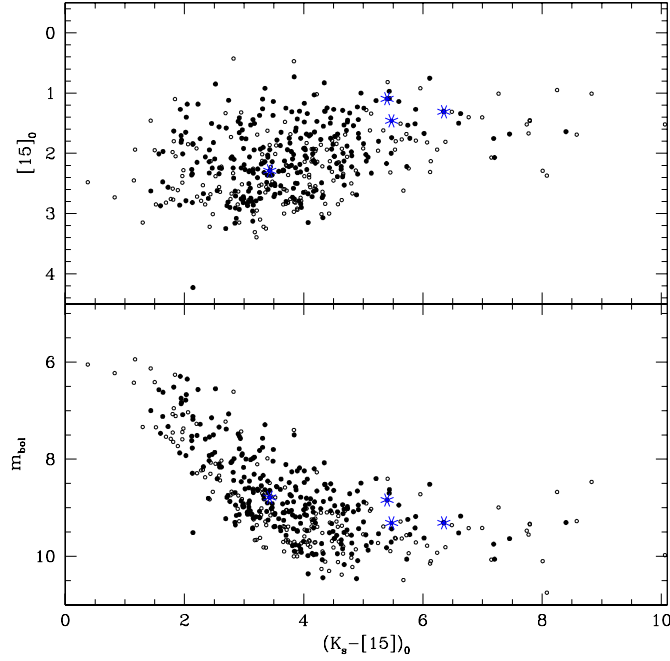
Figure 5.1: Lower panel: *Apparent bolometric magnitudes, m_{bol}, versus $(K_S−[15])_0$. Filled circles indicate objects with detected SiO maser emission, and open circles objects with no SiO detection. The four starred symbols show stars with observed OH emission (Chapter III). When both DENIS and 2MASS K_S measurements are available, or when both ISOGAL and MSX 15μm measurement are available, the average flux density is adopted.* **Upper panel:** *Apparent $[15]_0$ magnitudes versus the $(K_S−[15])_0$ colour. Symbols are as in the lower panel.*

tudes using the bolometric corrections described in Appendix A and the average of the two K_S–band flux densities. The average flux densities at 15 μm, when both ISOGAL and MSX 15μm measurement were available, was used.

The apparent bolometric magnitudes are plotted against the $(K_S−[15])_0$ colour in Fig. 5.1. There is an misleading correlation because the range in $[15]_0$ is small compared with the range in K_{s0}, and m_{bol} is dominated by the near-infrared flux.

There is a tail of stars at faint apparent bolometric magnitudes with a wider colour spread and redder $(K_S−[15])_0$ colours (Fig. 5.1) (which is the consequence of selection of MSX sources, Chapter III). These redder colours are indicative of higher mass-loss rates.

5.2.1 Variability

Bolometric magnitudes of known Mira variables are found to vary up to 2 mag from minimum to maximum light (e.g. Whitelock et al. 1991, 2000).

Since we are using single epoch observations taken at random phase, the obtained bolometric magnitudes are also at a random phase.

Figure 5.2 shows that there is an rms scatter of ~ 0.35 mag between $m_{\rm bol}^{2MASS}$ and $m_{\rm bol}^{DENIS}$, which is mainly due to variability (Chapter III). There is a tight correlation between $m_{\rm bol}$ and $K_{\rm S}$ since both quantities are related by the bolometric correction $BC_{K_{\rm s}}$ (Appendix A). If we assume that all stars are sinusoidally variable with maximum-to-minimum amplitudes A_i, and that 2MASS and DENIS measurements are unrelated in time, then the rms of the amplitude distribution is equal to the rms of the differences between two measurements at random phase, i.e. 0.35 mag.

The observed scatter is only a lower limit to the stellar flux variability, because it only accounts for the near-infrared variation. However, since the dominant part of the stellar energy distribution of a Mira star is at near-infrared frequencies and since its pulsation amplitude decreases at lower frequencies, this variation is nearly that of the bolometric flux.
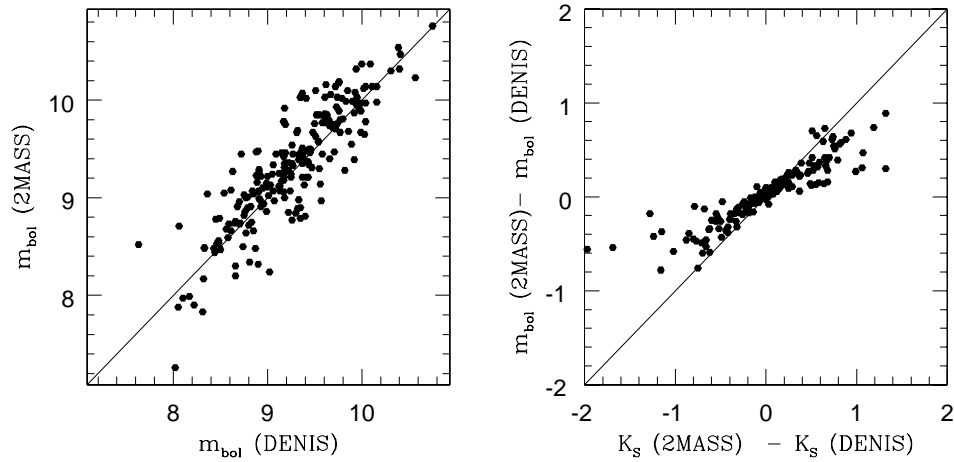
Figure 5.2: Left panel: *Apparent bolometric magnitudes derived using 2MASS data versus apparent bolometric magnitudes using DENIS data.* **Right panel:** *Differences in $m_{\rm bol}$ versus the corresponding differences between DENIS-$K_{\rm S}$ and 2MASS-$K_{\rm S}$.*
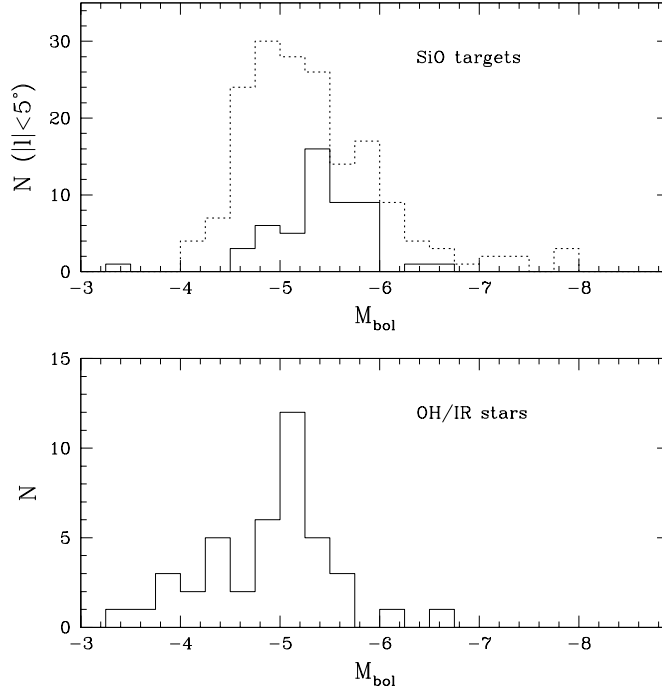
Figure 5.3: *Distribution of absolute bolometric magnitudes for an adopted distance of 8 kpc. SiO targets identified as possible foreground objects on the basis of their extinction (Chapter IV) are omitted from the plot.* **Upper panel:** *The dotted line shows the distribution of all SiO targets with $|l| < 5°$. The continuous line shows the distribution of SiO stars with $(A_{K_S} > 2.0$ mag); most of them belong to the Nuclear Disk (see Sect. 5.6).* **Lower panel:** *For comparison the distribution of absolute magnitudes of a sample of OH/IR stars within $1°$ from the Galactic centre (Ortiz et al. 2002) is shown.*

5.3 SiO targets with $|l| < 5°$

5.3.1 Luminosities

We derive the "absolute" bolometric magnitudes, M_{bol}, of 252 sources within the central $5°$ of the Galactic Centre adopting a distance of 8 kpc. Their "absolute" bolometric magnitudes, as shown in Fig. 5.3, ranges from -4 to -8 mag, with a peak around -5.0 mag. Our SiO targets appear to have mostly luminosities above that of the tip of the red giant branch at $M_{bol} \sim -3.6$ (Ferraro et al. 2000), where the helium flash stops the ascent of the star on the red giant branch. This is typical for long period variable (LPV) stars in old metal-rich globular clusters.

Only two SiO targets (#77 and #347) have M_{bol} fainter than -4.0 mag; those stars could be in the early AGB phase or at a larger distance, or could have lower initial masses than the bulk of the SiO targets.

Another 33 (11%) of all SiO targets within 5 degrees from the Galactic Centre have $M_{\rm bol} < -6.5$ mag, and even brighter than -7.2 mag, which is the classical AGB limit (Iben & Renzini 1983). The maximum average luminosity observed for Galactic Mira stars corresponds to $M_{\rm bol} = -5.5$ mag (Glass et al. 1995; Olivier et al. 2001; Whitelock et al. 1991). Since the $K_{\rm S}$–band luminosity of a Mira star varies by up to about 2 magnitudes, for a single epoch measurement at random phase, we expect a distribution extending to $M_{\rm bol} = -6.5$ mag. The 33 targets brighter than this limit, could be either foreground stars, massive, young AGB stars, or evolved massive stars (red supergiants) (Nagata et al. 1993; Schuller 2002).

Near-infrared spectroscopy could reveal their true nature (e.g. Schultheis et al. 2003). By combining extinction information and luminosity Messineo et al. found that 20 of the 33 bright sources are likely to be foreground stars (Chapter IV). Their total extinction (interstellar plus circumstellar), which was calculated by assuming a photospheric colour for the central star, appears to be lower than the average interstellar extinction of stars in their respective surrounding fields.

We find five sources (#31, #75, #92, #128, #294) with $M_{\rm bol} < -7.2$ mag that cannot be explained as foreground on the basis of their extinction. One of them (#92) is classified as a possible red supergiant stars by Nagata et al. (1993). The bolometric magnitude given by Nagata et al. is in good agreement with our measurement. It is not unlikely that some of our other bright sources are also red supergiants.

5.3.2 Initial masses and ages

Estimates of the initial mass of pulsating AGB stars is problematic due to uncertainties in the pulsation mode, effective temperature (i.e., stellar radii), and of the mass-loss history (e.g. Marigo et al. 1996; Vassiliadis & Wood 1993). A degeneracy between age and metallicity further complicates the analysis of the distribution of stellar colours and luminosities (e.g. Frogel & Whitford 1987; van Loon et al. 2003; Whitelock et al. 1991).

The maximum luminosity reached at the end of the AGB phase strongly depends on the metallicity and initial mass of the star: a lower metallicity leads to a higher luminosity for a given initial mass.

Assuming solar metallicity and using the relation from Marigo et al. (1996) between the initial mass and maximum luminosity reached before the onset of the superwind (Renzini & Voli 1981; Vassiliadis & Wood 1993), we derive a distribution of initial masses for our SiO targets that ranges from 1.0 to 4.0 $M_\odot$. This range is perhaps wider than the real due to the variability and our use of single epoch observations. For a solar metallicity, the majority of the SiO targets ($M_{\rm bol} = -4.5$ to -5.5) has ages ranging from 0.8 to 5 Gyr (Girardi et al. 2000). However, these are lower limits since stars with higher than the assumed solar metallicity would stay longer on the main sequence and would therefore be older when they reach the AGB.

A reliable empirical calibration of mass and age is possible only for Mira stars in globular clusters. Bulge Mira stars are more massive and/or metal rich than

Mira stars in Galactic globular clusters (e.g. Whitelock et al. 1991), as follows from their longer pulsation period (up to 800 days vs. 200-300 days in globular clusters) and higher luminosity. The most luminous AGB star in globular clusters has $M_{\rm bol} = -4.8$ mag (Guarnieri et al. 1997), while in the bulge they can reach -5.5 mag (Glass et al. 1995; Whitelock et al. 1991).

The presence of an intermediate age population ($2.2 M_\odot <$ initial mass $< 8.0 M_\odot$) in the inner Galaxy was suggested by, e.g., Cole & Weinberg (2002); van Loon et al. (2003). However, most of these studies are based on photometric observations of only giant stars. Because of differential reddening and the degeneracy between metallicity and age those studies could not securely confirm the presence of such a young population.

To infer the age of a stellar population it is crucial to detect the main-sequence turn-off. Using deep near-infrared photometry Zoccali et al. (2003) studied the stellar population of a bulge field at latitude $b = 6°$, from main–sequence stars to the AGB tip. They estimated an age of 10 Gyr for the field population and did not observe any other turn–off that could suggest the existence of an intermediate age population. Their number of luminous AGB stars agrees with that predicted for a population of that age. However, Zoccali's field is at $b = 6$ ° and it may not be representative of the in–plane population of the inner Galaxy.

Feltzing & Gilmore (2000) studied stars in the Baade's window field using visual HST data and also concluded that bulge stars are generally old, although the existence of a young and metal–rich population cannot be ruled out.

Evidence for a younger component comes from the distribution of OH/IR stars, in the central bulge that have a vertical scale height < 100 pc (Sevenster 1999b). They could belong to a distinct in–plane component. Furthermore, low latitude OH/IR stars stars and SiO targets do not trace the axisymmetric and old (8-10 Gyr) bulge population studied by Ng & Bertelli (1996), but the longitude–velocity diagram of maser stars shows evidence for a Galactic bar (Messineo et al. 2002; Sevenster 1999b). The masing population could be related to a more recent star formation event, e.g., triggered by the formation of the Galactic bar (e.g. Cole & Weinberg 2002; Sevenster 1999b; Sjouwerman et al. 1999).

New near–infrared photometric observations down to the main-sequence turn–off for inner Galactic fields at low latitude are important for improving our understanding of Galactic stellar population history, and can verify the possible existence of an intermediate age population.

Near–infrared spectroscopy would yield estimates of the metallicity of masing stars. The SiO targets, being bright at near–infrared wavelengths, are ideal targets for such a spectroscopic program.

5.3.3 Red Supergiant stars ?

Red supergiant stars are massive stars (> 9 M$_\odot$), which are burning helium (or carbon) in non-degenerate cores. They are often located in OB associations. The luminosity distribution of the SiO targets within $5°$ from the Galactic Centre,

shown in Fig. 5.3, suggests that a few red supergiant stars are also included, as supported by other indications described below.

IRAS counterparts of our SiO targets are mostly located in region IIIa of the IRAS two–colour diagram (Chapter III). Previous studies of IRAS sources have shown that most of the sources in region IIIa are O–rich AGB stars, but 26% may be red supergiant stars (Josselin et al. 1996; Winfrey et al. 1994).

Weak SiO maser emission is found in semiregular AGB and red supergiant stars (Alcolea et al. 1990), but red supergiants with large amplitudes are strong SiO emitters and their SiO maser intensity is comparable to that of Mira stars (Alcolea et al. 1990). The central star has an extended shell, generated by the strong pulsations as in LPVs, where the SiO maser activity takes place.

The line profile of the SiO masers normally has several components a few $km\,s^{-1}$ wide over a range from $10\,km\,s^{-1}$ (giant) to $20\text{-}40\,km\,s^{-1}$ (supergiant) (Alcolea et al. 1999; Le Bertre & Nyman 1990). Our entire sample has an average SiO maser line width of $4.6\,km\,s^{-1}$ with a scatter of $2.3\,km\,s^{-1}$. There are 12 sources with line width $> 9\,km\,s^{-1}$: #31, #71, #87, #113, #117, #129, #135, #173, #190, #203, #223, #232. These spectra look similar to the broad and multiple peaked spectra typical of red supergiants (Cho et al. 1998; Haikala 1990). Seven of those 12 are located within $5°$ of the Galactic centre, and 4 (#31, #87, #113, #129) are also very luminous ($M_{bol} < -6.5$ mag). The velocity–longitude distribution of bright ($M_{bol} < -6.5$ mag) stars detected in our SiO maser survey appears distinct from that of the nuclear disk component or from bulge stars. The linear dependence of v and l suggests (see Sect. 5.7) that it is probably a Galactic disk component.

5.4 Comparison with OH/IR stars

For a comparison with our SiO targets, we also consider a sample of OH/IR stars (AGB stars with 1612 MHz OH maser emission) within $1°$ from the Galactic Centre (from Table 3 of Ortiz et al. 2002), a region fully mapped at 1612 MHz (Lindqvist et al. 1992; Sevenster et al. 1997a; Sjouwerman et al. 1998). Ortiz et al. found ISOGAL counterparts for all OH sources in ISOGAL fields, counterparts which are typically bright at 15 μm and have very red $(K_S-[15])_0$ colours (reaching 12 mag; see upper panel of Fig. 5.4), which is indicative of high mass loss rates.

To directly compare luminosities of OH/IR stars with those of SiO targets, bolometric magnitudes must be calculated in the same way. We therefore calculated the interstellar extinction A_{K_S} toward each OH/IR star using 2MASS stars within $2'$ from the position of the OH/IR star, following the procedure described in Chapter IV. Extinctions, A_{K_S}, are found systematically larger (by up to 0.6 mag) than those adopted by Ortiz et al. (2002). This is due to our use of the (H, K_S) data, which are less sensitive to extinction and therefore less affected by a low–extinction bias than (J, H) or (J, K_S) data used by Ortiz et al. (2002). We adopted the near–infrared mean flux densities of the OH/IR stars given by Wood et al. (1998). When using Mathis' extinction law (for comparison with Ortiz et al. 2002)
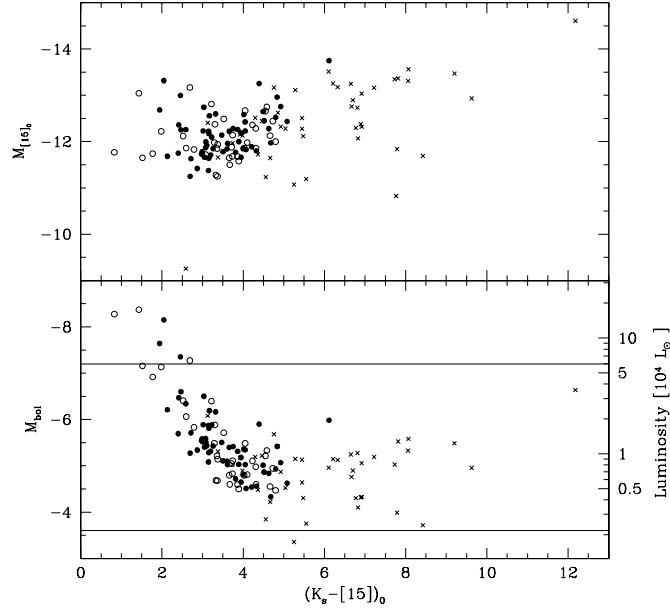
Figure 5.4: Lower panel: *"Absolute" bolometric magnitudes, M_{bol}, versus dereddened $(K_S-[15])_0$, adopting a distance of 8 kpc. When both DENIS and 2MASS K_S measurements, or both ISOGAL and MSX 15μm measurements are available, the average flux density is adopted. Circles show SiO targets from the ISOGAL fields of Ortiz et al. (2002), they cover about $\sim 0.84°$. Filled and open symbols indicate SiO maser detections and non–detections, respectively. For comparison, crosses show OH/IR stars within 1° from the Galactic Centre with a known period and ISOGAL counterpart (Ortiz et al. 2002). The line at $M_{bol} = -3.6$ indicates the location of the tip of the red giant branch and the line at $M_{bol} = -7.2$ the AGB limit.* **Upper panel:** *"Absolute" $[15]_0$ magnitudes, $M_{[15]}$, versus dereddened $(K_S-[15])_0$. Symbols are as in the lower panel.*

we obtained bolometric magnitudes consistent with those of Ortiz et al. (2002): since the spectral energy distribution of an OH/IR star peaks long-ward of 3μm (due to the presence of a thick circumstellar envelope), its bolometric magnitude is less sensitive to near–infrared interstellar extinction corrections than for SiO targets. However, when we adopt the mid–infrared extinction law suggested by Lutz et al. (as for the SiO targets, Chapter IV) we obtain bolometric magnitudes for the OH/IR stars brighter by up to 0.6 mag. Whenever a bolometric magnitude determination via direct integration (Sect. 5.2) was not possible, it was estimated using the bolometric correction described in the Appendix.

Figure 5.3 shows a comparison between the bolometric magnitude of our SiO targets (Sect. 5.2) with that of the OH/IR stars.

The peak of the OH/IR magnitude distribution is at ~ -5.1 mag, and translates

to an initial stellar mass of about 1.8 $M_\odot$ and an age of about 2 Gyr, using the models of Girardi et al. (2000) with solar metallicity. The peak for OH/IR stars appears consistent with the median of the bolometric magnitudes of SiO targets in the central $5°$, although the distribution of the latter is broadened by variability and the use of single epoch observations.

For the 96 SiO targets (58 detections) from the same ISOGAL fields as the OH/IR stars of Ortiz et al. (2002), Fig. 5.4 shows the absolute bolometric magnitude of both OH/IR and SiO stars plotted against their $(K_S-[15])_0$ colour. Distributions appear to differ in that SiO targets have bluer colours (due to our selection, Chapter III). This indicates that OH/IR stars have thicker envelopes due to higher mass–loss rates.

Note that here we are comparing only our SiO targets with known OH/IR stars. We imposed colour constraints for our target selection and we tried to be complementary to previous OH/IR studies by discarding the reddest mid- and near–infrared colour sources. It is quite well possible that there are SiO masing stars with colours much redder than what we considered, though according to Nyman et al. (1993) there should be a cut–off in the 86 GHz SiO maser intensity for very optically thick circumstellar envelopes.

In contrast to SiO targets, there are no OH/IR stars brighter than $M_{\rm bol} = -6.5$ (for a distance of 8 kpc) in our sample. The luminous SiO targets tend to be bluer than fainter ones, suggesting a thinner circumstellar envelope, which could also explain the lack of 1612 MHz OH maser line emission. Therefore, our sample includes luminous SiO masing AGB stars or red supergiants, with moderate mass–loss rates, not masing in OH. If the mass–loss rate increases with time (e.g. Lewis 1989) these objects could later also show 1612 MHz OH maser emission, which is more likely for thicker envelopes (Sevenster et al. 2001; Habing 1996).

In the chronological sequence of circumstellar masers presented by Lewis (1989), as first suggested by Bedijn (1987), circumstellar envelopes of AGB stars gradually evolve under slowly increasing rates of mass loss. Since the SiO masing shell is near the photosphere, the first maser emission to appear is that from SiO, while OH maser emission appears as the shell grows. The SiO maser emission is then the first to disappear when the mass loss declines.

The distributions of bolometric magnitudes of both SiO and OH/IR stars, as seen in Fig. 5.3, peak at about the same value, which suggests that both populations trace the same epoch of star formation, but SiO masing stars have less evolved circumstellar envelopes (see also Chapter III). This is supported also by the different distribution of SiO and OH/IR stars in the period–luminosity diagram (Sect. 5.5).

5.5 Period–Luminosity relation

Our SiO targets include 15 LPVs from the sample of Glass et al. (2001), Chapter II. Figure 5.5 plots their bolometric magnitudes against their periods, showing that they fall above the period–luminosity distribution of Mira stars in the Sgr–I field
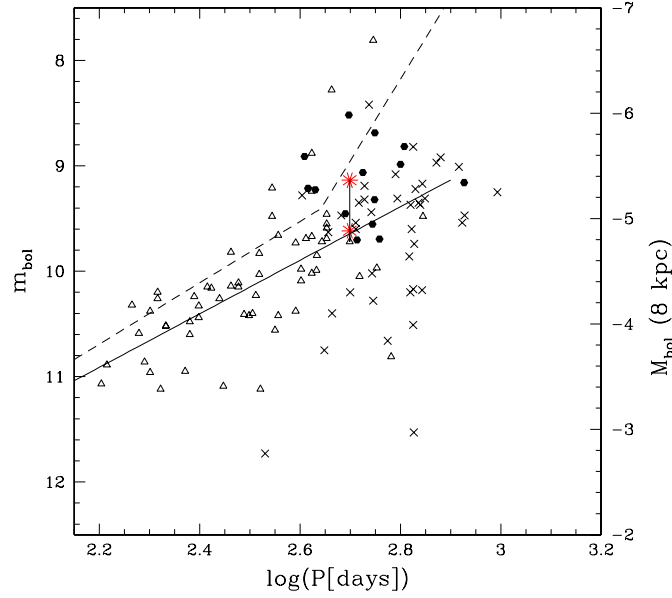
Figure 5.5: *The period–luminosity relation of LPV stars. Dots represent 15 LPV stars in our SiO maser sample located within 24′ from the Galactic Centre (Glass et al. 2001). They have a bright ISOGAL counterpart, but no known OH maser emission. Triangles show Mira stars located in the Sgr–I field (Glass et al. 1995), for which we plot the mean bolometric magnitudes. For #153, the only SiO target located in the Sgr–I field, we plot both magnitudes (stars) obtained using DENIS and 2MASS data, and connect them to the mean $m_{\rm bol}$ value found by Glass et al. (1995) with a vertical line. Crosses show OH/IR stars with ISOGAL counterpart (Ortiz et al. 2002). The continuous line represents the relationship found by Glass et al. (1995), while the dashed line is a fit for LMC Mira stars (Hughes & Wood 1990), assuming a distance modulus of 18.55 mag for the LMC and 14.5 mag for the Galactic Centre.*

(Glass et al. 1995). However, in the Sgr–I field Mira stars with period longer than 450 days are rare. Our SiO stars may support a steepening of the period–luminosity relation for period longer than 450 days, as observed in the Magellanic Clouds (Hughes & Wood 1990).

The standard deviation in the period–luminosity relation of Mira stars in Sgr–I is 0.36 mag (Glass et al. 1995), which partly arises from the spread in distance, and partly from the uncertainty in the apparent bolometric magnitude. A spread of ± 2 kpc in distance at a distance of 8 kpc causes a spread in $M_{\rm bol}$ of ± 0.55 mag. Bolometric magnitudes given by Glass et al. (1995) were obtained adopting the mean values of monitored infrared flux densities. The period–luminosity relation obtained using mean magnitudes of Mira stars in the Magellanic Clouds is less sensitive to distance uncertainties, resulting in a scatter of only 0.15 mag (Feast

et al. 1989).

Our sample has one SiO star located in the Sgr–I field, #153. Its $m_{\rm bol}$ calculated using DENIS data is 9.62 mag, identical to the mean value obtained by Glass et al. (2001). When using 2MASS data we find $m_{\rm bol} = 9.14$ mag. Considering the pulsation amplitude $\Delta K = 1.38$ mag (Glass et al. 1995), both measurements are consistent.

The 15 LPV/SiO targets in the Galactic Centre from Glass et al. (2001) suffer from strong extinction ($A_{\rm K_S}> 2$ mag) and using the kinematic information for the 11 which were detected in our SiO maser survey, we conclude that they are members of the central nuclear disk (see Sect. 5.6). They are therefore at about the distance of the Galactic centre. Assuming an isotropic distribution of stars in the nuclear disk, a range of longitudes of $\pm1.5°$ translates to a distance range of ±200 pc, and a corresponding distance modulus range of ±0.05 mag. Their dispersion on the period–luminosity plane is mostly due to the uncertainty in the bolometric magnitude ($\sim$0.35 mag, see Sect. 5.2) and in the extinction (Chapter IV).

Since we selected bright ISOGAL and MSX sources (Chapter II) and since mid–infrared flux density correlates with period (see the 12μm period–luminosity relation in Whitelock et al. 1991), it is not surprising that the LPVs we observed have periods above 400 days (Fig. 5.5). Imai et al. (2002) searched for SiO maser emission toward the entire sample of Mira stars near the Galactic centre detected in K–band by Glass et al. (2001) and confirmed the expected increase of the detection rate with increasing period. While for periods below 300 days the SiO maser detection rate is below 20%, above 400 days it rises to 60% . OH/IR stars also have typical periods above 400 days (Fig. 5.5). Thereby, SiO and OH maser emission mainly trace long period AGB variables.

Unlike Mira stars, OH/IR stars do not follow a period–luminosity relation in the Galactic Centre region (Ortiz et al. 2002, and references therein). Most of them for a given magnitude have a longer period than that predicted by the Mira period–luminosity relation, so OH/IR stars and SiO targets are differently distributed.

Pulsation models predict that due to a dramatic increase of the mass loss rate (superwind phase), a Mira star significantly stretches its pulsation period, while its luminosity remains almost constant (Vassiliadis & Wood 1993), and becomes an OH/IR star. OH/IR stars have then longer periods for a given luminosity than those found in Mira stars.

5.6 Stars in the the Nuclear Disk and a fourth dimension: extinction

The line of sight extinction is a useful fourth dimension along with position (l, b) and velocity to characterise various Galactic components.

Around zero longitude our stellar longitude–velocity $(l - v)$ diagram reveals a stellar nuclear disk, which follows the high velocity gaseous **nuclear disk** (e.g. Binney et al. 1991; Burton & Liszt 1978).
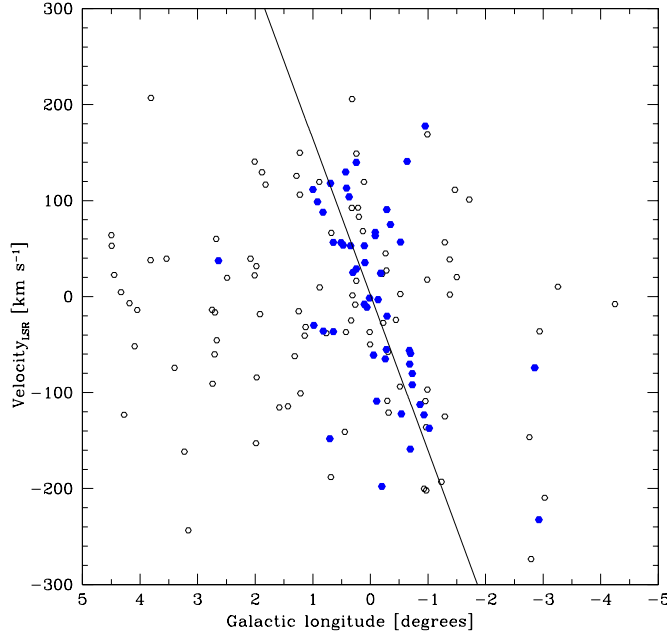
Figure 5.6: *Stellar longitude–velocity diagram of our 86 GHz SiO masers. Filled circles indicate sources with interstellar extinction A_{K_S} above 2 mag. Most of these belong to the fast rotating nuclear disk. The continuous line indicates our best fit to the nuclear disk component.*

There is a unique correspondence between interstellar extinction and velocity. When we select SiO targets at interstellar extinction $A_{K_S} > 2$ mag (Fig. 5.6), we find that most of these stars kinematically trace the nuclear disk. Their line–of–sight velocities range from $\sim +150$ to ~ -200 km s^{-1}, similar to the gaseous nuclear disk line–of–sight velocities (cf. the ^{13}CO $(l - v)$ diagram in Fig. 4 of Bally et al. 1988). Therefore, the extinction enables us to identify individual stars belonging to the nuclear disk.

The stellar nuclear disk rotates rapidly around the Galactic Centre: our best–fit yields a gradient of $162(\pm 40)$ km s^{-1} per degree longitude. This slope is consistent with a value of $180(\pm 15)$ km s^{-1} found for OH/IR stars with high circumstellar expansion velocity located within $1°$ of the the Galactic Centre (Lindqvist et al. 1992).

To investigate whether the 56 SiO targets with $A_{K_S} > 2$ mag also show distinct physical properties, their bolometric magnitude distribution is shown in Fig. 5.3. The distribution peaks at -5.4 mag, a peak slightly more luminous than the average luminosity of SiO targets within $5°$. However, their luminosity is consistent with those of variable AGB stars. There is only one SiO target with $M_{\mathrm{bol}} < -6.5$ mag, #99, which may be a young star. Its location ($l = 0.8°$; $v = -36.0$ km s^{-1}; 2σ

away from our best fit) indicates that it is probably unrelated to the nuclear disk in origin and kinematics.

The 11 LPVs from Glass et al. (2001) that we detected at 86 GHz (see also Sect. 5.5) all belong to the nuclear disk population, as their positions ($|l| < 1.5, |b| < 0.5$), their interstellar extinctions ($A_{\mathrm{K_S}} > 2.0$ mag) and their line–of–sight velocities confirm.

5.7 Bolometric magnitudes and the $l - v$ diagram

Different Galactic components give a different signature in the $(l - v)$ diagram. However, a stellar $(l - v)$ diagram alone is not sufficient to locate individual stellar components, mainly due to the velocity dispersion of the stars, that smooths various features. The inclusion of additional distance information will notably improve the understanding of the $(l - v)$ diagram. The stellar bolometric magnitude may serve as a first approximation of distance.

In section 5.3, we have already noticed the presence of a group of stars brighter than the typical luminosity of a Mira star at its maximum ($M_{\mathrm{bol}} = -6.5$ mag) when we assume a distance of 8 kpc. In Figure 5.7 we illustrate the $l - v$ diagram of SiO targets with M_{bol} fainter and brighter than -6.5 mag. The bright sample appears to be distributed differently from the faint sample, since it has a low velocity dispersion (~ 30 km s^{-1}), independently of longitude. The stars that were classified as foreground stars on the basis of extinction consideration (crosses in Fig. 5.7; see also Chapter IV), almost all belong to the bright group. This indicates that the bright stars are closer on average to the Sun than fainter ones and that their luminosities are overestimated by assuming the distance of the Galactic centre. But then how nearby are those stars? Do they trace a specific Galactic component?

An estimate of their distance can be inferred by assuming circular orbits. However, this assumption clearly does not hold for the central kiloparsecs, due to both the presence of a bar and the fact that bulge stars might have a velocity dispersion larger than the rotation velocity. Hence, we calculated Galactocentric distances, under the assumption of circular orbits, for SiO targets at longitudes $> 10°$. We adopted the relation between the longitude, radial velocity and distance (Burton 1988):

$$v = R_\odot [\frac{V(R)}{R} - \frac{V(R_\odot)}{R_\odot}]\sin(l), \qquad (5.1)$$

where $V(R)$ is the circular rotation velocity at Galactocentric distance R, the Galactocentric distance of the Sun is taken to be $R_\odot = 8.0$ kpc, and the circular velocity of the Sun $V(R_\odot) = 200$ km s^{-1}. Adopting $V(R) = V(R_\odot)(R/R_\odot)^{0.1}$ km s^{-1} (Binney et al. 1991), and inverting equation (1), it follows that:

$$R = \frac{8.0}{(1 + \frac{v}{(200 \times \sin(l))})^{1.11}} \text{(in kpc)}, \qquad (5.2)$$
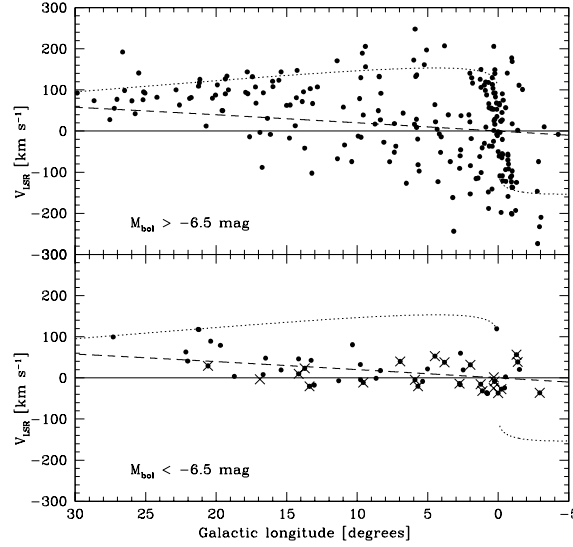
Figure 5.7: *Longitude–velocity diagram of SiO targets.* **Upper panel:** *SiO targets with $M_{\rm bol} > -6.5$ mag (assuming a distance modulus for the Galactic centre of 14.5 mag). The dotted line shows the curve defined by the line-of-sight velocities of tangent points to circular orbits, as predicted by Eq. 5.1. The dashed line indicates a circular orbit at a galactocentric distance of 5 kpc.* **Bottom panel:** *Dots indicate SiO targets with $M_{\rm bol} < -6.5$ mag. Crosses indicate SiO targets classified as foreground on the basis of extinction (Chapter IV).*

Bright sources are found to have an almost homogeneous distribution in Galactocentric distance, from 0 to 15 kpc. Fainter stars (Fig. 5.8) peak at about 3 kpc from the Galactic centre, i.e. at about the corotation radius of ~ 3.4 kpc (e.g. Englmaier & Gerhard 1999).

Since interstellar extinction increases with distance, another independent way to estimate distances is to use a model of dust distribution in the inner Galaxy. Using the implementation of Drimmel et al. (2003) based on COBE/DIRBE data, we calculated for each line of sight toward a SiO target the interstellar extinction as a function of distance. By interpolating the models at the values of derived interstellar extinction (Chapter IV), we have estimated distances to each SiO target.

The model of Drimmel et al. does not include the nuclear disk molecular complex and therefore it fails in reproducing the distance of nuclear disk stars. It predicts that all SiO targets are within a Galactocentric distance of 5 kpc and confirms a peak around corotation.

We used two independent methods to estimate distances, one based on kinematics and another based on extinction. Although the uncertainty are large (see right panel of Fig. 5.8), from both methods we find that most of SiO targets have a Galactocentric distance within 5 kpc, with a peak around corotation. The bright
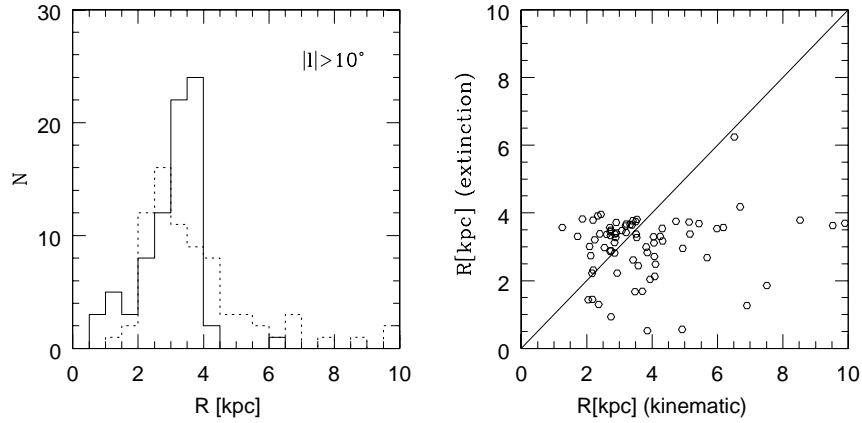
Figure 5.8: Left side:*The continuous histogram shows the distribution of Galactocentric distances inferred for SiO targets at longitudes l > 10° using interstellar extinction estimates towards the line of sight of each SiO target and a model of Galactic dust distribution (Drimmel et al. 2003). The dotted histogram shows the distribution of Galactocentric distances inferred for SiO targets at longitudes l > 10° assuming circular orbits.* **Right side***: Distance estimates from interstellar extinction versus kinematic distances.*

stars, however, do not seem confined at a specific Galactocentric distance.

It is difficult to argue about the nature of each single SiO target. The difference in distance modulus of a star at the Galactic centre and at a Galactocentric distance of 5 kpc is 2.1 mag, thus we might have overestimated the luminosity of the SiO target stars. The true luminosity of the "bright" stars could be below the AGB limit ($M_{bol} < -7.2$ mag) and therefore they could be all AGB stars, rather than red supergiants. However, the luminosity range of these two classes of stars overlaps, and some of them could still be red supergiants as the SiO maser line widths and the low velocity dispersion suggest. Near–infrared spectroscopy is needed to distinguish between AGB and red supergiants. Furthermore, a near-infrared monitoring program would provide pulsation periods and therefore another independent estimate of the distance of each SiO target.

We are currently working on a kinematic study of the SiO targets based on a more realistic Galactic gravitational potential, which will be presented in a forthcoming paper.

5.8 Conclusion

Bolometric magnitudes for SiO target stars were computed from available flux density measurements. Adopting a distance of 8 kpc for all stars within 5° from the Galactic Centre we find a peak in the luminosity distribution at $M_{bol} = -5.1$ mag, which coincides with the peak shown by OH/IR stars in the Galactic Centre

(e.g. Ortiz et al. 2002). Assuming a solar metallicity this peak magnitude corresponds to stars with an initial mass of 1.8 M$_\odot$ and an age of about 2 Gyr.

Our sample includes 15 LPVs from the sample of Glass et al. (2001). We found that these fall above the period–luminosity relation found by Glass et al. (1995), thus differing from OH/IR stars. This supports a chronological sequence for circumstellar masers proposed by Lewis (1989). We also find evidence for a steepening of the bulge period–luminosity relation for periods larger than 450 days, as found for Magellanic Cloud LPVs.

In contrast to OH/IR stars (Ortiz et al. 2002), SiO targets contain a significant fraction (11%) of blue and luminous stars (M$_{\rm bol}$ < -6.5 mag). These stars are most likely massive AGB stars, or red supergiant stars, foreground with respect to the bulge. Their longitude–velocity distribution has a low velocity dispersion, which identifies a component, distinct from the bulge, perhaps related to the disk or to the molecular ring. A full dynamical analysis of SiO stars will be presented in a subsequent paper.

We found a unique relation between interstellar extinction and kinematic properties of SiO stars. Those with $A_{\rm K_S}$ > 2.0 mag belong to the stellar Nuclear Disk.

Appendix A: Bolometric corrections

The bolometric correction for a given photometric band is defined as $BC_\lambda = m_{\rm bol} - m_\lambda$. Bolometric corrections for late–type stars as a function of spectral type or colour are used to derive stellar luminosities. However, there are uncertainties in their estimates and applicability. Stars of different temperature, metallicity and mass–loss rate have a different energy distribution and therefore a different bolometric corrections. Variability is also a complication for a proper determination of the bolometric correction. Long period variables are characterised by extended atmospheres and their energy distribution differs from other static late–type giants because of water absorption seen from the J–band to the L–band (Frogel & Whitford 1987; Matsuura et al. 2002). The amount of absorption varies from star to star and with stellar phase. At the present time there are a number of already completed near–infrared monitoring programs of large amplitude AGB stars, in the solar neighbourhood, in the South Galactic Cap and in the Magellanic Clouds, which provide accurate average bolometric magnitudes of oxygen–rich large amplitude variables (Olivier et al. 2001; Whitelock et al. 2000, 1994, 2003). We use

these data to derive various bolometric corrections for these type of objects and compare these with results for stars in the inner Galaxy.
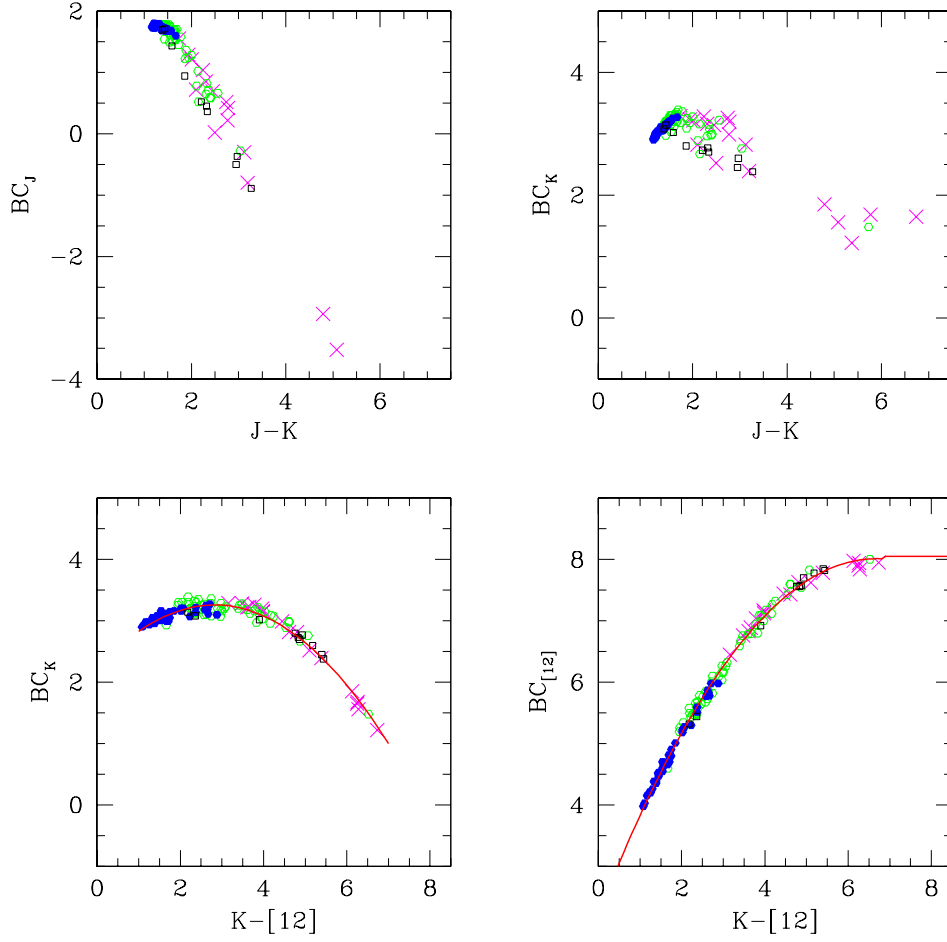
A.1 Bolometric corrections of monitored LPV stars

In order to have a large sample of LPV stars, well studied and covering a wide range of colours, we assembled photometric catalogues of LPV stars from Olivier et al. (2001) and Whitelock et al. (2000, 1994, 2003). All near–infrared magnitudes are in the SAAO system (Carter 1990). Stellar fluxes are corrected for reddening only in the work of Olivier et al. (2001). However, the effect of interstellar extinction is negligible because these stars are nearby or outside of the Galactic plane, and because the bulk of their energy is emitted at infrared wavelengths. Bolometric magnitudes are reported by the authors and, with the exception of the Hipparcos sample, were derived for each star by integrating under a spline curve fitted to the mean near–infrared ($JHKL$) flux densities and the IRAS 12 and 25 μm flux densities as a function of frequency, and using two extrapolations for longer and shorter wavelengths as described in Whitelock et al. (1994). For the sample of low mass–loss Mira stars observed by Hipparcos (Whitelock et al. 2000) bolometric magnitudes were calculated by fitting blackbody curves to the ($JHKL$) flux densities as a function of frequency. The blackbody fitting is a good approximation of these low mass–loss stars and for them blackbody and spline–fit bolometric magnitudes agree to better than 0.2 mag (Whitelock et al. 2003). Figure A.1 shows various bolometric corrections versus colours. The IRAS 12 μm magnitude, [12], is obtained adopting a zero point of 28.3 Jy (Beichman et al. 1988). BC_K is well correlated with $K - [12]$ rather than $J - K$. The least–squares polynomial fits to the bolometric correction BC_K and $BC_{[12]}$, which give a good match to the data ($\sigma = 0.08$ mag) over the range $1.0 < (K - [12]) < 7.0$, shown by the continuous lines in Fig. A.1, are given by:

$$BC_K = 2.219 + 0.7351(K - [12]) - 0.1299(K - [12])^2$$

$$BC_{[12]} = 2.219 + 1.735(K - [12]) - 0.1299(K - [12])^2.$$

These two curves are complementary to each other. Practically for $K - [12]$ smaller than 4 mag it is better to use BC_K due to the flatness of the curve. For $K - [12]$ redder than 4 mag BC_K decreases steeply with increasing colour, while $BC_{[12]}$ is more stable. The narrowness of (BC_K, $K - [12]$) and ($BC_{[12]}$, $K - [12]$) sequences also suggests that they do not depend on metallicity; in fact, the Magellanic Clouds objects also follow the same relation. Instead, the (BC_K, $J - K$) sequence depends on metallicity as found by Frogel & Whitford (e.g. 1987) comparing local stars and bulge stars.

Figure A.1: *Monitored LPV stars - Bolometric corrections as a function of various colours. Filled circles represent LPV stars in the solar vicinity detected by Hipparcos (Whitelock et al. 2000); open circles represent LPV stars in the Southern Galactic Cap (Whitelock et al. 1994); crosses indicate local high mass–loss LPV stars (Olivier et al. 2001); squares represent obscured LPV stars in the Large Magellanic Cloud (Whitelock et al. 2003). The IRAS 12μm magnitude is defined as* $[12] = -2.5 \log F_{12}[\mathrm{Jy}]/28.3$.
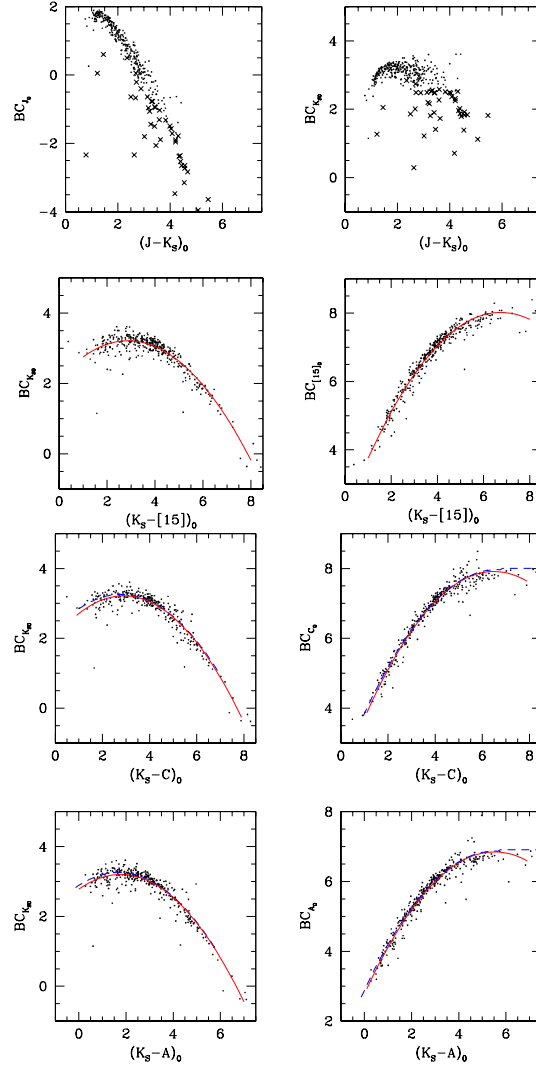
Figure A.2: *SiO targets - Bolometric corrections versus colours. Crosses are sources with $(K_{\rm S}-[15])_0$ redder than 5 mag. Only sources with bolometric magnitudes well determined are plotted, i.e. when the extrapolation to shorter wavelengths has a negligible contribute to the integrated bolometric magnitude ($< 20\%$). The 2MASS dataset is plotted. DENIS data are plotted only for sources with poor 2MASS photometry. When both ISOGAL and MSX 15μm measurement are available, then the average flux density is adopted. Continuous lines indicate our best fits. Dashed lines show the relation found for monitored LPV stars, adapted using the equation $A - [12] = 1.15, C - [12] = 0.05$ mag (Chapter IV).*

A.2 Bolometric corrections for stars in the inner Galaxy

For the SiO targets we derived bolometric magnitudes as described in Sect. 5.2. Bolometric corrections for the K_S and 15 μm band are computed from the m_{bol} and plotted against the dereddened $(K_S-[15])_0$ colour in Fig. A.2. Identical results are found using separately 2MASS m_{bol} and K_S or DENIS m_{bol} and K_S and/or ISOGAL [15] or MSX D (15μm) band magnitudes. The plotted continuous line is a least–squares polynomial fit, which gives a good match to the data ($\sigma = 0.25$ mag) over the range $1.0 < (K_S-D)_0 < 8.0$:

$$BC_{K_s} = 2.138 + 0.745(K_s - [15])_0 - 0.1294(K_s - [15])_0{}^2.$$

Analogously, using the MSX A (8μm) band, the following fit is obtained as a function of $(K_S-A)_0$ colour in the range $0.0 < (K_S-A)_0 > 7.0$ ($\sigma = 0.25$ mag):

$$BC_{K_s} = 2.780 + 0.475(K_s - A)_0 - 0.1337(K_s - A)_0{}^2.$$

Eventually, using the MSX C (12μm) band, the following fit is obtained as a function of $(K_S-C)_0$ colour in the range $1.0 < (K_S-C)_0 < 8.0$ ($\sigma = 0.25$ mag):

$$BC_{K_s} = 2.037 + 0.813(K_s - C)_0 - 0.1398(K_s - C)_0{}^2.$$

The fit to our SiO targets for $(K_S-C)_0 < 2$ mag gives a bolometric correction $BC_{K_{S_0}}$ smaller (up to 0.1 mag) than those derived for Hipparcos Mira stars, which have a similar $(K - [12])$ colour. However, within the uncertainty of the fits the two curves derived are consistent.

References

Alcolea, J., Bujarrabal, V., & Gomez-Gonzalez, J. 1990, A&A, 231, 431

Alcolea, J., Pardo, J. R., Bujarrabal, V., et al. 1999, A&AS, 139, 461

Bally, J., Stark, A. A., Wilson, R. W., & Henkel, C. 1988, ApJ, 324, 223

Baud, B., Habing, H. J., Matthews, H. E., & Winnberg, A. 1979, A&AS, 35, 179

Bedijn, P. J. 1987, A&A, 186, 136

Beichman, C. A., Neugebauer, G., Habing, H. J., Clegg, P. E., & Chester, T. J. 1988, in NASA RP-1190, Vol. 1 (1988)

Binney, J., Gerhard, O. E., Stark, A. A., Bally, J., & Uchida, K. I. 1991, MNRAS, 252, 210

Blitz, L. & Spergel, D. N. 1991, ApJ, 379, 631

Blommaert, J. A. D. L., van Langevelde, H. J., & Michiels, W. F. P. 1994, A&A, 287, 479

Burton, W. B. 1988, in Galactic and Extragalactic Radio Astronomy, 295–358

Burton, W. B. & Liszt, H. S. 1978, ApJ, 225, 815

Carter, B. S. 1990, MNRAS, 242, 1

Cho, S., Chung, H., Kim, H., et al. 1998, ApJS, 115, 277

Cole, A. A. & Weinberg, M. D. 2002, ApJ, 574, L43

Cutri, C. M., Skrutskie, M. F., & Van Dyk, S. 2003, avalaible on line at
  `http://www.ipac.caltech.edu/2mass/`

de Vaucouleurs, G. 1964, in IAU Symp. 20: The Galaxy and the Magellanic
  Clouds, 195

Deguchi, S., Fujii, T., Izumiura, H., et al. 2000a, ApJS, 130, 351

—. 2000b, ApJS, 128, 571

Drimmel, R., Cabrera-Lavers, A., & López-Corredoira, M. 2003, A&A, 409, 205

Egan, M. P., Price, S. D., Moshir, M. M., et al. 1999, AFRL-VS-TR-1999, 1522

Englmaier, P. & Gerhard, O. 1999, MNRAS, 304, 512

Epchtein, N., de Batz, B., Copet, E., et al. 1994, Ap&SS, 217, 3

Feast, M. W., Glass, I. S., Whitelock, P. A., & Catchpole, R. M. 1989, MNRAS, 241,
  375

Feltzing, S. & Gilmore, G. 2000, A&A, 355, 949

Ferraro, F. R., Montegriffo, P., Origlia, L., & Fusi Pecci, F. 2000, AJ, 119, 1282

Frogel, J. A. & Whitford, A. E. 1987, ApJ, 320, 199

Girardi, L., Bressan, A., Bertelli, G., & Chiosi, C. 2000, A&AS, 141, 371

Glass, I. S., Matsumoto, S., Carter, B. S., & Sekiguchi, K. 2001, MNRAS, 321, 77

Glass, I. S., Whitelock, P. A., Catchpole, R. M., & Feast, M. W. 1995, MNRAS, 273,
  383

Groenewegen, M. A. T. & de Jong, T. 1993, A&A, 267, 410

Guarnieri, M. D., Renzini, A., & Ortolani, S. 1997, ApJ, 477, L21

Habing, H. J. 1996, A&A Rev., 7, 97

Haikala, L. K. 1990, A&AS, 85, 875

Hughes, S. M. G. & Wood, P. R. 1990, AJ, 99, 784

Iben, I. & Renzini, A. 1983, ARA&A, 21, 271

Imai, H., Deguchi, S., Fujii, T., et al. 2002, PASJ, 54, L19

Izumiura, H., Deguchi, S., Fujii, T., et al. 1999, ApJS, 125, 257

Josselin, E., Loup, C., Omont, A., Barnbaum, C., & Nyman, L.-A. 1996, A&A, 315,
  L23

Le Bertre, T. & Nyman, L.-A. 1990, A&A, 233, 477

Lewis, B. M. 1989, ApJ, 338, 234

Lindqvist, M., Winnberg, A., Habing, H. J., & Matthews, H. E. 1992, A&AS, 92, 43

Loup, C., Groenewegen, M. A. T., Cioni, M. R., et al. 2004, in preparation

Marigo, P., Bressan, A., & Chiosi, C. 1996, A&A, 313, 545

Matsuura, M., Yamamura, I., Cami, J., Onaka, T., & Murakami, H. 2002, A&A,
  383, 972

Messineo, M., Habing, H. J., Menten, K. M., Omont, A., & Sjouwerman, L. O.
  2004a, A&A (Chapter IV)

—. 2004b, A&A, 418, 103 (Chapter III)

Messineo, M., Habing, H. J., Sjouwerman, L. O., Omont, A., & Menten, K. M. 2002, A&A, 393, 115 (Chapter II)

Nagata, T., Hyland, A. R., Straw, S. M., Sato, S., & Kawara, K. 1993, ApJ, 406, 501

Nakada, Y., Onaka, T., Yamamura, I., et al. 1991, Nature, 353, 140

Ng, Y. K. & Bertelli, G. 1996, A&A, 315, 116

Nyman, L.-A., Hall, P. J., & Le Bertre, T. 1993, A&A, 280, 551

Olivier, E. A., Whitelock, P., & Marang, F. 2001, MNRAS, 326, 490

Omont, A., Gilmore, G. F., Alard, C., et al. 2003, A&A, 403, 975

Ortiz, R., Blommaert, J. A. D. L., Copet, E., et al. 2002, A&A, 388, 279

Price, S. D., Egan, M. P., Carey, S. J., Mizuno, D. R., & Kuchar, T. A. 2001, AJ, 121, 2819

Renzini, A. & Voli, M. 1981, A&A, 94, 175

Schuller, F. 2002, PhD Thesis: Université Pierre et Marie Curie, Paris 6.

Schuller, F., Ganesh, S., Messineo, M., et al. 2003, A&A, 403, 955

Schultheis, M., Lançon, A., Omont, A., Schuller, F., & Ojha, D. K. 2003, A&A, 405, 531

Sevenster, M. N. 1999, MNRAS, 310, 629

Sevenster, M. N., Chapman, J. M., Habing, H. J., Killeen, N. E. B., & Lindqvist, M. 1997a, A&AS, 122, 79

—. 1997b, A&AS, 124, 509

Sevenster, M. N., van Langevelde, H. J., Moody, R. A., et al. 2001, A&A, 366, 481

Sjouwerman, L. O., Habing, H. J., Lindqvist, M., van Langevelde, H. J., & A., W. 1999, "The Central Parsecs of the Galaxy" ASP Conf. Series 186 (p. 379)

Sjouwerman, L. O., van Langevelde, H. J., Winnberg, A., & Habing, H. J. 1998, A&AS, 128, 35

van Loon, J. T., Gilmore, G. F., Omont, A., et al. 2003, MNRAS, 338, 857

Vassiliadis, E. & Wood, P. R. 1993, ApJ, 413, 641

Whitelock, P., Feast, M., & Catchpole, R. 1991, MNRAS, 248, 276

Whitelock, P., Marang, F., & Feast, M. 2000, MNRAS, 319, 728

Whitelock, P., Menzies, J., Feast, M., et al. 1994, MNRAS, 267, 711

Whitelock, P. A., Feast, M. W., van Loon, J. T., & Zijlstra, A. A. 2003, MNRAS, 342, 86

Winfrey, S., Barnbaum, C., Morris, M., & Omont, A. 1994, Bulletin of the American Astronomical Society, 26, 1382

Wood, P. R., Habing, H. J., & McGregor, P. J. 1998, A&A, 336, 925

Zoccali, M., Renzini, A., Ortolani, S., et al. 2003, A&A, 399, 931

Chapter 6

Considerations on the dynamics of maser stars in our Galaxy.

A preliminary report on an ongoing study by
H.J. Habing, M. Messineo, G. van de Ven, M. Sevenster and K.H. Kuijken

6.1 Introduction

In this thesis we present results from a survey of SiO maser stars undertaken for the explicit reason to investigate stellar kinematics and dynamics in the inner regions of the Milky Way. This survey is a continuation of the thesis project of M. Sevenster in which she looked at 1612 MHz (18cm) for OH/IR stars with the VLA in the northern hemisphere and with the ATCA in the southern hemisphere (Sevenster et al. 1997a,b, 2001). The results of Sevenster's survey have been presented and analysed in several papers (Debattista et al. 2002; Sevenster et al. 1999; Sevenster 1999a).

In discussing the velocities of the SiO maser stars we came across a question that until now has not been studied in depth: can the line-of-sight velocities (v_{los})[1] of SiO and OH maser stars in the forbidden quadrants of the longitude-velocity, $(l - v)$, diagram be explained by a rotating bar, and if so, can they be used to constrain the parameters of this bar? A full answer requires two consecutive steps: a) to find a potential and orbits in this potential that will fill the required areas of the $(l - v)$ diagram; 2) to find a physical explanation why stars fill these orbits. To answer this question we have started numerical calculations of the orbits in a gravitational potential and compared the predicted longitudes and line-of-sight velocities with those of the observations. Here we describe the first preliminary results of this ongoing study.

---

[1]We will use the term "line-of-sight velocity" instead of the more common term "radial velocity" to avoid confusion: in the kinematic and dynamical discussion "radial velocity" will be used for the motion along the radius vector from the Galactic Centre

6.2 Available evidence for a Galactic bar

To date, there is clear evidence that the Galactic gravitational field has a weak bar. This was first proposed by de Vaucouleurs (1964) based on the analysis of HI gas velocities and it was later confirmed by, e.g., Binney et al. (1991) and Bissantz et al. (2003). Other evidence comes from the asymmetry around $l = 0°$ seen in the COBE data (e.g. Binney et al. 1997; Blitz & Spergel 1991; Weiland et al. 1994), star counts (Nakada et al. 1991; Whitelock & Catchpole 1992), and microlensing studies (Paczynski et al. 1994).

Stellar maser emission provides a unique tool for studying stellar kinematics. Unbiased samples of stellar line-of-sight velocities in the inner Galaxy are obtained through stellar OH and SiO maser searches, and these are not affected by interstellar extinction. In this small chapter we focus on the kinematics and spatial distribution of maser stars, whose properties have been discussed in the previous chapters or in the existing literature.

6.2.1 Asymmetry in the longitude distribution of maser stars

The data-set resulting from the OH/IR maser surveys by Sevenster et al. (1997a,b, 2001) uniformly covers the entire longitude range from $-45°$ to $+45°$. It can therefore be used very well to study a possible symmetry in star counts around $l = 0°$. By plotting $l/|l|$ against $|l|$ in a cumulative fashion, a deviation from (axial) symmetry in the inner Galaxy shows up as a non–horizontal section. In part of the sample ($-10° < l < 10°$) an asymmetry was found that could be explained most naturally by a triaxial (m=2) component in the inner Galaxy, rather than a m=1 asymmetry (Sevenster 1999b). Here we present the same figure of the cumulative distribution (Fig. 6.1), but for a larger sample of OH/IR stars. The distribution is given for OH/IR stars as well as for MSX sources with AGB colours (as defined in Sevenster 2002) in the same region ($|b| < 3°$). For OH/IR stars, there is an over-density at negative longitudes close to $l = 0°$. At larger absolute longitudes, the over-density is at positive longitudes; the slope of the curve is positive. Around $l = 40°$, the curve seems to level out, but this cannot be assessed in more detail as the sample doesn't go out far enough.

All these aspects are explained by a bar-like density distribution sampled out to distances well beyond the centre of the Galaxy, up to the far end of the bar. For the MSX sources, the initial negative slope is not seen and the curve starts to rise at lower longitudes. This may be explained by the same bar-like distribution sampled out to smaller distances (for a more detailed discussion see Sevenster 1999b).

Different models used to describe the density distribution of the bar lead to different values of the semi-major axis (a) of the bar and the viewing angle (ϕ), the angle between the line-of-sight and the major axis. However, they do not vary independently, and possible models seem to range very roughly from $\phi = 20°$ and $a = 3$ kpc to $\phi = 50°$ and $a = 2$ kpc; this relation is not necessarily linear. From measurements of the pattern speed (e.g. Debattista et al. 2002) we only have

an upper limit for the semi–major axis of about 3 kpc, so it will probably be hard to constrain the viewing angle as described here. However, if some parameters or even the functional form of the bar density are known from other arguments, this will limit the degrees of freedom considerably.
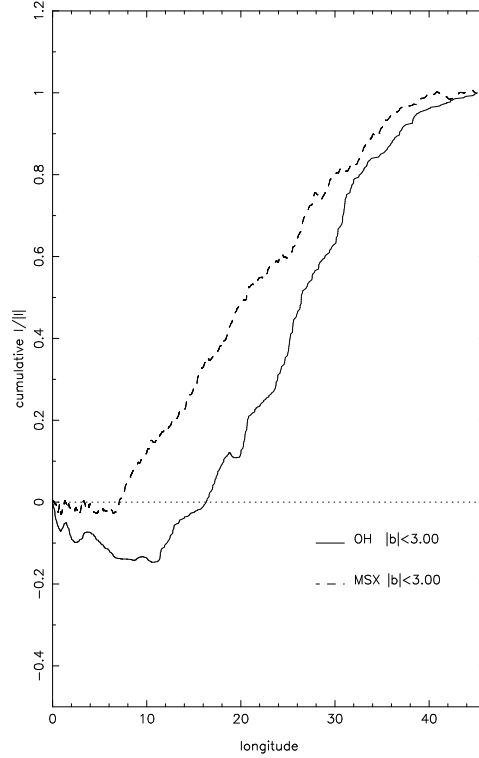

Figure 6.1: *On the horizontal axis the absolute longitude, $|l|$, is displayed and on the vertical axis the cumulative sum of $l/|l|$.*

6.2.2 Longitude–velocity diagram

We will use three observational $(l - v)$ diagrams. In the top panel of Fig. 6.2 the CO line spectrum from Dame et al. (2001) is shown; the middle panel shows the OH/IR stars observed by Sevenster and collaborators and the lower panel shows the SiO masers studied in this thesis.

If a cloud is located at the tangent point to the line of sight of a circular orbit around the Galactic centre (GC), its velocity vector will point entirely along the line-of-sight; the velocity at the tangent point is the highest velocity seen along a given line-of-sight. It will be called the terminal velocity, v_{term}. An analytic

131
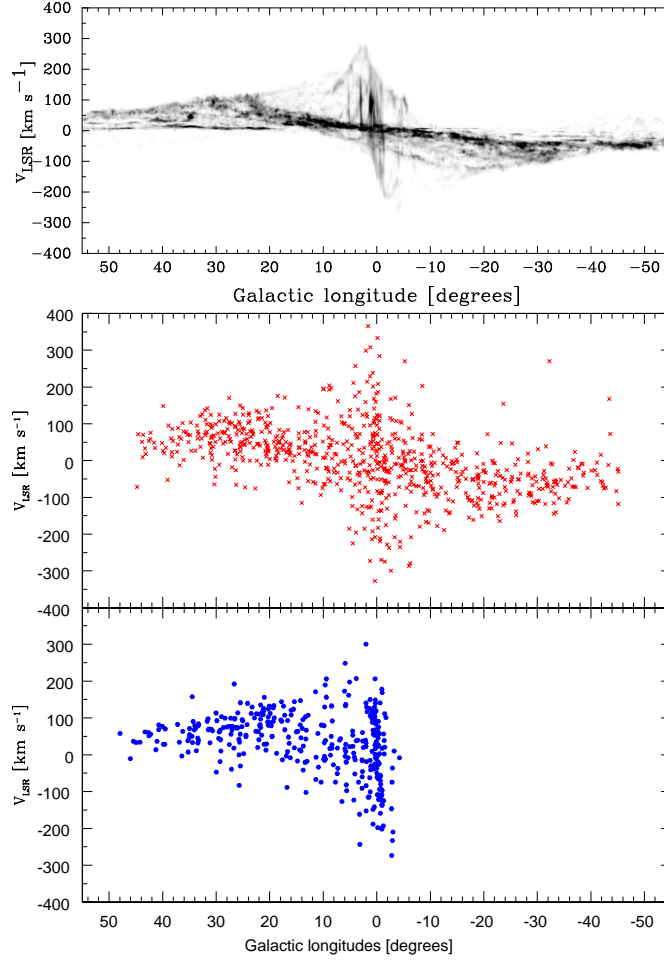
Figure 6.2: *Longitude–velocity diagrams. In the upper panel the CO distribution from Dame et al. (2001) is shown; the middle panel shows the sample of 766 OH/IR stars by Sevenster et al. (1997a,b, 2001); the lower panel shows the distribution of the 271 SiO masing stars from Chapter II plus another ~ 90 unpublished SiO maser detections.*

relation exists between terminal velocity and longitude: $v_{\mathrm{term}} = v_{\mathrm{los}}(R_{\mathrm{tang}}) - V_\odot \sin(l)$. This is plotted in Fig. 6.3, as two continuous curves, adopting a constant tangential velocity, $V_\odot$ of 220 km s^{-1}, all the way to the GC. The terminal velocity relation gives a good approximation to the highest velocity of the CO gas outside longitudes of about $\pm 20°$, confirming that the gas in the Galactic plane moves largely in circular orbits around the GC. Most of the stars appear also constrained

by the same curve. However, since stars have higher velocity dispersions than the gas, some stars cross the edge defined by the gas terminal velocity by up to $60 \, \mathrm{km \, s^{-1}}$.

There is a lower density gas region at positive velocities between longitudes $20°$ and almost $0°$ and similarly at negative velocities and longitudes between $0°$ and $-20°$. Gas simulations show that a barred potential explains the gas distribution well, including the low–density regions (Athanassoula & Bureau 1999). Gas on intersecting orbits will collide with itself and a steady flow is not possible. The gas looses angular momentum and it will flow into smaller orbits at lower energies. Holes seem to appear also in the stellar $(l - v)$ diagram of the maser stars, but they can not be explained in the same way.

In the region close to the GC, not only the holes in the gas $(l - v)$ distribution, but also the presence of stars at forbidden velocities in the two quadrants ($l > 0$ and $v_{\mathrm{los}} < 0$) and ($l < 0$ and $v_{\mathrm{los}} > 0$) show that the assumption of circular orbits breaks down. In figure 6.3, where maser stars are over–plotted on the CO gas, the curve $-V_\odot \sin(l)$ is drawn. At positive (negative) longitudes the stars above (below) this curve could move on circular *prograde* orbits. This apparently applies to all maser stars in the longitude range $345° > l > 15°$. However, forbidden velocities at longitudes $|l| < 15°$ are a clear sign of non–circular orbits. Both the OH and the SiO masers populate these regions within pretty much the same boundaries.

6.2.3 Nuclear Disk

The distribution of gas in the inner one degree from the Galactic centre, the circumnuclear zone (CMZ) or nuclear ring, is well described by a disk with a radius of about 200 pc radius (Combes 1991; Morris & Serabyn 1996). This disc appears in the $(l - v)$ diagram as a distinct feature: a strong correlation between longitude and velocity, at longitudes $-1.4 < l < 1.5°$, with maximum velocities of about 200 $\mathrm{km \, s^{-1}}$. Since the gas is a collisional medium, intersecting orbits are forbidden to gas. Dynamical models in a barred potential predict 2 kinds of orbits: X1, along the major axis of the bar, and X2 perpendicular to the X1. When the X1 start to be self–intersecting the gas moves inward in to the lower energy X2 orbits. The transition between the cusped X1 orbit and the X2 appear as a shock region where atomic gas is possibly converted in molecular gas. In principle, stars can populate the intersecting X1 orbits not accessible to gas clouds.

A strong correlation between longitude and velocity is seen also in the maser stars. It was first seen in OH/IR stars within $1°$ from the GC (Lindqvist et al. 1992; Sjouwerman et al. 1998) and clearly appears in our SiO maser stars (Fig. 6.2). A linear regression fit using the OH/IR stars gives a slope of $180 \, \mathrm{km \, s^{-1} \, pc^{-1}}$ (Lindqvist et al. 1992), consistent with that derived for SiO targets (Chapter V).

As seen in Chapter V, nuclear disk stars are highly obscured ($A_{\mathrm{K_S}} > 2$ mag). The use of extinction estimates enabled us to exclude possible foreground objects and to select individual stellar members of the nuclear disk. Furthermore, since SiO targets are very bright at near–infrared wavelengths (Chapter III), they are
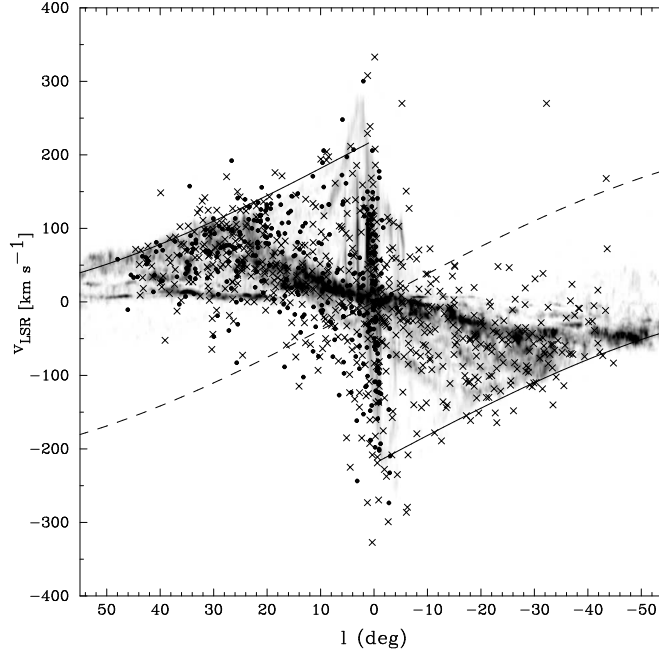
Figure 6.3: *This $(l-v)$ diagram shows the maser stars on the CO map. Symbols are as in Fig. 6.2. Continuous lines show the expected terminal velocities under the assumption of circular orbits. The dashed line is the curve $-V_\odot \sin(l)$, which corresponds to the opposite of the velocity of the Sun along the line-of-sight. At positive (negative) longitudes the stars on circular orbits above (below) this curve are moving prograde in the Galactic standard of rest. The remaining regions are then the forbidden regions.*

ideal for follow–up spectroscopic studies of the nuclear–disk population.

6.3 A simple dynamical model

In an axisymmetric potential, the angular momentum of each star, $L = r^2 \, \partial\phi/\partial t$ is conserved and thus the stars will keep the same direction (i.e. $\partial\phi/\partial t$ will not change sign) when a star moves along its orbit. Clockwise moving stars (i.e. with positive line-of-sight velocity) seen at a positive longitude will move away from us (after correction for LSR motion). At negative longitudes these clockwise rotating stars are all coming toward us (i.e. $v_{\text{los}} < 0$). In the $(l - v)$–diagram counter rotating stars will appear *only* in the "forbidden quadrants" ($l > 0$ and $v_{\text{los}} < 0$) and ($l < 0$ and $v_{\text{los}} > 0$).

Kinematic deviations from what would be expected in an axisymmetric poten-

tial were found by Sevenster et al. (2000), when modelling the underlying distribution function (DF). The observed line-of-sight dispersions for instance could not be explained by an axisymmetric model with σ_R equal to σ_z. Moreover, to explain the stars in the forbidden quadrants, isotropic components had to be invoked.

A barred potential explains the Galactic kinematics well. Several N–body dynamical models of the barred Milky Way exist (e.g. Fux 1997). They can be compared with observations qualitatively, but do not allow a real fit to the data. The latter is possible with the few dynamical models that are built by superposition of either (analytical) DF components (Sevenster et al. 2000) or of numerically integrated orbits (e.g. Häfner et al. 2000; Zhao 1996). The latter method is also known as Schwarzschild's method and is more general than the DF method, as it does not require a priori assumptions about the form of the DF, which is even more complicated by the fact that E_J is the only known integral of motion.

For the population of maser stars, no realistic dynamical model with a barred potential has yet been constructed. Therefore we started to calculate orbits in a barred potential with the ultimate goal to predict the observed distribution of maser points in the $(l - v)$ diagram. This is work under way, but the first results are promising. In the following we briefly sketch the various assumptions and steps made for our calculation and some first results.

6.3.1 Geometry

We adopt a Cartesian coordinate system (x, y, z), corotating with the bar–like bulge at a (clockwise) angular speed of $\Omega_b = 60$ km s^{-1} kpc^{-1}(Debattista et al. 2002). The origin of the coordinate system is at the Galactic centre, the x–axis is aligned with the major axis of the bar–like bulge and the y–axis with its minor axis. The Sun is assumed to lie at a distance $R_\odot$ from the Galactic centre, in the Galactic plane. The Sun-GC line makes an angle ϕ w.r.t. the long–axis of the bulge. We fix the Sun's distance to the Galactic centre at $R_\odot = 8$ kpc and its (clockwise) azimuthal velocity to $V_\odot = 200$ km s^{-1}. For a given mass model, this leaves two free parameters: the angular speed Ω_b of the bar-like bulge and the angle ϕ of the Sun w.r.t. to long–axis of this bulge.

6.3.2 Equations of motion

We calculate numerically the orbits of stars in a frame of reference that is rotating in the Galactic plane at an angular speed, $\vec{\Omega_b} = (0, 0, \Omega_b)$, solving the equation:

$$\ddot{\mathbf{r}} = -\nabla \Phi_{\text{eff}} - 2 \left(\mathbf{\Omega_b} \times \dot{\mathbf{r}} \right).$$ (6.1)

In the right–hand side of this equation the first term is the acceleration induced by the effective gravitational potential; the second term is the Coriolis acceleration. The Coriolis acceleration introduces a dependence of the acceleration in the

x–direction on the velocity in the y–direction and vice versa. For further explanations see Binney & Tremaine (1987).

6.3.3 Gravitational potential

As a first qualitative study of the stellar dynamics in our Milky Way we consider the non–axisymmetric planar logarithmic potential (Binney & Tremaine 1987)

$$\Phi(x,y) = \frac{1}{2} v_0^2 \ln \left(R_C^2 + x^2 + \frac{y^2}{q^2} \right),$$ (6.2)

with constant velocity v_0, core radius R_C and axial ratio $q \leq 1$. Near the centre ($R \equiv \sqrt{x^2 + y^2} \ll R_C$) the logarithmic potential approximates that of a two-dimensional harmonic oscillator, such that the corresponding central density is nearly homogeneous. Going outwards the rotation curve rapidly flattens to $v_c \sim v_0$. The constant axial ratio implies that the influence of the non–axisymmetry is similar at all radii. Although at larger radii this is not realistic for our Galaxy, the orbits calculated in this rotating potential are still representative as they become nearly circular beyond the corotation radius.

6.3.4 First results

Taking the above logarithmic potential with $v_0 = 200 \text{ km s}^{-1}$, $R_C = 0.14$ kpc and $q = 0.9$, we calculated a set of closed orbits by numerically solving Eq. (6.1) with $\Omega_b = 60 \text{ km s}^{-1} \text{ kpc}^{-1}$. We used a fifth order Runge-Kutta algorithm as described in "Numerical Recipes" (Press et al. 1992). A representative example of these orbits in the XY-plane and in the $(l - v)$ diagram, is shown in Fig. 6.4.

We have just started these simulations and we need to further compare our model to observations in a quantitative way. However, as already proposed by Binney et al. (1991) for the gas, it clearly appears from the simple superposition of the orbits in the $(l - v)$ diagram that orbits from the X1 and X2 families can explain the observed forbidden stellar velocities.

6.4 Summary and future plans

In summary, the SiO and OH maser stars have a similar distribution in the velocity-longitude diagram. Their forbidden velocities are difficult to understand in an axisymmetric potential, but they can be understood in a rotating barred potential.

The disk maser stars beyond longitudes $|l| > 15°$ are probably moving on loop orbits. Outside of the bar region the potential must be close to axisymmetry as observed in the terminal velocities of the gas.

For stars within longitudes $|l| < 15°$, their forbidden velocities can be explained by X1/X2 orbits.
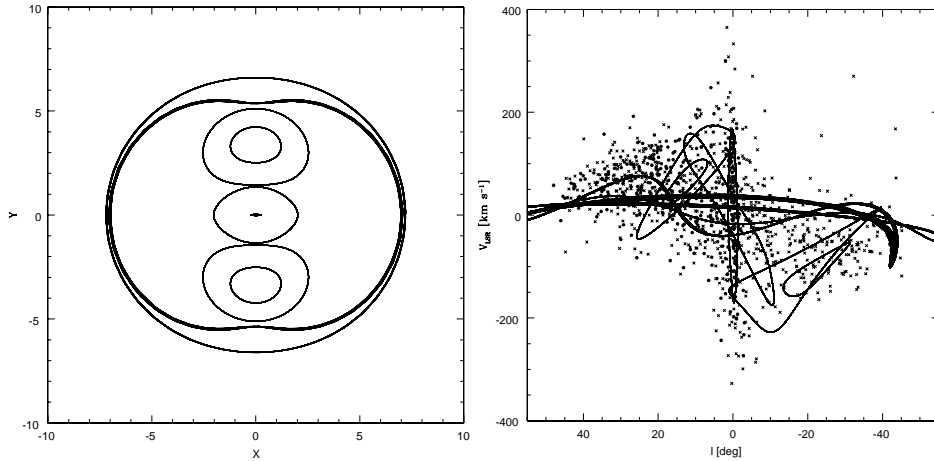
Figure 6.4: *Left panel: (x, y) plot of an example of closed orbits calculated in a rotating logarithmic potential (see text). Right panel: the same orbits projected in a $(l-v)$ diagram assuming $\phi = 45°$.*

The most realistic potential currently available is that obtained by the Basel group (Bissantz et al. 2003; Englmaier & Gerhard 1999). This is based on a mass model of the Milky Way derived from the dust corrected COBE maps. We plan to use the Basel potential to calculate a library of orbits and to fit these orbits to the available kinematics of maser stars. The fit can be done by maximising the likelihood of the line-of-sight velocity distribution at the (discrete) observations.

References

Athanassoula, E. & Bureau, M. 1999, ApJ, 522, 699

Binney, J., Gerhard, O., & Spergel, D. 1997, MNRAS, 288, 365

Binney, J., Gerhard, O. E., Stark, A. A., Bally, J., & Uchida, K. I. 1991, MNRAS, 252, 210

Binney, J. & Tremaine, S. 1987, Galactic dynamics (Princeton, NJ, Princeton University Press, 1987, 747 p.)

Bissantz, N., Englmaier, P., & Gerhard, O. 2003, MNRAS, 340, 949

Blitz, L. & Spergel, D. N. 1991, ApJ, 379, 631

Combes, F. 1991, ARA&A, 29, 195

Dame, T. M., Hartmann, D., & Thaddeus, P. 2001, ApJ, 547, 792

de Vaucouleurs, G. 1964, in IAU Symp. 20: The Galaxy and the Magellanic Clouds, 195–+

Debattista, V. P., Gerhard, O., & Sevenster, M. N. 2002, MNRAS, 334, 355

Englmaier, P. & Gerhard, O. 1999, MNRAS, 304, 512

Fux, R. 1997, A&A, 327, 983

Häfner, R., Evans, N. W., Dehnen, W., & Binney, J. 2000, MNRAS, 314, 433

Lindqvist, M., Habing, H. J., & Winnberg, A. 1992, A&A, 259, 118

Messineo, M., Habing, H. J., Menten, K. M., Omont, A., & Sjouwerman, L. O. 2004a, A&A in preparation (Chapter V)

Messineo, M., Habing, H. J., Menten, K. M., Omont, A., & Sjouwerman, L. O. 2004b, A&A, 418, 103, Chapter III

Messineo, M., Habing, H. J., Sjouwerman, L. O., Omont, A., & Menten, K. M. 2002, A&A, 393, 115, Chapter II

Morris, M. & Serabyn, E. 1996, ARA&A, 34, 645

Nakada, Y., Onaka, T., Yamamura, I., et al. 1991, Nature, 353, 140

Paczynski, B., Stanek, K. Z., Udalski, A., et al. 1994, ApJ, 435, L113

Press, W. H., Teukolsky, S. A., Vetterling, W. T., & Flannery, B. P. 1992, Numerical recipes in FORTRAN. The art of scientific computing (Cambridge: University Press, —c1992, 2nd ed.)

Sevenster, M., Saha, P., Valls-Gabaud, D., & Fux, R. 1999, MNRAS, 307, 584

Sevenster, M. N. 1999a, MNRAS, 310, 629

Sevenster, M. N. 1999b, MNRAS, 310, 629

Sevenster, M. N. 2002, AJ, 123, 2772

Sevenster, M. N., Chapman, J. M., Habing, H. J., Killeen, N. E. B., & Lindqvist, M. 1997a, A&AS, 122, 79

Sevenster, M. N., Chapman, J. M., Habing, H. J., Killeen, N. E. B., & Lindqvist, M. 1997b, A&AS, 124, 509

Sevenster, M. N., Dejonghe, H., Van Caelenberg, K., & Habing, H. J. 2000, A&A, 355, 537

Sevenster, M. N., van Langevelde, H. J., Moody, R. A., et al. 2001, A&A, 366, 481

Sjouwerman, L. O., van Langevelde, H. J., Winnberg, A., & Habing, H. J. 1998, A&AS, 128, 35

Weiland, J. L., Arendt, R. G., Berriman, G. B., et al. 1994, ApJ, 425, L81

Whitelock, P. & Catchpole, R. 1992, in ASSL Vol. 180: The center, bulge, and disk of the Milky Way, 103

Zhao, H. S. 1996, MNRAS, 283, 149

Chapter 7

The ISOGAL survey and the completeness analysis

7.1 Introduction

The ISOGAL project is an ISO infrared survey of specific regions in the Galactic Plane, which were selected to provide information on Galactic structure, the stellar populations and mass-loss, and the recent star formation history of the inner disk and Bulge of the Galaxy. Several (about 25) scientific papers have been published based on the ISOGAL data. They present studies of the Galactic structure, an analysis of the complete AGB population, and studies of infrared dark clouds and young stellar objects (Omont et al. 2003).

The survey was performed at 7 and 15 μm with ISOCAM, covering 16 square degrees with a spatial resolution of 3-6$''$and a sensitivity of 10-20 mJy, two orders of magnitude deeper than IRAS at 12μm, and a factor 10 deeper than the MSX A band (8μm).

The 7 and 15 μm ISOGAL data were combined with the I, J, K_s (effective wavelengths 0.79, 1.22 and 2.14 μm) ground-based data from the DENIS survey, resulting in a 5-wavelength catalogue of point sources. The combination of mid- and near-infrared measurements permits a determination of the nature of the individual sources and of the interstellar extinction towards them.

A complete overview of the first scientific results from ISOGAL data is given by Omont et al. (2003), while the description of the point source catalogue is given in an Explanatory Supplement (Schuller et al. 2003).

In the present chapter I will briefly describe the survey and than I will move to the description of the ISOGAL completeness analysis (Sect. 1.4 below), to which I contributed significantly.

7.2 Observations

The ISOGAL observational program –250 hours of observing time– is one of the largest ISO programs. The ISOCAM observations were taken from January 1996 to April 1998, i.e., over the whole ISO mission.

The observed fields ($\sim$16 deg^2) are distributed along the inner Galactic Disk, mostly within $|\ell| < 30°$, $|b| < 1°$, as shown in Figure 1.
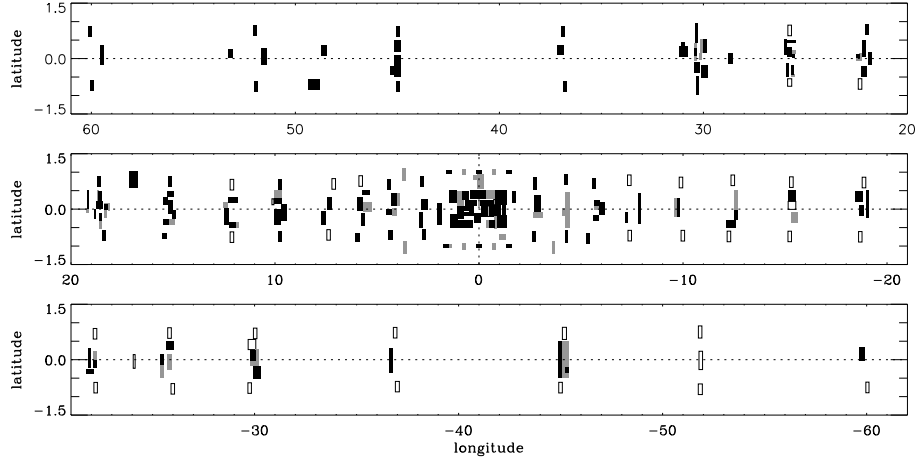
Figure 7.1: *Galactic map of ISOGAL fields with $|\ell| < 60°$. Black, grey and open boxes show fields which have been observed at both 7 & 15 μm, at 7 μm only and at 15 μm only, respectively. Twenty–one additional northern fields (not displayed) were also observed, at $\ell \approx +68°$, $+75°$, $+90°$, $+98°$, $+105°$, $+110°$, $+134°$, $+136°$, & $+138°$. Figure adapted from Schuller et al. (2003).*

Detailed information on the observation parameters and on the field positions is available in the ISOGAL Explanatory Supplement (Schuller et al. 2003) and on the ISOGAL web server `www-isogal.iap.fr/`.

Most of the observations were performed with the broad filters $LW2$ and $LW3$ and a pixel scale of $6''$. A few regions around the Galactic centre were observed with the narrow filters $LW5$ or $LW6$, and $LW9$ and a pixel scale of $3''$, to reduce the effects of bright sources that would saturate the detector (thus moving the saturation limit from $Flux_{12} > 6$ Jy to $Flux_{12} > 20$ Jy). A list of the ISOCAM filters used for the ISOGAL survey is given in Table 7.1.

The observations, performed in raster mode ($\sim$0.1 deg^2), were oriented in Galactic coordinates. At each raster position 19 basic ISOCAM frames (32 x 32 pixels) were taken, resulting in a total integration time of 21 s per raster position. The raster steps were typically $90''$ in one direction and $150''$ in the other direction, and each sky point was observed for a maximum of 4 times, with an average of 1.5. Only 384 of the 463 raster positions were used for the production of the first ISOGAL point source catalogue, because only one raster was used in case of overlapping areas to avoid redundancy. The total number of ISOGAL fields (rectangular area of the sky whose edges are aligned with the galactic axes and observed by ISOGAL) is 263. They can be divided in 43 fields (FA) only observed at 7 μm, 57 fields (FB) only observed at 15 μm, and 163 fields (FC) observed at both 7 and 15μm.

Systematic cross-identification with the near-infrared $I, J, K_{\rm s}$ sources of the

Table 7.1: *ISOCAM filters used for ISOGAL: reference wavelengths and bandwidths, zero point magnitudes and flux densities, and total observed area. Table adapted from Schuller et al. (2003).*

Filter	λ_{ref} [μm]	$\Delta\lambda$ [μm]	ZP[a] [mag]	$F_{mag=0}$ [Jy]	Area [deg^2]
LW2	6.7	3.5	12.39	90.36	9.17
LW5	6.8	0.5	12.28	81.66	0.64
LW6	7.7	1.5	12.02	64.27	2.97
LW3	14.3	6.0	10.74	19.77	9.92
LW9	14.9	2.0	10.62	17.70	3.53

[a]The magnitude of a source with a flux density F_ν expressed in mJy is given by $mag = ZP - 2.5 \times log(F_\nu)$

DENIS survey was an integral part of the ISOGAL program and special DENIS observations were performed for this purpose (Simon 2004). DENIS data were available for 95% of the fields surveyed with ISOCAM.

7.3 Data processing and analysis

Data reduction was performed with standard procedures of the CAM Interactive Analysis Package (CIA version 3). A sophisticated pipeline was developed for the ISOGAL data (Schuller et al. 2003), which involves more steps than the standard treatment of ISOCAM data (see ISOCAM Handbook, Blommaert et al. 2003). This was necessary because of the extreme conditions of the ISOGAL observations. In addition to the usual problems, i.e. glitches, dead pixels and the time-dependent behaviour of the detectors, one needs also to consider bright background emission, crowding, high spatial density of bright sources (which causes pixel-memory effects), and the short integration time.

The point sources were extracted using a dedicated PSF fitting routine (Schuller et al. 2003).

The completeness of point source extraction has been systematically addressed through retrieval of artificial sources, which is described in the next section.

7.4 Artificial sources

Synthetically reproducing the complete process of photometric measurements is the only way to properly characterise all undesired effects associated with observations in a crowded field.

An artificial star experiment consists of adding artificial stars to ISOGAL images, and re-extracting all point sources with the same pipeline as the one used to generate the ISOGAL catalogue. The analysis of input magnitudes of artificial

sources with those in output enables one to characterise the effects of crowding on the photometric quality and the completeness of the extracted point source catalogue.

Artificial star experiments were conducted on ISOGAL images following a procedure similar to that applied by Bellazzini et al. (2002):

- The magnitude of artificial stars was randomly extracted from the observed luminosity function.

- The goal of the procedure is to study the effects of crowding. Therefore, it is of primary importance that the artificial stars do not interfere with each other. The interference between artificial stars would, in fact, change the actual crowding and affect the results of the artificial experiment study. To avoid this serious bias, one can divide the image (or raster in the ISOGAL case) into grids of cells of known width (20 pixels). One artificial star is randomly positioned in each cell, avoiding the border of the cell in order to control the minimum distance between adjacent artificial stars.

- The stars were simulated using the point-spread-function (PSF) determined directly from the average ISOGAL data corresponding to the observational setup (filter, pixel scale). A new image was then built by adding the artificial stars and their Poisson photon noise into the original raster image.

- The measurements process was performed in the same way as the original measures.

- The output magnitudes were recorded, as well as the positions of the lost stars.

- To generate a significant number of artificial stars, for each image, the whole process was repeated between 100 and ∼300 times, depending on the source density and image size. A total of 5×10^3 to 4×10^4 sources were generated.

As an example, figure 7.2 shows the differences between input and output magnitudes, $mag_{input} - mag_{output}$, obtained for the raster TDT=83600913 (filter=$LW2$, pixel scale 6″), which is centred at longitudes $1.37°$ and latitude $-2.63°$, covers a region of $0.22 \times 0.24°$, and has a density of 6660 sources per deg^{-2}. A number of 55 artificial star were added each run and a total of 350 runs were performed.

The distribution of the difference is not symmetric. There is a strong concentration at zero, but also a positive tail of stars. This means that the output magnitudes are brighter then the input ones and this is due to the blending between artificial stars and real stars. When an artificial star is blended with a fainter source its output magnitude will be brighter than its input magnitude because of the flux contributed by the fainter blended source. Artificial sources having an output magnitude +0.75 mag brighter than their input magnitude were considered lost. In fact, if at the position of the artificial star one measures a point source more than 0.75 mag brighter than the magnitude of the input artificial star, this
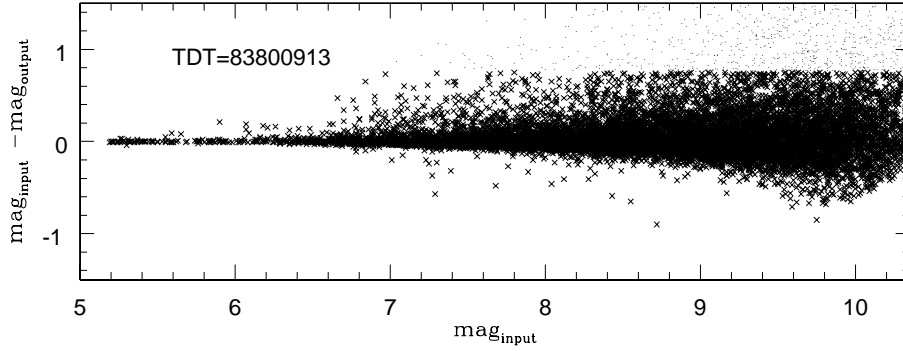
Figure 7.2: *Differences between the input and output magnitudes of the 19250 artificial stars vs. input magnitudes for the raster TDT=83600913. If the difference is larger then 0.75 mag the artificial star is considered lost.*

means that the artificial star falls on a brighter real source and in this case the star actually recovered is the real one.

Artificial star simulations were conducted on 35 images (total area ~ 2 deg^2) selected to have all possible observational setups and different crowding levels (the source density ranges from 0.0017 to 0.03 sources per pixel). Artificial star experiments were used to evaluate both random and systematic photometric errors due to crowding, as well as the completeness level of the extraction as a function of source density.

Output magnitudes were generally found to be brighter than input magnitudes. This bias is very small for bright stars, but can reach 0.3 magnitude for the faintest ones in the densest fields, where the probability of blending with real stars is higher (see Fig. 7.3).

The completeness of the extraction was quantified by analysing for each simulation the fraction of retrieved simulated sources as a function of input magnitude. A smooth curve appears which drops at faint magnitudes. The magnitude where this fraction becomes less than 50% depends on the density of the field. The point source catalogues extracted from the various ISOGAL rasters were found at least 50% complete down to the faintest end in fields with low stellar density, but this was not the case in denser regions.

For each observational setup (combination of pixel scale and filter) a relation between the estimated 50% completeness limit and the field source density was derived and used to define the limiting magnitude of each ISOGAL observation, corresponding to the faintest sources that were included in the published catalogue. The completeness limit depends on the source density, on the intensity and the structure of the local diffuse background, and on the filter. The sensitivities reached at 7 and 15 μm for standard ISOGAL conditions are summarised in Table 7.2.
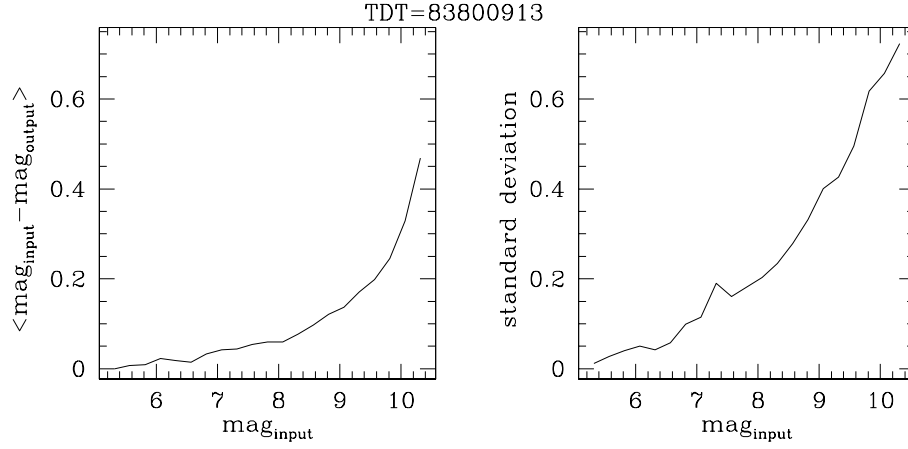
Figure 7.3: Left-panel: *Mean differences between the input and recovered magnitudes per bin of input magnitude, relative to the 19250 artificial stars simulated for the raster TDT=83600913.* **Right-panel:** *Standard deviation of the differences between the input and recovered magnitudes as a function of the input magnitude.*

Table 7.2: *Sensitivities[1] at 7 and 15 μm for typical ISOGAL conditions . Table adapted from Omont et al. (2003).*

Region[2]	Source density	Background	Pixel	Filter	7 μm		15 μm	
					mag	flux (mJy)	mag	flux (mJy)
A	low	weak	6″	broad	10	9	8.7	7
B	high	moderate	6″	broad	9	22	8	12
C	very high	strong	3″	narrow	8.4	35	7	30
D	high	very strong	6″	narrow	7.7	55	6.5	45

[1] Sensitivity limits of ISOGAL sources published in PSC *Version 1*, corresponding approximately to detection completeness of 50% (Schuller et al. 2003).
[2] Typical regions:
A Lowest density Bulge fields, $|b| \geq 2°$
B Standard Disk fields, $|b| < 0.5°$, $|\ell| \leq 30°$
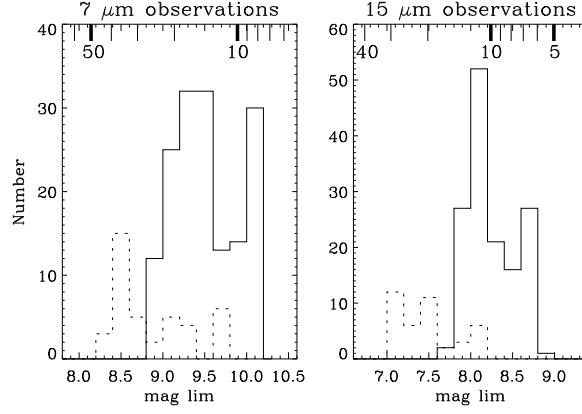C Central Bulge/Disk fields, $|b| < 0.3°$, $|\ell| \leq 1°$
D Most active star formation regions such as M16, W51.

The distribution of limiting magnitudes, for all ISOGAL observations is shown in Fig. 7.4. Since most observations were done with the broad *LW*2 and *LW*3 filters, these histograms show that the typical reached sensitivity is around 20 mJy at 7 μm and 12 mJy at 15 μm.

Figure 7.4: *Distribution of the magnitudes at which the catalogues become incomplete at the 50% level for the broad filters LW2 and LW3 (full lines), and for the narrow filters (dotted lines). The logarithmic scales at the top of each panel show the corresponding flux densities in mJy for LW2 and LW3. A small correction has to be applied for the corresponding flux densities with narrow filters. Figure adapted from Schuller et al. (2003).*

About $\approx$25% of extracted point sources fall below these magnitude limits. Analysing the quality flags of discarded sources, the photometric cut is far more severe for moderate quality sources than for good quality ones.

The completeness findings have been complemented and checked by the results of several repeated observations (in one case with 3″ pixels, rather than the typical 6″ pixels, and hence with greatly reduced crowding), and by comparison with DENIS (or 7 μm) red giant source counts.

7.5 Concluding remarks

In summary the ISOGAL PSC (version 1.0) contains 106 150 sources. It gives I, J, K_s, [7], [15] magnitudes, at five wavelengths (0.8, 1.25, 2.15, 7 & 15 μm); DENIS associations (I,J,K_s) are given when available. About half of the sources have 7-15 μm associations and 78% have DENIS associations. Quality flags are provided for each source at each wavelength, as well as for source associations, and only sources with a reasonable quality and with a magnitude above the 50% completeness limit are included in the catalogue (Schuller et al. 2003).

References

Bellazzini, M., Fusi Pecci, F., Montegriffo, P., et al. 2002, AJ, 123, 2541

Blommaert, J. A. D. L., Siebenmorgen, R., Coulais, A., et al., eds. 2003, The ISO Handbook, Volume II - CAM - The ISO Camera

Omont, A., Gilmore, G. F., Alard, C., et al. 2003, A&A, 403, 975

Schuller, F., Ganesh, S., Messineo, M., et al. 2003, A&A, 403, 955

Simon, G. 2004, in preparation

Nederlandse samenvatting

Op een heldere avond kunnen we aan de hemel een witte, op sommige plekken onderbroken band van licht tegenkomen. Wat we zien zijn miljoenen sterren die samen de schijf van ons eigen sterrenstelsel, de Melkweg, vormen. De Melkweg is opgebouwd uit een enorme bolvormige halo die grotendeels uit donkere materie bestaat, verder een grote, vlakke schijf van gas en sterren, en in het midden van de Melkweg bevindt zich een verdikking in de schijf, de lens (zie fig. 1). Sterren in de schijf van de Melkweg draaien rond het centrum, waarvan we nu weten dat het een zwart gat bevat. Hoe dichter een ster bij het centrum staat, des te korter is de tijd die het de ster kost om één keer rond te gaan. De zon bevindt zich op een afstand van ongeveer 26.000 lichtjaren van het centrum van de Melkweg en beweegt met een snelheid van zo'n 220 km per seconde rond het centrum. Zelfs met deze snelheid kost het ons zonnestelsel rond de 226 miljoen jaar om één keer rond het centrum van de Melkweg te gaan.

Het bestuderen van onze Melkweg is belangrijk voor ons begrip van de vorm, het ontstaan en de ontwikkeling van sterrenstelsels in het algemeen. De structuur en dynamica van het gas en de sterren die deel uit maken van de Melkweg kunnen door hun relatieve nabijheid (vergeleken met andere sterrenstelsels) in groot detail worden bestudeerd. Maar omdat wij ons ook zelf in de Melkweg bevinden krijgen we te maken met projectie-effecten die het ons lastig maken om de grote schaal structuur van de Melkweg te achterhalen.

De Melkweg: een spiraalstelsel met een balk in het centrum

De sterren en het gas in de schijf van de Melkweg liggen gegroepeerd in vier spiraalarmen. Wijzelf bevinden ons aan de rand van de Orion spiraalarm, tussen de Sagittarius arm en de Perseus arm in.

Over het algemeen is de lens in het centrale deel van een sterrenstelsel ofwel bolvormig, net als een bal, of uitgerekt tot een balk, waarbij de spiraalarmen aan de uiteinden van de balk ontstaan. De beweging van zowel gas als sterren geeft aan dat zich in het centrum van de Melkweg een balk bevindt. Ofschoon we tegenwoordig overtuigd zijn van het bestaan van deze balk in het centrum van de Melkweg, weten we nog nauwelijks iets af van zijn eigenschappen, zoals zijn lengte en dikte, of de hoek waaronder we de balk zien.
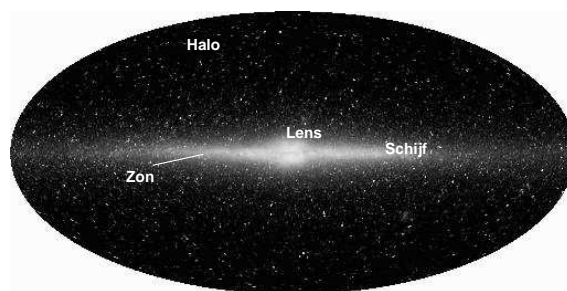
Figuur 1: *Deze afbeelding gemaakt met de COBE satelliet laat zien hoe onze Melkweg eruit ziet in het nabij-infrarode deel van het spectrum, waar het meeste licht afkomstig is van geëvolueerde sterren genaamd rode reuzen. De extinctie door interstellair stof is veel zwakker op infrarode golflengten dan op golflengten in het zichtbare deel van het spectrum. Door nu juist op deze golflengten te kijken kunnen we ons dus een veel beter beeld vormen van de Melkweg.*

Interstellaire extinctie

Een van de grootste problemen die we tegenkomen bij het bestuderen van de structuur van onze Melkweg is de verduistering door interstellair stof die sterker wordt naarmate we dichter bij het centrum van de Melkweg komen. Interstellair stof dat zich langs de gezichtslijn bevindt absorbeert en verstrooit het licht afkomstig van de sterren die we waarnemen. Dit effect genaamd extinctie (of 'uitdoving') zwakt de helderheid van de ster af en het maakt het spectrum van het sterlicht roder. Het sterspectrum laat zien hoe het licht afkomstig van de ster verdeeld is over de verschillende golflengten. Voor licht in het zichtbare deel van het spectrum is de extinctie zeer hoog, maar voor langere golflengten, zoals in het nabije- en mid-infrarode deel van het spectrum, is de extinctie minder sterk (zie fig. 2). Op infrarode golflengten kunnen we dus een veel duidelijker beeld krijgen van onze Melkweg. In de afgelopen tien jaar zijn verschillende onderzoeken (surveys) uitgevoerd op infrarode golflengten om de structuur en de vormingsgeschiedenis van onze Melkweg te achterhalen. Deze data bevat een schat aan informatie over de opbouw van sterpopulaties die er nog op wacht om volledig geanalyseerd te worden.

Dit promotie-onderzoek gaat over de bepaling van de structuur en samenstelling van de binnenste delen van onze Melkweg, daarbij gebruik makend van geëvolueerde sterren (sterren die al het grootste deel van hun leven achter de rug hebben) om het zwaartekrachtsveld in dit deel van de Melkweg in kaart te brengen. Het zwaartekrachtsveld kan ons namelijk meer vertellen over de verdeling van massa in de Melkweg.
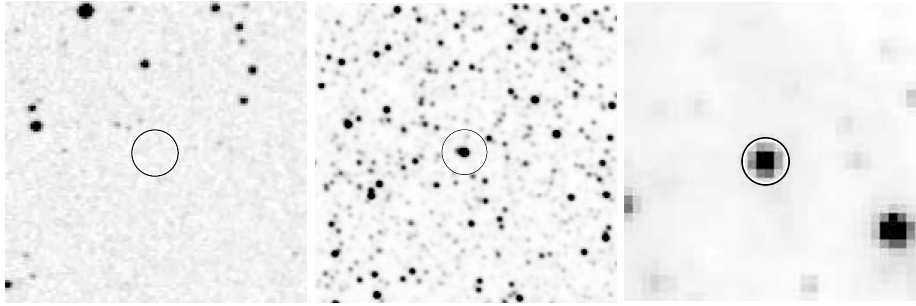
Figuur 2: *Op verschillende golflengten ziet de hemel er heel anders uit! Deze figuur laat hetzelfde gebied aan de hemel (afmeting 1/20° × 1/20°) zien op 3 verschillende golflengten. De linker afbeelding laat zien hoe het gebied in zichtbaar licht eruit ziet. Er zijn maar weinig sterren zichtbaar vanwege de hoge interstellaire extinctie. Deze foto is gemaakt met de telescoop op Mt. Palomar. De middelste afbeelding laat hetzelfde gebied zien in het nabij-infrarood; deze afbeelding is afkomstig uit de 2MASS survey. Rechts staat een ISOGAL afbeelding in het mid-infrarode deel van het spectrum. Hierin kunnen we alleen sterren zien met een circumstellaire mantel. De omcirkelde ster hebben wij gedetecteerd in onze zoektocht naar SiO maser straling (het is nr. 12 uit onze catalogus). Uit de SiO maser lijn afkomstig van deze ster hebben wij afgeleid dat deze ster zich met een snelheid van -193 km per seconde langs de gezichtslijn beweegt.*

Geëvolueerde sterren en de massaverdeling en kinematica van de Melkweg

De meeste sterren die we kunnen zien op infrarode golflengten zijn geëvolueerde reuzesterren, koude (rode) sterren die aan hun oppervlakte typisch zo'n 3000 K warm zijn (ter vergelijking: onze zon heeft een oppervlaktemperatuur van zo'n 6000 K!). Wij noemen ze reuzesterren vanwege hun grote omvang: als de zon een reuzester is geworden zal haar straal groter zijn dan de aardbaan. De sterren waar we het hier over hebben zijn ongeveer even zwaar of wat zwaarder dan onze eigen zon (tot zo'n 6 keer zo zwaar). Ofschoon deze sterren relatief koud zijn voor sterbegrippen zijn ze toch heel helder: typisch 3000 keer helderder dan onze zon. Rode reuzen verbranden waterstof en/of helium in een schil rond hun kern. Hun leeftijd ligt tussen de 1 en de 15 miljard jaar; ze zijn bijna aan het eind van hun leven aangekomen.

Geëvolueerde sterren hebben sterke winden die de ster omhullen met een mantel van gas en stof. De aanwezigheid van stof is vastgesteld uit een overschot aan infrarood licht dat van deze sterren afkomt. Stof absorbeert namelijk licht afkomstig van de ster en zendt dit weer uit op (voornamelijk) infrarode golflengten. We weten dat zich ook gas in de mantel rond deze sterren moet bevinden omdat we straling meten die wordt uitgezonden door sommige moleculen (zoals CO) op
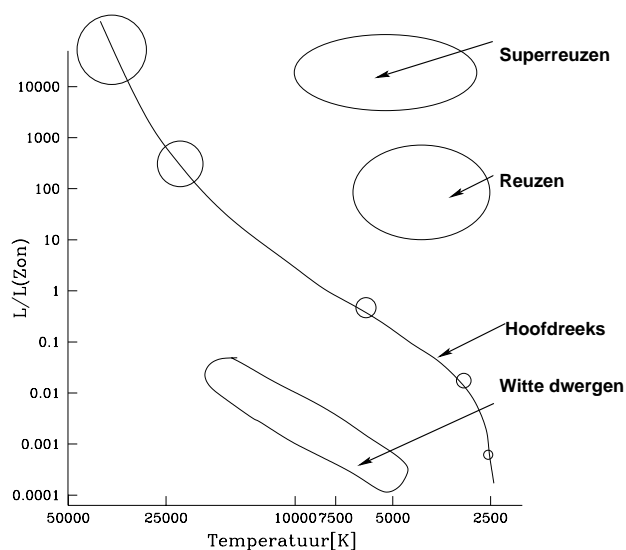
Figuur 3: *Grafiek van de helderheid van een ster (de 'magnitude') versus de temperatuur van de ster (de 'kleur'): dit type figuur heet een Hertzsprung-Russell (of HR) diagram, of ook wel een kleur-magnitude diagram. Astronomen gebruiken 2 criteria om sterren in deze figuur te classificeren. Het eerste criterium gebruikt het spectrum van de ster, de kleur van het licht dat de ster uitzendt. De kleur hangt af van de temperatuur van de ster. Zo ziet een hete ster (zoals Sirius) er blauw uit, terwijl een koele ster (zoals Betelgeuze) er rood uitziet. De zon is bijvoorbeeld geel. Het tweede criterium gebruikt de helderheid van de ster, dus eigenlijk de energie die per seconde door de ster wordt uitgezonden. Sterren liggen niet kris-kras verspreid in een HR diagram, maar ze liggen op bepaalde banden (reeksen). Elk van deze banden correspondeert met een zekere fase in het leven van de ster, i.e. een zekere manier waarop kernfusie plaatsvindt in het centrum van de ster.*

golflengten van een millimeter of iets minder dan een millimeter. Deze circumstellaire mantels zenden bovendien vaak maserstraling uit (het equivalent van laserstraling maar dan in het millimeter deel van het spectrum), afkomstig van moleculen zoals OH, SiO en H_2O (water). We kunnen deze maserstraling opvangen uit alle delen van de Melkweg. De golflengte van deze maserlijnen lijkt in de waarnemingen verschoven ten gevolge van het Doppler effect, hetzelfde effect waardoor een naderende ambulance een hogere toon lijkt te hebben dan één die weg rijdt. Daarom kunnen we door heel nauwkeurig de golflengte van de maseremissie te meten de snelheid van deze sterren langs de gezichtslijn bepalen.

Geëvolueerde reuzesterren die helder zijn op infrarode golflengten zijn vanwege bovenstaande redenen uitermate geschikt om de geschiedenis, de structuur en de kinematica (de beweging van o.m. sterren) van de Melkweg te achterhalen.

Deze sterren zijn gevormd op verschillende tijdstippen in de geschiedenis van de Melkweg, zoals blijkt uit hun onderlinge leeftijdsverschillen, waardoor zij ons in staat stellen om meer te weten te komen over stervorming in verschillende perioden van het bestaan van de Melkweg. Hun ruimtelijke verdeling wordt bepaald door het zwaartekrachtsveld van de Melkweg, daarom kunnen wij hen ook gebruiken om de massaverdeling die dit zwaartekrachtsveld in de Melkweg veroorzaakt te bepalen. Tenslotte kan de maser-emissie in deze sterren worden gebruikt om nauwkeurig de snelheden van deze sterren te achterhalen, waardoor ze heel goed bruikbaar zijn om de kinematica van de Melkweg te bestuderen.

Onze survey van SiO masers

In dit promotie-onderzoek hebben wij gegevens geanalyseerd uit verschillende surveys in het infrarood, en wij hebben ook SiO maserlijnen waargenomen rond geëvolueerde reuzesterren. De twee hoofddoelen van dit onderzoek zijn ten eerste het bepalen van de snelheid langs de gezichtslijn van de waargenomen sterren en ten tweede het bepalen van de massaverdeling van sterren in de binnenste delen van onze Melkweg. Eigenschappen van geëvolueerde sterren, zoals hun helderheid en massaverlies, kunnen ons verder iets vertellen over de voorwaarden waaronder masers in dit type sterren voorkomen.

Overzicht van dit proefschrift

We hebben gezocht naar SiO maserstraling afkomstig van sterren die in het infrarode deel van het spectrum helder zijn. Het resultaat was dat we het aantal van deze sterren (en daarmee ook hun snelheid langs de gezichtslijn) dat bekend was in de binnenste delen van de Melkweg bijna hebben kunnen verdubbelen. In **hoofdstuk 2** tonen we ons onderzoek dat is uitgevoerd met de IRAM 30 meter telescoop, die zich op de Pico Veleta in Spanje bevindt. De sterren die we selecteerden hebben dezelfde kleur als geëvolueerde sterren en bovendien verandert hun helderheid op een periodieke manier. We hebben deze criteria gebruikt omdat al bekend was dat maser-emissie vaker voorkomt bij dergelijke sterren. We vonden SiO masers in 271 van de onderzochte sterren, waarmee het aantal snelheden dat is bepaald voor sterren in de binnenste delen van de Melkweg met behulp van maser lijnen is verdubbeld.

De verdeling van energie van deze sterren over de verschillende golflengtegebieden (afgeleid uit de helderheid van de sterren in het nabije- en mid-infrarode deel van het spectrum) kan worden gebruikt om de helderheid en het massaverlies van deze sterren te bepalen. In **hoofdstuk 3** presenteren wij de helderheid van de 441 sterren die we hebben onderzocht op maserstraling op golflengten tussen 1μmen 25μm(ter vergelijking: het licht dat we met onze ogen zien heeft golflengten tussen de 0.4μmen 0.8μm) . Metingen gedaan op verschillende tijdstippen laten zien dat de meeste van deze bronnen in helderheid variëren. Hun kleur lijkt op die van veranderlijke geëvolueerde sterren in de zonsomgeving

151

waarvan we weten dat ze worden omgeven door een dunne mantel.

Om de intrinsieke helderheid van een ster te kunnen bepalen moeten we corrigeren voor interstellaire extinctie. We doen dit door de verdeling in het kleurmagnitude diagram (fig. 3) van de door ons waargenomen geëvolueerde sterren te vergelijken met de verdeling in het kleur-magnitude diagram van geëvolueerde sterren waarvan we de extinctie kennen. In **hoofdstuk 4** voeren we deze analyse uit, om daarmee de extinctie voor al onze SiO maserbronnen in de verschillende delen van de Melkweg te bepalen. Uit onze analyse volgen ook nieuwe, interessante waarden voor de interstellaire extinctie op verschillende golflengten.

In **hoofdstuk 5** berekenen we de intrinsieke helderheid van onze SiO sterren. Als we aannemen dat alle sterren die minder dan 5° van het Melkwegcentrum af staan dezelfde afstand tot de zon hebben, dan vinden we dat de piek in de helderheidsverdeling van onze sterren samenvalt met de piek in de verdeling van geëvolueerde sterren met OH maser emissie die zich in de buurt van het Melkwegcentrum bevinden (deze piek ligt bij ongeveer 8000 keer de helderheid van de zon). Onze data laat zien dat het belangrijkste verschil tussen sterren met OH masers en sterren met SiO masers is dat sterren met OH masers meer massa verliezen per jaar dan sterren met SiO masers. Sterren met SiO masers zijn echter makkelijker waar te nemen op golflengten in het nabij-infrarood dan sterren met OH masers, waardoor het makkelijker is om sterren met SiO masers te gebruiken om meer te weten te komen over de sterren in het midden van de circumstellaire mantel.

Een voorlopige bespreking van de banen van onze SiO maser sterren en een opzet voor onderzoek dat we in de toekomst willen doen wordt besproken in **hoofdstuk 6**. De beweging van de SiO maser sterren bevestigt het bestaan van een balk in het centrale deel van onze Melkweg. We zijn begonnen met een volledige analyse van de dynamica van onze sterren met als doel het verfijnen van de parameters die de balk beschrijven.

Tenslotte beschrijven we in **hoofdstuk 7** in het kort de ISOGAL survey, een survey in het mid-infrarood van het vlak van de Melkweg, maar voornamelijk in de richting van het Galactisch centrum. Deze survey is uitgevoerd om de structuur van de Melkweg te bepalen, in het bijzonder in gebieden in het centrum van de Melkweg en in gebieden waar de interstellaire extinctie groot is. Het is erg lastig om van afzonderlijke sterren de positie en helderheid te bepalen om daarmee een betrouwbare catalogus samen te stellen. In dit hoofdstuk beschrijven wij simulaties die gebruikt kunnen worden om de nauwkeurigheid van helderheden afgeleid uit de ISOGAL afbeeldingen te bepalen.

Curriculum Vitae

I am the daughter of Lucia and Leonardo Messineo; sister of Celestina and Saro. I was born at 2 o'clock on a starry night in a place called Salinella, high in the Sicilian mountains. From there in the night you almost always see many stars, but my grandmother told me not to count them because one could never finish. I attended elementary school in Petralia Soprana and intermediate and high school in Bagheria. I began studying Astronomy at the University of Bologna in the fall of 1989. I graduated on March 21st 1997 cum laude with a thesis entitled "the mixing problem in stellar evolution and the primordial He abundance determination from population ratios in globular clusters", which I did under the supervision of Prof. Francesco Ferraro from Bologna University and Prof. Flavio Fusi Pecci from the Bologna Observatory. In 1998 I went to Baltimore for six months as a summer student to work at the Space Telescope Science Institute with Dr. Antonella Nota on ISO data of LBV stars. In 1999 I worked at the Bologna Observatory on HST photometry of the globular cluster NGC 288 in collaboration with Dr. Michele Bellazzini. On December 1st 1999, I started my PhD research in Leiden under the supervision of Prof. Harm Habing. For the first year I worked on the ISOGAL catalogue, after which my research turned to late-type stars in the inner Galaxy. This work has been done in collaboration mainly with Prof. Harm Habing, Prof. Karl Menten from the Max-Planck-Institut fuer Radioastronomie in Bonn, Prof. Alain Omont from the Institut d'Astrophysique de Paris and Dr. Lorant Sjouwerman from the National Radio Astronomy Observatory in Socorro. During the past four years I have enjoyed observing with the IRAM 30m telescope in Spain four times as well as with the Heinrich Hertz Telescope in Arizona, with the ESO 3.6m and the CTIO 4m telescopes in Chile. I spent some weeks visiting the Institut d'Astrophysique de Paris, ESA in Villafranca del Castillo, Spain, and the CTIO in La Serena, Chile. I attended the YERAC 2000 school in Granada (Spain), the NOVA 2000 school in Dwingeloo (The Netherlands), and conferences in Angra dos Reis (Brazil), Sendai (Japan) and Kona (Hawaii). I gave invited presentations at the Max-Planck-Institut fuer Radioastronomie in Bonn (Germany), and at the Stichting Astronomisch Onderzoek in Nederland (ASTRON) in Dwingeloo. In September 2004 I will start working as a fellow at ESO in Garching (Germany).

Nawoord

The list of people I have interacted with, learnt from and spent time with during my PhD at Leiden Observatory is very long, and I apologise if I do not mention you all here.

During my first year Wing Fai was still in Leiden, always willing to answer my technical questions. Maria Rosa, Wouter, Inga, Garrelt, Pedro, Petra, Dominic, Yvonne and I were Harm's group and we used to have a group meeting every Friday, but someone would always complain because the two Italian girls would speak too long!! I spent a lot of time with Roderik, Dominic and Jes, being my officemates and I thank you for being so patient with me.

I used to visit the office of the computer group, which was next to mine, at least once per day reporting obscure behaviours of my computer and I am grateful to David, Tycho, Erik and Aart for always being very helpful. And the management assistants were always great! in particular I had the pleasure to work closely with Kirsten in organising the AGB workshop.

I had the privilege to work with wonderful people and great scientists, among them Karl, Alain, Lorant and Maartje: thanks for your support.

In the past months it has been a great pleasure to start working with Glenn on stellar dynamics and to create the ROTBAAN consortium!

I am indebted to Kirsten, Melanie and Frank for their careful reading of my manuscripts and to Dominic for translating the summary of this document into Dutch.

My numerous changes of apartments brought me to very close friendships with Maria Rosa, Petra, Emanuela and Elena, with whom I have shared so many cups of good coffee and tea.

Infine vorrei ringraziare particolarmente la mia famiglia per avermi incoraggiato nei miei studi e per aver sempre accettato tutte le mie scelte e la mia lontananza.

Grazie tanto!

Bedankt iedereen!